

**Development of Monolithic Regenerator Technology  
for Low Temperature (4 K) Gifford-McMahon Cryocoolers.**

by

**Walter Roberto Mérida Donis  
BSc., Trent University, 1993**

A Thesis Submitted in Partial Fulfillment of the  
Requirements for the Degree of

**MASTER OF APPLIED SCIENCE**

in the Department of Mechanical Engineering

We accept this thesis as conforming  
to the required standard

[Redacted Signature]

---

Dr. John A. Barclay, Supervisor (Department of Mechanical Engineering).

[Redacted Signature]

---

Dr. Nedjib Djilali, Departmental Member (Department of Mechanical Engineering).

[Redacted Signature]

---

Dr. Tapan Bose, Outside Member (Hydrogen Research Institute, Department of Physics,  
Université du Québec à Trois Rivières).

[Redacted Signature]

---

Dr. Toru Kuriyama, External Examiner (Toshiba Research and Development Center,  
Kawasaki, Japan).

© Walter Roberto Merida Donis, 1996

University of Victoria

All rights reserved. This thesis may not be reproduced in whole or in part, by photocopy  
or other means, without the written permission of the author.

Supervisor: Dr. John A. Barclay

### ABSTRACT

A two-stage regenerative cryocooler has been selected to produce and maintain the low temperatures required by the superconducting magnet system in an active magnetic regenerative liquefier (AMRL). By using a mechanical cryocooler, the need for liquid cryogens has been eliminated, thereby simplifying the overall system design. The operation of practical AMRLs requires relatively large magnetic fields (e.g., 8 T). Currently, these fields can only be produced via low-temperature superconducting magnets that typically operate at liquid helium temperatures (4.2 K).


Obtaining non-zero cooling powers below 10 K is difficult when regenerative cryocoolers are used. This is mainly because the volumetric heat capacity of pressurized helium (the working fluid) is much higher than the corresponding value for lead (the material commonly used in low temperature regenerators). A commercial two-stage Gifford-McMahon cryogenic refrigerator has been successfully modified to reduce its minimum, no-load temperature from  $6.1 \pm 0.1$  K to  $3.42 \pm 0.05$  K at a nominal operating frequency of 1.2 Hz. The cooling power at  $4.2 \pm 0.1$  K was measured to be 0.430 W with zero load at the first stage. The superconducting magnets in the AMRL have been designed to operate at 4.5 K. The refrigeration power available at this temperature was measured to be 0.504 W with a simultaneous second-stage load of 20W at  $42.8 \pm 0.5$  K.


The required modifications to the GM cryocooler included the selection, preparation and characterization of appropriate magnetic regenerator materials, their fabrication into highly efficient and reliable cryogenic regenerators, and the modification of the frequency of operation. A novel and proprietary manufacturing technique was also developed to ensure the structural integrity of the second-stage regenerator without the use of spherical particles. This technique used irregularly-shaped particles made of rare-earth/transition


metal alloys held together by a cryogenic epoxy matrix. The bonding of the entire regenerator into a monolithic yet porous bed makes it highly stable and resistant to mechanical and thermal stresses. In addition, the high cost associated with the production of spherical particles has been eliminated. To the author's knowledge, this is the first time that such a technique has been used to achieve sub liquid helium temperatures with a two-stage GM cryocooler.


Lastly, a general purpose, cryogen free materials characterization system was conceptually designed as a potential application for the modified GM cryocooler. The modularity implemented in this design makes it possible to exchange material samples or entire experimental inserts without interrupting the operation of the superconducting magnet system. The conceptual design of an experimental insert to measure heat capacity has also been included as part of this work. The temperature range covered by this insert ranges from 4 to 300 K with magnetic field intensities up to 8 T.

Examiners:

  
\_\_\_\_\_  
Dr. John A. Barclay, Supervisor (Department of Mechanical Engineering).

  
\_\_\_\_\_  
Dr. Nedjib Djilali, Departmental Member (Department of Mechanical Engineering).

  
\_\_\_\_\_  
Dr. Tapan Bose, Outside Member (Hydrogen Research Institute, Department of Physics, Université du Québec à Trois Rivières).

  
\_\_\_\_\_  
Dr. Toru Kuriyama, External Examiner (Toshiba Research and Development Center, Kawasaki, Japan).

# Table of Contents

Abstract .....	ii
Table of Contents .....	iv
List of Figures .....	x
List of Tables. ....	xvi
Units and Conversion factors .....	xviii
Nomenclature .....	xix
Constants .....	xxiv
Acronyms and abbreviations .....	xxiv
Acknowledgments .....	xxvi

## Chapter 1

### 1.0 Introduction

1.1 Motivation .....	1
1.2 The Evolving Energy System .....	3
1.2.1 Past and Present Evolutionary Patterns .....	3
1.2.2 The Future Energy System .....	4
1.3 Alternative Transportation Fuels (ATFs) .....	6
1.3.1 Current Role of Alternative Fuels .....	8
1.4 Alternative Fuels: Barriers and Attractors .....	12
1.4.1 Attractor - Energy Security .....	12
1.4.2 Attractor - Environmental Concerns .....	13
1.4.3 Attractor - Geopolitical Changes .....	15
1.4.4 Barrier - Low Volumetric Energy densities .....	17
1.4.5 Barrier/Attractor - Economics .....	18
1.5 The Cfs Natural Gas Liquefier Project .....	19

1.6 Thesis Objectives .....	22
-----------------------------	----

## Chapter 2

### 2.0 Background and Previous Work

2.1 The Magnetocaloric Effect (MCE).....	23
2.2 Magnetic Refrigeration (MR) Systems .....	24
2.3 The Cfs Active Magnetic Regenerative Liquefier (AMRL).....	25
2.4 Superconducting Materials Technology.....	26
2.4.1 Conductively Cooled SCM Systems .....	28
2.5 Passive Regenerators.....	29
2.5.1 The Gifford-McMahon (GM) Refrigerator .....	31
2.5.2 4 K GM Cryocoolers .....	34
2.6 Selection Criteria for the Large Thermal Mass Regenerator Materials in Low Temperature (4 K) GM Cryocoolers .....	39
2.7 Traditional Manufacturing Techniques for Regenerator Materials.....	41
2.7.1 Gas Atomization.....	41
2.7.2 Centrifugal Atomization.....	43
2.8 Current Research on Alternative Regenerator Geometries .....	44
2.8.1 Wire Screens .....	44
2.8.2 Perforated Plates.....	44
2.9 New Monolithic Regenerators using Irregularly-shaped RE/TM Particles.....	45

## Chapter 3

### 3.0 Experimental Techniques

3.1 Experimental Chamber.....	47
3.2 Thermal Insulation .....	49
3.2.1 Vacuum Insulation .....	49
3.2.2 Radiation Shielding.....	50
3.2.2.1 Multilayer Insulation (MLI) .....	50
3.2.3 Heat Leaks.....	52

3.3 Instrumentation and Data Acquisition (DAQ) System.....	52
3.3.1 Computer System .....	53
3.3.2 Data Acquisition Board.....	53
3.3.3 Signal Conditioning and Multiplexing.....	53
3.3.4 Transducers .....	55
3.3.4.1 Temperature .....	55
3.3.4.2 Gas Flow and Pressure Drop .....	56
3.3.5 DAQ Software.....	58
3.4 Characterization of a Commercial GM Cryocooler .....	60
3.4.1 The Cold Head .....	61
3.4.2 The Helium Compressor .....	63
3.4.3 Accessories.....	65
3.5 Performance Characteristics.....	66
3.5.1 Cool-down Times.....	67
3.5.2 Cooling Power.....	67

## **Chapter 4**

### **4.0 GM Cryocooler Modifications**

4.1 Performance Parameters.....	70
4.2 Reverse Engineering of the Second-stage Regenerator in a Conventional GM Cryocooler.....	71
4.2.1 Regenerator Assembly.....	74
4.3 Regenerator Materials Preparation.....	76
4.3.1 Alloy Preparation .....	77
4.3.2 Sample Characterization .....	78
4.3.3 Particle Fabrication .....	80
4.4 Possible Methods to Prevent Particle Disintegration .....	82
4.4.1 Metallic Vapour Coating.....	82
4.4.2 Immersion in a Molten Metal Bath .....	84
4.4.3 Monolithic Regenerator Beds Using a Cryogenic Epoxy.....	85

4.5 Fabrication of monolithic Regenerator Beds.....	86
4.6 Structural Integrity Tests .....	88
4.7 Regenerator Beds Using RE/TM Alloys .....	91
4.7.1 Regenerator 1: A Two-layer, Hybrid Regenerator Bed.....	91
4.7.2 Regenerator 2: A Three-layer, Hybrid Regenerator Bed.....	95
4.7.2.1 Degradation of Performance Due to Particle Fragmentation.....	96
4.7.3 Regenerator 3: A Three-layer, Monolithic Regenerator Bed .....	97
4.8 Refrigeration Power .....	100

## Chapter 5

### 5.0 Conclusions and Future Work

5.1 Summary .....	102
5.1.1 Validation of Baseline Regenerator Manufacturing Techniques ...	103
5.1.2 New Manufacturing Techniques for Brittle Regenerator Materials	103
5.1.3 Refrigeration Power Available at 4.2 K .....	105
5.1.4 Cryogen Free Materials Characterization System (CFMCS) .....	106
5.2 Recommendations and Future Work.....	107
5.2.1 Cleanliness .....	107
5.2.2 Sealing.....	107
5.2.3 Material Layers in Hybrid Regenerators .....	111
5.2.4 Regenerator Size .....	112
5.2.5 Increased Expansion Volume(s).....	113
5.2.6 Cycle Frequency .....	113
5.2.7 Valve Timing.....	114
5.2 Implementation of a GM Cryocooler in the Overall AMRL Project .....	114

<b>References</b> .....	115
-------------------------	-----

## **Appendix A**

The Magnetocaloric Effect (MCE).....	129
--------------------------------------	-----

## **Appendix B**

Magnetic Refrigeration Cycles.....	132
------------------------------------	-----

## **Appendix C**

Magnetic Refrigeration Systems .....	134
--------------------------------------	-----

## **Appendix D**

Heat Capacity of Solids at Low Temperatures.....	137
--	-----

## **Appendix E**

Selection Criteria for Cryogenic Regenerator Materials with High Thermal Mass..	139
---	-----

## **Appendix F**

Heat Leaks.....	142
-----------------	-----

## **Appendix G**

Calculation of the Required Masses for Arc-melted RE/TM Samples .....	149
---	-----

## **Appendix H**

Thermal Masses in the Second-stage Regenerator of a GM Cryocooler.....	151
--	-----

## **Appendix I**

Error Analysis.....	158
I.1 DAQ System Resolution.....	158
I.2 Applied Excitation Error.....	159
I.3 Thermoelectric Voltages and Zero Offsets .....	160
I.4 Ground Loops and Electromagnetic Noise .....	161
I.5 Lead Wire Resistance.....	162
I.6 Sensor Self-heating .....	162
I.7 Sensor Calibration.....	163
I.8 Interpolation Uncertainty .....	163
I.9 Total Error.....	167

I.10 Other Sensors .....	168
--------------------------	-----

## **Appendix J**

DAQ Software Documentation .....	172
J.1 List of SubVIs .....	172
J.1.1 AI Config.vi .....	172
J.1.2 AI Start.vi .....	173
J.1.3 AI Read.vi .....	174
J.1.4 General Error Handler.vi .....	174
J.1.5 V2T CFS.vi 1.1 .....	174
J.2 Front Panel Controls .....	175
J.3 Indicators .....	179

## **Appendix K**

Variable Temperature and Field Cryostat .....	180
K.1 Comparison with Current Technologies .....	181
K.2 A Novel Cryogen Free Materials Characterization System (CFMCS) .....	186
K.2.1 Superconducting Magnet Subsystem .....	189
K.2.2 Sample Cooling Loop .....	189
K.2.3 Sample Exchange Chamber .....	191
K.3 Experimental Insert .....	192
K.4 Instrumentation .....	195
K.5 Control System .....	197

# List of Figures

Figure 1-1: The architecture of the energy system. ....	2
Figure 1-2: Global primary energy source substitution (F = share of total market). Smooth lines represent model predictions. Historical data are superimposed as jagged lines. ....	5
Figure 1-3: Total projected number of AFVs in the United States by 1995. ....	9
Figure 1-4: Annual (1993) primary energy supply by sector (a), and by energy source (b). ....	12
Figure 1-5: Annual emissions of "criteria pollutants" in the United States (1990). ....	13
Figure 1-6: Volumetric energy densities for some ATFs compared to diesel and gasoline. These values correspond to the fuel under typical storage conditions for each fuel. ....	18
Figure 1-7: Schematic diagram of the CNG/LNG refueling station being designed by the Cfs Group. ....	21
Figure 2-1: The magnetocaloric effect manifests itself as a change in temperature. ....	23
Figure 2-2: Conceptual comparison between magnetic and conventional refrigeration cycles. ....	24
Figure 2-3: Schematic diagram of the rotary AMR for natural gas liquefaction being developed by the Cfs group. ....	25
Figure 2-4: Critical surface for NbTi. ....	27
Figure 2-5: The cycle of operation in a two-stage GM cryocooler. ....	33
Figure 2-6: Comparison between the volumetric heat capacity of lead and helium gas at different pressures. ....	35
Figure 2-7: Planar view of the conductively cooled magnet system in the AMRL. ....	38
Figure 2-8: Volumetric heat capacities of some RE/TM alloys compared to lead. ....	40
Figure 2-9: Schematic representation of a typical gas atomization apparatus [123]. ....	42
Figure 2-10: Two common implementations of centrifugal atomization techniques. Rotating consumable electrode (a) and spinning disk (b). ....	43

Figure 3-1: Schematic diagram of the experimental setup used to test the GM cryocooler.....	48
Figure 3-2: Schematic representation of heat transfer as a function of gas pressure ( $D$ = distance between warm and cold bodies).....	49
Figure 3-3: Schematic layout of the DAQ system. ....	54
Figure 3-4: Schematic representation of the apparatus used to measure the pressure drop across different regenerator beds.....	57
Figure 3-5: The main control panel for GM DAQ 1.0.....	59
Figure 3-6: KelCool 130™ cold head; motor casing (a), gas return and supply lines (b, c), electrical connector (d), first and second stage enclosures (e, f), first and second stage copper flanges (g, h).....	61
Figure 3-7: Cold head internal assembly; drive unit (1), displacer enclosure (2), first and second stage regenerator containers (3,4), first stage dynamic seal (5), second stage seal assembly (6), second stage seal retainer (7), first stage seal retainer (8), scotch yoke connecting link (9), scotch yoke pin (10), first stage connecting pin (11), room temperature O-ring (12).....	62
Figure 3-8: Drive unit subassembly; crank housing (1), valve housing (2), scotch yoke (3), stepping motor (4), electrical connector (5), crank assembly (6), motor housing (7), gas return and supply line connections (8,9), valve housing retainer (10), O-rings (11-15).....	63
Figure 3-9: Schematic diagram of the UCC 110S compressor. The components include: helium compressor module (1), heat exchanger (2), low pressure helium reservoir (3), oil separator (4), vapour adsorber (5), relief valve (6), bypass valve (7), oil filter (8), oil solenoid valve (9), gas supply connection (10), gas supply pressure gauge (11), gas charge connection (12), gas return connection (13), gas return pressure gauge (14), cooling water connections (15, 16). ....	64
Figure 3-10: Schematic representation of the refilling adapter using to purge the cold head space after exposure to air. ....	66

- Figure 3-11: Typical cool-down times for the GM cryocooler operating with parasitic thermal loads only ( $D1/2 = \pm 0.05$  K,  $D2/2 = \pm 0.5$  K)..... 67
- Figure 3-12: Temperature at the second stage as a function of cooling load. .... 68
- Figure 3-13: First stage temperature as a function of cooling load at the second stage.... 69
- Figure 4-1: Cutaway view of the stainless steel body for the KelCool 130™ cold head.71
- Figure 4-2: Exploded view of the displacer assembly; connecting pin to drive mechanism (1), first-stage regenerator container, regenerator space (3), first-stage end plug (4), stainless steel pins (5, 9), universal joint (6), second-stage regenerator container (7), second-stage end plug (8). .... 72
- Figure 4-3: The second-stage regenerator container assembly includes first stage end plug (1), universal joint (2), second stage regenerator container (3), second-stage end plug (4), perforated brass plate (5), gas exhaust holes (6), second-stage seal groove (7), stainless steel pin (8), regenerator space (9). The stainless steel screens used at the ends of the regenerator space are not shown. .... 73
- Figure 4-4: The second-stage seal assembly. The retaining ring (A), holds the piston-seal (B) closed when the displacer is lowered into the stainless steel casing. During operation, the backup spring (C) forces the seal against the wall of the casing. .... 75
- Figure 4-5: Modified plug assembly: phenolic plastic plug (a), retaining ring (b), stainless steel screens (c), perforated plate (d). .... 76
- Figure 4-6: X-ray spectral analysis for the RE/TM alloys prepared. .... 79
- Figure 4-7: The composition of the RE/TM samples as measured by Energy-dispersive X-ray spectral analysis (A to F = Er<sub>3</sub>Ni, G to L = ErNi<sub>0.9</sub>Co<sub>0.1</sub>). The columns at the beginning of the series represent the expected compositions for each alloy. .... 80
- Figure 4-8: Schematic diagram of the mechanical mortar and pestle apparatus. The operating parameters that gave the best results were: a = 2.5mm, b = 1.0mm, F1 = 150rpm, F2 = 60rpm. The amount of material processed was only a few

- grams at the time to allow a higher yield of particles in the desired size range. .... 81
- Figure 4-9: Size distribution for the irregularly-shaped,  $\text{Er}_3\text{Ni}$  particles produced by mechanical crushing. The results obtained with  $\text{ErNi}_{0.9}\text{Co}_{0.1}$  were similar. .... 82
- Figure 4-10: Schematic representation of the apparatus used to test vapour coating techniques (the heater around the metal vapourizer is not shown). .... 83
- Figure 4-11: The excess epoxy solution was removed by suction (a), and by applying positive pressure to one end of the regenerator bed (b). .... 87
- Figure 4-12: Comparison between the two different epoxy removal techniques. The theoretical curve corresponds to McDonald's modification of Ergun's equation. .... 88
- Figure 4-13: A monolithic bed of  $\text{GdAl}_2$  was used to perform structural integrity tests at cryogenic temperatures. .... 89
- Figure 4-14: Apparatus used for structural integrity tests (a), (b) solenoid valves, (c), (d) buffer volume reservoirs, (e) helium gas inlet, (f) wiring to generator. .... 90
- Figure 4-15: The manufacturing technique for a hybrid, monolithic regenerator bed. The process included: removal of excess epoxy solution by pressurized gas (a), extraction of the monolithic bed from a Teflon tube (b), insertion into a regenerator container (c), and sealing of the entire assembly by gluing the end plug in place (d). .... 92
- Figure 4-16: Pressure drop across the hybrid  $\text{Er}_3\text{Ni} + \text{ErNi}_{0.9}\text{Co}_{0.1}$  regenerator bed. The fluid used was helium gas at a mean pressure of 100psig (at room temperature). .... 93
- Figure 4-17: The performance of REG2 degraded rapidly with time. The operation of the GM Cryocooler was halted after approximately 12 hours of continuous operation. .... 96
- Figure 4-18: Modified manufacturing technique for monolithic regenerator beds. The epoxy mixture was applied directly to the entire regenerator assembly. The intermediate step involving a Teflon tube was eliminated. .... 98

Figure 4-19: The minimum, no-load temperatures obtained with REG3. ....	99
Figure 4-20: Measured temperature at the second stage of the GM cryocooler as a function of cooling load. ....	100
Figure 4-21: Measured temperature at the first stage of the GM cryocooler as a function of second-stage cooling load. ....	101
Figure 4-22: The ultimate temperature obtained with the GM cryocooler immediately after it was purchased (Balzers), and after it was modified (Cryofuels). The horizontal plane represents the normal boiling point of helium (4.2 K). ..	101
Figure 5-1: Cross sectional view of spring-energized seals. ....	108
Figure 5-2: In spring-energized seals, the spring force remains constant over a wide range of deflections. ....	109
Figure 5-3: Two alternative mounting techniques for the second-stage seal: housing mounting (a), and piston mounting (b). ....	109
Figure 5-4: An optimized hybrid regenerator using four layers of different materials (A = ErNi <sub>0.9</sub> Co <sub>0.1</sub> , B = Er <sub>0.9</sub> Yb <sub>0.1</sub> Ni, C = Er <sub>3</sub> Ni, D = Pb). The temperature profile is assumed to be linear. ....	112
Figure B-1: Schematic representation of idealized T-S diagrams for some common magnetic refrigeration cycles. Magnetic Carnot cycle (a), magnetic Ericsson cycle (b), magnetic Brayton cycle (c), and AMR cycle. ....	132
Figure B-2: Adiabatic temperature change in gadolinium as a function of both temperature, and magnetic field strength. ....	133
Figure E-1: Magnetic entropy and de Gennes factors for the trivalent lanthanide ions.	141
Figure G-1: The main input windows for a spreadsheet program designed to calculate material masses. ....	149
Figure H-1: Approximated heat capacity curves for different materials and helium gas at different pressures. The approximations for RE/TM alloys are not valid at temperatures higher than 25 K. ....	153
Figure H-2: A linear temperature profile across a regenerator bed. ....	154
Figure K-1: The MaglabVSM® magnetometer from Oxford Instruments™. ....	182

Figure K-2: Sample pucks used in the PPMS®. The samples in the picture have been wired to perform four different types of measurement: electrical properties of a SQUID (a), heat capacity (b), Hall effect (c), and electrical resistivity (d). .....	182
Figure K-3: The sample space in the PPMS®. ....	183
Figure K-4: A schematic representation of the Pulselab® system from Oxford Instruments™. ....	184
Figure K-5: A cryogen-free SCM system with a variable temperature insert.....	185
Figure K-6: A conceptual representation of the CFMCS currently under development at UVic. ....	187
Figure K-7: Heat exchangers will be attached to the first and second stages of the cryocooler.....	190
Figure K-8: Assembly drawing of the experimental insert designed to measure heat capacity.....	193
Figure K-9: Cooling and measurement positions for heat capacity measurements. ....	194

# List of Tables

Table 1-1 : Physical and chemical properties of some ATFs compared to diesel and gasoline.....	7
Table 1-2 : Emissions in grams per vehicle-mile for some ATFs during a full fuel cycle (RFG= Reformulated gasoline)[21]. .....	14
Table 2-3: Desirable characteristics in an ideal regenerator compared to the actual properties of practical devices.....	31
Table 2-4: Prices for some rare-earth metals (purity = 99.9%). .....	41
Table 3-1: Summary of heat leaks into the GM cryocooler.....	52
Table 3-2: Measurement precision for a PCI-MIO16XE50 DAQ board at different gain settings.....	53
Table 3-3: Calibration specifications for the ruthenium oxide resistor used to measure the temperature at the second stage of the cryocooler.....	56
Table 3-4: Summary of the specifications for a two-stage GM cryocooler.....	60
Table 3-5: Specifications for the UCC 110S Helium compressor.....	65
Table 4-1: Typical masses used for the preparation of RE/TM alloys ( $\pm 0.002\text{g}$ ).....	78
Table 4-2: Physical properties for Stycast® 1266 epoxy.....	86
Table 4-3: Monolithic regenerator beds using 200mm copper particles and diluted epoxy solutions.....	87
Table 4-4: Particle-size distribution in REG2 after 12 hours of continuous operation. The total amount of fragmented particles was approximately 20% of the original total mass for both materials. All masses were measured to a precision of $\pm 0.002\text{ g}$ .....	97
Table 4-5: Summary of the results obtained with different regenerators at the second stage of the modified GM cryocooler.....	100
Table D-1: Debye characteristic temperatures of some selected elements (in Kelvins, at $T = qD/2$ ). The values for heavy rare-earths are lower than those found in transition metals. ....	137

Table D-2:	Electronic heat capacity coefficients for selected elements .....	138
Table E-1:	The theoretical magnetic moments of TM and RE compared to the observed values.....	140
Table H-1:	Polynomial coefficient for the approximated heat capacity curves ( $C_p$ in $J K^{-1} cm^{-3}$ , $T$ in $K$ , $x$ in $cm$ ).....	153
Table H-2:	Comparison between the total thermal masses below certain temperatures.	156
Table I-1:	Polynomial coefficients for the transfer function used for PRTs operating under a constant current of 1.000 mA. ....	165
Table I-2:	Interpolation errors at different temperature ranges for values calculated using Equation I-11. ....	165
Table I-3:	Polynomial coefficients for the transfer function used for the ruthenium oxide sensor operating under a constant current of 10.000 mA.....	166
Table I-4:	Interpolation errors at different temperature ranges for the ruthenium oxide sensor.....	167
Table I-5:	Calibration data for the MKS® flowmeter used to measure helium flow.	168
Table I-6:	Calibration data for the ruthenium oxide resistive sensor. The predicted temperature values were obtained using Equations I-12, I-13, and I-14. ...	170
Table I-7:	Typical voltage data for uncalibrated PRTs. The temperature values are compared to those predicted by Equation I-11.....	171
Table K-1:	Design specifications for the SCM subsystem in the CFMCS.....	189
Table K-2:	Typical magnetic field-induced errors and thermal response times for different sensors. ....	196

# Units and Conversion Factors

Although every effort has been made to maintain a consistent system of units, the use of SI conventions in engineering applications is sometimes impractical. The conversion factors required to convert different units to SI are given in the following table:

To convert from	to	multiply by
<b>Length</b>		
inch	m	$2.54000 \times 10^{-2}$
foot	m	$3.04800 \times 10^{-1}$
<b>Area</b>		
square inch	m <sup>2</sup>	$6.45160 \times 10^{-4}$
square foot	m <sup>2</sup>	$9.29030 \times 10^{-2}$
<b>Volume</b>		
cubic inch	m <sup>3</sup>	$1.63871 \times 10^{-5}$
gallon (U.S.)	m <sup>3</sup>	$3.78541 \times 10^{-3}$
liter (L)	m <sup>3</sup>	$1.00000 \times 10^{-3}$
<b>Pressure</b>		
psia	Pa	$6.8947 \times 10^{+3}$
atm	Pa	$1.01325 \times 10^{+5}$
torr	Pa	$1.33322 \times 10^{+2}$
<b>Energy</b>		
Btu	J	$1.05506 \times 10^{+3}$
kW hr	J	$3.60000 \times 10^{+6}$
<b>Thermal Conductivity</b>		
Btu hr <sup>-1</sup> ft <sup>-1</sup> °F <sup>-1</sup>	W m <sup>-1</sup> K <sup>-1</sup>	1.73073
cal s <sup>-1</sup> cm <sup>-1</sup> °C <sup>-1</sup>	W m <sup>-1</sup> K <sup>-1</sup>	$4.18680 \times 10^{+4}$
<b>Heat Transfer Coefficient</b>		
Btu hr <sup>-1</sup> ft <sup>-2</sup> °F <sup>-1</sup>	W m <sup>-2</sup> K <sup>-1</sup>	5.67826
cal s <sup>-1</sup> cm <sup>-2</sup> °C <sup>-1</sup>	W m <sup>-2</sup> K <sup>-1</sup>	$4.18680 \times 10^{+4}$
<b>Temperature</b>		
°C = 5/9 (°F - 32)		
K = °C + 273.15		

# Nomenclature

Symbol	Meaning	Units:
$\bar{\lambda}$	Molecular mean free path	m
$\alpha$	porosity	
$\varepsilon$	Additive, worst-case error	
$\varepsilon^x$	Statistical, most probable error	
$\chi(T,H)$	Magnetic susceptibility as a function of temperature and magnetic field intensity	
$\delta C$	Thermal expansion correction for heat capacity	$J\ kg^{-1}\ K^{-1}$
$\theta_D$	Debye temperature	K
$\varepsilon_{DAQ}$	Resolution of DAQ system	V
$\gamma_e$	electronic specific heat coefficient	$J\ kg^{-1}\ K^{-1}$
$\Delta H_{vap}$	Specific heat of vaporization	$J\ kg^{-1}$
$\mu_i$	Electrochemical potential of species i	$J\ mol^{-1}$
$\Delta P$	Pressure drop	Pa, $Pa\ m^{-1}$
$\Delta T_{ad}$	Adiabatic temperature change	K
$\Delta T_{ad}(T,H)$	Adiabatic temperature change as a function of temperature and magnetic field intensity.	K
$\theta_{xx}$	Integrated thermal conductivity from $T = 0$ to $T = xx$	$W\ m^{-1}$
$a$	number of free electrons per atom	
A1	Area of the first stage cylindrical enclosure.	$m^2$
A1_He	Area at either end of the first stage cylindrical enclosure.	$m^2$
A2	Area of the second stage cylindrical enclosure.	$m^2$

## Nomenclature (continued)

A2_He	Area at either end of the second stage cylindrical enclosure.	$m^2$
aPpsi	Constant used to approximate the thermal conductivity of helium gas at pressure P	$W m^{-1} K^{-1}$
bPpsi	Coefficient used to approximate the thermal conductivity of helium gas at pressure P	$W m^{-1} K^{-2}$
C	Heat capacity	$J kg^{-1} K^{-1}$
$C(T,H)$	Heat capacity as a function of temperature and magnetic field intensity	$J kg^{-1} K^{-1}$
$C_E$	Electronic heat capacity	$J kg^{-1} K^{-1}$
$C_H$	Heat capacity at constant magnetic field intensity	$J kg^{-1} K^{-1}$
$C_L$	Lattice heat capacity	$J kg^{-1} K^{-1}$
$C_M$	Magnetic heat capacity	$J kg^{-1} K^{-1}$
$C_P$	Heat capacity at constant pressure	$J kg^{-1} K^{-1}$
$C_v$	Heat capacity at constant volume	$J kg^{-1} K^{-1}$
Dcopper	Diameter of the copper heater wire	m
Din1	Inner diameter of the first stage stainless steel housing	m
Din2	Inner diameter of the second stage stainless steel housing	m
Dout1	Outer diameter of the first stage stainless steel housing	m
Dout2	Outer diameter of the second stage stainless steel housing	m
Dshield	Diameter of the radiation shield	m
Dvessel	Diameter of the experiemntal chamber	m
eAlT	emissivity value for aluminum temperature	

## T

**Nomenclature (continued)**

e <sub>brassT</sub>	emissivity value for polished brass at temperature T	
e <sub>ssT</sub>	emissivity value for stainless steel at temperature T	
Fe	Emissivity factor	
g	gyromagnetic ratio	
G	De Gennes factor	
H	Applied magnetic field	A m <sup>-1</sup>
H <sub>c</sub>	Critical applied field	A m <sup>-1</sup>
I <sub>copperY</sub>	Electrical current required to power the heater at stage Y	A
I <sub>phosphorY</sub>	Electrical current required to power the sensors at stage Y	A
J	Total quantum number	
<b>J</b>	Total atomic angular momentum vector	
J <sub>c</sub>	Critical current density	Am <sup>-2</sup>
k <sub>T</sub>	Thermal conductivity	W m <sup>-1</sup> K <sup>-1</sup>
k <sub>T</sub> P <sub>psi</sub> (T)	Temperature-dependent thermal conductivity of helium gas at pressure P	W m <sup>-1</sup> K <sup>-1</sup>
k <sub>T_MLI</sub> stageY	Thermal conductivity value for the MLI around stage Y	W m <sup>-1</sup> K <sup>-1</sup>
L	Orbital quantum number	
<b>L</b>	Total atomic orbital angular momentum vector	
L <sub>copper_stageY</sub>	Length of copper wire to stage Y	m
L <sub>shield</sub>	Length of radiation shield	m
L <sub>ss1</sub>	Length of the first stage stainless steel	m

housing

## Nomenclature (continued)

$L_{ss2}$	Length of the second stage stainless steel housing	m
$L_{vessel}$	Length of the experimental chamber	m
$M$	Magnetization	A m <sup>-1</sup>
$M_m$	Atomic or molecular weight	kg mol <sup>-1</sup>
$m_s$	Mass of a given material sample	kg
$n$	ions/atoms per mole	mol <sup>-1</sup>
$N_{MLI}$	Number of layer of supersinsulation	
$n_e$	number of electrons per unit volume	m <sup>-3</sup>
$N_i$	Amount of species i	mol
$N_{leads\_copper1}$	Number of lead wires	
$P$	Pressure	Pa
$Q_{c1}$	Conductive heat leak along the first stage stainless steel container walls	W
$Q_{c2}$	Conductive heat leak along the second stage stainless steel container walls	W
$Q_{cond\_HePpsi\_stageY}$	Total conductive heat leak into stage Y due to the presence of pressurized helium at pressure P	W
$Q_{copper\_stageY}$	Conductive heat leak into stage Y through copper wires	W
$Q_{in}$	Heat input	J
$Q_{MLIstageY}$	Heat leak through MLI around stage Y	W
$Q_{rad\_Y}$	Radiative heat leak into stage Y	W
$R_{copper}$	Electrical resistivity of the copper wires	$\Omega$ m <sup>-1</sup>
$R_{phosphor}$	Electrical resistivity of the Phosphor Bronze instrumentation wires	$\Omega$ m <sup>-1</sup>

$S$  Entropy  $\text{J K}^{-1}$

## Nomenclature (continued)

$S$	Spin quantum number	
$\mathbf{S}$	Total atomic spin angular momentum vector	
$S_{\text{electronic}}$	Magnetic contribution to total entropy	$\text{J K}^{-1}$
$S_{\text{lattice}}$	Lattice contribution to total entropy	$\text{J K}^{-1}$
$S_{\text{magnetic}}$	Electronic contribution to total entropy	$\text{J K}^{-1}$
$T_1$	Temperature at the second stage of the cryocooler	$\text{K}$
$T_2$	Temperature at the first stage of the cryocooler	$\text{K}$
$T_3$	Room temperature	$\text{K}$
$T_c$	Critical temperature	$\text{K}$
$T_C$	Curie Temperature	$\text{K}$
$T_f$	Final temperature	$\text{K}$
$T_i$	Initial temperature	$\text{K}$
$U$	Internal Energy	$\text{J}$
$V$	Volume	$\text{m}^3$
$V_+, V_-$	Polarity-dependent voltage reading from a temperature sensor under constant current excitation	$\text{V}$
$v_a$	speed of sound in a solid	$\text{m s}^{-1}$
$V_m$	Molar volume	$\text{m}^3 \text{mol}^{-1}$
$V_m$	Molar volume	$\text{m}^3 \text{mol}^{-1}$
$V_o$	Sum of thermoelectrical and zero offset voltage errors	$\text{V}$

## Constants

Constant Name	Symbol	Value	Units
Planck's constant	$h$	$6.626 \times 10^{-34}$	J s
Gas constant	$R$	8.3144	J K <sup>-1</sup> mol <sup>-1</sup>
Avogadro's number	$N_o$	$6.02205 \times 10^{23}$	mol <sup>-1</sup>
Mass of electron	$m_e$	$9.10953 \times 10^{-31}$	kg
Permeability of free space	$\mu_o$	$4\pi \times 10^{-7}$	W m <sup>-2</sup> K <sup>-4</sup>
Bohr magneton	$\mu_B$	$9.2741 \times 10^{-24}$	J T <sup>-1</sup>

## Acronyms and Abbreviations

ADC	Analog to digital converter
AFV	Alternative fuel vehicle
AMRL	Active magnetic regenerative liquefier
ANG	Absorbed natural gas
ATF	Alternative transportation fuel
CAD	Computer aided design
CAE	Computer aided engineering
CAM	Computer aided manufacturing
CFMCS	Cryogen free materials characterization system
CNG	Compressed natural gas
DAC	Digital to analog converter
DAQ	Data Acquisition
EMF	Electro-motive force
EPACT	Energy Policy Act
GM	Gifford-McMahon
ICE	Internal combustion engine
IESVic	Institute for Integrated Energy Systems at the University of Victoria

IIASA International Institute for Applied Systems Analysis

## **Acronyms and Abbreviations (continued)**

ITS	International temperature scale
LEV	Low emission vehicle
LNG	Liquid natural gas
MLI	Multi layer insulation
NAFTA	North American free trade agreement
NG	Natural gas
NGV	Natural gas vehicle
PCI	Peripheral component interconnect
PRT	Platinum resistance thermometer
R&D	Research and development
RAM	Random access memory
RE/TM	Rare earth transition metal
SCM	Superconducting magnet
SCXI	Signal conditioning extension module
STP	Standard temperature and pressure
ULEV	Ultra low emission vehicle

# Acknowledgments

The last three years represent an extremely busy period of my life. The time spent working with the Cryofuel Systems group has been both intellectually challenging and rewarding. I feel privileged to have been involved with such an exceptional group whose support and encouragement have made this work possible. In particular, I would like to express my appreciation to the following people:

- Dr. John A. Barclay for his enthusiasm, encouragement, and high expectations. His flexibility and understanding towards my “other jobs” allowed me to make ends meet and are also deeply appreciated.
- Mr. Bruce Kaye at the Esquimalt Defence Research Detachment (EDRD) for his invaluable work in the preparation and characterization of rare-earth material samples. The collaboration with EDRD was essential for the successful completion of this thesis.
- Mr. Frank Havig and Mr. Rodney Katz for their help in the machine shop and for teaching me that, yes,  $\pm 0.001$ ” does make a difference.
- Mr. Kenneth D<sup>G</sup>Head Kratchsmar for sharing my adventures with the DAQ system.
- Sue Walton, Dolores Bogusz, and Suzanne Stevens for their expertise in handling all the bureaucracy at UVic.
- My fellow graduate students for all the practical jokes.

The design of the variable temperature and field cryostat was done in close collaboration with other researchers. Special thanks to Patrick McKenzie, David Shepherd, and Aaron Fyke, for their efforts in the design of a heat capacity insert, a gas cooling loop, and all the preliminary calculations required to specify a list of components. Special recognition should also be given to Mr. Ian McIntyre for his expert contribution to the generation of a full set of engineering drawings.

I would also like to acknowledge the natural Sciences and Engineering Council of Canada (NSERC) and Centra Gas for their funding of this work and the projects associated with it. I also wish to thank Dr. Alan Slavin and Dr. John Earnshaw for all their help, teachings and friendship during my undergraduate years at Trent.

Finally, I would like to thank my parents and the rest of my family for their unconditional support during all these years.

# Chapter 1: Introduction

## 1.1 Motivation

According to various international organizations [1][2][3][4] the total global population is expected to double from 5.3 billion people in 1990 to slightly more than 10 billion in 2060. Approximately 75% of these people will live in urban areas and the corresponding total primary energy requirements are expected to increase up to threefold by 2050 [5]. Satisfying these increased energy needs while simultaneously minimizing environmental impacts will require technological advances and also the clarification of current concepts and perceptions associated with the role of energy in our societies [6].

The term “energy system”, for example, has been often misused to refer to the energy sector. Figure 1-1 shows the energy system’s architecture as proposed by contemporary researchers [7][8].

The energy sector is just part of the overall energy system, and it is focused on producing and selling energy currencies such as gasoline and electricity. However, people purchase energy services such as transportation, nutrition, health-care, and communication [9]. This distinction is extremely important because it is the services and not the sources that drive the energy system.

In recent years, the global energy system has experienced a migration towards technologies that reflect the attention given to the service end of the energy chain, as well as to environmental, geopolitical and economic factors. In the particular case of the transportation sector, the transition to new technologies has been characterized by a global increase in the use of alternatives to the traditional transportation fuels (gasoline, diesel and JetA).

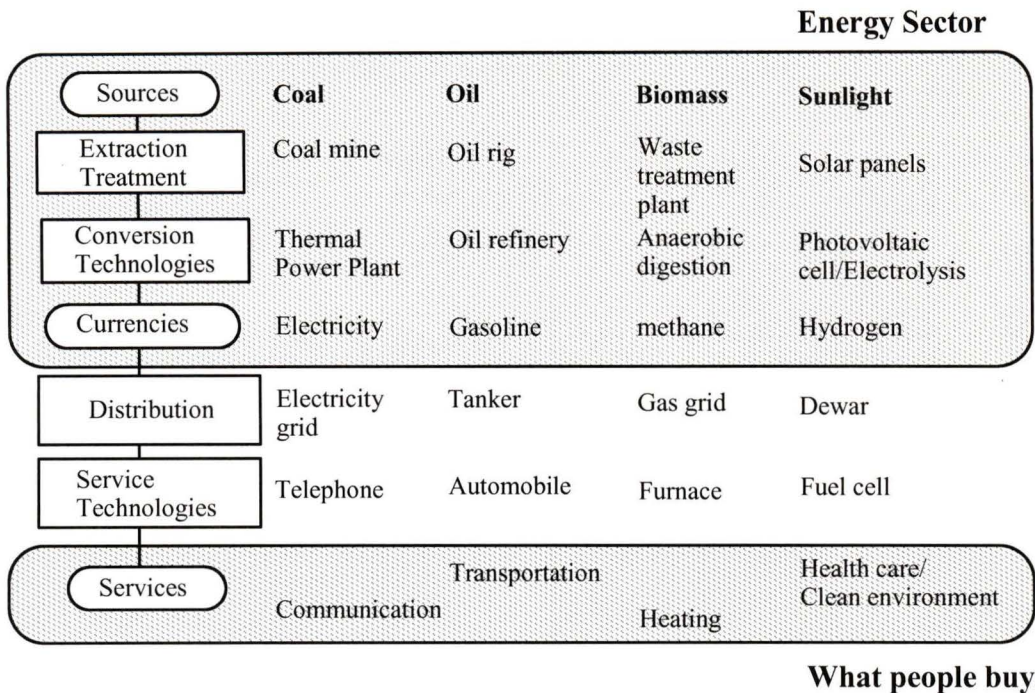


**Figure 1-1: The architecture of the energy system [7][8].**

In the United States, these so-called replacement and alternative transportation fuels (ATFs) have been defined, for example, by the Energy Policy Act of 1992 (EPACT), and they include compressed and liquefied natural gas, liquefied petroleum gases, biofuels, methanol, ethanol, hydrogen and electricity [10]. The identification of attractors and barriers affecting the widespread use of ATFs is one of the mission objectives of the Institute for Integrated Energy Systems (IESVic) at the University of Victoria. IESVic is engaged in the analysis, development and implementation of novel energy systems for transportation that, ideally, “offer a foundation for economic growth and diversification” and, simultaneously, “cause minimal environmental intrusion and reduce climate destabilizing emissions” [11]. The Cryofuel Systems (Cfs) Group is one of three synergistic research entities operating within IESVic. Cfs was specifically created to provide technological solutions to some of the challenges encountered during the transition to alternative transportation fuels. These challenges can be better appreciated by considering some of the similar developments that have taken place in the past.

## **1.2 The Evolving Energy System**

Historically, the evolution of the energy system has been characterized by changes in the energy sources of choice and a continuous sequence of technology replacements. Before the industrial revolution, all the energy services had to be provided by harnessing natural energy flows (wind, hydrological resources, etc.) or by using animal and human power. The only available transformation technology was based on the conversion of chemical energy into heat and light via combustion (fuel-wood, candles, etc.). The availability of power was limited by site-specific factors (animals, wind, water, etc.), and typical energy consumption was low [12]. The industrial revolution dramatically increased the rate of evolution of the energy system.

### **1.2.1 Past and Present Evolutionary Patterns**

The first dramatic change in the architecture of the energy system was triggered by an advance in conversion technologies from one energy form to another. At the end of the eighteenth century, the invention of the steam engine allowed coal to replace wood as the primary energy source. The steam engine also represented the first technology capable of converting fossil energy resources into useful work. This change eliminated the restrictions imposed by site specific factors (coal could be easily mined and transported), and it also gave birth to the first transportation revolution.

The second evolutionary stage was characterized by the introduction of electricity as the first energy currency that could be converted into light, heat or work at the point of use. Other innovations such as the electric motor, and the internal combustion engine represented a diversification of end-use technologies (light bulbs, automobiles, and aircraft) that had profound effects on society as a whole. However, this second transition was not driven by technological advances alone: changes in primary energy supply were just as important. The most important of these changes was initiated in 1859 when oil wells were first drilled in Eastern Pennsylvania. Eventually, cable-rig drilling technology,

and advances in chemical engineering and refining techniques allowed the replacement of coal by oil. At the time, coal supply was still as plentiful as it is today [13].

None of these transitions was motivated by a depletion of the sources being replaced, but rather by the attractive characteristics of the newly found substitutes. At the beginning of the 20th century, electric illumination replaced oil lamps. This new technology was not a cheaper alternative, but it provided brighter light, safer homes (low risk of fires), and a cleaner service. In the case of wood vs. coal, the latter had a higher volumetric energy density, and was also easier to transport and store. Oil, on the other hand, presented much better characteristics for distribution, and its derived products could be used for transportation (cars, trains and aircraft), electricity generation, home-heating, and for a variety of other uses. This versatility allowed oil to emerge as the predominant energy source, and to remain unchallenged as the leading option in the transportation fuel markets of the last several decades.

## **1.2.2 The Future Energy System**

According to many energy analysts [14][15][16], hydrogen and electricity represent the only combination of energy currencies that can provide all the required energy services and simultaneously eliminate the negative environmental impacts of the current energy system. While electricity will continue to provide the present types of services, some other energy services (most notably transportation) depend on chemical fuels and feedstocks [17].

The major barriers to the widespread use of  $H_2$  as a fuel are associated its low volumetric energy density, lack of refueling infrastructure and higher cost when compared to gasoline. These limitations imply a need for improvements in the technologies currently used for liquefaction, storage, and distribution. Breakthroughs in these crucial areas will drive the evolution of the energy system just as similar technological advances have done in the past. The transition to an ultimate hydrogen era, however, will be preceded by the popularization of other ATFs such as natural gas and propane.

Figure 1-2 shows data published by the International Institute for Applied Systems Analysis (IIASA) [5]. The evolutionary stages described in previous sections can be easily appreciated by following the relative shares of primary energy sources in the global energy market.

According to these general trends, natural gas (NG) will be the next dominant primary energy source following the current oil-dominated era. Some of the reasons behind these predictions include the following:

- NG can be used as a high-quality feedstock for the production of low cost

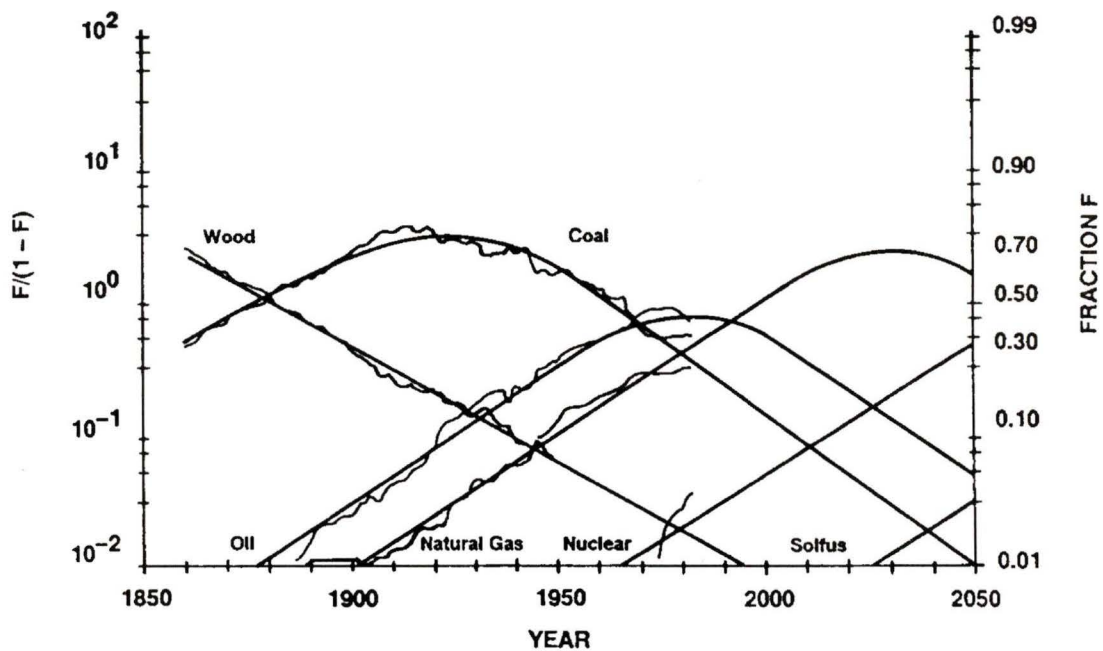


**Figure 1-2: Global primary energy source substitution ( $F$  = share of total market). Smooth lines represent model predictions. Historical data are superimposed as jagged lines (Solfus refers to future energy sources such as solar power and fusion) [5].**

methanol and hydrogen .

- NG can be used directly as an end-use fuel or as a primary energy source for electricity generation.
- Unlike oil, the supply of NG is not concentrated in a few geographical regions, and it is an abundant resource in North America.
- NG benefits from the existence of a large, underground distribution infrastructure.

- When used in dedicated engines, NG produces less harmful emissions than gasoline and diesel with current engine technology.
- NG is already a commonly used fuel with well known characteristics.

### 1.3 Alternative Transportation Fuels (ATFs)

In addition to NG, other ATFs have gained popularity in the last few years. According to the definitions given by EPACT, ATFs are essentially fuels with “[the] ...*potential ability to both improve the environment and reduce the U.S. dependence on imported petroleum.*”. These definitions also include mixtures with gasoline or with other ATFs. A list recently published by the U.S. Department of Energy (DOE) includes the following:

- M-85 : a mixture of 85% methanol and 15% gasoline.
- M-100 : also known as “neat” (100%) methanol.
- E-85 : a mixture of 85% ethanol and 15% gasoline.
- E-95 : a fuel consisting of 95% ethanol and 5% gasoline.
- LPG : liquefied petroleum gas (propane).
- CNG : compressed natural gas.
- LNG : liquefied natural gas.
- Hydrogen
- Electricity

Additional options include hythane, a mixture of 15% hydrogen and 85% methane (5% H<sub>2</sub> by energy content), as well as fuels derived from biomass. This last option can be particularly attractive if the production of fuel is combined with the treatment of domestic and municipal organic waste via aerobic or anaerobic digestion technologies [18].

ATFs can be classified according to their characteristics under standard temperature and pressure (STP) conditions. The fuels that are gases must be cooled and/or to be kept in their liquid state. The term “cryofuels” has been used elsewhere [19] to refer to the group of fuels that have these special storage requirements. These fuels are important not only because they are domestically available but also because, on an energy equivalent basis, they cost less than diesel or gasoline. In addition to economic factors, ATFs also have very attractive properties that allow better engine performance. The most important

physical and chemical properties that have an effect on ICE performance\* are described in Table 1-1 [21].

**Table 1-1: Physical and chemical properties of some ATFs compared to diesel and gasoline [21].**

Property	Gasoline	Diesel	Methanol	Propane	Methane	Hydrogen
Chemical formula	C <sub>4</sub> to C <sub>12</sub>	C <sub>3</sub> to C <sub>25</sub>	CH <sub>3</sub> OH	C <sub>3</sub> H <sub>8</sub>	CH <sub>4</sub>	H <sub>2</sub>
Molecular weight (g/mol)	100-105	200 (avg.)	32.04	44.1	16.04	2.02
Normal boiling point (K)	310-478	461-616	338.15	231.07	111.63	20.27
Freezing point (K) at P <sub>eq</sub>	233.15	235.65	175.65	85.52	90.69	13
Self ignition temperature (K)	530.37	588.71	737.04	755.4	813.15	847
Density at nbp (kg/m <sup>3</sup> )	700			507.3	422.3	70.8
ΔH <sub>vap</sub> at nbp (kJ/kg)	309			425	510	446
Heat of combustion (MJ/L), [Btu/gal]	(32.08) [115,000]	(35.81) [128,400]	(15.84) [56,800]	(23.57) [84,500]	(5.52) [19,800]	(-) [-]
Flammability limits (vol%); {high},[low]	{7.6} [1.4]	{6} [1]	{36} [7.3]	{9.5} [2.2]	{15} [5.3]	{74} [4.1]
Octane number (average)	86-94	NA	100	104	120+	130+

The major difference between ATFs and gasoline is related to their lower volumetric energy densities. This results in limited vehicular range, and special requirements for on-board storage equipment. Fuel volatility is also an important property because it is crucial for engine start-up, especially in cold weather. This is particularly important for spark-ignition engines.

In the case of gaseous ATFs (CNG, LPG), volatility is not a problem. Alcohols and their mixtures (M-85, M-100, E-85), on the other hand, are less volatile than gasoline and this results in cold-start and misfiring problems. Solutions to these limitations include the addition of an on-board supply of a volatile fuel for startup (gasohol, propane, etc.), and the use of computer-controlled starting systems.

\* The two different types of ICE (spark ignition and compression ignition) require fuels with different characteristics. Reference [21] provides a more detailed analysis.

In a spark ignition engine, premature self-ignition of the fuel may result in engine “knocking” which is undesirable. A fuel’s octane number gives an indication of a its tendency to knock. In general, the higher the octane number, the larger the compression-ratio threshold before knocking occurs. All the ATFs discussed thus far have higher octane numbers than gasoline. In addition, they have higher self-ignition temperatures, and most of them are much lighter than air (at room temperature). This results in an added safety advantage if they are accidentally spilled: the fuels will dissipate quickly instead of accumulating on the ground or flowing into sewage or water systems. However, higher octane numbers imply that none of the ATFs can be effectively used in unmodified compression ignition engines. Special ignition devices and other modifications are being currently investigated to allow ATFs to operate on these engines.

Even with all these technological advances, more development is necessary before ATFs acquire a significant share in the current transportation markets.

### **1.3.1 Current Role of Alternative Fuels**

The current use of AFVs is almost completely limited to fleets [20], and over 40% of the ownership is concentrated in the private sector [21]. In 1993 there were more than 210 million vehicles in the North America but only 475,000 were classified as alternative fuel vehicles (AFVs) operating on one or more of the fuels defined by EPACT. Natural gas (CNG and LNG) is used on only 100,000 AFVs, and about 50% of this total corresponds to vehicles registered in Canada. These figures are just one example of the minimal role that alternative fuels play in the transportation markets.

Most of the AFVs being used today use LPG which, unlike the other ATFs, is very popular in private fleets. This preference can be associated with tax incentives, ease of engine conversion, support from large oil companies, and environmental benefits. Figure 1-3 shows the projected number of AFVs in use in the United States by 1995 [21].

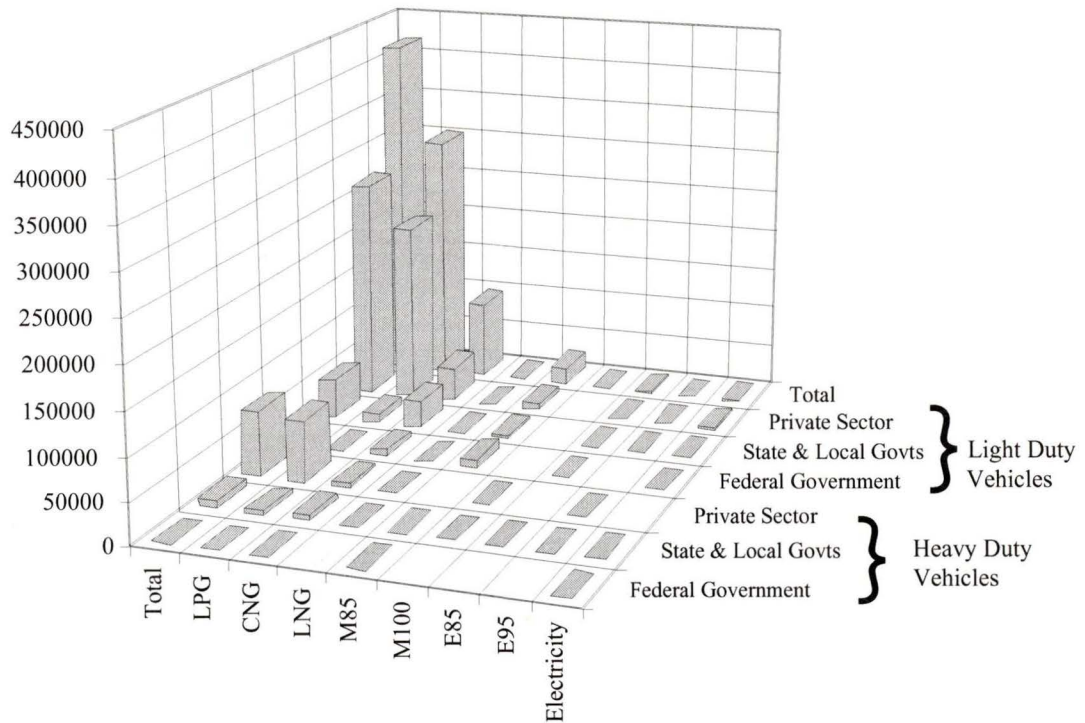


**Figure 1-3: Total projected number of AFVs in the United States by 1995 [21].**

Alcohols and their mixtures (methanol, M85, E95, etc.) are corrosive substances that require special materials for storage tanks, hoses and connecting valves. Additional vehicular components include special sensors to determine the amount of alcohol in the fuel, flame arrestors to prevent sparks during refueling and, sometimes, a cold-start system on board. Dual engines operating on two or more fuels must accommodate for the fuel with the lower octane number (i.e., gasoline). The corresponding compression ratios are therefore not modified to produce the maximum efficiencies attainable with neat alcohols.

Methanol and ethanol in their neat forms are best suited for spark-ignition engines. When compared to gasoline, both fuels can provide greater thermal efficiencies and power output, and better antiknock characteristics. Their heats of vapourization, however, are relatively high and this provides an increased cooling to the fuel-air mixture. Cooler mixtures imply higher densities (i.e., more power due to higher mass throughput), but they can also result in cold-start problems, and higher emissions of unburned fuel.

The use of alcohols in compression-ignition engines has been limited. To date, the addition of an ignition source such as a glow plug, for example, has been necessary to use these fuels in compression-ignition engines. Warmup misfiring and cold-start problems are the major limitations of current alcohol-fueled vehicles. These limitations, along with the added complexity (peripheral components) detract from the potential gains in efficiency and environmental benefits associated with alcohols as fuels.

Natural gas is the ATF with the fastest growing market. The number of vehicles operating on CNG increased 42% from 1992 to 1993, and it is expected to increase by 69% between 1993 and 1995 [22]. Most of these were converted light-duty vehicles (cars, minivans, and vans), but dedicated NG engines are also being designed for buses and other heavy duty applications. NG can be stored as a compressed gas (CNG), as an adsorbed chemical compound in porous metals (ANG) [23], or as cryogenic liquid (LNG).

A CNG vehicle stores fuel as a compressed gas between 2400 and 3600 psi (16.65 and 24.92 MPa). However, at these pressures the volumetric energy density of CNG is still less than 25% of the corresponding volume of gasoline. The fabrication of cheaper and lighter CNG tanks is the subject of intense research. Recent advances include cold-drawn aluminum tanks with a low-cost fiberglass reinforcement around the aluminum liner. Other improvements include the addition of electronic control modules based on oxygen sensors. These systems adjust the fuel mixture flow to improve performance and minimize emissions [24]. Although dual-fuel (gasoline/NG) vehicles have been successfully introduced, the increased complexity and the extra weight associated with carrying two fuel-storage systems have hindered their popularization. The number of LNG-fueled vehicles is also expected to show a significant growth. LNG vehicles carry their fuel as a slightly pressurized, cryogenic liquid. Carrying the NG as a liquid results in an increased vehicle range between refueling over equivalent sized CNG systems. In addition, some of the impurities present in NG ( $H_2O$  and  $CO_2$ ) are removed during liquefaction.

Hydrogen and electricity have also been classified as ATFs but the number of vehicles currently running on either of these fuels is negligible. Electric vehicles use batteries as energy storage devices to drive an electric motor rather than an ICE. This eliminates the need for fuel handling systems or additional engine components. These vehicles are also more environmentally friendly\* and less noisy than their gasoline counterparts. However, the energy densities in batteries are very low.

A typical light duty vehicle requires about 30 batteries weighing over 500 kg [25]. This provides enough energy for a range of only 45 to 50 miles between recharges. In addition, batteries must be replaced every few years which implies that disposal and recycling procedures must be designed and regulated.

Hydrogen vehicles can rely on traditional internal combustion engines (running on hydrogen or hythane), or on more advanced technologies based on fuel cells. Fuel cells using proton-exchange membranes convert hydrogen to electricity via a low temperature electrochemical process. The electricity produced is used to power an electric motor, and all the other vehicle subsystems. By avoiding combustion these devices can obtain the best combination of high efficiencies (60% idle, 40% at full power) [26] and environmental compatibility (the only byproducts of the conversion process are water vapour and heat)<sup>†</sup>.

Although LNG and liquid hydrogen have attractive characteristics as vehicular fuels, several barriers have to be overcome before they can be widely used in the transportation markets.

---

\* Although the generation of electricity carries some penalties (e.g., pollution from a coal-powered plant), these problems are more easily controlled at a central location instead of at each individual vehicle.

† This does not include pollutants that could be generated during H<sub>2</sub> production.

## 1.4 Alternative Fuels: Barriers and Attractors

### 1.4.1 Attractor - Energy Security

One of the major drivers giving impetus to the adoption of ATFs in North America is the desire to minimize the current dependence on foreign oil. The total annual energy supply for North America was reported to be almost 100 EJ for 1993 [27]. The transportation sector represents 25% of the total energy requirements but only a negligible amount of this total is derived from ATFs. In the United States, ATFs represented less than 0.3% of the transportation fuel market for 1993 [22]. The rest is almost exclusively dependent on oil and more than 50% of this total corresponds to imported oil.

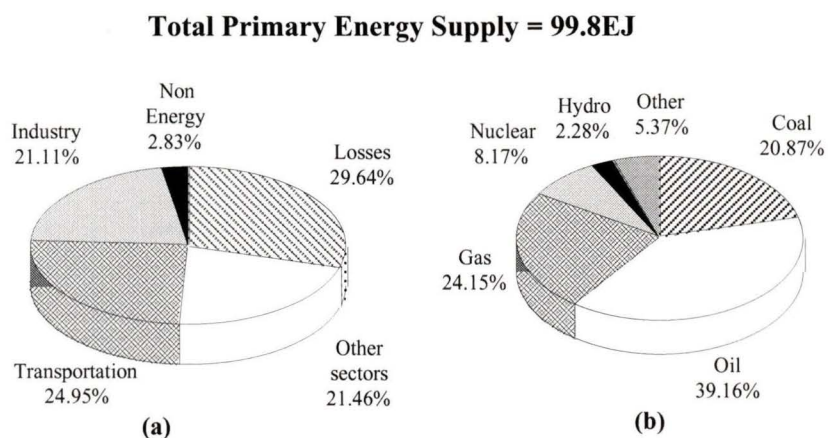


**Figure 1-4: Annual (1993) primary energy supply by sector (a), and by energy source (b) [22].**

Natural gas accounts for almost one fourth of the total energy supply, but only a negligible amount is used by the transportation sector. Events such as the oil crisis of the 1970's and the Persian Gulf war in the early 1990's demonstrated how volatile and unpredictable some of the supply regions can be. These and other events have triggered a series of government measures in North America. Most of these measures are aimed at developing ATFs as an insurance against the possibility of future oil shortages and/or high prices.

## 1.4.2 Attractor - Environmental Concerns

Another important driver in favour of ATFs is related to the negative effects of the current energy system on the environment. Some of the substances commonly classified as pollutants occur naturally in the atmosphere, but anthropogenic sources have dramatically increased their concentrations above the natural baseline levels.

Since the industrial revolution in the nineteenth century, the concentration of CO<sub>2</sub> has increased by more than 25%, CH<sub>4</sub> concentrations have increased by more than 100%, and the concentration of N<sub>2</sub>O has increased by about 8% [28]. The transportation sector is responsible for a large percentage of some of the emissions that affect air quality. These emissions can be classified into two main groups:

- Emissions that are harmful to human health, and
- Greenhouse gases that may contribute to global climatic disruption

The first group includes substances such as CO, NO<sub>x</sub>, SO<sub>2</sub>, and non-methane volatile organic compounds (NMVOCs). The major environmental impact of these substances is related to their role as tropospheric ozone precursors\*. Figure 1-5 shows the 1990 total emissions of CO, NO<sub>x</sub>, and NMVOCs in the United [21].

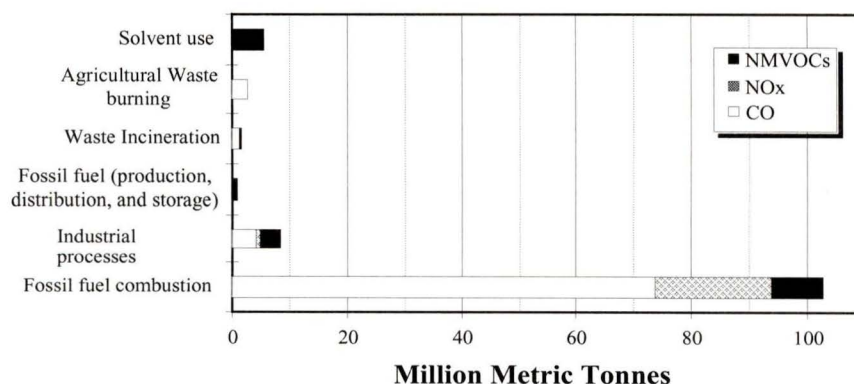


**Figure 1-5: Annual emissions of “criteria pollutants” in the United States (1990) [21].**

\* This refers to the ozone formed close to the ground, not to the ozone present in the stratosphere. Tropospheric ozone is an irritant that affects human respiratory systems.

Greenhouse gases (GHGs) include CO<sub>2</sub>, CH<sub>4</sub>, N<sub>2</sub>O, Hydrofluorocarbons (HFCs), Polyfluorocarbons (PFCs), and water vapour. The fraction of GHGs produced by the transportation sector may contribute to global climatic change by at least three different processes\*. CO<sub>2</sub> represents the largest fraction of total GHGs emissions in the United States. The transportation sector is responsible for more than 30% of this total [22]. All the ATFs previously discussed produce less CO<sub>2</sub> than gasoline and most of them also produce less CO. The total emission estimates for some of the ATFs in a full fuel cycle† are given in Table 1-2 [21].

**Table 1-2 : Emissions in grams per vehicle-mile for some ATFs during a full fuel cycle (RFG= Reformulated gasoline)[21].**

	Gasoline	RFG	Methanol from NG	Ethanol from Corn	CNG	LPG from Oil & Gas
CO <sub>2</sub>	359.3	359.7	334.7	325.5	244.4	266.3
CH <sub>4</sub>	0.319	0.335	0.497	0.57	1.559	0.241
N <sub>2</sub> O	0.055	0.055	0.055	0.039	0.052	0.052
NO <sub>2</sub>	0.652	0.669	1.024	1.867	0.569	0.52
CO	7.46	6.368	7.37	5.445	3.677	5.601

Assumptions: (a) flared gas is completely burned to CO<sub>2</sub> and H<sub>2</sub>O with no CH<sub>4</sub>, NMOC, CO, NO<sub>x</sub> or N<sub>2</sub>O, (b) values have been derived using a 30mile/gallon gasoline efficiency vehicle.

Although ATFs can reduce the amount of GHGs and harmful emissions liberated into the atmosphere, the environmental factor is not likely to be the major driving force behind ATF popularization.

The computer models used to predict the effects of GHGs on global climate have recently come under scrutiny. Some opponents of GHG-related legislation argue that the results of these models have exaggerated the possible effects of emissions on global temperature

\* (i) direct heating of the atmosphere due to fuel combustion, (ii) absorption of solar energy that would otherwise be reflected into space, and (iii) depletion of the stratospheric ozone layer.

† This implies that tail-pipe emissions are not considered in isolation. Instead, the full fuel cycle (end use combustion, distribution, fuel production, etc.), and vehicle characteristics are included in the analysis.

change. Until the scientific community reaches a consensus on this and other matters, the adoption of ATFs cannot rely on environmental concerns alone.

### **1.4.3 Attractor - Geopolitical Changes**

Some of the government measures adopted in North America have taken the form of specific legislation affecting the use of ATFs. Some others have taken the form of general public awareness and information campaigns through the media.

In the United States, the Clean Air Act (CAA) of 1970 prescribed limits for the concentrations of pollutants in exhaust gases from cars, buses and trucks [29]. The Alternative Motor Fuels Act of 1988 (AFMA) was aimed at supporting the development of ATF's, and the production of alternative fueled vehicles (AFV's). The Clean Air Act Amendments of 1990 (CAAA) set numerical standards for maximum emission levels, but they did not specifically require the use of ATF's (gasoline and diesel could still be used as long as these standards were met). Replacing 30% of the projected motor fuels by the year 2010 became a national goal as stated in EPACT, and it required at least 50% of the replacement fuels to be generated from domestic sources.

Canadian legislation has sometimes lagged its American counterpart, but indications of similar final goals can be found as early as 1970 when the first federal vehicle emission regulations began. These regulations were aimed at reducing the lead content in gasoline and they culminated with a federal ban in 1990. Current Canadian standards for light duty vehicles (LDVs) are the same as those found in the United States. The Canadian government has also issued a Memorandum of Understanding with Original Equipment Manufacturers (OEMs) in which all 1994 and 1995 LDVs sold in Canada are required to comply with EPA emission standards [30]. The Alternative Fuels Act of 1995 approved under Bill S-7 of the Canadian Senate [31] is also another indicator of these general trends. Bill S-7 will require the federal government and Crown corporations to convert 75% of their transportation fleets to ATFs by the year 2004.

Mexican legislation is still being developed, but environmental concerns and the inclusion in the North American Free Trade Agreement (NAFTA) of 1994 make the need for similar measures all the more evident. At 2,250m above sea level, México City is the most densely populated city in the world (~18 million inhabitants spread over 200,000 hectares). This city has 3.5 million commercial vehicles used for the transportation of goods, 2.7 million cars, 77,000 buses, 65,000 taxis, and 289 trolleys and light trains. Subway passengers average 4.5 million per day, and about 25.5 million people go through México City's airport in one year [32]. Factories and automobiles produce about 5 million tons of airborne pollutants per year [33]. It is possible to compare these numbers with the national totals by considering that, in 1992, there were 7.5 million cars, 106,000 passenger busses, and 3.5 million light duty trucks in Mexico [34]. Of these, only a negligible fraction operates on ATF's.

The Mexican government has introduced some measures aimed at decreasing vehicle emissions. In January 1992, President Salinas created the Metropolitan Commission for Pollution Prevention and Control. One of the goals of this commission was to convert 299,000 vehicles to NG, propane or other ATFs over a three-year period. Buses from the metropolitan transit authority and minibuses operated by independents subcontractors were the prime targets for fuel conversion. Although México could have NG reserves comparable to those found in Canada [35], the country is expected to import NG for the next 20 years (in 1992, México imported 96 million cubic feet of NG from the United States) [35]. This is because the national oil company, Pemex, has a monopoly on the exploration and extraction of all hydrocarbons in México. Pemex is the fifth largest oil company in the world and it represents one of the most significant entities in the Mexican economy. The existing monopoly, however, limits the amount of funding available for the development of gas wells and prevents the exploitation of the estimated 70 trillion cubic feet of NG [35] available under the deserts in the north, and under the waters of the Gulf of México in the south.

Unlike NG, propane is produced abundantly in México, and LPG will be the preferred choice for vehicle conversion (at least in the short run). This preference will be based on the availability of conversion kits, and the proven performance record of LPG as a vehicular fuel. In addition, ATV owners will also enjoy certain incentives and exemptions. Under the “Hoy no circula” program, for example, owners are not supposed to drive their cars one day a week. Converted vehicles will be exempted from this requirement.

Some other changes include amendments to federal laws in the areas of natural gas and petroleum pipelines, petrochemicals, electric power, and foreign investment. Under the 1995 Amendment to Mexican federal law, domestic or foreign investors may transport, store, and distribute natural gas. Any investor may also construct, operate and own natural gas pipelines, installations and equipment provided the required authorization has been obtained from the Secretariat of Energy. All these changes are very important because the use of ATFs will remain mainly driven by legislation for some time. The use of AFVs will only become popular when the cost, refueling infrastructure, and vehicular performance match or exceed current standards.

#### **1.4.4 Barrier - Low Volumetric Energy densities**

The major disadvantage of ATFs when compared to gasoline is related to their relatively low volumetric energy densities. This implies that, to travel the same distance in vehicles of equal thermal efficiency, a larger volume of ATF is required.

Carrying some of the ATFs as liquids increases vehicular range, but the current costs of liquefaction are very high. The lack of affordable and efficient refueling infrastructures is one of the biggest barriers for the widespread use of ATFs.

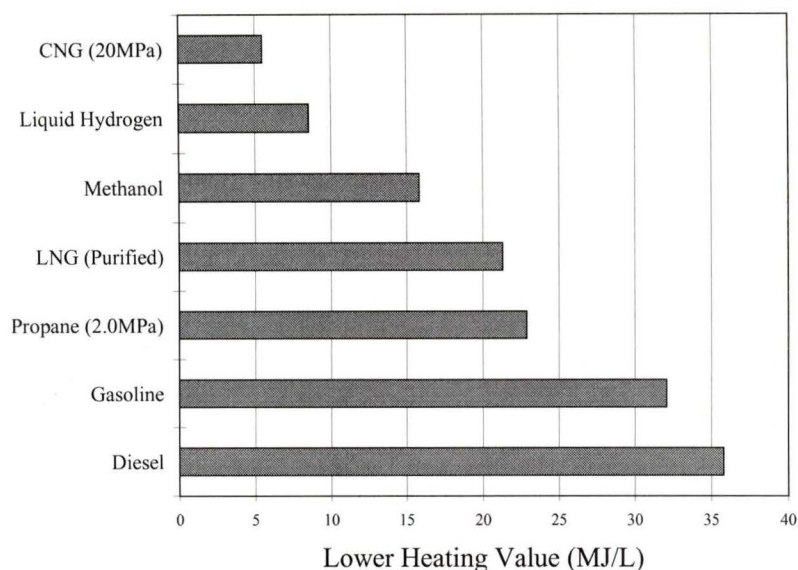


**Figure 1-6: Volumetric energy densities for some ATFs compared to diesel and gasoline. These values correspond to the fuel under typical storage conditions for each fuel [21].**

### 1.4.5 Barrier/Attractor - Economics

ATFs will not become serious competition for traditional fuels unless their use can be made economical. The cost of fuel, as delivered to the consumer, has been identified by fleet owners as the most important criterion when considering the conversion to ATFs. The current challenge consists of delivering ATFs at prices that are lower than the prices for conventional fuels.

NG has some attractive characteristics when compared to diesel and gasoline. On an energy equivalent basis, the price of NG feedstock is lower than the price of conventional fuels. However, the final price delivered to the customer, depends on other factors such as the cost associated with the refueling infrastructure, NG feedstock prices, liquefier efficiency, road taxes and vehicle conversion costs.

A full analysis of NG economics must take into consideration site-specific factors such as fleet size, local taxes,, etc. In most cases, the analysis must be performed on a case by

case basis. Such analysis is out of the scope of this thesis, but a number of excellent references are available. These publications include the work by Barclay et al. [36][37] and Powars et al. [38].

Reducing the cost associated with NG liquefaction is a good way to reduce the total refueling system capital cost (the liquefier of conventional integrated liquefier/refueling stations can represent as much as 50% of the total refueling station [38]).

Following this analysis, the Cfs group has identified the lack of cost-effective refueling infrastructure as a crucial barrier to the increased use of ATFs. Accordingly, the current research efforts are aimed at the development of integrated liquefaction and refueling systems capable of providing CNG and LNG after processing NG feedstock from existing distribution pipelines. The core of these integrated refueling systems will be the NG liquefier.

## **1.5 The Cfs Natural Gas Liquefier Project**

Natural gas has been identified as the most promising candidate to replace traditional transportation fuels during the transition to an ultimate hydrogen era [36][39][40]. The Cfs' program is focused on the development of low-cost, fleet-size refueling systems for liquid and compressed natural gas vehicles with an emphasis on novel liquefaction technologies. The immediate goal of current research efforts is the development and construction of an active magnetic regenerative liquefier (AMRL) prototype that will be used to efficiently liquefy natural gas.

At the heart of the AMRL is the magnetic regenerator subsystem and associated magnetic materials. The Cfs project has developed suitable magnetic refrigerant materials for the design and construction of an optimized magnetic NG liquefier. In addition, Cfs is also extending the database of existing magnetic refrigerant materials from  $\sim 110\text{K}$  to  $\sim 20\text{K}$ . These refrigerants would be useful for a AMRL designed to

produce liquid hydrogen. This work represents part of a collaborative research effort with the Hydrogen Research Institute at the Université du Québec à Trois-Rivières (UQTR).

The Cfs group has also developed fleet-sized refueling systems for NG. These systems will use NG directly from local distribution grids, and deliver distributed CNG and LNG to vehicles and storage tanks. The NG will be purified to remove water vapour and CO<sub>2</sub> that would otherwise freeze during liquefaction. The LNG produced can be dispensed as a liquid or compressed and vapourized to form CNG. Vapourization of the LNG can be achieved via a counterflow heat exchanger that will also precool the incoming NG stream prior to liquefaction.

One of the most important components of this systems is the NG liquefier. This device must be capable of cooling the NG from ambient temperature to its liquefaction temperature at atmospheric pressure (approximately 112 K). The NG liquefier accounts for a significant fraction of the total capital cost of the refueling station. This implies that the capital and operating costs of the liquefier should be minimized. After reviewing current liquefaction technologies, the Cfs group has chosen magnetic refrigeration as an excellent candidate to meet both requirements. With the appropriate selection of materials, magnetic refrigeration cycles can achieve high efficiencies and low operating costs. Figure 1-7 shows a schematic diagram of a Cfs LNG/CNG refueling station.

The immediate goal of the current research efforts at Cfs consists of the construction of a 100 gal/day NG liquefier. This liquefaction system will be based on an active magnetic regenerative refrigerator (AMRR), and will be the first prototype of its kind in the world. The current specifications require the AMRR to span the temperature range between 250 K and 110 K. A conventional gas cycle refrigerator will cool the NG from ambient temperature to 250 K and provide the heat sink for the AMRL at near 250 K.

The AMRR uses regenerative heat exchangers (regenerators) to span the temperature range between 110 K and 250 K. A regenerator is a highly efficient and compact heat

exchanger in the form of a porous solid bed. A heat exchange fluid is periodically forced through this bed and, during the first half of an operation cycle, the fluid is cooled by depositing heat on the regenerator matrix. During the second half of the cycle, the direction of fluid flow is reversed and the regenerator matrix cools by transferring the stored heat back to the fluid.

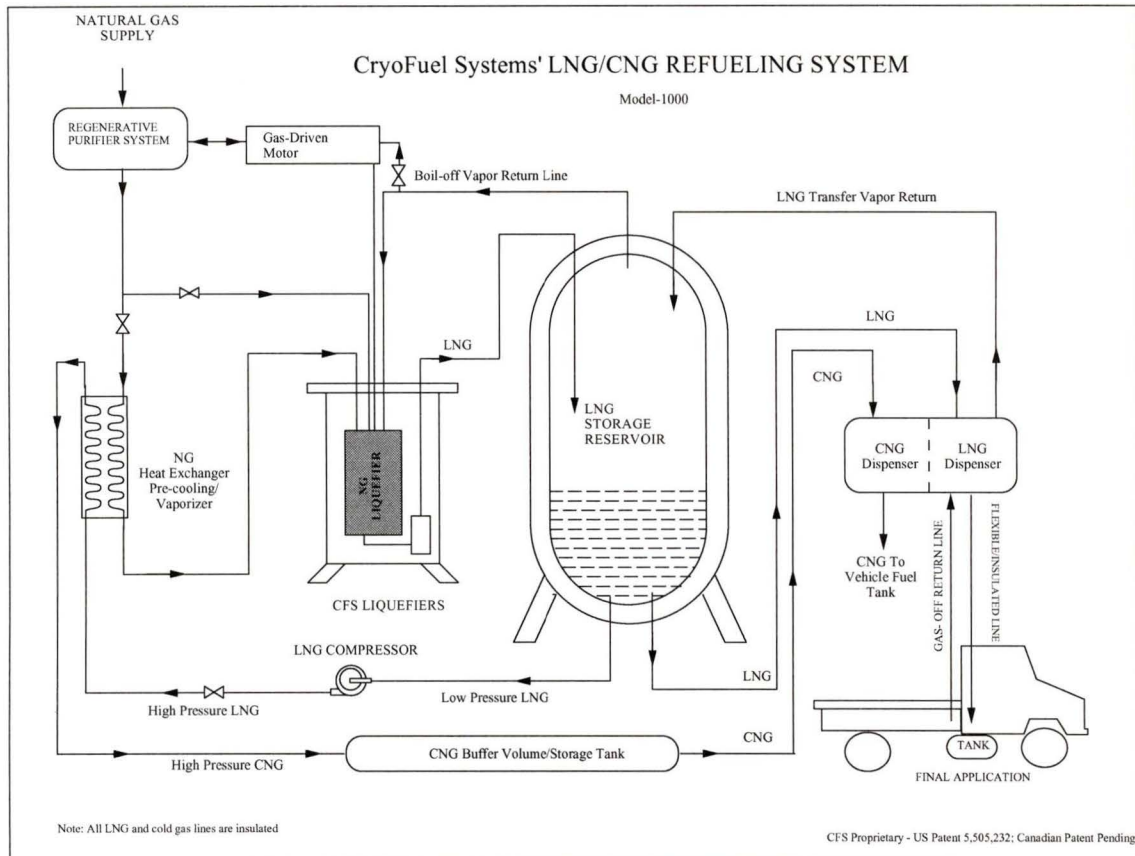


**Figure 1-7: Schematic diagram of the CNG/LNG refueling station being designed by the Cfs Group.**

The AMRR's operation is based on a natural phenomenon called the magnetocaloric effect (see Appendix A), and it involves the periodic magnetization and demagnetization of special materials during one refrigeration cycle. The magnetic fields required during this process are relatively high (e.g., 8 T, or about 150,000 times the Earth's magnetic field), and they can only be produced by superconducting magnets (SCMs). Current technology and manufacturing limitations require SCMs to operate at cryogenic

temperatures (typically 4.2 K). The refrigeration system used to produce and maintain these low temperatures is the focus of the work being presented here.

## **1.6 Thesis Objectives**

Due to the complexity of the AMRL prototype, it has been necessary to separate the overall project into manageable sub-projects. The work covered in this thesis is focused on the design and implementation of a modified cryogenic refrigeration unit that will be used to cool the superconducting magnet system in the AMRL. The specific objectives are as follows:

- Reverse engineering and modification of a commercially available, two-stage Gifford-McMahon (GM) cryogenic refrigerator.
- Identification, evaluation and selection of passive magnetic regenerator materials for the second stage of this refrigerator.
- Preparation and characterization of the selected alloys.
- Manufacture of highly-efficient and structurally stable regenerators for the temperature range between 40 K and 4 K.
- Testing of the modified GM refrigeration unit.

## Chapter 2

# Background and Review of Prior Work

This chapter covers some of the fundamental concepts associated with the AMRR and some of its subsystems. The analysis starts with a brief overview of the magnetocaloric effect and magnetic refrigeration systems. Subsequent sections describe superconductivity and the cryogenic refrigeration unit used to cool the SCM subsystem in the AMRL. The discussion is then focused on the performance parameters for this unit, and on the modifications required to achieve the operating temperatures required for low temperature SCMs. The last sections in the chapter deal with the cryogenic regenerator materials used to achieve lower temperatures and larger cooling powers. The previous work found in the literature is presented as required.

### 2.1 The Magnetocaloric Effect (MCE)

The magnetocaloric effect (MCE) is observed when certain magnetic materials are exposed to an externally applied magnetic field. If the field is applied under adiabatic conditions, the magnetic material will experience a temperature increase during magnetization, and a temperature decrease as the field is removed and the material demagnetized (see Figure 2-1).

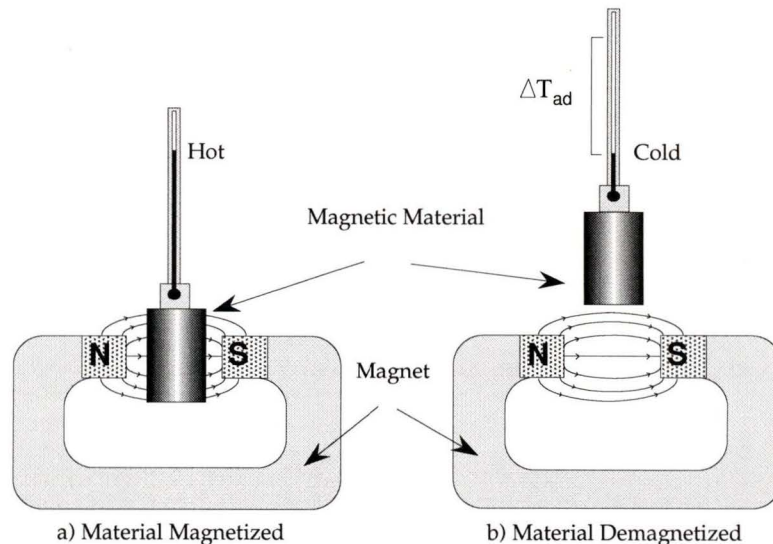


**Figure 2-1: The magnetocaloric effect manifests itself as a change in temperature.**

$\Delta T_{ad}$  represents a change in temperature resulting from a change in the external field intensity under adiabatic conditions (see Appendix A for a more detailed analysis). This change in temperature is the observable phenomenon associated with the magnetocaloric effect and it forms the basis of magnetic refrigeration.

## 2.2 Magnetic Refrigeration (MR) Systems

Although magnetic refrigeration is based on a different physical phenomenon, its implementation is analogous to traditional systems based on gas-compression cycles as illustrated in Figure 2-2.

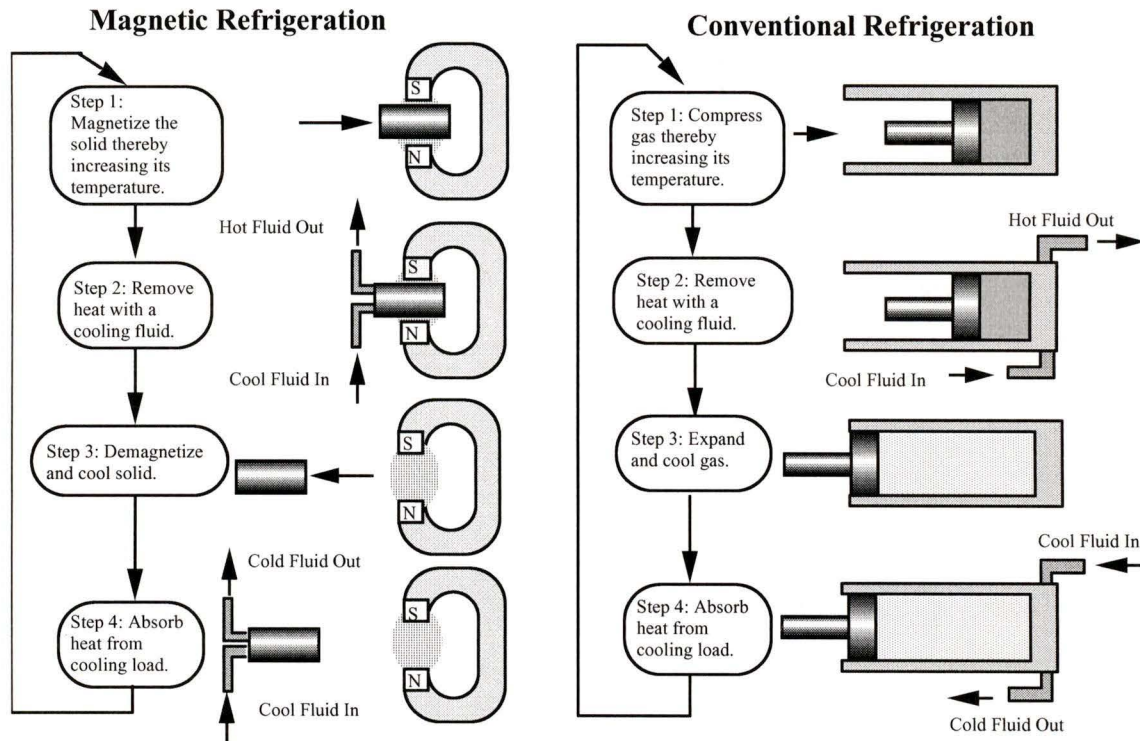


**Figure 2-2: Conceptual comparison between magnetic and conventional refrigeration cycles.**

The choice of a given thermodynamic cycle depends on the temperature range of interest, and on the particular operating parameters of the magnetic refrigerator (see Appendix B). Although magnetic refrigeration systems have been used in a variety of applications (see Appendix C), the device being developed at the Cfs laboratories will be the first magnetic natural gas liquefier in the world.

### 2.3 The Cfs Active Magnetic Regenerative Liquefier (AMRL)

The NG liquefier developed by the Cfs group is a rotary device based on an active magnetic regenerative refrigeration (AMRR) cycle. In this particular implementation, the magnetic working material also functions as a thermal regenerator. To accomplish this dual function, the regenerator geometry consists of an annular container filled with magnetic particles. This container rests on a racetrack and can be rotated to enter and exit a region (a 90° sector) where a high magnetic field is applied. As the material enters the high magnetic field region, its temperature increases due to the MCE. While in this region, the heat transfer fluid absorbs heat causing the average temperature in the regenerative magnetic bed of particles to be reduced. The absorbed heat is then carried into the external heat exchanger and rejected to the environment.

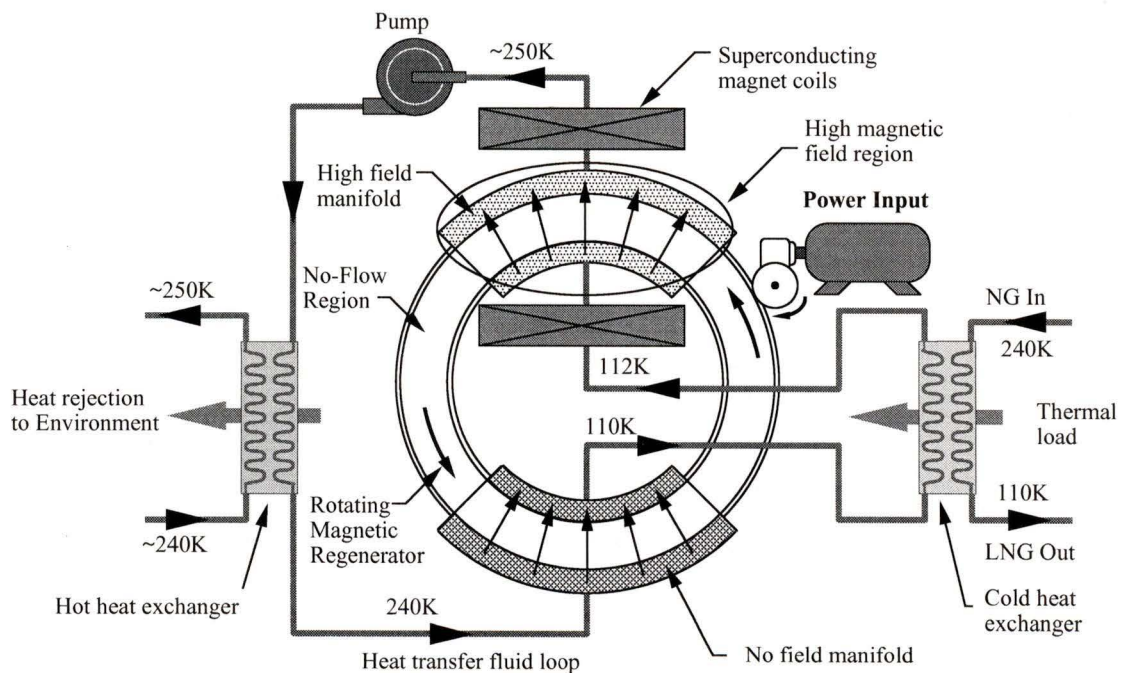


**Figure 2-3: Schematic diagram of the rotary AMR for natural gas liquefaction being developed by the Cfs group.**

As the regenerator exits the high magnetic field region, its average temperature decreases further as the field intensity decreases and the material is demagnetized. As the rotation continues, the regenerator enters a second manifold where it absorbs heat from a heat

transfer fluid. The cooled fluid can now absorb heat from a cooling load (the NG stream) and, finally, the regenerator exits the manifold region and is ready to repeat the cycle.

The detailed operation of the AMRL has been described elsewhere [75]. The work presented here is only focused on one of its components. Specifically, this thesis addresses the cooling requirements for the superconducting magnet subsystem.

## 2.4 Superconducting Materials Technology

Superconductivity is a natural phenomenon that occurs in certain materials and is characterized by the complete absence of electrical resistivity below a certain critical temperature  $T_c$ . This abrupt change in the physical properties of materials was first observed by Kamerlingh Onnes in 1911 while measuring the electrical resistivity of mercury as a function of temperature [76].

In addition to  $T_c$ , two other parameters are necessary to characterize the superconducting state. These parameters are the critical magnetic field,  $H_c$ , and the critical current density,  $J_c$ . These three parameters are related to each other and they define a material-dependent surface in T-J-H space (see Figure 2-4). Any combination of T-J-H values outside this surface represents a normal (non-superconducting) state for a given material.

Practical superconducting magnet systems were not developed until the 1960's [77]. A superconducting (SC) magnet is simply an electromagnet that can induce large magnetic fields ( $\mu_0 H = 10$  T or more) with essentially no resistive losses\*. These devices are used in a wide variety of applications such as particle physics research, low purity ore separators [78], and magnetic resonance imaging (MRI) scanners [79].

One of the alloys of niobium and titanium (NbTi) and the intermetallic compound of niobium and tin ( $Nb_3Sn$ ) are the most popular low- $T_c$  superconductors. NbTi has lower

---

\* Once an electric current has been established in a SC material, it is estimated that it will persist for a very long time ( $10^6$  years) without any noticeable resistive losses.

values for  $H_c$  and  $J_c$ , but its metallurgical properties are superior to those found in  $Nb_3Sn$ .  $NbTi$  is a ductile material that can be easily drawn to fabricate thin wire. It can also be extruded together with other materials such as copper and aluminum. These processes do not require special equipment and can be carried out with conventional wire handling machinery.  $Nb_3Sn$ , on the other hand, is a brittle material whose fabrication requires very carefully controlled temperature conditions. However, the possibility of producing higher magnetic fields at higher temperatures often offsets the higher costs associated with  $Nb_3Sn$  magnets. In the particular case of the Cfs project, the AMRL prototype uses a split-pair  $Nb_3Sn$  magnet designed to produce a 8 T field at an operating temperature of 4.5 K. These particular design specifications cannot be satisfied with a  $NbTi$  magnet of similar geometry [80].

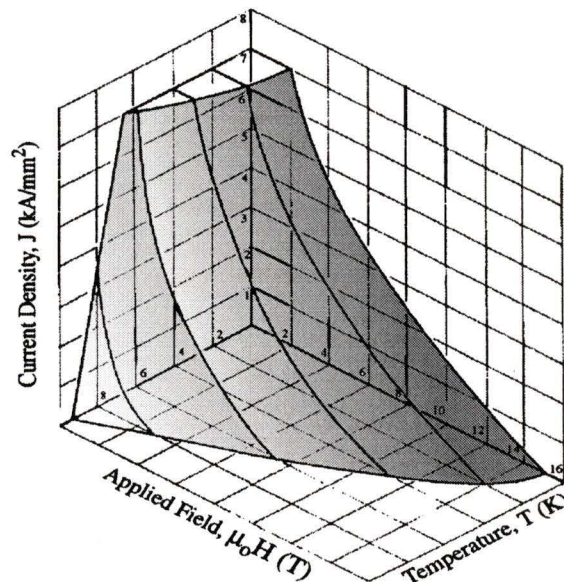


**Figure 2-4: Critical surface for NbTi.**

Until recently, superconductivity had been restricted to materials (metals and alloys) with  $T_c$ -values of less than 23 K. In 1986, Bednorz and Muller discovered a ceramic material (La-Ba-Cu-O) with superconducting properties at 30 K [81]. This precipitated an onrush of ceramic based superconductors with transition temperatures as high as 95 K ( $YBa_2Cu_3O_7$ ) by 1987 [82]. The ceramic-based materials are commonly known as high temperature (high- $T_c$ ) superconductors while the metallic and alloy materials are called

low temperature (low- $T_c$ ) superconductors. Currently, the brittle nature of most ceramic superconductors imposes serious manufacturing limitations, so low- $T_c$  superconductors remain essential to the designer and manufacturer of commercial AMRL systems.

### 2.4.1 Conductively Cooled SCM Systems

Traditional superconducting magnet systems have relied on a bath of liquid helium to maintain the SCMs at their operating temperatures (typically 4.2 K). This approach requires the use of highly effective Dewar vessels with thermal shields usually cooled by a bath of liquid nitrogen. The liquid cryogens used in these systems must be replenished or recondensed as they boil off from the inevitable heat leaks. This is not only uneconomical, but also requires additional operator training. Additional safety considerations also result in the overall SCM system being relatively complex.

Conductively-cooled SCM systems rely on a completely different refrigeration technique that uses a mechanical refrigerator instead of a liquid helium bath. In this case, the SCM is in thermal contact with a heat sink capable of providing the required refrigeration to maintain the magnet at its operating temperature. Using a mechanical cooler simplifies the overall system design by eliminating the need for Dewar vessels and the peripheral components required for safely refilling and storing liquid cryogens.

The use of conduction-based cooling systems for SCM applications is relatively new. The first conceptual design was proposed by Hoenig in 1983 [83] and it included a two-stage Gifford-McMahon (GM) cryocooler (Section 2.5.1) to cool a  $Nb_3Sn$  magnet. A few years later, Furuyama and coworkers [84] developed the first conductively cooled SCM system based on Hoenig's design. This system used two GM cryocoolers instead of one.

During the early 90s, other researchers [85][86][87] were successful in cooling  $Nb_3Sn$  magnets via conduction. In most cases, however, the maximum magnetic fields achieved were low (1-3 T) because the operating temperatures for the  $Nb_3Sn$  magnets were high (i.e., above 10 K).

Improved SCM designs using only one GM cryocooler relied on high- $T_c$  current leads for magnets operating at approximately 10 K [77][88][89][90]. The main obstacle in all these systems was related to the low cooling capacities available at temperatures below 20 K. Devices capable of reaching 4 K made use of a Joule-Thompson (J-T) stage precooled by a two-stage GM cryocooler.

GM cryocoolers have become very popular in conductively-cooled SCM applications. At least four companies have developed systems capable of replacing the refrigeration systems based on liquid cryogenes. Some of the advantages associated with a GM cryocooler include the following:

- It is a highly reliable refrigerator, with an mean time between failures (MTBF) in the order of 10,000 hours.
- There is less wear and tear of seals and other mechanisms due to relatively low cycle speeds ( $\leq 2.5\text{Hz}$ ).
- The direction of gas flow is periodic which makes the system more tolerant to gas impurities
- It uses highly efficient thermal regenerators which are compact and easy to build.
- The compressor portion of the system is isolated which minimizes vibration and increases modularity.
- Because the system operates on electrical motors, it is relatively easy to design completely automated (computerized) control systems.
- It eliminates the need for liquid cryogenes thereby simplifying overall system design.

The performance of GM cryocoolers depends to a large extent on the effectiveness of the thermal regenerators used. Regenerator design is a non trivial matter with requirements that are often conflicting or mutually exclusive. The following section describes some of these requirements.

## **2.5 Passive Regenerators**

The first regenerative heat exchanger was conceived by Robert Stirling in 1815 during the design of an engine now known as the Stirling engine. This device was intended for the production of power from furnace heat. However, 46 years after Stirling's suggestion

Alexander Kirk used a regenerative cycle for the production of ice [91]. Since then, many regenerative refrigeration cycles have been developed. These cycles include:

- Stirling
- Gifford-McMahon
- Vuilleumier
- Orifice pulse tube, and
- Magnetic cycles such as: Brayton, Ericsson, and AMR (see Appendix C).

A passive regenerator is a compact and highly effective heat exchanger in the form of a porous, finely-divided solid mass. A working fluid is forced alternately and periodically through this porous matrix. Based on this periodic flow, the regenerator can absorb heat from the hot working fluid on one stage of a regenerative cycle, and then return the heat to the cold fluid on another stage of the cycle. This periodic transfer of relatively large quantities of heat (compared to the thermal load) allows regenerators to extend the temperature range of a refrigerator beyond that produced by isentropic compression and expansion processes.

Regenerators are very complex thermodynamic devices and the theoretical understanding of their behaviour is still a subject of intense research. A thorough analysis of regenerator theory requires the use of numerical methods and is beyond the scope of this thesis. The interested reader is referred to the excellent works by Schmidt and Wilmott [92], Timmerhaus and Flynn [93], and Walker [94]. Table 2-3 shows a brief summary of the desirable characteristics in an ideal regenerator [95] compared to those found in real devices.

The requirements listed in Table 2-3 affect the operation of the regeneration during pseudo steady state conditions. These conditions correspond to the so-called periodic flow in which the temperature profile within the regenerator repeats itself after each cycle. Static and dynamic factors such as eddy diffusivity, flow channeling, and heat shuttle effects make regenerator operation even more complicated. Although the design of optimized regenerators is a difficult task, these devices have been successfully used in a variety of refrigerators (including GM cryocoolers).

**Table 2-3: Desirable characteristics in an ideal regenerator compared to the actual properties of practical devices.**

Ideal Regenerator	Practical Regenerators
Infinite thermal mass compared to the thermal mass of the working fluid being heated or cooled	Finite thermal mass compared to the working material mass flow. In the case of GM cryocoolers, the volumetric thermal mass of the regenerator is sometimes smaller than that of the working fluid (e.g., at $T < 10$ K).
Infinite heat transfer coefficient(s) and/or infinite specific surface area.	Finite heat transfer due to finite heat transfer coefficients and finite specific surface areas. Typical values are $h \geq 100$ s of $\text{W m}^{-2} \text{K}^{-1}$ , and $A \geq 10^4 \text{ m}^2 \text{ m}^{-3}$ .
Zero void volume	Finite porosity values. Typical values range from 0.3 to 0.7.
Zero pressure drop associated with fluid flow through the regenerator	Real friction factors imply the need for non-zero pumping powers. In addition, finite pressure drop values limit the length of the regenerator. This also imposes a lower limit to the size(s) associated with internal geometries (e.g., particles with diameters $< 100 \mu\text{m}$ are seldom used).
Zero longitudinal conduction	Parasitic heat leaks along the regenerator bed can be minimized but not eliminated.
Linear temperature profile from the hot to the cold end of the regenerator bed	Real material properties vary as a function of temperature and result in non-linear temperature profiles.

### 2.5.1 The Gifford-McMahon (GM) Refrigerator

The GM cryogenic refrigerator (GM cryocooler) was invented by William Gifford and Howard McMahon in the mid 1950's [96][97]. This device was rapidly converted into a successful commercial product whose reliability, low maintenance requirements, and simple design made it very popular for cryogenic applications. Today, GM cryocoolers are widely used for cryopumping, cooling of SCMs in MRI systems, and in a variety of other applications.

A conventional two-stage GM-cryocooler consists of an enclosed cylindrical space containing a displacer and regenerator assembly (see Figure 2-5). This assembly is

connected to a drive mechanism\* and it can be moved in a periodic fashion inside the cylinder. At each stage, the spaces on either side of the displacer are separated by a dynamic seal which forces the gas to flow through a thermal regenerator. The gas supply subsystem consists of a gas compressor and aftercooler, reservoir volumes to keep the inlet and outlet pressures constant, and valves to control the flow of working fluid (usually high purity helium gas). The valves are coupled to the driving mechanism in order to synchronize fluid flow with the reciprocating motion of the displacer. The work required to move the displacer is minimal because the pressure drop across the regenerator bed is relatively small. However, the power input to the compressor is significant and overall efficiencies are low (no work is recovered from gas expansion).

Additional refrigeration stages can be added to a GM cryocooler without any significant increase in complexity. This is particularly useful because most cryogenic applications require refrigeration at more than one temperature (pre-cooling before liquefaction, cooling of radiation shields to reduce heat leaks, etc.). Multistage GM cryocoolers require additional regenerators, displacers and heat exchangers, but the valving and mechanical drive mechanisms can be common to all the stages in the device.

To explain the operation of a two-stage GM device, assume that the cycle starts with the displacer at the bottom of the cylinder and the low-pressure valve closed. At this point, the high pressure valve opens and high pressure gas enters and fills the enclosed spaces (regenerator, connecting lines and the volume at the top of the displacer).

---

\* The driving mechanism usually consists of a crank shaft connected to a motor. Other possibilities include the use of "cryomatic gas balancing" which eliminates the mechanical drive (motion is achieved via the pressure differential arising from the working fluid entering or leaving the enclosed space).

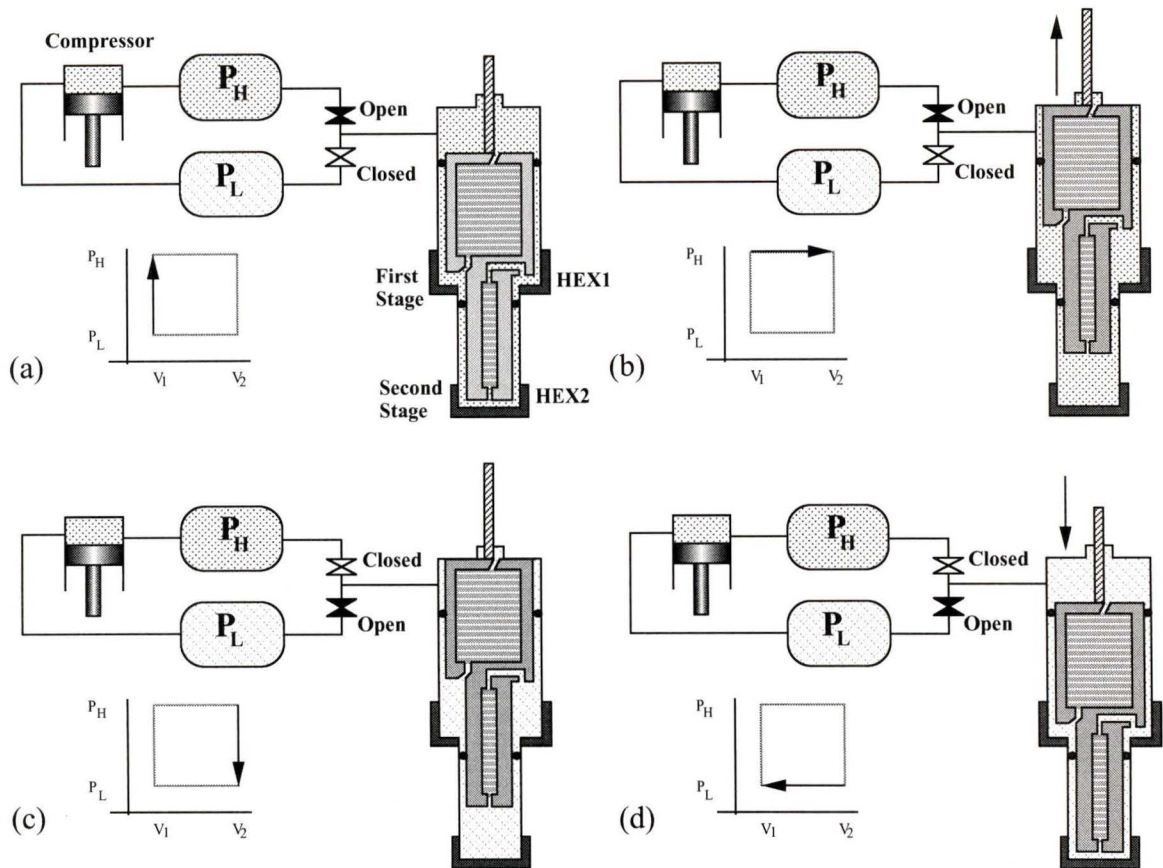


**Figure 2-5: The cycle of operation in a two-stage GM cryocooler. Notice that the displacer and regenerators have been combined into a single unit. The cycle includes flow of pressurized helium at  $P_H$  (a), upward motion of the displacer (b), isovolometric expansion of the gas to a new pressure  $P_L$  (c), downward motion of the displacer to its original position (d). The schematic PV diagram corresponds to the second-stage volume. The driving mechanism is not shown.**

The next step in the cycle corresponds to the motion of the displacer from the bottom to the top of the cylinder. This motion forces high pressure gas through the regenerator. Because the gas is cooled as it flows through the regenerator matrix, it will decrease in volume and more gas will flow into the system to maintain the high pressure constant.

Once the displacer has reached the top of the cylinder, the low pressure valve is opened and the gas in the entire system expands. This expansion results in a decrease in the temperature of the gas that is finally left in the space at the bottom of the displacer (work is done to force the rest of the gas out) .

Lastly, the displacer moves from the top to the bottom of the cylinder (with the exhaust valve still open) and the cold gas can accept a cooling load via the low temperature heat exchanger and as it moves back through the regenerator. At the end of the stroke, the low-pressure valve is closed and the cycle is repeated.

### 2.5.2 4 K GM Cryocoolers

Conventional two-stage GM cryocoolers use lead as the second stage regenerator material. These devices can reach temperatures as low as 6.5 K with zero thermal load at the second stage [98]. Below this temperature the volumetric heat capacity of lead decreases rapidly while the corresponding values for pressurized helium increase (see Figure 2-6) This thermal-mass imbalance between the regenerator and the pressurized helium makes it impossible for the regenerator matrix to absorb enough heat to cool the gas sufficiently before it expands.

One possible solution to this limitation was proposed by Buschow et al. more than 20 years ago [99]. They suggested that lanthanide materials with low magnetic ordering temperatures ( $< 10$  K) could be used as cryogenic regenerators. However, the high price of the proposed materials (e.g., Rh) prevented the commercialization of this design. Thirteen years later, Hashimoto et al. revisited this idea at the Tokyo Institute of Technology [100]. These authors described a series of rare-earth/transition metal (RE/TM) alloys such as  $(\text{Er}_{1-x}\text{Dy}_x)\text{Ni}_2$  and  $\text{Er}(\text{Ni}_{1-x}\text{Co}_x)$  as potential low temperature regenerator materials. One of the most important results of this investigation was the design of a hybrid regenerator with layers of different materials. The layered structure attempted to match the temperature profile in the regenerator matrix with the relatively narrow heat capacity peaks of each material (see Section 2.6).

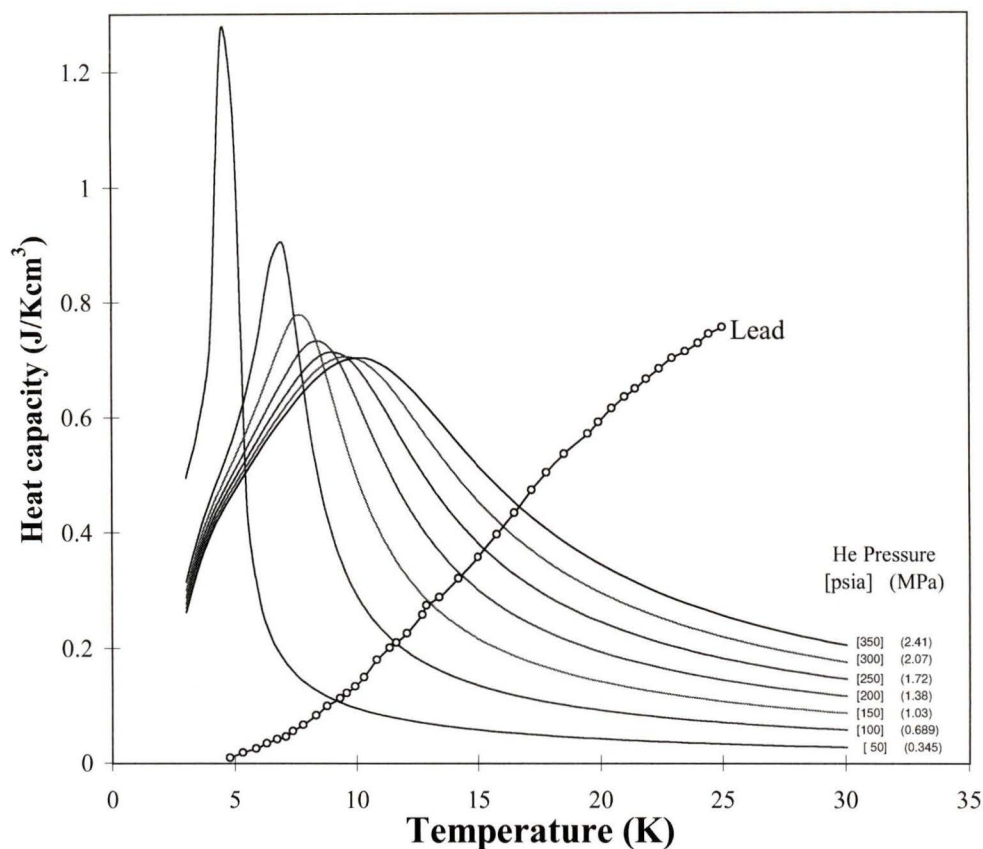


**Figure 2-6: Comparison between the volumetric heat capacity of lead and helium gas at different pressures.**

By 1989, Yoshimura et al. [101] at the Mitsubishi General research Laboratory in Japan had put to practice the discoveries of Buschow et al. The Japanese group reported on the successful liquefaction of helium by a three-stage GM cryocooler. The first and second stages in this device used conventional regenerator materials (phosphor bronze and lead, respectively). The third stage regenerator consisted of a two layer hybrid using GdRh and  $Gd_{0.5}Er_{0.5}Rh$  as the regenerator materials.

Further developments included the work by Sahashi et al. [102] and Kuriyama et al. [103] at the Toshiba R&D center in Kawasaki, Japan. In these publications, the authors described a low temperature regenerator that could be used at the second stage of a two-stage GM cryocooler. This regenerator consisted of a hybrid structure using lead and  $Er_3Ni$  (a new alloy) as the regenerator materials. The device built by Kuriyama et al. used

this regenerator and was the first two-stage GM cryocooler to achieve temperatures below 5 K.

Although the development of new regenerator materials was the most important factor enhancing the performance of GM devices, other modifications were also to reach liquid helium temperatures. For example, in addition to modifying the second stage regenerator, Kuriyama and coworkers had to optimize other operating parameters such as valve timing and cycle frequency. These and other factors have been the subject of intense research in the past few years [104][105].

The application of improved GM cryocoolers to cool SCM systems was almost immediate. In 1993 Masuyama et al. [106] reported on a conductively cooled NbTi magnet capable of producing 6.3 T at 6 K. Because the cooling capacity at the second stage was low (~500 mW), this magnet system required two GM cryocoolers: one to cool the current leads and radiation shields, and the other to cool the magnet.

The development of new regenerator materials such as  $\text{ErNi}_{0.9}\text{Co}_{0.1}$  [107],  $\text{Er}_3\text{Co}$  and  $\text{Er}_{0.9}\text{Yb}_{0.1}\text{Ni}$  [108] has made it possible to build two-stage GM cryocoolers with larger cooling powers at 4.2 K. Examples of such devices include the cryocoolers developed by Kuriyama et al. [109] and Tsukagoshi et al. [110] which can provide slightly over 1W of cooling power at 4.2 K.

Recent developments in GM cryocooler technology have also included the work by Satoh et al. [111] at the R&D Center of Sumitomo Heavy Industries in Japan. Their device uses a  $\text{Er}_3\text{Ni}/\text{Er}_{0.9}\text{Yb}_{0.1}\text{Ni}$  hybrid regenerator (50%/50% by volume) and it can provide 1.5 W of cooling power at 4.2 K. The major modifications in this device consisted of optimizing the valve timing, increasing the size of the second-stage expansion volume, and using 500 g of  $\text{Er}_3\text{Ni}$  and 500 g of  $\text{Er}_{0.9}\text{Yb}_{0.1}\text{Ni}$  for the second-stage regenerator.

The largest cooling capacity for a two-stage GM cryocooler has been recently reported by Takashi et al. [112] This cryocooler uses the same  $\text{Er}_3\text{Ni}/\text{Er}_{0.9}\text{Yb}_{0.1}\text{Ni}$  hybrid regenerator, but it can provide 2.2 W of cooling power at 4.2 K. The two major modifications required to obtain such a large cooling capacity consisted of i) increasing the expansion space volume at the second stage (the diameter was changed from 25.4mm to 60mm), and ii) using a multilayer regenerator separated by metallic screens placed between two felt mats.

Even if a variety of possible regenerator materials have been developed in the last few years, [113] all the cryocoolers discussed thus far use erbium-based alloys in their second stage regenerator. The brittle nature of these alloys is a serious limitation that can compromise the structural integrity of the regenerator matrix.

During normal operation, the regenerator is exposed to a periodic pressure wave that can cause particle fragmentation. Unless particle disintegration is prevented, the resulting microscopic metallic powders ( $< 40 \mu\text{m}$ ) will be carried by the moving gas thereby contaminating other parts of the system. This contamination can seriously damage the sliding seals, valving mechanism and other close tolerance components. The presence of these powders outside the regenerator produces a parasitic thermal load due to friction. In addition, small particles can fill the interstitial sites between larger ones thereby increasing the pressure drop across the regenerator and decreasing the flow of gas to the expansion spaces.

The structural limitations of RE/TM-based regenerators can be circumvented in a number of ways. One possibility consists of using pure RE metals instead of the RE/TM alloys. Pure neodymium, for example, is a ductile material that has been successfully used to replace the erbium-based alloys. Chafe et al. [114] modified a conventional GM cryocooler using this material and managed to obtain approximately 500mW of cooling power at 4.2 K. Although the cooling powers are modest, devices using Nd regenerators are more reliable than their Er-based counterparts. In addition, a Nd-based cryocooler

with large cooling capacity has been recently reported [115]. The second-stage regenerator in this device uses a stack of perforated Nd plates instead of a packed bed of particles (see Section 2.8.2). Other approaches include the use of spherical particles to increase the reliability of regenerators made of RE/TM materials will be discussed later (Section 2.7), the work presented in this thesis includes an alternative technique to ensure structural integrity in RE/TM regenerators, while simultaneously reducing the associated manufacturing costs.

Figure 2-7 shows a planar section view of the conductively cooled magnet system in the AMRL [80]. The selection criteria and manufacturing techniques associated with cryogenic regenerator materials are discussed in the following sections.

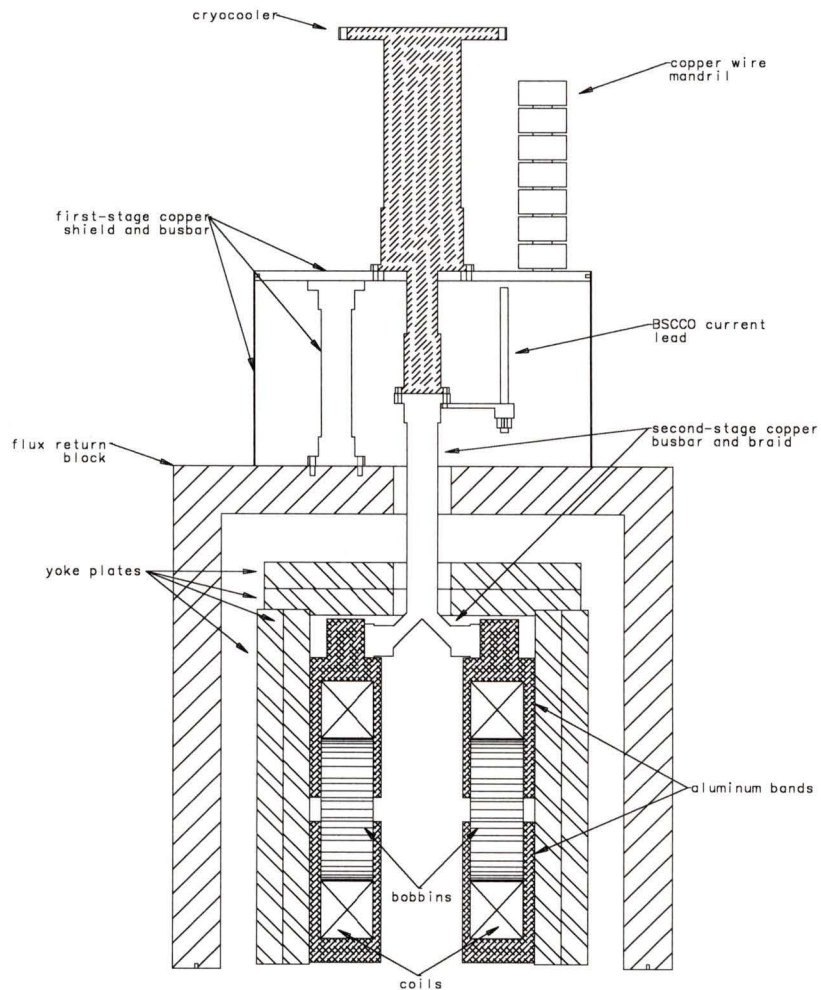


**Figure 2-7: Planar view of the conductively cooled magnet system in the AMRL.**

## 2.6 Selection Criteria for the Large Thermal Mass Regenerator Materials in Low Temperature (4 K) GM Cryocoolers

The performance of multistage GM cryocoolers depends to a large extent on the effectiveness of the thermal regenerators used. Common regenerator materials include phosphor bronze, copper, stainless steel and lead. The most common regenerator geometries are packed beds of particles, stacks of packed screens or perforated plates and other configurations with large specific surface areas. Phosphor bronze screens and lead shot are usually used in the first stage regenerator. These regenerators cover the temperature range between room temperature and 30-40 K [116]. Hardened lead particles containing 1-5% antimony are routinely used as the second-stage regenerator material. This regenerator spans the temperature range between the first stage and 6.5 - 10 K. As discussed in Section 2.5.2, devices reaching liquid helium temperatures require the use of different materials in the second stage regenerator. The selection criteria associated with these materials are discussed in the following sections.

The main requirement for a cryogenic regenerator material is a large thermal mass per unit volume. The only significant factors determining the heat capacity of lead are related to the lattice and electronic contributions discussed in Appendix A. Both  $C_L$  and  $C_E$  decrease rapidly with temperature (see Appendix D). In the case of lead, these contributions are essentially zero below 5 K (see Figure 2-6). If a regenerator material is to be effective below this temperature, it must have a contribution to the heat capacity with different physical origins. As discussed in section 2.1, the magnetic properties of the material can provide an additional contribution,  $C_H$ , to the total heat capacity.

A magnetic phase transition is accompanied by an increase in heat capacity due to a large entropy change near the phase transition temperature. Following these ideas, several authors [100][102][103][113] have proposed a series of selection parameters for materials with high heat capacities at low temperatures. The most important criteria are as follows:

1. Low Debye temperature,  $\theta_D$ .
2. Magnetic ordering temperature in the appropriate range.

3. Large magnetic entropy.
4. Large number of magnetic atoms per unit volume.
5. Presence of lanthanide elements from the beginning or the end of the series.
6. Broad (or narrow) heat capacity peaks.

According to these criteria (see Appendix E), the best candidate materials are alloys containing heavy lanthanides with large magnetic entropy values (e.g., Er, Dy, Ho, etc.). The temperature-dependent, heat capacity values for some of these alloys are shown in Figure 2-8.

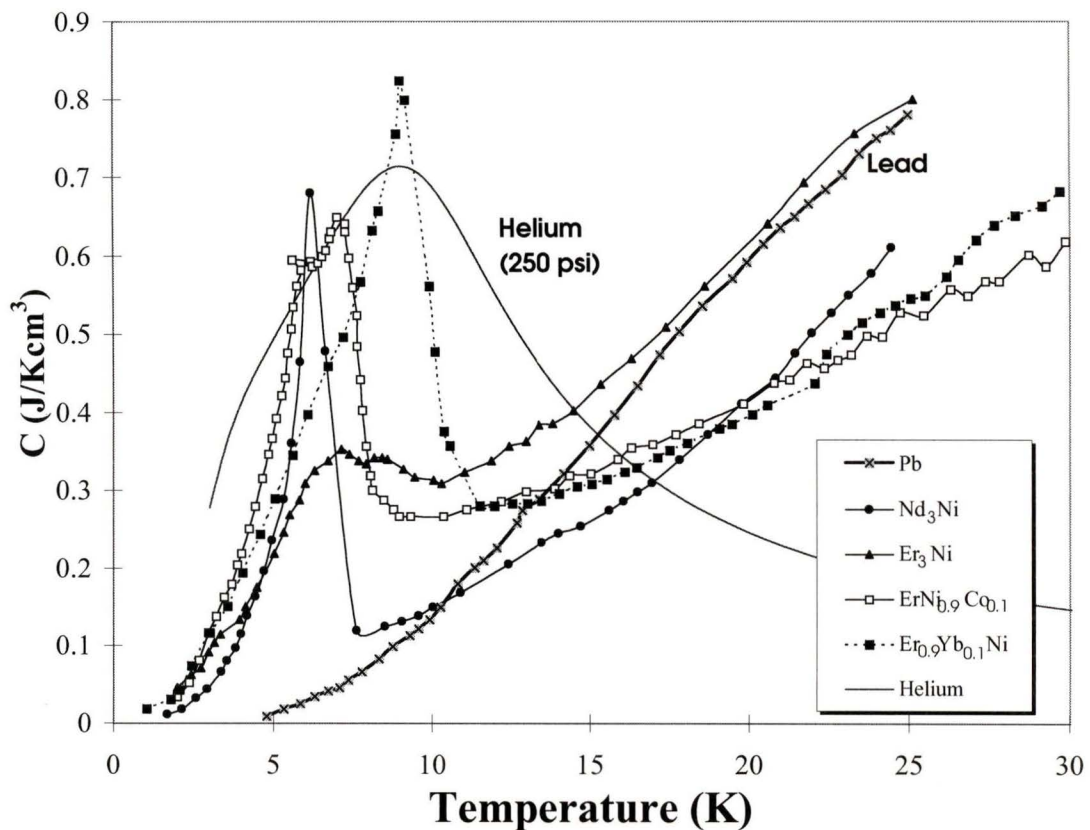


**Figure 2-8: Volumetric heat capacities of some RE/TM alloys compared to lead [109][111][113].**

In addition to possessing large heat capacity values and other fundamental properties, regenerator materials must also comply with more pragmatic requirements. None of these materials will be useful unless it can be converted into a simple, reliable, and highly

effective regenerator in a cost-effective manner. In the case of regenerators for GM cryocoolers, the cost of the magnetic materials is by itself significant (see Table 2-4) [117][118].

**Table 2-4: Prices for some rare-earth metals (purity = 99.9%).**

<b>Metal</b>	<b>Price/kg (U.S. Dollars)</b>
Nd	450
Gd	255
Tb	840
Dy	265
Er	570
Yb	800

The following sections describe some of the manufacturing techniques associated with regenerator materials as well as some of the limitations encountered when RE/TM alloys are used.

## **2.7 Traditional Manufacturing Techniques for Regenerator Materials**

The most common geometry for the second-stage regenerators in GM cryocoolers consist of a bed of packed, spherical particles. Recent studies [119][120][121] have shown that the high reactivity and brittleness of lanthanide metals and compounds impose serious restrictions on the commercial production of practical regenerators. The following sections describe some of the common manufacturing techniques used to produce spherical particles and some of the other possible geometries. A novel manufacturing technique to produce structurally stable regenerators with irregularly-shaped RE/TM particles is described in Section 2.9.

### **2.7.1 Gas Atomization**

Gas atomization has been successfully used to produce very fine metal powders (~ 100  $\mu\text{m}$ ). In order to produce these powders, a controlled flow of molten metal is forced through a nozzle (see Figure 2-9). The emerging metal stream is disintegrated by high

velocity jets of atomizing gas. The resulting particles are subsequently collected at the bottom of the apparatus.

The particle size can be controlled by varying the size and shape of the nozzle, the velocity of the gas jets, the composition of the molten metal, and other parameters. Lower velocity of the atomizing jet, for example, results in larger particle size ( $\sim 400 \mu\text{m}$ ) but the production rates are low [122].

Although gas atomization is widely used to make metal powders, the results obtained with rare-earth alloys have shown limitations. One of the major problems is that gas atomized particles have significant internal voids [121][122]. This additional empty space increases the effective porosity in a regenerator thereby reducing its thermal mass. In addition, smaller particles (satellites) are found attached to the outer surface of the semi spherical powders. These satellites can easily break free from the surface and become a source of contamination similar to that described in Section 2.5.2.

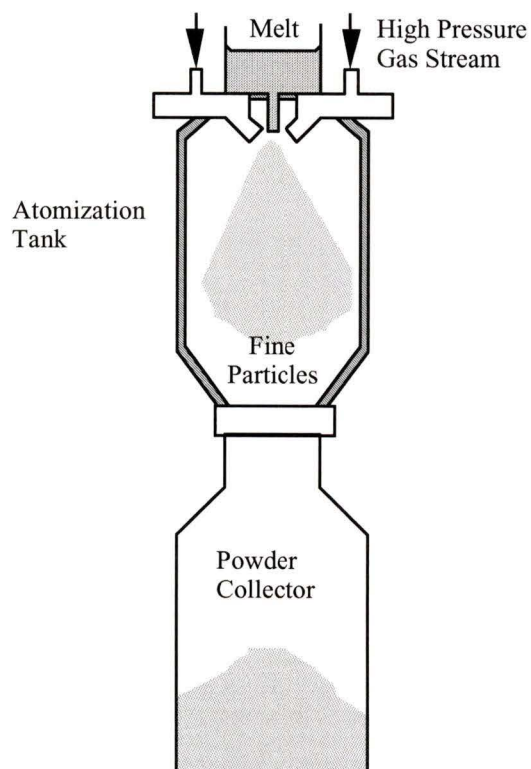


**Figure 2-9: Schematic representation of a typical gas atomization apparatus [123].**

## 2.7.2 Centrifugal Atomization

The most common centrifugal atomization techniques use a rotating, consumable electrode, or a stream of molten metal that is projected onto a disk rotating at high speed (up to 35,000rpm) [123]. The resulting particles are cooled by gas streams (helium is sometimes used to enhance heat transfer). These techniques are capable of producing high yields of particles in a particular size range (30 to 50% for particles with a diameter of  $100 \pm 20 \mu\text{m}$ ) [124].

The rotating electrode method is a single step process that melts and pulverizes the metal at once. Centrifugal atomization, on the other hand, is a two step process that requires melting the alloy prior to pulverizing it. This additional step makes it possible to superheat the alloy and obtain particles of homogeneous composition. This is not always possible when the rotating electrode method is used (especially for alloys of extended solid/liquid ranges) [125]. In addition, preparing the starting billet is difficult because the RE/TM alloys are usually very brittle. For these reasons, centrifugal atomization is the preferred option to produce high quality, semi spherical particles.

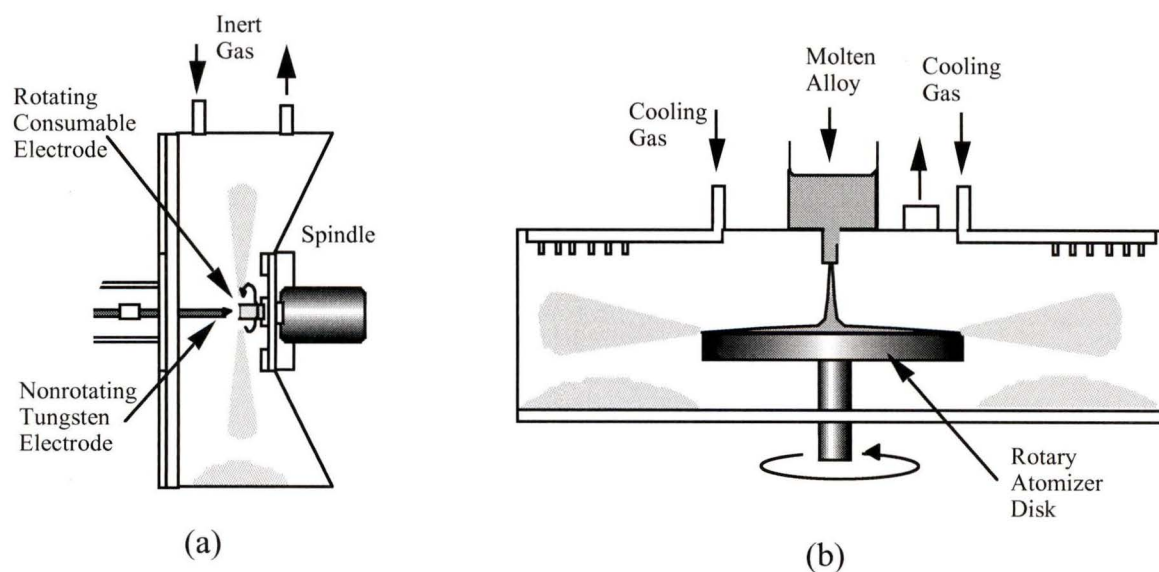


**Figure 2-10: Two common implementations of centrifugal atomization techniques. Rotating consumable electrode (a) and spinning disk (b) [123].**

## **2.8 Current Research on Alternative Regenerator Geometries**

Although beds of spherical or semi spherical particles have been the most practical choice for cryogenic regenerators, the associated manufacturing costs are high. Alternative geometries have received some attention recently. In all cases, the cost of manufacturing is the main factor to consider. Several companies have also patented certain manufacturing methods making alternative techniques desirable.

### **2.8.1 Wire Screens**

Wire screens have been successfully used as regenerator materials even if their porosity values (70%) are generally higher than the corresponding values for beds of packed spheres (40%). To improve the performance of a bed of packed screens, it is necessary to increase the mesh number. This implies that the wire itself must be drawn to very small diameters (for a standard 400 mesh screen, the wire diameter is about 25  $\mu\text{m}$ ).

Alloys containing heavy rare earths tend to be extremely brittle and drawing them into thin wires is very difficult. Reid [124] has reported on a collaborative effort between the Cfs group, the Materials Research Centre at AMES laboratories, and Supercon Inc., a company specialized in the manufacture of superconducting wire. The aim of this work consisted of drawing dysprosium metal into thin wires.

The results of these investigations showed that it is possible to draw rare earth metals and alloys into thin wires of appreciable length. However, the manufacturing costs associated with weaving these wires into screens are high (US\$5,000-10,000) [124]. This is mostly because the few screen manufacturers in North America are reluctant to use unfamiliar materials to produce low volumes of high mesh products [124].

### **2.8.2 Perforated Plates**

Stacks of perforated plates can drastically reduce the effective porosity in a regenerator thereby increasing the thermal mass per unit volume. Chafe et al. [120] have recently

reported on the use of Nd plates in the second stage regenerator of a two-stage GM cryocooler. This regenerator is built by precisely forming small (0.2 mm) flow holes through Nd disks. These disks are prepared using a technique similar to that used to fabricate superconducting wire. GM devices using this type of regenerator are potentially capable of providing 2 W of refrigeration power at 4.2 K.

Although perforated plates show lots of promise as an effective regenerator geometry, producing thin plates from RE/TM alloys will be difficult. This regenerator geometry has not yet been explored by the Cfs group.

## **2.9 New Monolithic Regenerators using Irregularly-shaped RE/TM Particles.**

Most of the RE/TM alloys that have been identified as excellent cryogenic regenerator materials are very brittle. This characteristic simplifies the production of fine, irregularly-shaped particles (by simple crushing and sieving), but also implies the need for the structural integrity considerations discussed in Page 37. Other groups have relied on fabrication techniques that ensure the production of perfectly round particles [122][125]. With this type of geometry, the regenerator beds are much more stable over time and the contamination problems are drastically reduced (spheres can withstand larger mechanical loads without breaking). Because particle disintegration is prevented, the possibility of clogging the regenerator are also minimized. However, the fabrication costs associated with spherical particles in the appropriate size range (100 to 400  $\mu\text{m}$ ) are extremely high. Most of the costs are related to manufacturing techniques that require sophisticated and expensive hardware.

The work being presented in this thesis includes a novel manufacturing technique for monolithic cryogenic regenerators. This technique uses irregularly-shaped RE/TM particles with an effective diameter between 250 and 300  $\mu\text{m}$ . These particles are imbedded in a cryogenic epoxy coating matrix that prevents their relative motion during operation. Three important regenerator characteristics are provided by this design:

- (i) the specific surface area and total pressure drop are not compromised because only a small amount of epoxy is used, and
- (ii) the intrinsic brittle character of the RE/TM materials is overcome by making the regenerator monolithic. Particle disintegration is eliminated producing a robust and reliable passive regenerator.
- (iii) Low values of longitudinal thermal conductivity are preserved because the point contacts between neighbouring particles do not provide a good conductive path.

The bonding of the entire regenerator into a monolithic yet porous bed makes it highly stable and resistant to structural and thermal stresses. In addition, the high cost associated with the production of spherical particles has been eliminated.

To the author's knowledge, this is the first time that such a technique has been used to improve the second-stage performance of a GM cryocooler. The manufacturing techniques developed as part of this thesis will be described in the following chapters.

# Chapter 3

## Experimental Procedures

As explained in Chapter 2, a conventional, two-stage GM cryocooler was selected to provide the cryogenic refrigeration required by the SCMs in the AMRL. Although low temperature (4 K) GM units have recently become available, there is a significant price difference between these devices and their lead-based counterparts (depending on the vendor, this difference can range from US\$20,000 to US\$30,000).

This chapter is focused on the performance of the GM cryocooler immediately after it was purchased and the modifications that were required to achieve liquid helium temperatures. The chapter starts with a general description of the experimental setup and the vacuum chamber used to carry all the tests. The discussion is then focused on the GM cryocooler and its components. The results of comparing the manufacturer's specifications and the actual observed performance are given in Sections 3.5.1 and 3.5.2.

### 3.1 Experimental Chamber

The chamber used for all the experiments described in this work was specifically designed and built to test the GM cryocooler. This chamber consisted of an aluminum cylindrical container (OD = 61 cm, length = 92.5 cm) with a removable flange at one end. This flange was sealed with a standard, room-temperature O-ring.

The pumping system consisted of a rotary vane mechanical pump for rough vacuum levels (atmospheric pressure to  $10^{-2}$  torr), and a turbomolecular pump to maintain high vacuum ( $10^{-2}$  to  $10^{-7}$  torr). The pump was connected to the vacuum chamber by a flexible stainless steel line. The pumping system was in continuous operation during all tests and

provided a nominal pressure of  $5 \times 10^{-6}$  torr (0.667 mPa) inside the vessel. This pressure was measured with an inverted magnetron vacuum gauge and recorded manually.

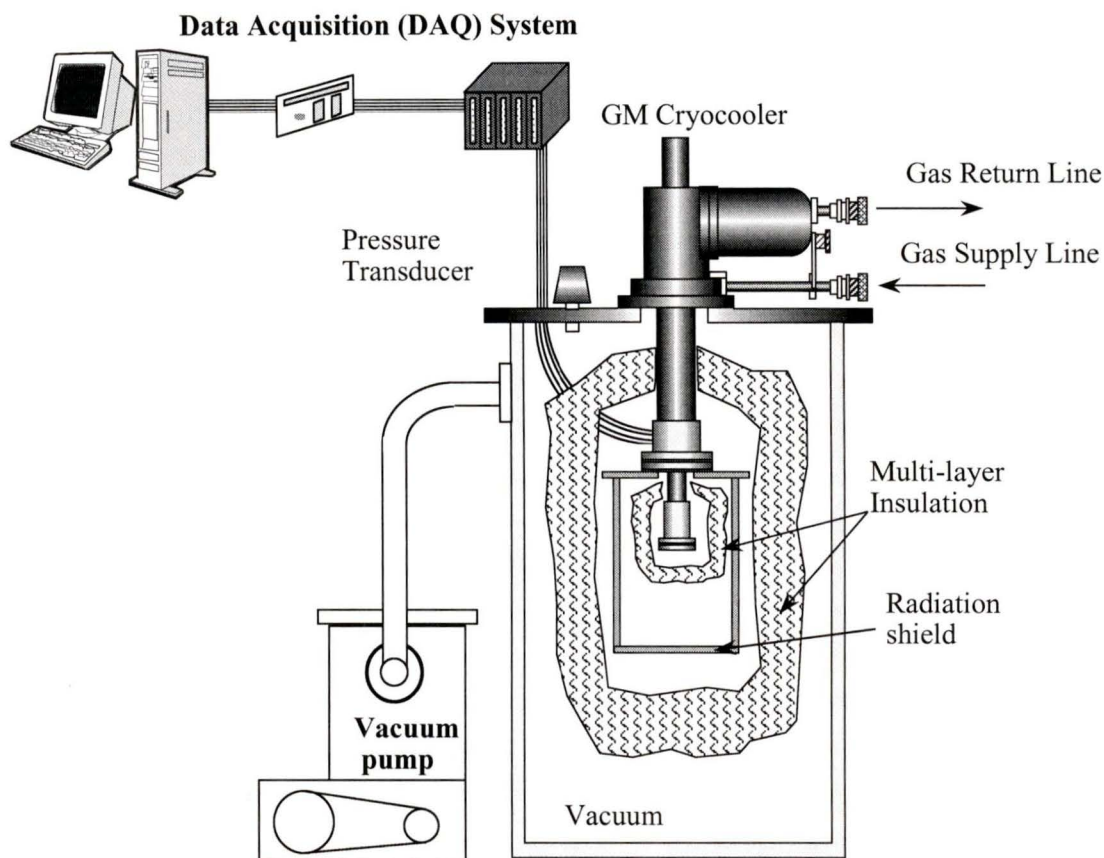


**Figure 3-1: Schematic diagram of the experimental setup used to test the GM cryocooler.**

The reduced pressures inside the experimental chamber were required to minimize convective heat leaks. This and other experimental techniques are essential for measurements carried out at cryogenic temperatures. Some of these techniques are discussed in the following sections.

### 3.2 Thermal Insulation

In order to insulate two surfaces maintained at different temperatures, it is necessary to minimize the conductive, convective and radiative heat transfer mechanisms. The

different techniques used to comply with each of these requirements are discussed in the following sections.

### 3.2.1 Vacuum Insulation

The ability to transfer heat through a gaseous medium is related to the total number of gas molecules available. By reducing this number, it is possible to decrease the total heat transferred from warm to cold surfaces. To accomplish this, the gas present between these surfaces must be removed. Evacuated chambers applying this technique are widely used in cryogenic applications. The relationship between heat transfer and gas pressure is shown schematically in Figure 3-2.

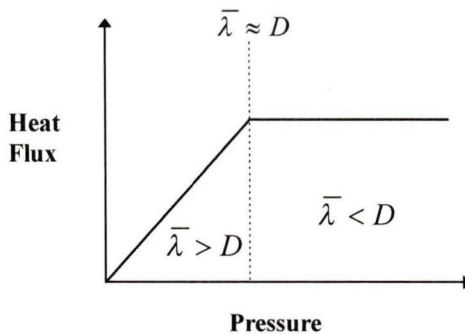


**Figure 3-2: Schematic representation of heat transfer as a function of gas pressure (  $D$  = distance between warm and cold bodies).**

At ordinary pressures, the gas (in most cases air) can be treated as a continuous medium and heat transfer is more or less independent of gas pressure. As the gas is evacuated, heat transfer continues at a more or less constant rate but the mean free path of the gas molecules,  $\bar{\lambda}$ , increases steadily. When this value becomes comparable to the distance between warm and cold surfaces, the gas cannot be considered a continuum anymore. Under this free-molecular flow regime, the gas molecules collide with the container walls more often than they collide with each other. In most cases, a vacuum pressure of  $10^{-5}$  torr (1.333 mPa) or lower is sufficient to virtually eliminate heat transfer through a gaseous medium [125]. In addition, the elimination of air around cryogenic components prevents water vapour and other gases from condensing or solidifying on cold surfaces.

### **3.2.2 Radiation Shielding**

Electromagnetic radiation does not require a medium to be transmitted. Hence, the only way to prevent radiative heat transfer between warm and cold bodies consists of intercepting the radiation at an intermediate temperature. The thermal shields used for this purpose must be made of materials with low emissivity and high thermal conductivity. In the case of the GM cryocooler, the radiation shield consisted of a cylindrical enclosure made of highly polished brass. The top of this cylinder was bolted to the first stage of the GM cryocooler and the entire shield was maintained at a constant temperature of approximately 40 K.

According to Radebaugh [126], the thermal conductance of soldered indium joints is higher than the corresponding values for pressed joints. However, a bolted junction allowed easy removal of the thermal shield and was simpler than a semi-permanent, soldered contact. Other authors [127][128] have also reported on the benefits of using indium foil and a thin layer of Apiezon™ thermal grease [129] to obtain lower contact resistances.

Following these practices, indium foil was used between the shield cover and the copper flange at the first stage. Similar procedures were used to join the copper flanges and the heaters used to apply simulated cooling loads.

#### **3.2.2.1 Multilayer Insulation (MLI)**

Another insulation technique used to minimize radiation leaks consists of placing multiple layers of a reflective material between the warm and cold surfaces. The most common materials used for this purpose are aluminum foil, copper foil, and aluminized Mylar sheets [125]. Low conductivity spacers such as nylon nets, fiber glass mats or glass fabrics are used to separate the individual layers. These spacers minimize the conduction of heat via conduction but can be eliminated by simply crinkling or embossing the

individual sheets. In this way, there are only a few discrete contact points for conduction to occur.

According to Gathright and Reeve [130], the concurrent use of vacuum insulation and at least 20 layers of Mylar insulation can reduce the radiative heat leak to a few watts per square meter (for warm and cold surfaces at 294K and 77K, respectively).

The effective thermal conductivity of MLI can be decreased by increasing the number of layers but only up to a certain point. If too many layers are tightly compressed, the effective thermal conductivity in the direction normal to the plane of the sheets starts to increase [131]. In addition, the thermal conductivity of MLI in the direction parallel to the sheets is about three orders of magnitude larger than the conductivity in the normal direction [125][132]. This implies that the performance of MLI will degrade if the edges of the sheets are allowed to have a good thermal contact with warm surfaces.

Another requirement for good MLI performance consists of removing the residual gas present between adjacent layers. Small vent holes or slits in the foil layers have been used to ensure the removal of trapped gas. Scurlock and Saul [133] have reported on the use of carbon-filled glass-fiber paper as the separating material between layers. According to these authors, the carbon surfaces absorbed the gases that could be released due to outgassing of the radiation shield materials.

During the experiments described in this thesis, aluminized Mylar sheets were used between the first stage copper flange and the radiation shield wall. MLI was also used to wrap the entire cold head inside the vacuum chamber. The number of layers used in either case varied between 25 and 30.

### 3.2.3 Heat Leaks

The total heat leaks into the cold regions of the experimental chamber have been calculated in Appendix F. Table summarizes the total heat leaks associated with each of the possible heat transfer mechanisms.

**Table 3-1: Summary of heat leaks into the GM cryocooler (in watts).**

	First Stage	Second Stage	Total
Convection	not calculated	not calculated	-
Conduction	0.630	$5.08 \times 10^{-2}$	$6.81 \times 10^{-1}$
Radiation	$2.00 \times 10^{-5}$	$4.83 \times 10^{-8}$	$2.00 \times 10^{-5}$
Joule heating {RuO <sub>2</sub> } [PRTs]	{ $8.70 \times 10^{-10}$ } [ $8.70 \times 10^{-6}$ ]	{ $1.74 \times 10^{-10}$ } [ $1.74 \times 10^{-6}$ ]	{ $1.04 \times 10^{-9}$ } [ $1.04 \times 10^{-5}$ ]
Joule heating <sup>a</sup>	$1.05 \times 10^{-6}$	$2.10 \times 10^{-7}$	$1.26 \times 10^{-6}$
<b>Total</b>	0.630	0.0508	0.681

<sup>a</sup> Heater lead wire

### 3.3 Instrumentation and Data Acquisition (DAQ) System

All the measurements presented in this work were carried out using a computerized data acquisition system. Obtaining reliable results from such a system depends on the proper operation of various interrelated components. These components can be classified into two main categories:

#### Hardware

- A computer
- DAQ Board
- Signal conditioning modules
- Transducers

#### Software

- DAQ Software
- Analysis software

Each of these components is briefly described in the following sections.

### 3.3.1 Computer System

The computer used for data acquisition was a Power Macintosh™ 9500 with 32MB of random access memory (RAM). Detailed specifications can be obtained from the manufacturer [134].

### 3.3.2 Data Acquisition Board

The data acquisition board used was a PCI-MIO16XE50 model available from National Instruments® [135]. This device is a multifunction analog, digital, and timing input-output (I/O) board especially designed for computers using the peripheral component interconnect (PCI) data bus. This board does not have switches, jumpers or potentiometers for configuration or calibration: these functions are completely under software control. Another important feature in this board is the ability to perform multiple measurements that are synchronized to a common triggering event. This is particularly important for real-time measurements and the detection of transient signals. The sampling rate can be as high as 20kSamples/second.

A 16-bit analog to digital converter (ADC) is used to transform the analog voltage inputs into a digital value. The precision associated with each of the available input ranges is shown in Table 3-2.

**Table 3-2: Measurement precision for a PCI-MIO16XE50 DAQ board at different gain settings.**

Gain	Voltage Range	Precision ( $\mu\text{V}$ )
1.0	-10 to +10V	$\pm 305.18$
2.0	-5 to +5V	$\pm 152.59$
10.0	-1 to +1V	$\pm 30.52$
100.0	-100 to +100mV	$\pm 3.05$

### 3.3.3 Signal Conditioning and Multiplexing

The DAQ board provides a maximum of 8 differential or 16 single-ended input channels. Because the DAQ system was concurrently used by more than one experiment, it was

necessary to increase the number of available channels. This was accomplished by external signal conditioning modules that connected (multiplexed) each of their inputs to a single input channel on the DAQ board. The signal conditioning modules used were SCXI-1102 models available from National Instruments®. Although these modules have been specifically designed to work with thermocouples, they can be easily adapted to work with a wide variety of sensors. The SCXI-1102 modules have 32 differential analog input channels. Each of these channels has a separate amplifier that can be individually programmed to have a gain of 1 or 100. Each input signal is also passed through a low-pass filter with a cutoff frequency of 1Hz. These two features offer an excellent option for the filtering and amplification of low-level, DC voltage signals. In addition, the high input impedances ( $\sim 10^9 \Omega$ ) of the operational amplifiers available at each channel minimize current leaks into the DAQ board. This is particularly important for cryogenic temperature sensors that have high output impedances (a few hundred k $\Omega$ ) and require constant-current excitation. All sensors were connected to the SCXI module using a compatible terminal block (SCXI 1300 from National Instruments®). In all cases, the input signals were treated as ground-referenced, differential voltages.

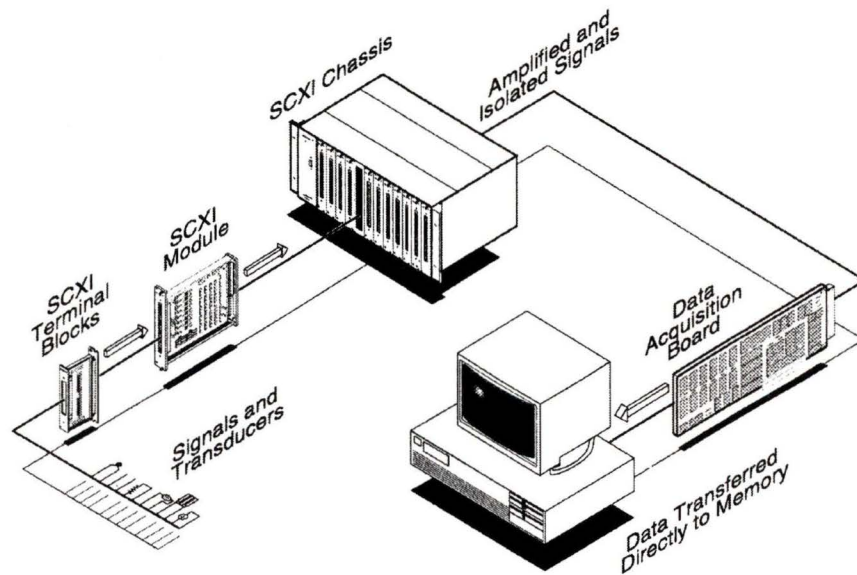


**Figure 3-3: Schematic layout of the DAQ system.**

### 3.3.4 Transducers

Transducers are essentially devices that convert a physical phenomenon into an electrical signal (usually a voltage) that can be measured by a DAQ system. In this work, three different types of transducers were used to measure temperature, pressure and fluid flow. Each of these sensors is briefly described in the following sections.

#### 3.3.4.1 Temperature

Uncalibrated platinum resistance thermometers (PRTs) were used to measure between ambient temperature and approximately 30 K. PRTs consist of a high purity platinum wire encapsulated in a ceramic container. The wire is usually annealed to eliminate mechanical strain and the container is filled with helium gas (~5 kPa) at room temperature. These sensors are widely used in cryogenic applications and they provide reliable and repeatable readings with reasonable accuracy (typically  $\pm 0.5$  K). Their response times, however, are relatively long (0.1-3 s, depending on the heat sink) [136].

The resistance change in the PRTs was measured by applying a constant current of  $1.000 \pm 0.005$  mA, and measuring the corresponding voltage across the resistor. The current excitation was obtained by a constant-current source (Model CS1000B from TRI Research®). This provided a voltage output of approximately 5 to 100 mV for a standard  $100\Omega$  PRT measuring temperatures between 40 and 298 K. Two of these sensors were used; one at the first stage of the cryocooler and one at the bottom of the radiation shield. The voltage signals were converted into temperature values by curve-fitting a standard resistance vs. temperature curve provided by the manufacturer. The curve fitting was carried out using TableCurve™ 2D version 4.0 [137], an automated software package that analyzes hundreds of possible equations to fit a given set of data. The candidate equations are then ranked according to the precision with which they reproduce the original data set. The transfer functions for all the sensors used in this work are included in Appendix I.

A calibrated ruthenium oxide, thick film resistor was used to measure the temperature at the second stage of the cryocooler (Model # RO-104GG1 from Scientific Instruments®). According to the manufacturer [140], this sensor was calibrated from 2.0 to 273 K using the International temperature Scale of 1990 (ITS-90).

Self-heating and good thermal contact are very important for sensors operating with a constant current excitation at cryogenic temperatures. In this work all the temperature sensors were mounted on special copper fittings that could be bolted to the cold surfaces. The sensor wires were thermally anchored to the first and second stages by a thin layer of GE7031 Varnish diluted with toluene. The instrumentation leads consisted of AWG-32 Phosphor-bronze wire. An excitation current of  $10\mu\text{A} \pm 0.05\%$  was provided by a constant-current source (Model 120CS from LakeShore® Cryotronics Inc.) [141]. The resulting voltage output ranged from 0.930V to 1.900V for temperatures between 293 and 3.5 K. The calibration specifications for the ruthenium oxide resistor are shown in Table 3-3. The transfer functions for different temperature ranges are included in Appendix H.

**Table 3-3: Calibration specifications for the ruthenium oxide resistor used to measure the temperature at the second stage of the cryocooler.**

Temperature Range (K)	Nominal Sensitivity ( $dR/dT$ , in $\Omega/K$ )	Nominal Resistance ( $k\Omega$ )	Accuracy (K)
2.0 - 4.2	13,700	214	$\pm 0.05$
4.2 - 20	6,590	165	$\pm 0.05$ to 0.1
20 - 77	703	120	$\pm 0.1$ to 0.2
77 - 100	103	107	$\pm 0.2$ to 0.4
100 - 273	43	103	$\pm 0.4$ to 1.0

### 3.3.4.2 Gas Flow and Pressure Drop

A test apparatus was designed and built to measure the pressure drop across different regenerator beds. This test rig used a differential pressure transducer and a mass

flowmeter (see Figure 3-4). Sealing was achieved by two thick wall, 1¼ in brass couplings Part No. B-125-K, from Kurt J. Lesker) [142]. The sensors used for these measurements are described in the following paragraphs.

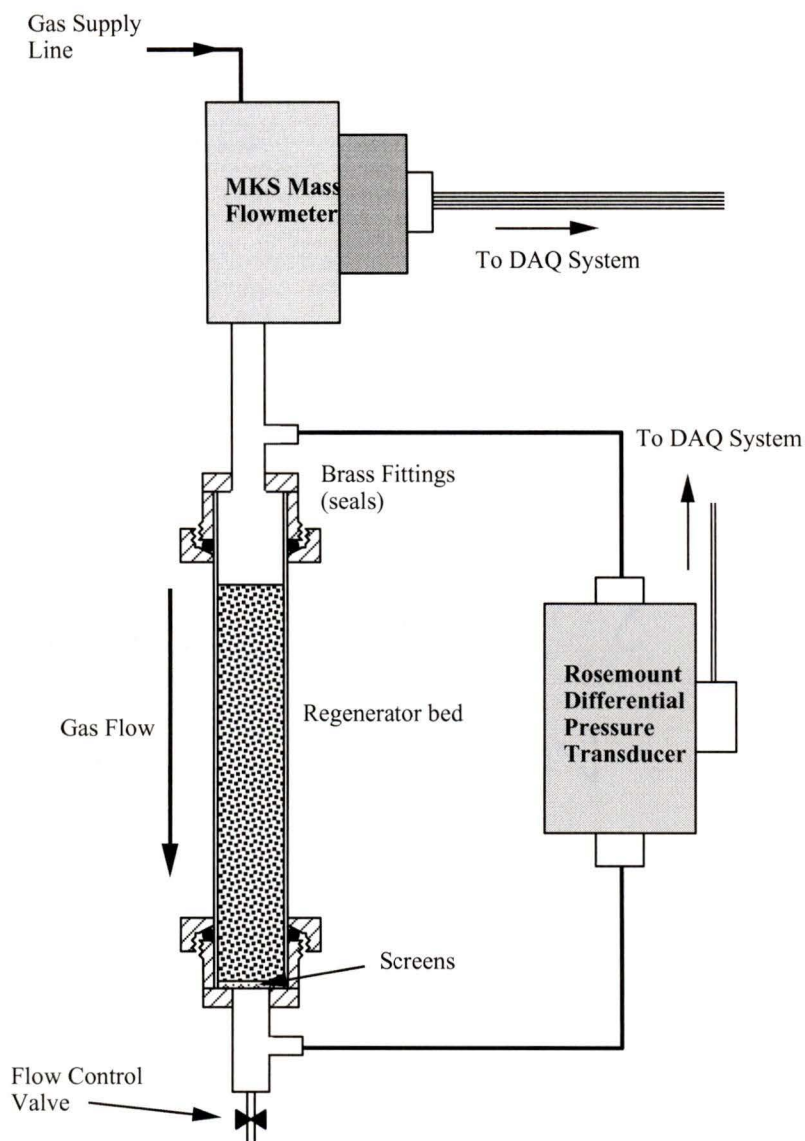


**Figure 3-4: Schematic representation of the apparatus used to measure the pressure drop across different regenerator beds.**

Gas flow was measured using two separate sensors (both were Bell Prover Model No. 1092A from MKS® Instruments, Inc.). Each of these instruments was calibrated following the MKS® calibration procedure No. QAP10170. The calibration gases were nitrogen and helium for standard flows of 0-500SLM and 0-250SLM, respectively. The conditions at the time of calibration were 19.5 °C and 773.11 torr (for nitrogen) and

20.4°C and 761.33 torr (for helium). The transfer function for this sensor is given in Appendix I.

The pressure drop across packed beds of irregularly shaped particles was measured using a differential pressure transmitter (Model 2024 from Rosemount® Inc.) [143]. This instrument contains a free-floating variable capacitance sensing diaphragm. The differential capacitance between this element and two capacitor plates is converted into an electrical signal. Differential pressures from 0 to 248.6 kPa produced a linear voltage output between 1.00 and 5.00 V (DC). According to the manufacturer, the accuracy in the measurements corresponds to  $\pm 0.25\%$  of the calibrated span (i.e.,  $\pm 621.5$  Pa for the experiments included in this work).

All the pressure-drop measurements were carried out at room temperature. The transfer function for the pressure transmitter is included in Appendix I.

### **3.3.5 DAQ Software**

All the software used to monitor the experiments described in this work was designed and developed using LabView® 3.1.1. This is an object-oriented programming environment specifically designed for data acquisition. GM DAQ 1.0 is the name of the main program used to monitor the temperature at the first and second stages of the GM cryocooler. This program has a graphical user interface that allows the user to enter the input channels to scan, the time between readings, the number of data points per channel, and other experimental details. The data was collected and saved on a file as tab-separated ASCII text. A typical scan consisted of 4000 readings per channel collected at a scan rate of 8000scans/second (i.e., data corresponding to 2s). This ensured that the temperature fluctuations during one or more full cycle(s) were averaged over time. A Detailed description of this program and the associated virtual instruments (VIs) is given in Appendix J. Figure 3-5 shows the main control panel for GM DAQ 1.0.

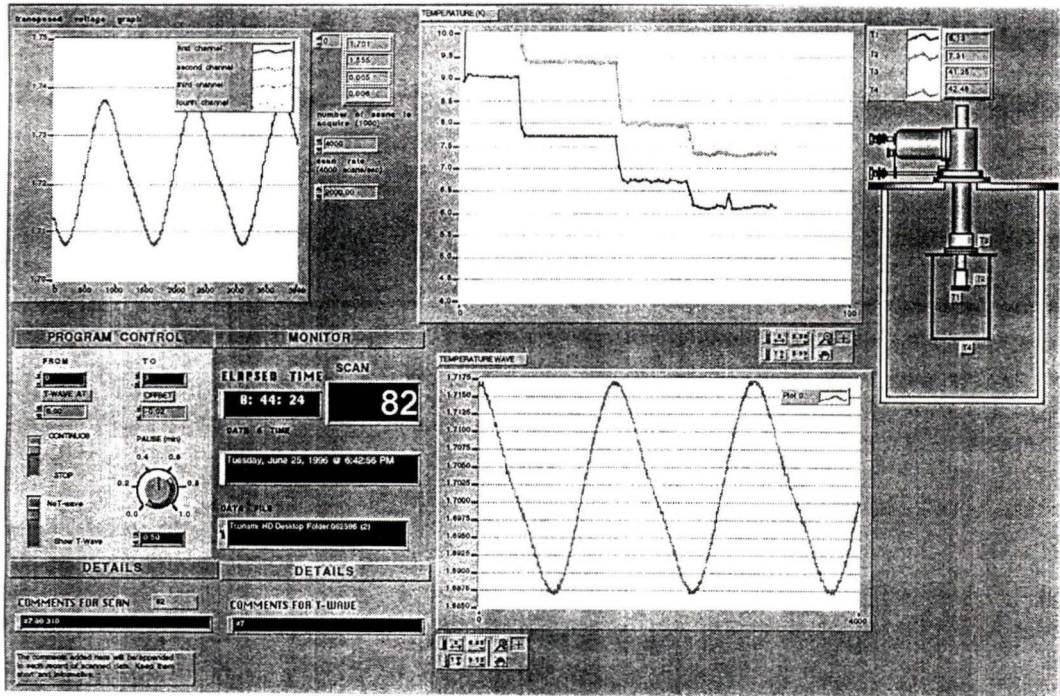


Figure 3-5: The main control panel for GM DAQ 1.0.

### 3.4 Characterization of a Commercial GM Cryocooler

After a careful search for all available suppliers of two-stage GM cryocoolers, a KelCool™ UCH 130 cryorefrigerator was purchased from Balzers [144]. Table 3-4 shows the quotations and model specifications from two suppliers (Balzers and CVI [145]).

**Table 3-4: Summary of the specifications for a two-stage GM cryocooler.**

	<b>Balzers</b>	<b>CVI</b>
<b>Model</b>	UCH 130	CGR 511
<b>Price (in Canadian dollars)</b>	\$ 30,022	\$ 31,602
<b>Delivery time</b>	4 weeks	8 weeks
<b>Warranty</b>	12 months	18 months
<b>Refrigeration capacity</b>	115 W at 77 K 15 W at 20 K (simultaneous)	60 W at 77 K 12 W at 20 K (not simultaneous)
<b>Lowest, no-load temperature</b>	6.5 K	10 K
<b>Variable speed DC motor controller</b>	Included	Not included
<b>Weight</b>	14 kg	17.2 kg
<b>Maintenance interval</b>	9,000 hours	15,000 hours
<b>Compressor type</b>	Scroll	Scroll
<b>Static charge pressure</b>	250 psig	210 psig
<b>Water coolant requirements</b>	3.0 gal min <sup>-1</sup>	1.0 gal min <sup>-1</sup>
<b>Electrical requirements</b>	200 - 230 V 3-phase, 60 Hz	208 V 3-phase, 60 Hz
<b>Nominal input power</b>	6.5 kW	5.5 kW
<b>Electrical standards</b>	Not CSA approved	CSA approved
<b>Oil adsorber life</b>	26,000 hours	NA
<b>Cold head control cable</b>	50 ft	10 ft
<b>Helium gas lines</b>	2 × 32 ft lines	2 × 10 ft lines

The main components shipped with the KelCool™ 130 model include the cold head itself, a scroll compressor for helium, self-sealing connecting hoses and other accessories used for re-filling and maintenance. Each of these components is described in the following sections.

### 3.4.1 The Cold Head

Figure 3-6 shows a picture of the cold head. The cylindrical enclosure at the top contains the drive unit subassembly. The combined displacer unit is enclosed by two concentric stainless steel cylinders.

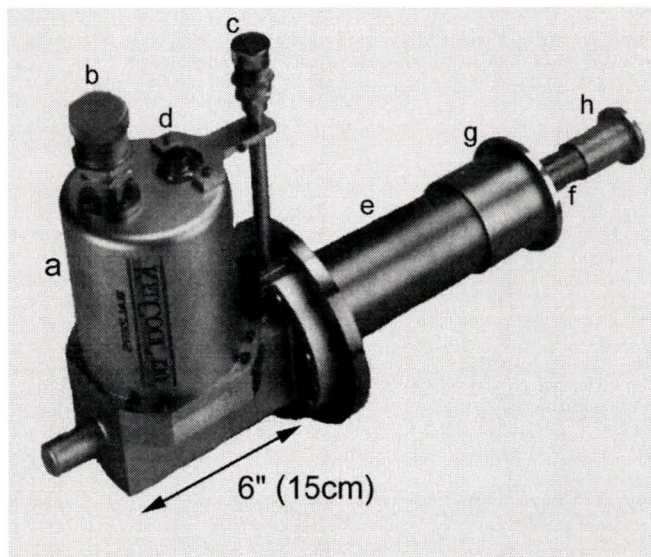


**Figure 3-6: KelCool 130™ cold head; motor casing (a), gas return and supply lines (b, c), electrical connector (d), first and second stage enclosures (e, f), first and second stage copper flanges (g, h).**

The copper flanges at the bottom of each stage function as heat exchangers that can be bolted to the region requiring refrigeration. The return and supply lines from the compressor are connected via the self-sealing fittings at the back of the motor casing. The five-pin electrical connector between these fittings is used to connect a motor controller that is included with the compressor. This connector can also be used to control the motor using a computerized motor controller.

Figure 3-7 shows the first and second-stage regenerator containers outside their stainless steel enclosure. These two cylinders move in unison, combining the regenerators and displacer into a single unit. The material used to make these containers is a cotton fabric base, phenolic plastic (grade LE Linen Phenolic) [146] which provides satisfactory performance at cryogenic temperatures.

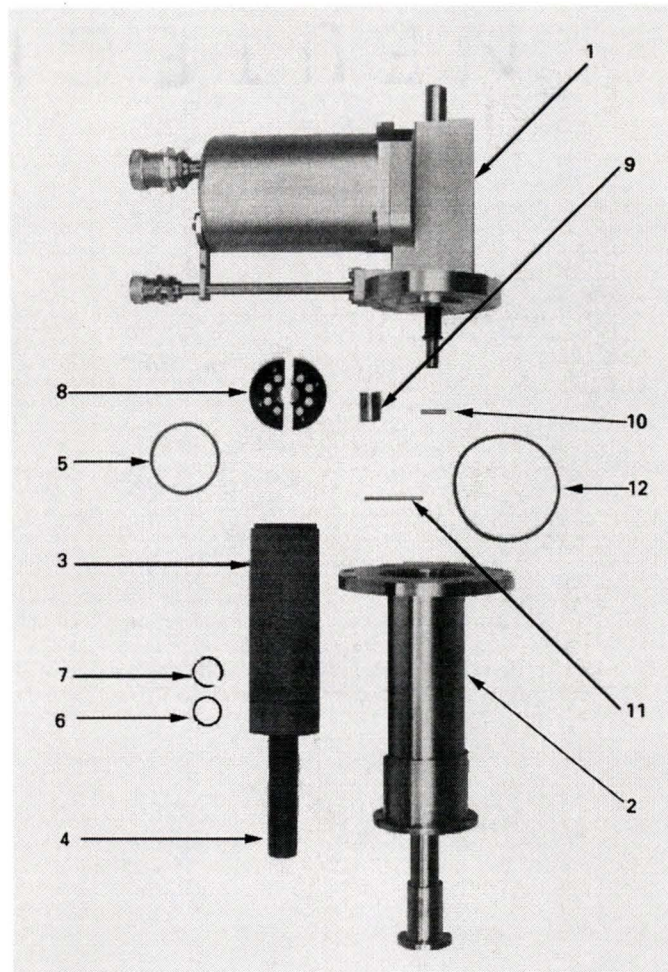


**Figure 3-7: Cold head internal assembly; drive unit (1), displacer enclosure (2), first and second stage regenerator containers (3,4), first stage dynamic seal (5), second stage seal assembly (6), second stage seal retainer (7), first stage seal retainer (8), scotch yoke connecting link (9), scotch yoke pin (10), first stage connecting pin (11), room temperature O-ring (12)**

The first stage regenerator consists of phosphor bronze screens and lead shot. The second stage regenerator uses hardened lead particles. Both containers have replaceable dynamic seals.

An exploded view of the motor enclosure reveals the simplicity of the drive mechanism (see Figure 3-8). An eccentric connection converts the motor rotation into reciprocating motion that is transferred to the displacer via a scotch yoke.

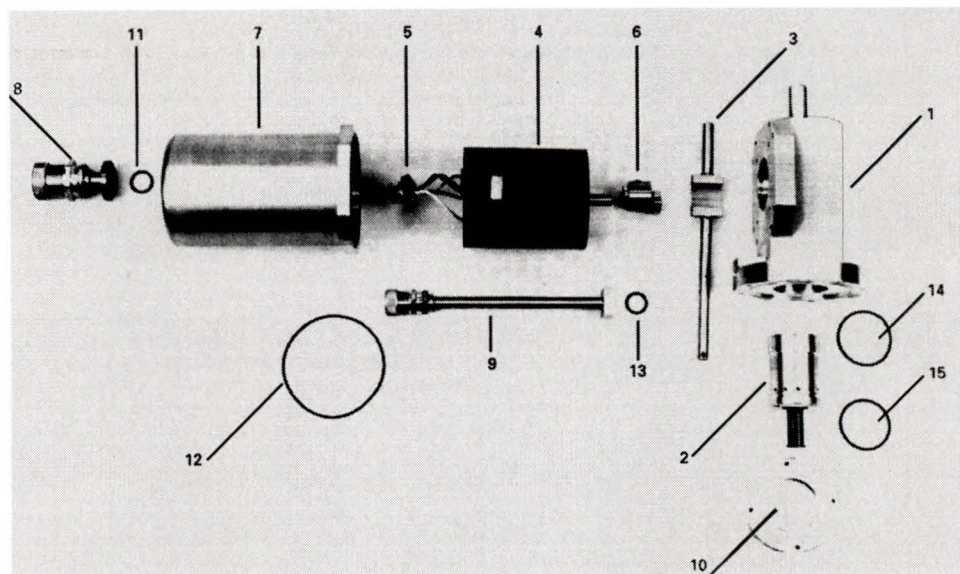


**Figure 3-8: Drive unit subassembly; crank housing (1), valve housing (2), scotch yoke (3), stepping motor (4), electrical connector (5), crank assembly (6), motor housing (7), gas return and supply line connections (8,9), valve housing retainer (10), O-rings (11-15).**

The yoke is also connected to a valve housing assembly. This implies that the reciprocating motion of the displacer controls and is coupled to the valving mechanism. Because the entire drive subassembly operates at room temperature, all the seals between the motor casing and the stainless steel container are simple O-rings.

### 3.4.2 The Helium Compressor

The Balzers Model UCC 110S supplied with the KelCool™ 130 unit is a single stage, scroll compressor. The advantages of this type of device include little vibration and noise during operation, simple design with only a few moving parts, and low maintenance requirements.

Figure 3-9 shows a schematic diagram of the compressor unit. Low pressure He gas enters a helium reservoir placed before the compressor module. During operation, this reservoir reduces the pressure fluctuations associated with the reciprocating motion of the displacer inside the cold head. The gas from the reservoir enters the suction chamber in the compressor module. This chamber reduces its volume as it rotates and delivers the

compressed gas to the discharge chamber. Valves are not required because these two chambers are not directly connected.

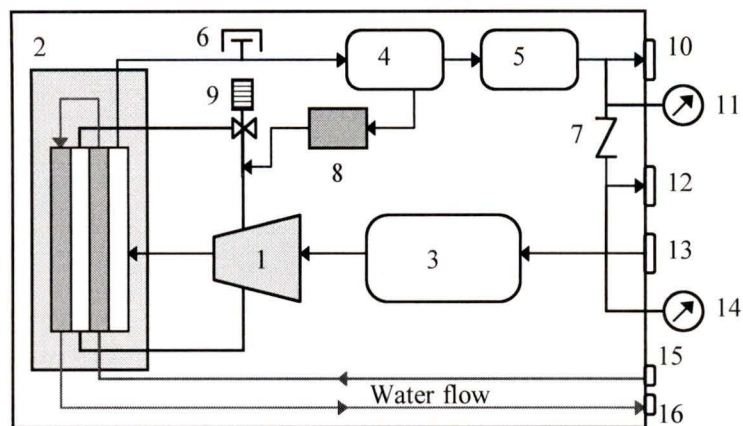


**Figure 3-9: Schematic diagram of the UCC 110S compressor. The components include: helium compressor module (1), heat exchanger (2), low pressure helium reservoir (3), oil separator (4), vapour adsorber (5), relief valve (6), bypass valve (7), oil filter (8), oil solenoid valve (9), gas supply connection (10), gas supply pressure gauge (11), gas charge connection (12), gas return connection (13), gas return pressure gauge (14), cooling water connections (15, 16).**

The compressed gas is cooled by oil injection into the compression module. Some of the added oil is removed by gravity and collected before the gas moves into the discharge passages. The rest of the compressed fluid consists of a high temperature gas/oil mixture. This mixture passes through the water-cooled heat exchanger where it rejects heat to the environment. This heat exchanger also cools the oil injected during compression. A solenoid valve prevents oil leaks into the compressor module when the system is turned off. Gas moving through the discharge lines is also used to cool the compressor's motor.

After the gas/oil mixture has been cooled, it passes through an oil separator where essentially all the liquid oil is removed. Any traces of gaseous oil that could still be present are removed by an oil adsorber located just before the gas supply line. Table 3-5 shows the specifications for the UCC 110S compressor.

**Table 3-5: Specifications for the UCC 110S Helium compressor.**

<b>UCC 110S Scroll compressor (PN: UC 010 916-T)</b>	
Electrical requirements	200-230V, 3-phase 60Hz or 200V, 3-phase, 50Hz
Electrical load	6.5kW (nominal)
Cooling requirements	11.4L/min (steady state).
Static charge pressure	250 psi (1.72MPa)
Working fluid	UHP He (99.995% min.)
Temperature range	5 to 40°C
Dimensions	51cm × 56cm × 72cm
Weight	105kg

The electrical module controlling the entire refrigeration system (including the cold head) is located inside the compressor unit. A temperature sensor and water flow meter are connected to this control module. If the temperature exceeds 49 °C or the water flow is below 11.4 L min<sup>-1</sup> the power to the entire system will be interrupted.

The main control panel consists of three switches located at the front of the compressor. These switches control the main power, the compressor, and the cold head separately. An on-board motor controller varies the frequency of operation in the cold head. The 8 available frequencies range from 56 to 144 rpm (0.93 to 2.4 Hz). Additional frequency control can be obtained with an external motor controller.

### **3.4.3 Accessories**

The compressor is connected to the cold head by two flexible, self-sealing supply and return lines. Because these lines are long (9.75 m), the cold head can be easily used in more than one experiment without moving the compressor. However, long lines increase the risk of gas contamination during purging and refilling. The adapter supplied by the manufacturer had to be connected at compressor end of the lines (i.e., it could not be attached to the cold head directly), and the purging and refilling procedures were time-consuming.

Contamination was not a concern if the unit ran continuously for an extended period of time. However, during the experiments presented here, the cold head was disassembled many times in order to modify the second stage regenerator. To minimize the risk of contamination, a custom-designed charge/purge adapter was designed and build as part of the work in this thesis (see Figure 3-10).

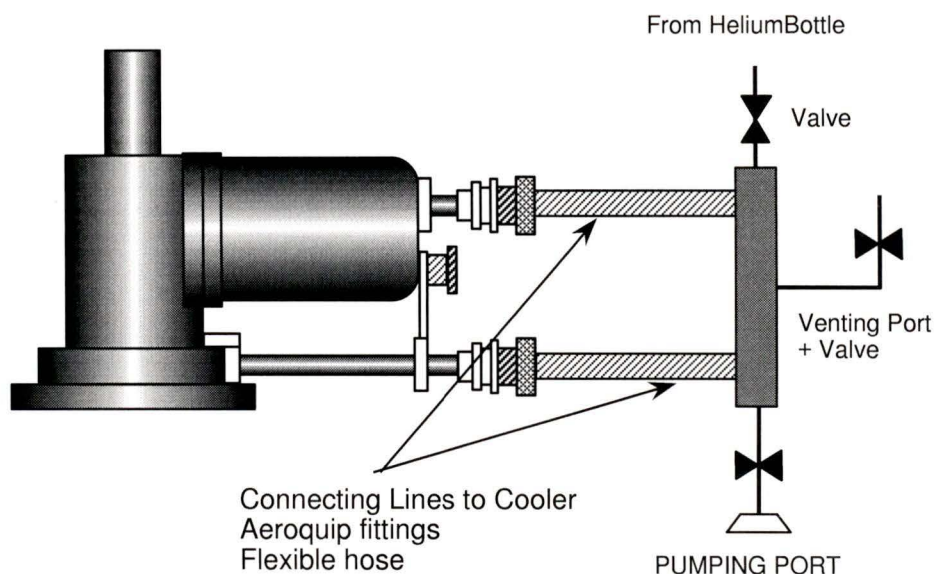


**Figure 3-10: Schematic representation of the refilling adapter using to purge the cold head space after exposure to air.**

This adapter made it possible to isolate the compressor and connecting lines from the cold head space: the only part of the system that was exposed to air was the cold head. The other parts (compressor + lines) remained charged with high purity helium at all times. This method also reduced the time required to purge and recharge the system after exposure to air.

### 3.5 Performance Characteristics

Before any modifications were initiated, the GM cryocooler was tested to verify the manufacturer's specifications and establish a proper baseline. The two areas of interest were the cooling times and the cooling power available at different temperatures.

### 3.5.1 Cool-down Times

Figure 3-11 shows a typical cooling curve for the GM cryocooler operating with only parasitic thermal loads. The lowest temperatures obtained were approximately 6 K and 37 K at the second and first stages, respectively. These results are comparable to the ultimate temperatures specified by the manufacturer.

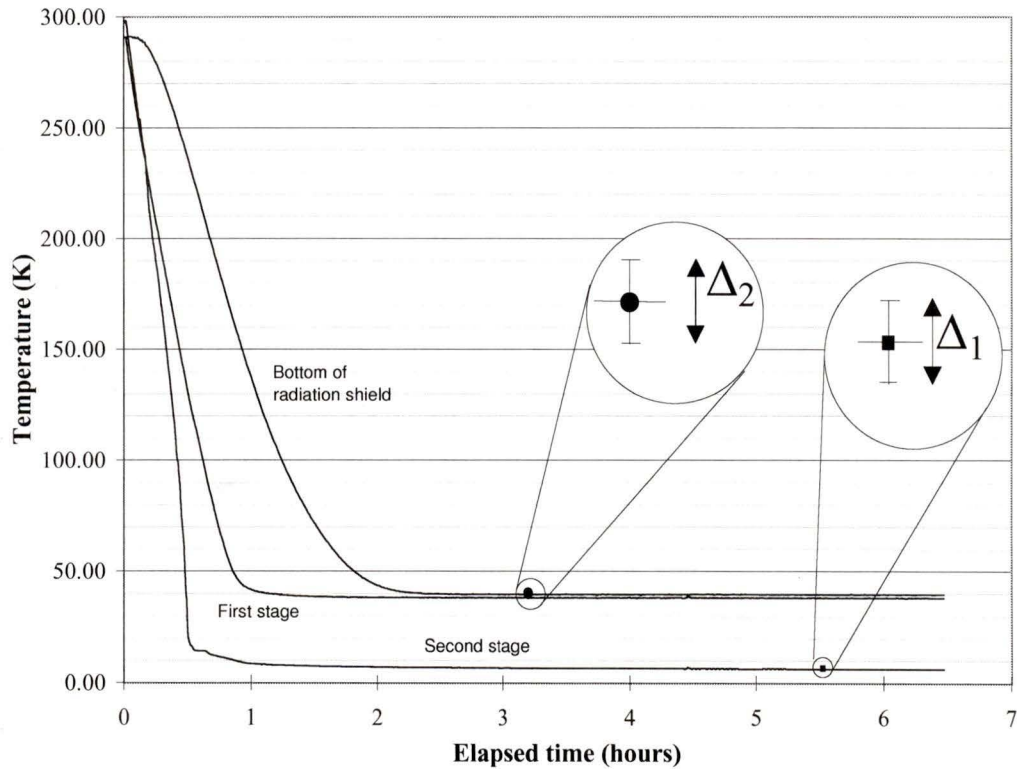


**Figure 3-11: Typical cool-down times for the GM cryocooler operating with parasitic thermal loads only ( $\Delta_1/2 = \pm 0.05$  K,  $\Delta_2/2 = \pm 0.5$  K).**

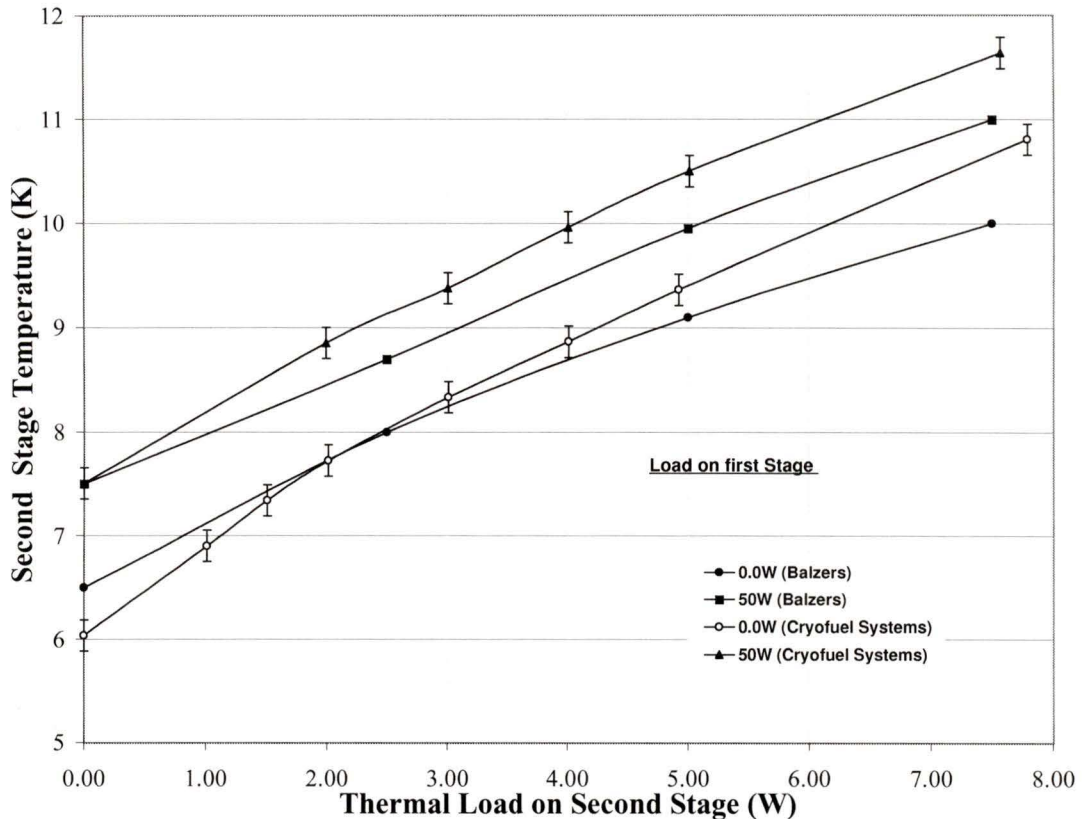
### 3.5.2 Cooling Power

Different cooling loads were created by delivering a known amount of electrical power to heaters located at the first and second stages of the cryocooler.

Each heater consisted of an aluminum bobbin wound with AWG-32 Nichrome wire [147]. This wire was thermally anchored to the aluminum bobbins by a thin layer of

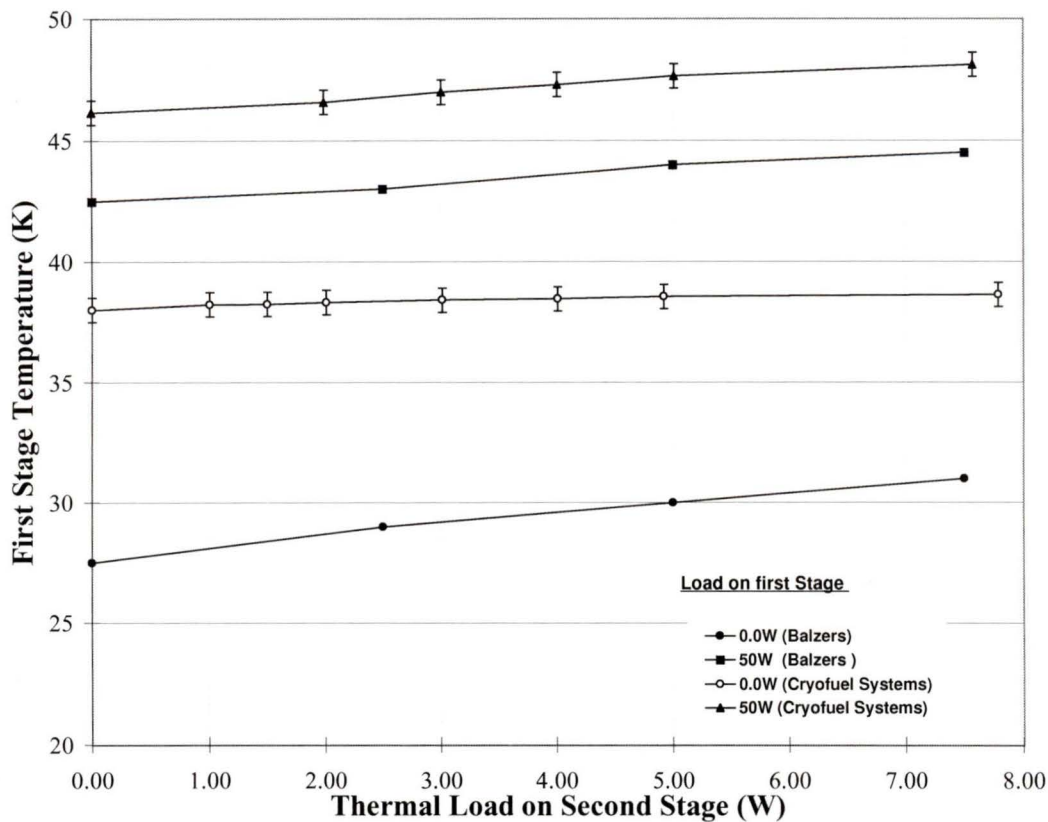
GE7031 insulating varnish [147], and the overall hater assembly was bolted to the first and second-stage copper flanges.

Figure 3-12 shows the variation of temperature with cooling load. As can be seen, the lowest temperature achieved at the lower stage is actually 0.5K lower than that specified by the manufacturer. This slight improvement was attributed to the enhanced radiation shielding which was different from that used by the manufacturer\*.



**Figure 3-12: Temperature at the second stage as a function of cooling load.**

\* The commercial unit was tested using a non-polished copper shield with no MLI between its walls and the second-stage cold head.



**Figure 3-13: First stage temperature as a function of cooling load at the second stage.**

As the cooling load was increased, the temperatures in both the first and second stages increased above the values published by the manufacturer. According to personnel at Balzers, however, these temperatures fell within typical performance curves for similar refrigeration units [148]. It was therefore decided to accept these results as satisfactory and proceed with the modifications required to achieve liquid helium temperatures.

# Chapter 4

## GM Cryocooler Modifications

### 4.1 Performance Parameters

The lowest (no load) temperature obtained with the KelCool™ 130 GM unit was approximately 6 K. The SCMs in the AMRL, however, are designed to operate at temperatures  $\leq 4.5$  K. Therefore the commercial unit needed modifications to achieve non-zero cooling powers at liquid helium temperatures.

The possible modifications have been previously documented by other researchers using similar systems. The reported changes to the operating parameters include:

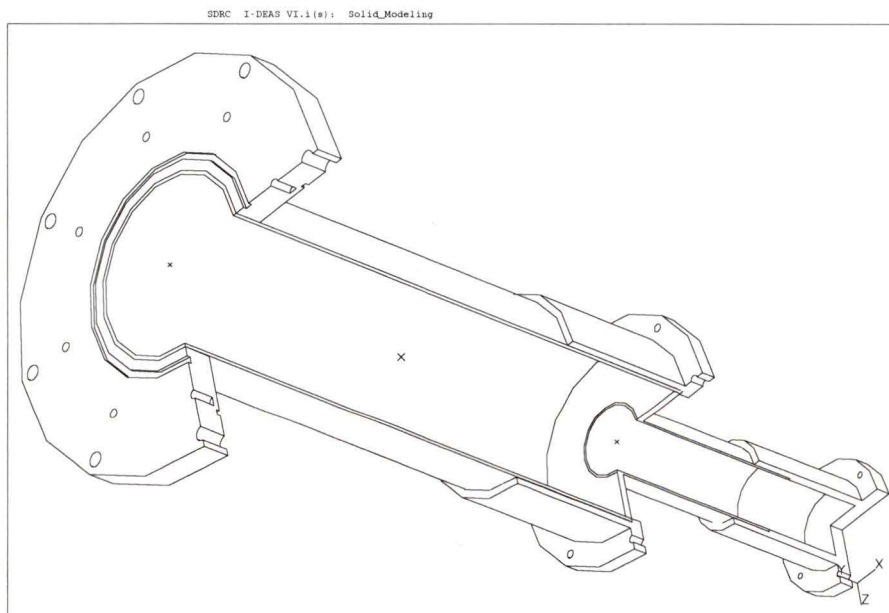
- Increasing the volumetric thermal mass of the low temperature regenerator by replacing lead with the RE/TM alloys described in Chapter 2.
- Altering the dimensions and geometry of the regenerator bed.
- Reducing the cycle speed
- Changing the valve timing (this can be accomplished by adding spacers and/or altering the scotch yoke).
- Increasing the expansion volume at the second stage.
- Changing the dimensions of the second-stage expansion volume.
- Changing the compressor capacity.

The first three options were explored in this work and found to produce successful results.

## 4.2 Reverse Engineering of the Second-stage Regenerator in a Conventional GM Cryocooler

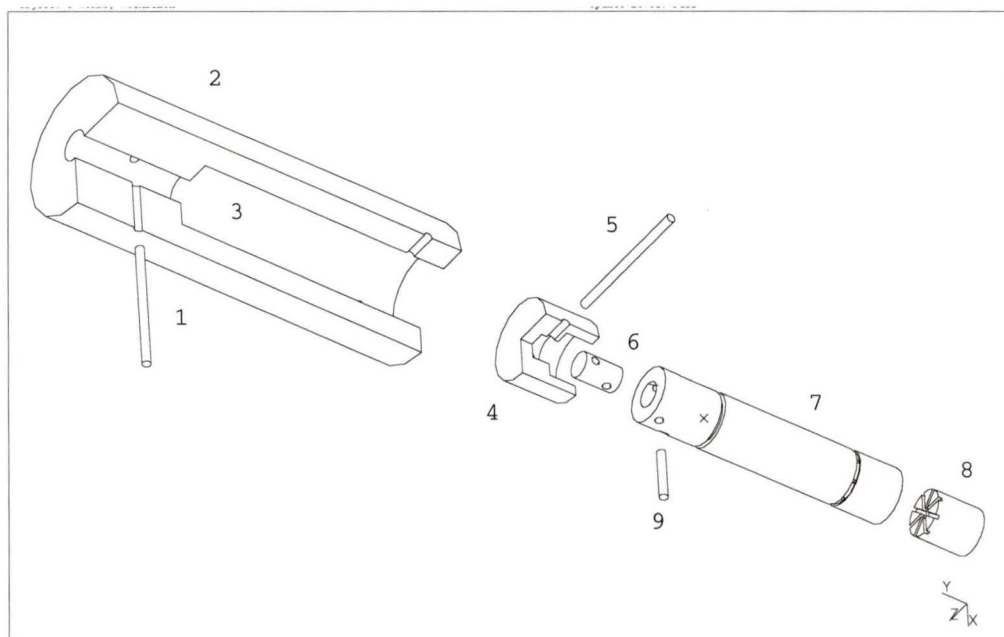
The first step in the modification process consisted of disassembling the cold head to gain access to the first and second-stage regenerator containers. Once these components were exposed, it was possible to generate the corresponding drawings required to duplicate the manufacturer's design. All the engineering drawings included in this work were created using I-DEAS™, a mechanical CAE/CAD/CAM software package [149]. Electronic versions of all drawings and solid model files were archived in the Cfs library [150].

Figure 4-1 shows the stainless steel casing that encloses the displacer assembly. As can be seen, the first stage copper flange is simply welded to the outside wall of the first stage body. The second-stage flange, on the other hand, is in direct contact with the gas in the lower expansion volume. This enhances the heat transfer between the cold gas and the walls of the cylinder. The wall thicknesses for the first and second stage bodies measured to be 0.068 in (1727  $\mu\text{m}$ ) and 0.038in (965  $\mu\text{m}$ ), respectively.



**Figure 4-1: Cutaway view of the stainless steel body for the KelCool 130™ cold head.**

Figure 4-2 shows the first and second-stage regenerator containers. The two containers fit tightly inside the stainless steel casing and are coupled by a universal joint. The plugs at the bottom of each container are permanently glued in place. During operation, the distance traveled by the displacers is approximately  $\frac{3}{4}$  of an inch (19 mm). The resulting first and second-stage expansion volumes are  $87 \text{ cm}^3$  and  $15.7 \text{ cm}^3$ , respectively.



**Figure 4-2: Exploded view of the displacer assembly; connecting pin to drive mechanism (1), first-stage regenerator container, regenerator space (3), first-stage end plug (4), stainless steel pins (5, 9), universal joint (6), second-stage regenerator container (7), second-stage end plug (8).**

Because the displacer assembly consisted of two permanently sealed containers, it was impossible to modify either of these units in a non destructive manner. It was therefore decided to keep the original parts intact, and to build replicas of the required components.

Changes to the first stage regenerator could have improved the cooling capacity above 40K, but the effect on the performance at the second stage have been shown to be minimal. It was therefore decided to concentrate the modification efforts on the second-stage regenerator only.

One of the first challenges encountered was related to the lack of information about the internal structure of the regenerator containers. This information was not available because the interior could not be exposed without destroying the part. In addition, some of the manufacturing techniques are proprietary, and they were not immediately available from the manufacturer.

After careful analysis of the available information, the first set of regenerator containers was designed and built. Figure 4-3 shows the one of these containers and the perforated brass plates used at either end of the regenerator space.

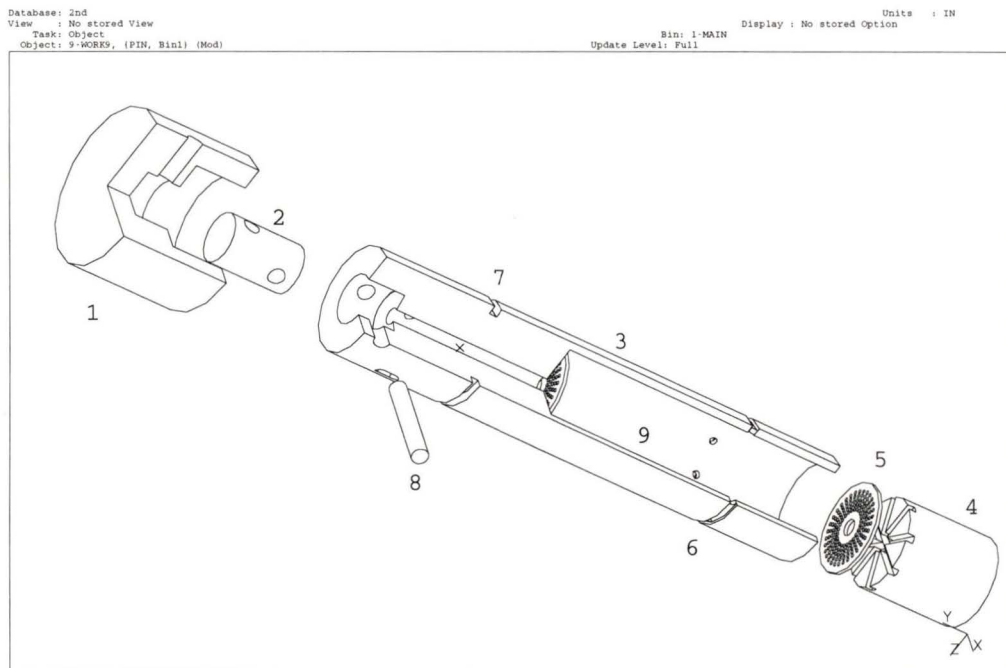


**Figure 4-3: The second-stage regenerator container assembly includes first stage end plug (1), universal joint (2), second stage regenerator container (3), second-stage end plug (4), perforated brass plate (5), gas exhaust holes (6), second-stage seal groove (7), stainless steel pin (8), regenerator space (9). The stainless steel screens used at the ends of the regenerator space are not shown.**

Stainless steel screens (400 mesh) were soldered to the brass plates to prevent the regenerator particles from leaving the regenerator space.

Both the container and the plug at the bottom were made of the same phenolic material used by the manufacturer. The plug was machined to be a loose fit (100  $\mu\text{m}$  clearance) and then glued in place using Stycast® 1266, a two-part epoxy that performs well at cryogenic temperatures [151]. The flow channels machined on the plug match the hole pattern on the regenerator container. In this way, the gas can flow from regenerator space into the expansion volume. The total regenerator volume was 28.57  $\text{cm}^3$ .

#### 4.2.1 Regenerator Assembly

The regenerator was assembled by first soldering one of the stainless steel screens along the edges of the perforated brass plates. The brass plate at the top end of the regenerator was then glued with the same two-part epoxy described before. The second brass plate was similarly glued to the bottom plug.

After the brass and screen assemblies were secured in place, the regenerator space was filled with lead particles [152]. Mechanical vibration was applied during this process to ensure proper settling of the particle bed. The last step consisted of gluing the second-stage plug in place.. A load of approximately 100 N was applied to the regenerator bed\*, and the entire assembly was left to cure for 24 h at room temperature.

Three different mean particle diameters were considered (100  $\mu\text{m}$ , 200  $\mu\text{m}$  and 300  $\mu\text{m}$ ). The first tests were carried out using 100  $\mu\text{m}$  and 200  $\mu\text{m}$  particles. In either case, the lowest temperature achieved at the second stage was only approximately 9 K. Decreasing the operating frequency of the cold head from 2.4 Hz to 0.9 Hz (and intermediate frequencies) was found to have no appreciable effect on the second-stage temperature.

The results of these preliminary experiments yielded some important information:

---

\* As the regenerator bed cools, the individual particles will experience thermal contraction. Preloading the bed minimizes the motion of particles inside the regenerator space.

- Soldering a screen disc to the edge of the brass plates was not enough to prevent the particles from migrating: a small amount ( $< 1$  g) of lead particles was found at the second-stage expansion volume. No trace of contamination was found anywhere else in the system.
- The tolerances associated with the second-stage seal assembly are very important. This assembly consists of a split-piston, ring-type seal with a C-shaped, stainless steel backup spring (see Figure 4-4). The ring is made of a Teflon-based material whose composition is proprietary to the manufacturer [153]. Our analysis shows that it is probably glass-filled rulon. Containers with grooves that were a few thousandths of an inch too wide performed much worse than containers with tight-fitting seals (see Section 4.7).

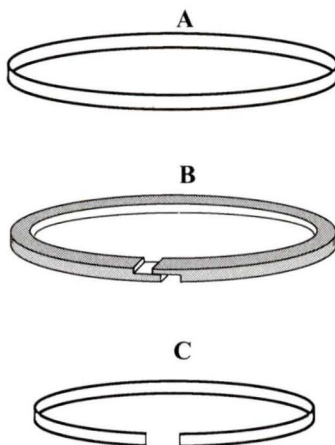


**Figure 4-4: The second-stage seal assembly. The retaining ring (A), holds the piston-seal (B) closed when the displacer is lowered into the stainless steel casing. During operation, the backup spring (C) forces the seal against the wall of the casing.**

After making these observations, a new regenerator was made using  $300\ \mu\text{m}$  lead particles and a new end-plate design. This time, the stainless steel screens were not soldered to the brass plates. Instead, a two-piece brass assembly was filled with 12 screen discs (400 mesh, wire diameter =  $0.0001''$ ). The brass pieces for the bottom end fit tightly on the phenolic plastic plug (see Figure 4-5). Once in position, the entire plug assembly could be glued at once. The brass/screen plug for the top end of the regenerator space was assembled in a similar manner.

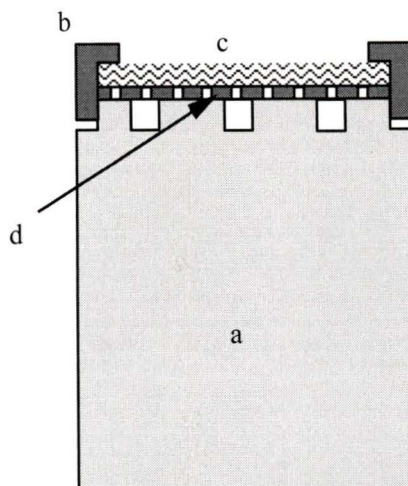


**Figure 4-5: Modified plug assembly: phenolic plastic plug (a), retaining ring (b), stainless steel screens (c), perforated plate (d).**

Once the regenerator container was built, the next step consisted of reproducing the original refrigeration performance using lead as the second-stage regenerator material. Reproducing these results ensured that the container was properly designed and that the function of each component was well understood.

The lowest temperature achieved with the new regenerator was  $6.1 \pm 0.1$  K. This temperature was the same as that obtained with the original unit immediately after it was purchased. This result proved that the initial performance could be reproduced with regenerators built in the CFS laboratory.

After this first success, the modifications required to reduce the lowest, no-load temperature below 6 K and to obtain non-zero cooling powers at 4.2 K were initiated. The first modification consisted of replacing the Pb particles with RE/TM alloys to increase the volumetric thermal mass of the regenerator.

### 4.3 Regenerator Materials Preparation

Following the analysis presented in Chapter 2,  $\text{Er}_3\text{Ni}$ ,  $\text{ErNi}_{0.9}\text{Co}_{0.1}$  and  $\text{Er}_{0.9}\text{Yb}_{0.1}\text{Ni}$  were selected as the best candidate materials for the second-stage regenerator in the GM

Cryocooler. The first two alloys were used to fabricate a series of regenerators described in the following sections. The third alloy was not used in this work because it was similar to  $\text{ErNi}_{0.9}\text{Co}_{0.1}$ .

### 4.3.1 Alloy Preparation

The RE/TM alloys were prepared by arc-melting the appropriate amounts of the required raw materials. A spreadsheet program was developed to calculate the required masses for alloys of different compositions (see Appendix G). The different materials were weighed using a high precision microbalance and the total mass of each alloy sample ranged from 50 to 70 g .

The arc-melter was designed and built in the Cfs laboratory. This device consisted of a stainless steel chamber that could be pumped, purged and eventually filled with an inert gas (99.98% pure Argon). A water-cooler copper hearth and a non-consumable tungsten electrode were connected to the terminals of a high-current, low-voltage power supply.

Each sample was placed in an individual pocket machined in the water-cooled copper hearth. The chamber was evacuated with a rough-vacuum pump and then pressurized with argon (up to 10 psig). This purging procedure was repeated five times to minimize the presence of oxygen inside the chamber. In addition, a small sample of titanium was melted for a few seconds before each run to react any remaining oxygen. The RE/TM alloys were then melted and flipped to ensure a homogeneous mixture. This procedure was repeated 10 times. Table 4-1 shows typical masses for the samples prepared.

As can be seen the sample masses were slightly different after the alloys were melted. These differences are related to losses during sample handling or to small amounts of material migrating between the pockets in the copper hearth (because these materials are so brittle, small chips were scattered as the samples were turned over during the melting process). The lack of evaporation, however, was a good initial indication that the samples had the required stoichiometry.

**Table 4-1: Typical masses used for the preparation of RE/TM alloys ( $\pm 0.002\text{g}$ ).**

Er (99.5%) Mass (g)	Ni (99.99%) Mass (g)	Co (99.9%) Mass (g)	Total Mass Before Melting (g)	Total Mass After Melting (g)	$\Delta m$ (%)
48.219	5.643		53.862	53.888	+0.026
47.769	5.592		53.361	53.347	-0.014
49.500	5.796		55.290	55.301	+0.011
53.892	6.306		60.198	60.210	+0.012
51.864	16.402	1.827	70.093	70.070	-0.033
46.624	14.723	1.646	62.993	63.002	+0.014
43.887	13.867	1.550	59.304	59.369	+0.109
49.540	15.647	1.747	66.934	67.004	+0.104

### 4.3.2 Sample Characterization

After the RE/TM samples were prepared, their composition was investigated using Energy Dispersive X-ray (EDX) spectral analysis [154]. Figure 4-6 shows the spectra collected for Er, Ni and Co standards as well as a spectrum for a sample of  $\text{ErNi}_{0.9}\text{Co}_{0.1}$ .

Although the composition of  $\text{Er}_3\text{Ni}$  was relatively easy to confirm by X-ray analysis, the spectrum for  $\text{ErNi}_{0.9}\text{Co}_{0.1}$  presented some difficulties. As can be seen in Figure 4-6, Er and Co have spectroscopic peaks at very similar energies ( $L_{\alpha}$  transition at 6949 keV and  $K_{\alpha 1}$  transition at 6929 keV, respectively) which make it difficult to isolate the individual contributions to the spectrum. This is the main reason for the discrepancies between the expected and observed composition values for the  $\text{ErNi}_{0.9}\text{Co}_{0.1}$  samples (see Figure 4-7). The percentage of Ni, however, was close to the expected value in all samples.

Inductively coupled plasma techniques were used to obtain a better indication of the Er/Ni/Co alloy composition [154]. The results of these tests confirmed that all the samples had the prescribed compositions and phases. This was a reassuring result that indicated that the heat capacity values in these materials should be the same as those published in the literature (see Chapter 2). It was therefore decided to proceed with the fabrication of particles from the different alloys.

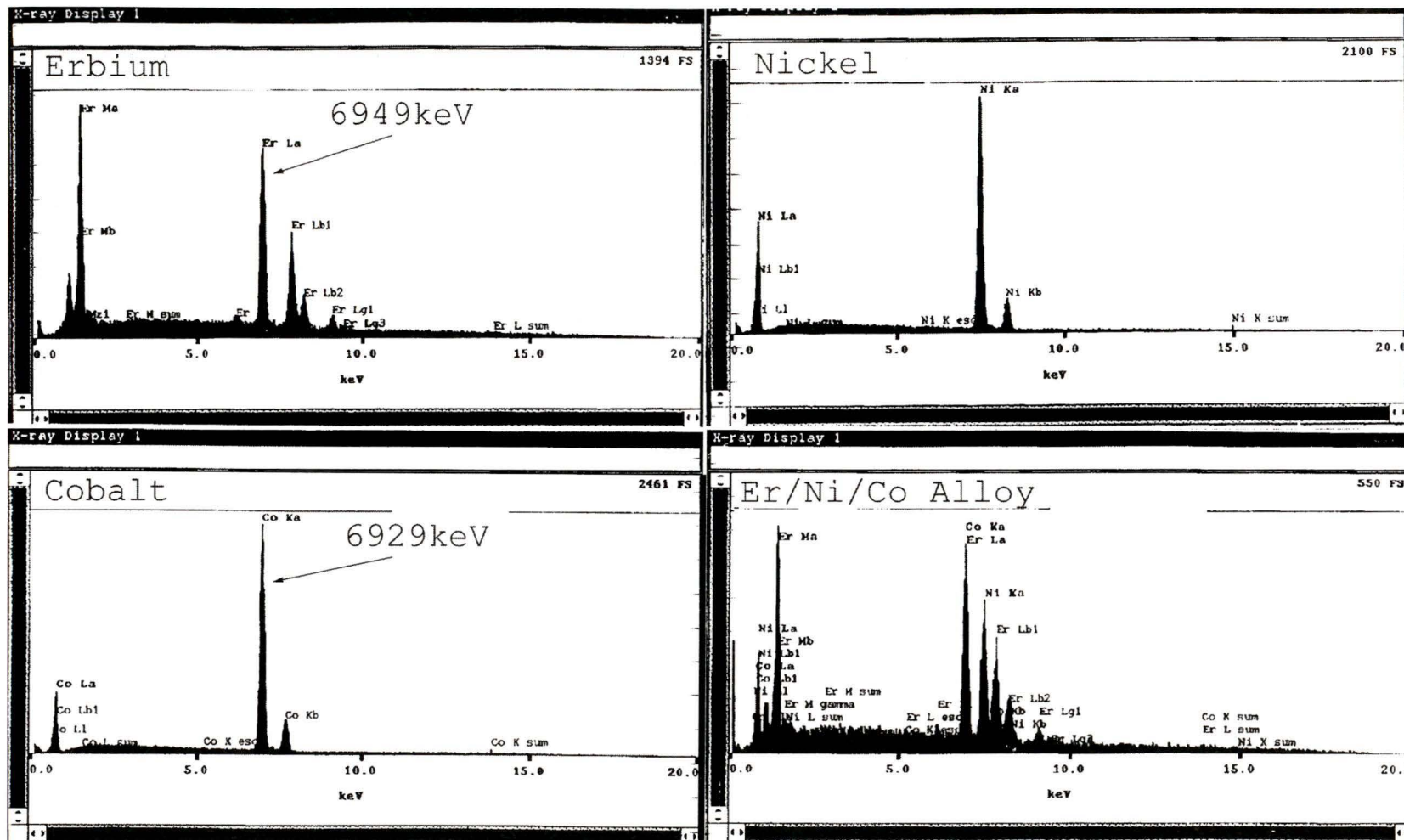
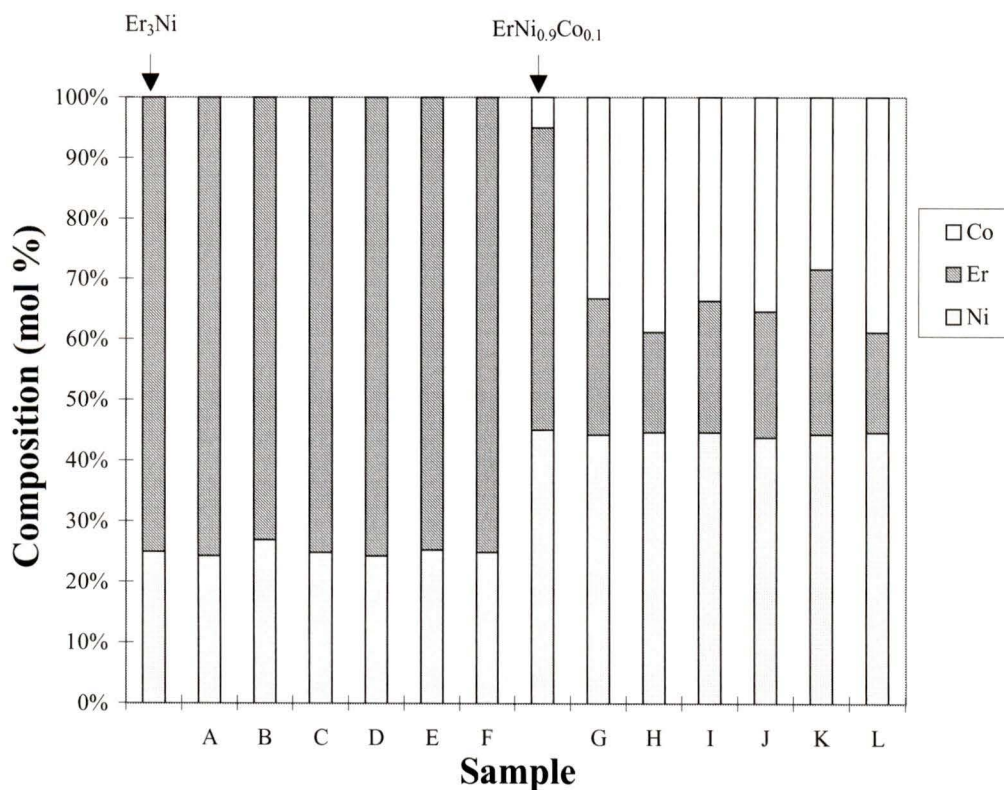


Figure 4-6: Energy dispersive X-ray spectral analysis for an Er-Ni-Co alloy.

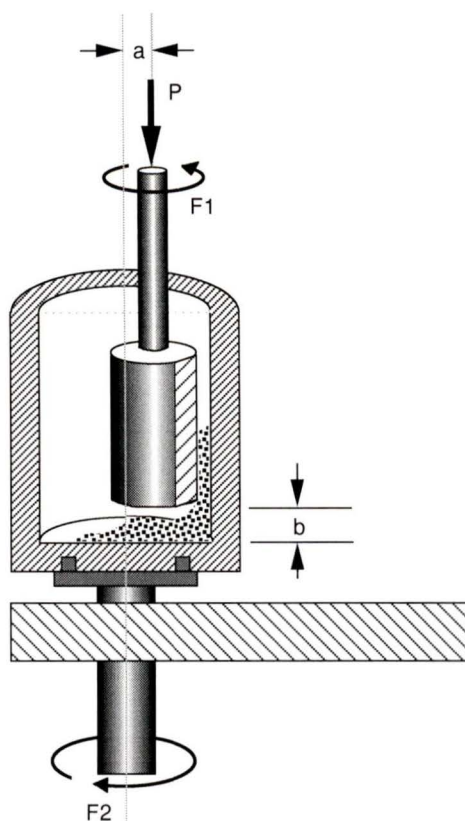


**Figure 4-7: The composition of the RE/TM samples as measured by Energy-dispersive X-ray spectral analysis (A to F =  $\text{Er}_3\text{Ni}$ , G to L =  $\text{ErNi}_{0.9}\text{Co}_{0.1}$ ). The columns at the beginning of the series represent the expected compositions for each alloy.**

### 4.3.3 Particle Fabrication

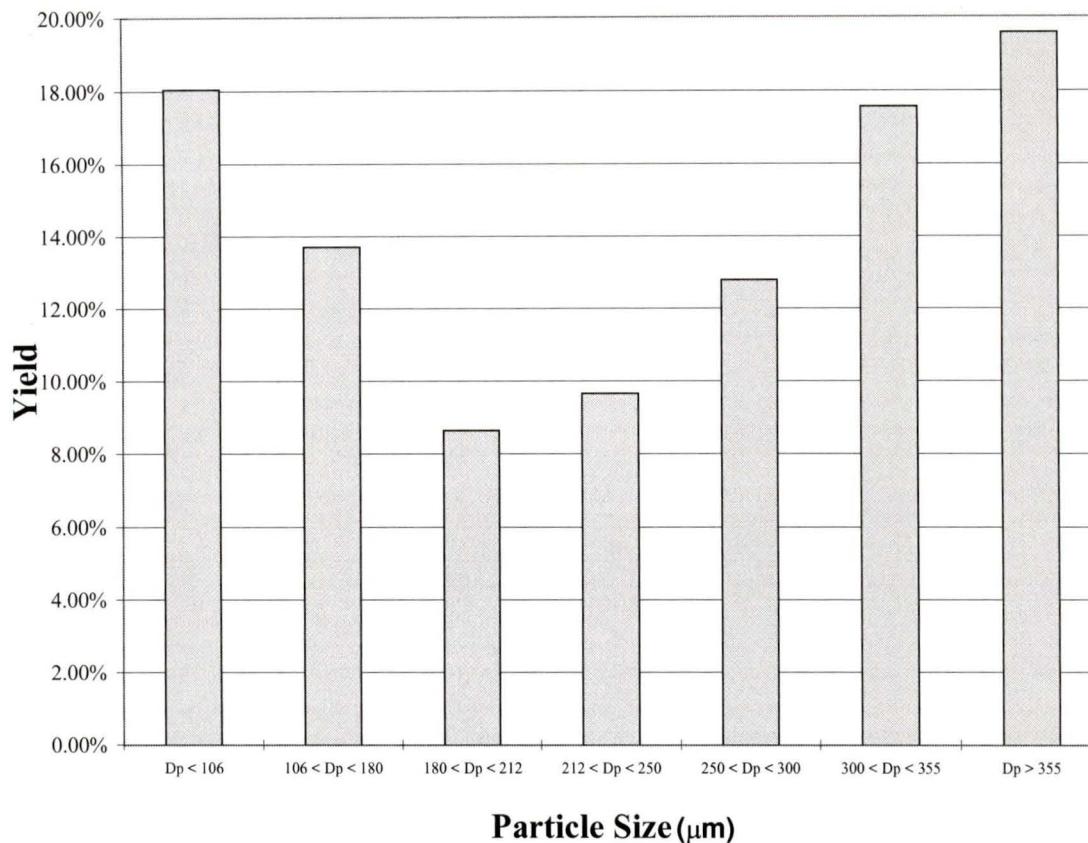
Irregularly-shaped particles were produced by mechanically crushing the RE/TM alloys using an automated mortar and pestle apparatus. The resulting powders were then sieved to separate the particles into different size ranges.

Figure 4-8 shows a schematic diagram of the mechanical mortar and pestle apparatus. The mortar and pestle had independent rotation axes and could spin at different frequencies. The gaps a and b in could also be controlled. The pressure applied to the pestle was controlled manually.



**Figure 4-8: Schematic diagram of the mechanical mortar and pestle apparatus. The operating parameters that gave the best results were:  $a = 2.5$  mm,  $b = 1.0$  mm,  $F1 = 150$  rpm,  $F2 = 60$  rpm. The amount of material processed was only a few grams at the time to allow a higher yield of particles in the desired size range.**

Although the yields for a given size range are low (see Figure 4-9) the results obtained with this technique were reliable and repeatable. In addition, larger particles can simply be crushed again to increase the yield of a smaller size. Smaller particles could also be re-melted but this is problematic because fine powders are easily dispersed by the plasma jets inside the arc-melter. One possible solution could consist of modifying the arc-melting techniques by machining deeper pockets in the copper hearth. This would contain the powders until they are completely melted, but turning the samples or even extracting the resulting ingots could be difficult. However, in the particular case of RE/TM alloys this limitation is not really a problem because the samples can be easily fragmented after each melt (to ensure homogeneity). In this manner, the smaller fragments can be extracted from the copper compartments at the end of the arc-melting process.



**Figure 4-9: Size distribution for the irregularly-shaped,  $\text{Er}_3\text{Ni}$  particles produced by mechanical crushing ( $D_p$  = mean particle diameter). The results obtained with  $\text{ErNi}_{0.9}\text{Co}_{0.1}$  were similar.**

#### **4.4 Possible Methods to Prevent Particle Disintegration**

As stated before, particle disintegration must be prevented to ensure the reliable operation of the second-stage regenerator. After the RE/MT particles were fabricated, a variety of possible methods to make them structurally stable were considered. Some of the most relevant options are described in the following sections.

##### **4.4.1 Metallic Vapour Coating**

One possible way to prevent particle disintegration would be to coat the irregularly-shaped particles with a thin layer of a ductile material such as tin or lead. This approach

would provide an enclosure for the brittle particles so that, if they were to disintegrate, the resulting fragments would be kept inside (thereby preventing contamination).

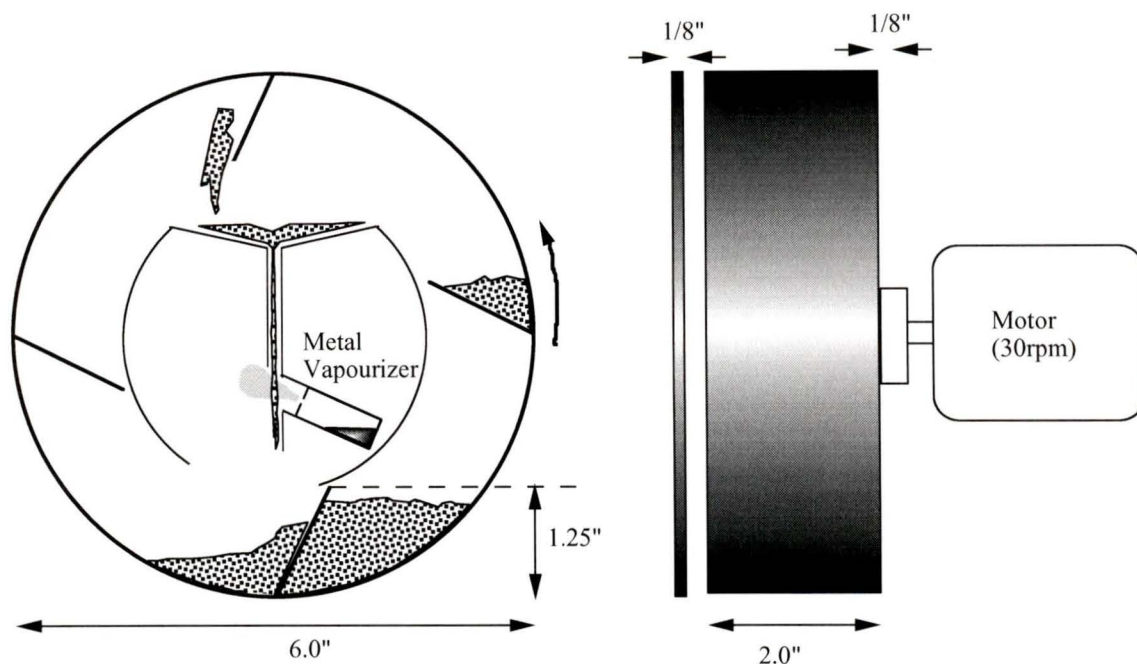


**Figure 4-10: Schematic representation of the apparatus used to test vapour coating techniques (the heater around the metal vapourizer is not shown).**

Figure 4-10 shows an schematic diagram of a prototype apparatus built to test this procedure. This apparatus was placed inside a vacuum chamber. As can be seen, a rotating drum lifted the irregular particles and dropped them into a funnel. As the particles fell, they passed in front of a boron nitride cylinder that contained a ductile metal (lead in this case). This cylinder was heated to produce a vapour stream that sprayed the particles as they passed. Preliminary experiments showed that the metal coating was not uniform and some areas on the particles were not covered with lead. In addition, to completely coat each particle it would have been necessary to have a layer of lead covering its entire surface. This extra layer of non-magnetic materials would have reduced the amount of RE/TM alloy and the regenerator (thereby reducing its volumetric thermal mass).

Another limitation as found when the particles were dropped into the metal funnel. Because these materials are so brittle, a significant fraction of the original particles was fragmented into smaller powders ( $< 40 \mu\text{m}$ ). This resulted in a reduction of the total yield of coated particles (the actual percentages were very low ( $< 2 \%$ ) and depended on the particle size range. These yields were not repeatable). One possible option to increase the yield of coated particles would be to increase the vapour pressure of the Pb stream. This, however, would require special pumping systems to handle the metal vapour (a cold trap could also be implemented to capture the metal particles before they reach the pump).

Vapour coating could be a very effective method to produce structurally stable regenerators. However, the manufacturing techniques and related hardware needed to obtain reasonable results would be very expensive, and would require the implementation of dedicated facilities. This was precisely the type of limitation that these experiments attempted to eliminate.

#### **4.4.2 Immersion in a Molten Metal Bath**

Another possible solution to coat irregular particles would consist of simply immersing the entire regenerator bed in a bath of a low melting point alloy (e.g., indium-gallium eutectic), and then removing the excess by flushing the bed with gas. Preliminary experiments using copper particles and Wood's metal (a low melting point alloy) showed that obtaining a uniform coating would be difficult (the entire regenerator bed had to be heated to a temperature higher than the melting point of the alloy). In addition, the wetting characteristics of In-Ga, Pb and other materials on RE/TM were not known.

Other limitations included magnetic dilution due to the addition of non-magnetic material(s), and the possibility of increasing the overall longitudinal thermal conductivity of the regenerator bed. These two characteristics would decrease the effectiveness of the regenerator (see Sections 2.5 and 2.6)

Although other techniques were considered, the fabrication of monolithic regenerator beds was chosen as the simplest way to produce reliable regenerators using irregularly-shaped particles. The following sections give a detailed description of the manufacturing techniques developed by the author.

#### **4.4.3 Monolithic Regenerator Beds Using a Cryogenic Epoxy**

This alternative route was focused not on the individual particles, but rather on the regenerator bed as a whole: the main reason for particle disintegration can be related to the relative motion of a single particle and the ensuing collisions or frictional wear as it comes in contact with its nearest neighbours. A monolithic bed (i.e., one in which each particle was held at a fixed position) would drastically reduce the possibility of particle disintegration.

The addition of epoxy to the regenerator matrix could have had undesirable effects on its performance. The heat transfer coefficient, for example, could have been reduced due to an extra layer of material between the regenerator particles and the working fluid. Also, the pressure drop could have been increased by the presence of epoxy in the interstitial sites between particles (i.e., the overall porosity may have been reduced). These considerations implied the need for some investigation on the minimum amount of epoxy required to ensure structural integrity, while simultaneously minimizing undesirable effects.

The type of epoxy was also an important factor to consider. During operation, the regenerator bed is exposed to mechanical stresses due to the periodic pressure wave associated with gas expansion (the pressure exerted on the monolithic bed can be as high as 1.72 MPa). Thermal cycling was another important factor to consider: during a typical run, the temperature decreased from 295 K to 10 K in about 30 minutes (see Chapter 3).

After some analysis, Stycast® 1266 from Emerson & Cumming Inc. [151] was selected as very good candidate to satisfy the mechanical and thermal properties required to ensure

the structural integrity of the regenerator. Stycast® 1266 is a two-part, room-temperature cure epoxy resin commonly used for cryogenic applications. Table 4-2 shows some of the physical properties and other characteristics found in this epoxy [155].

**Table 4-2: Physical properties for Stycast® 1266 epoxy.**

Mixed viscosity (cps)	650
Specific gravity	1.18
Hardness, Shore D	75
Compressive strength (psi) [kg cm <sup>-2</sup> ]	(10,000) [700]
Tensile strength (psi) [kg cm <sup>-2</sup> ]	(6,000) [422]
Flexural strength (psi) [kg cm <sup>-2</sup> ]	(20,000) [1,406]
Volume resistivity (Ω cm)	$6 \times 10^{14}$
Index of refraction	1.56
Mixing ratio (Part A:Part B)	100:28
Curing time (room temperature)	8 h
Post cure (at 93°C)	2 h
Pot life	½ h

#### 4.5 Fabrication of monolithic Regenerator Beds

The first step in making monolithic regenerator beds consisted of performing some preliminary experiments using 200 μm copper particles instead of the irregularly-shaped RE/TM particles. Copper was used because the application of epoxy is an irreversible process that does not allow the recovery of the regenerator materials (the raw materials required to make the RE/TM alloys are relatively expensive, and the available initial amounts were limited).

A stainless steel screen was soldered to the end of a 2.54 cm (OD) stainless steel tube. The tube was then filled with enough copper particles to make a column approximately 30 mm in length. Finally, a diluted solution of Stycast® 1266 epoxy in toluene was poured into the resulting column. The excess epoxy was removed by two different methods:

- a) applying suction to the bottom end of the column; and
- b) blowing pressurized gas from the top.

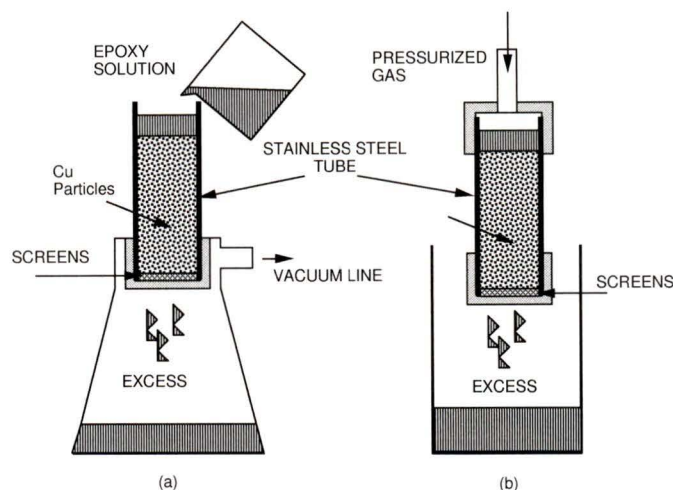


**Figure 4-11: The excess epoxy solution was removed by suction (a), and by applying positive pressure to one end of the regenerator bed (b).**

In either case, the procedure was repeated five times and then the epoxy was left to cure for 24 hours at room temperature. A post cure of 2 h at 93°C was also applied as recommended by the manufacturer. Some of the results obtained with different epoxy solutions and different excess-removal methods are shown in Table 4-3 and Figure 4-12.

**Table 4-3: Monolithic regenerator beds using 200  $\mu\text{m}$  copper particles and diluted epoxy solutions.**

Test Cylinder	Stycast® 1266 Epoxy Solution			Excess removal Method
	Part A (g)	Part B (g)	Toluene (mL)	
A	5.006	1.406	20.0	Pressurized gas (30psi)
B	5.037	1.431	30.0	Pressurized gas (20psi)
C	5.002	1.414	50.0	Pressurized gas (20psi)
D	5.492	1.550	30.0	Suction
E	5.492	1.551	10.0	Suction

The pressure drop across these cylinders was measured using the apparatus described in Section 3.3.4.2. As can be seen, method (b) produced the best results, removing most of the excess epoxy solution and bringing the pressure drop across the regenerator almost to its original value (i.e., to the pressure drop value prior to the addition of the epoxy mixture). In all cases, the fluid used to remove the epoxy was nitrogen gas at room temperature.

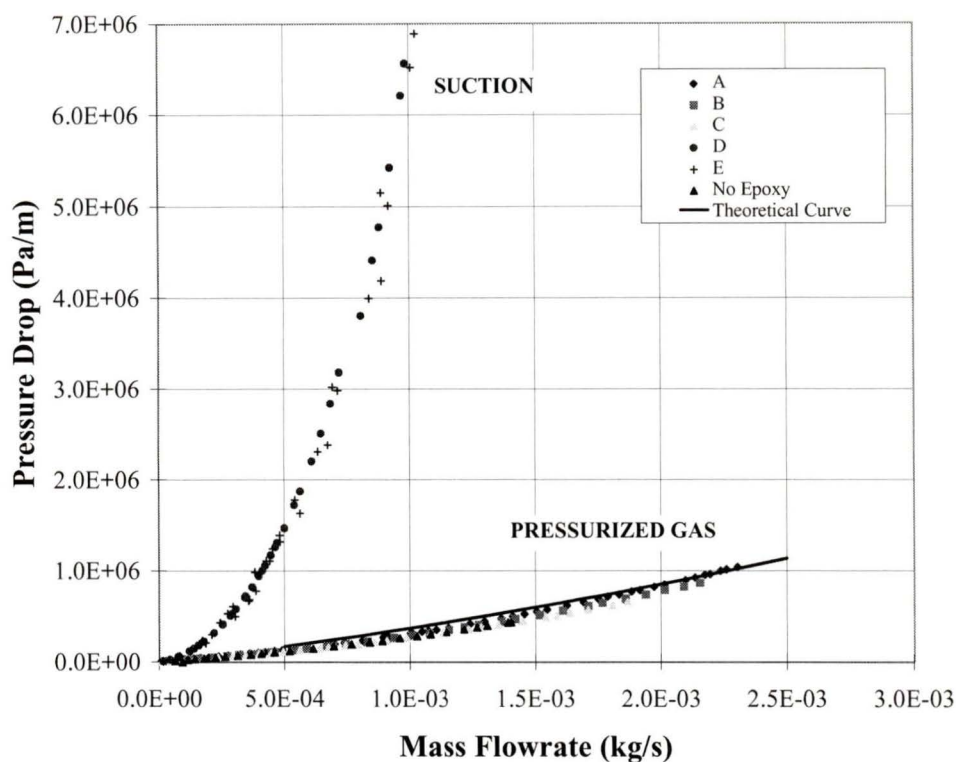


**Figure 4-12: Comparison between the two different epoxy removal techniques (error bars are not shown, see Appendix I for details). The theoretical curve corresponds to McDonald's modification of Ergun's equation.**

After establishing that the excess epoxy could be easily removed, it was decided to perform structural integrity tests using brittle materials instead of the copper particles.

#### 4.6 Structural Integrity Tests

The next step in the fabrication process consisted of making monolithic beds of RE/TM particles without the outer metal jacket used with the copper particles. By eliminating the stainless steel tube, it was possible to insert the monolithic regenerator bed directly into one of the phenolic containers described in Section 4.2. This was accomplished by using a Teflon tube instead of the stainless steel enclosure. The inner walls of this tube were sprayed with No.122-S Mold Release [151]. This substance prevented the epoxy mixture from gluing the bed of packed particles to the walls of the container. After the epoxy had cured, the entire bed was extracted from the Teflon tube (see Figure 4-13).

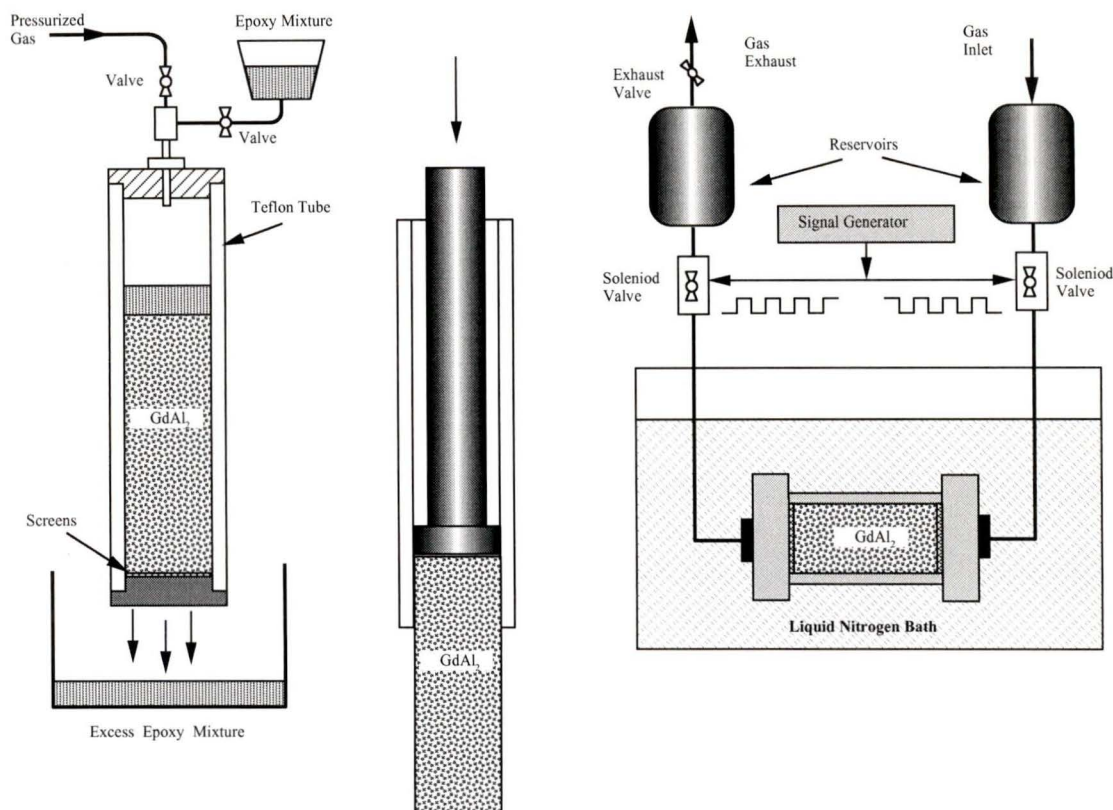


**Figure 4-13: A monolithic bed of  $GdAl_2$  was used to perform structural integrity tests at cryogenic temperatures.**

$GdAl_2$  is an easily produced brittle material whose mechanical properties are similar to those found in  $Er_3Ni$  and  $ErNi_{0.9}Co_{0.1}$ . Irregularly-shaped particles of this gadolinium alloy were used to make a monolithic bed using the techniques described in the previous paragraph. The resulting bed was then cut to the required length using a diamond-impregnated cutting disc. The addition of the epoxy mixture made the bed of packed particles strong enough to withstand cutting and clamping without breaking. The particles at the edges of the bed, however, could be easily removed and a small material loss (a few mg) occurred as the bed was cut and handled.

The final bed was glued to the inner walls of a cylindrical test cell made of brass. The ends of this cell were sealed using two end flanges, and a combination of Teflon O-rings,

and self-adhesive, Teflon-based material (Gore-Tex®) . Stainless steel screens were placed between the monolithic bed and the end flanges.

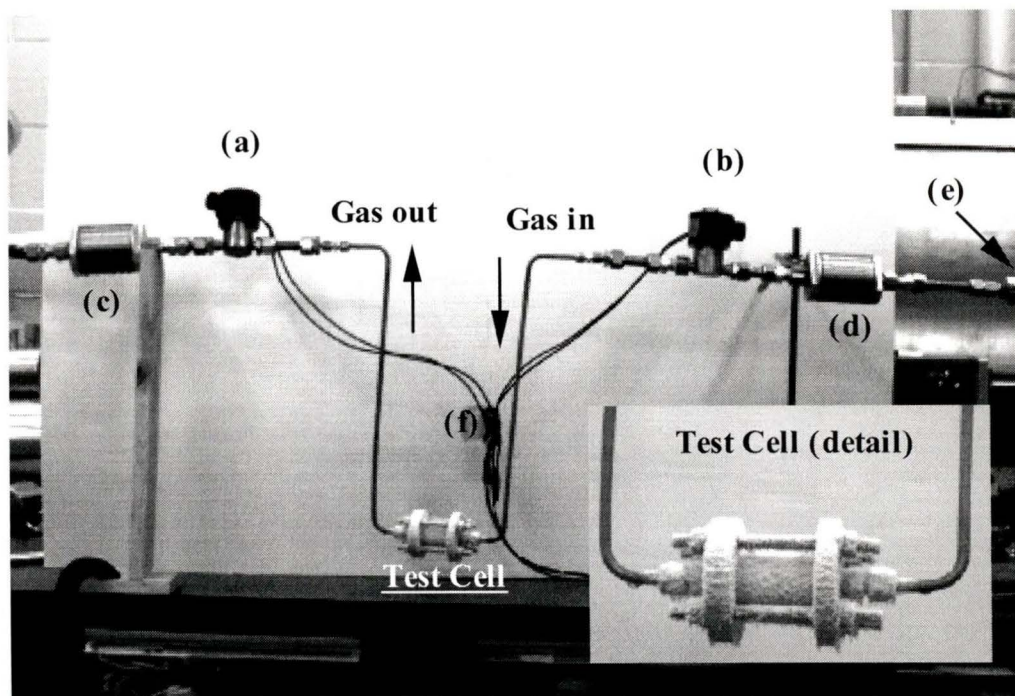


**Figure 4-14: Apparatus used for structural integrity tests (a), (b) solenoid valves, (c), (d) buffer volume reservoirs, (e) helium gas inlet, (f) wiring to signal generator.**

The aim of these tests was to simulate the mechanical stresses experienced by the regenerator during normal operation. To accomplish this, a pressure wave was simulated by controlling the flow of pressurized helium via two solenoid valves (see Figure 4-13 ). A signal generator transmitted a square-wave voltage to each of these valves. During each cycle, the gas pressures at either side of the monolithic bed were approximately 100 psig and 300 psig (0.790 MPa and 2.17 MPa), respectively. This pressure could be controlled by partially closing the exhaust valve shown in Figure 4-13. To test the reliability of the regenerator bed at cryogenic temperatures, the entire test cell was immersed in a bath of liquid nitrogen

The test cell was exposed to pressure-wave cycles at a frequency 2.4 Hz (the highest frequency of operation in the GM cryocooler). After 1000 cycles were completed, the total mass and pressure drop across the regenerator bed were compared to the corresponding values prior to testing. Neither the total mass, nor the pressure drop

showed any appreciable change. Lastly, a visual inspection of the monolithic bed revealed no observable damage or structural failure. These results indicated that no particle disintegration had occurred.

After obtaining these results, it was decided to proceed with the fabrication of monolithic beds using  $\text{Er}_3\text{Ni}$  and  $\text{ErNi}_{0.9}\text{Co}_{0.1}$  particles.

## **4.7 Regenerator Beds Using RE/TM Alloys**

Three different regenerator beds were fabricated. The results and manufacturing techniques associated with each of these beds are discussed in the following sections.

### **4.7.1 Regenerator 1: A Two-layer, Hybrid Regenerator Bed**

The first monolithic bed (hereinafter referred to as REG1) consisted of a two-layer hybrid using  $\text{Er}_3\text{Ni}$  and  $\text{ErNi}_{0.9}\text{Co}_{0.1}$  particles at the hot and cold ends of the regenerator, respectively. The particle size ranged from 250 to 300 $\mu\text{m}$ . The manufacturing technique is depicted in Figure 4-15.

The epoxy solution used in this case consisted of 6.426g of Stycast® 1266 epoxy ([5.010  $\pm$  0.002 g] part A + [1.416  $\pm$  0.002 g] part B) diluted in 40 mL of Toluene. This mixture was poured and flushed 5 times and the epoxy was left to cure for 24 hours at room temperature. A post cure of period 2 hours at 93°C was also included as recommended by the manufacturer.

After the monolithic bed was extracted from the Teflon tube, it was placed into one of the second-stage regenerator containers described in Section 4.2.1. The end plug assemblies (perforated plates + screens) at the top of the regenerator container, and on the bottom plug had been previously glued in place.

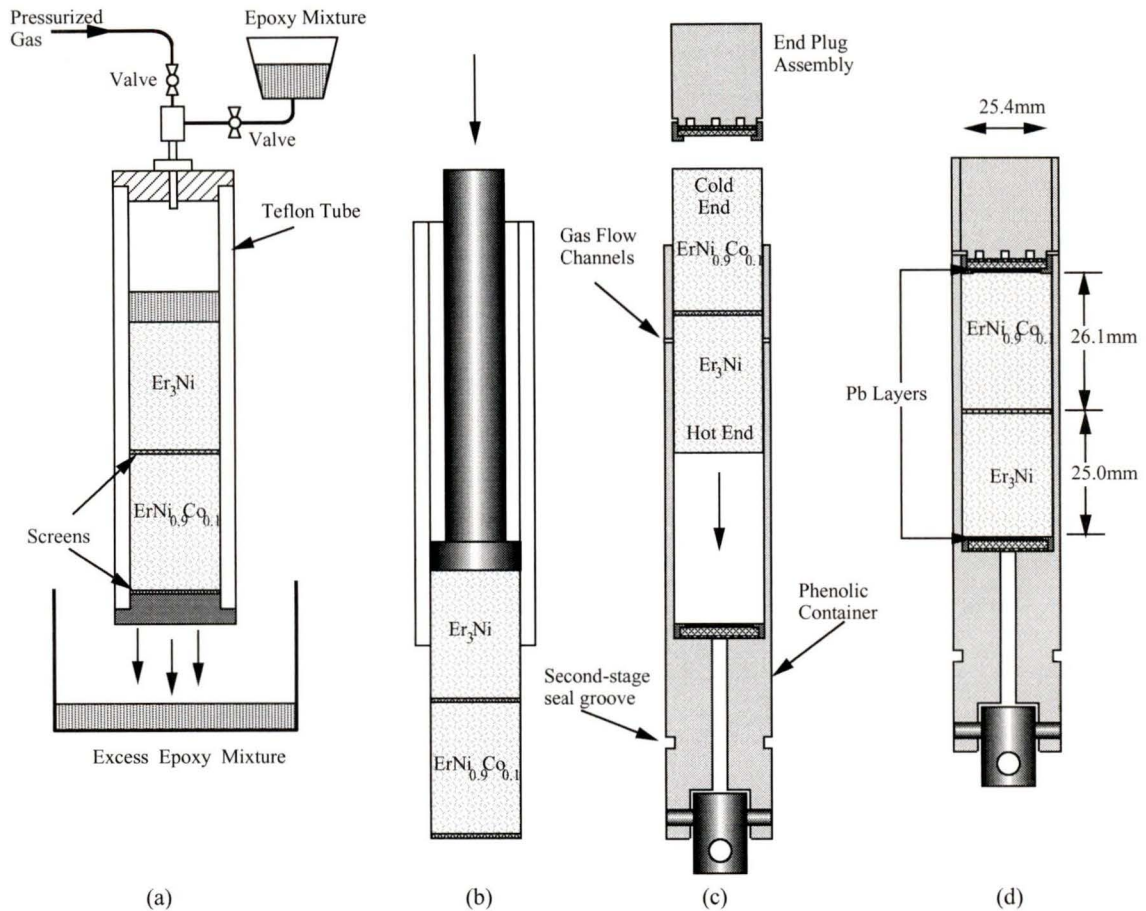


**Figure 4-15: The manufacturing technique for a hybrid, monolithic regenerator bed. The process included: removal of excess epoxy solution by pressurized gas (a), extraction of the monolithic bed from a Teflon tube (b), insertion into a regenerator container (c), and sealing of the entire assembly by gluing the end plug in place (d).**

Because the monolithic bed was very porous, the viscosity of the undiluted Stycast® epoxy was not enough to prevent absorption (i.e., instead of remaining on the surface, the epoxy quickly permeated the bed). It was therefore necessary to add 0.5 g of a cotton-fiber filler in order to make the epoxy more viscous and prevent it from migrating to the interior of the regenerator. A ~0.5 mm layer of this mixture was applied to the lateral surface of the regenerator bed being careful not to cover the ends. A thin layer (< 1mm) of 300µm lead particles was poured into the regenerator container. The monolithic bed was then inserted into the regenerator container and the excess epoxy/filler mixture was removed. Another thin layer of lead particles was deposited on top of the regenerator bed and then the whole assembly was sealed by gluing the second-stage plug in place.

By having a thin layer of lead at either end of the regenerator, it was possible to place a mechanical load on the bed during the curing period (i.e., the ductility of lead absorbed the load and prevented the bed from fracturing). In addition, if particle disintegration occurred, the layers of lead would have prevented the fine powders from leaving the regenerator space. A load of approximately 100 N was placed on the regenerator as the epoxy cured for 24 hours at room temperature.

Figure 4-16 shows the pressure drop in the  $\text{Er}_3\text{Ni}/\text{ErNi}_{0.9}\text{Co}_{0.1}$  bed before and after the epoxy mixture was added. These measurements are also compared to the pressure drop in the original lead-based regenerator provided by the manufacturer.

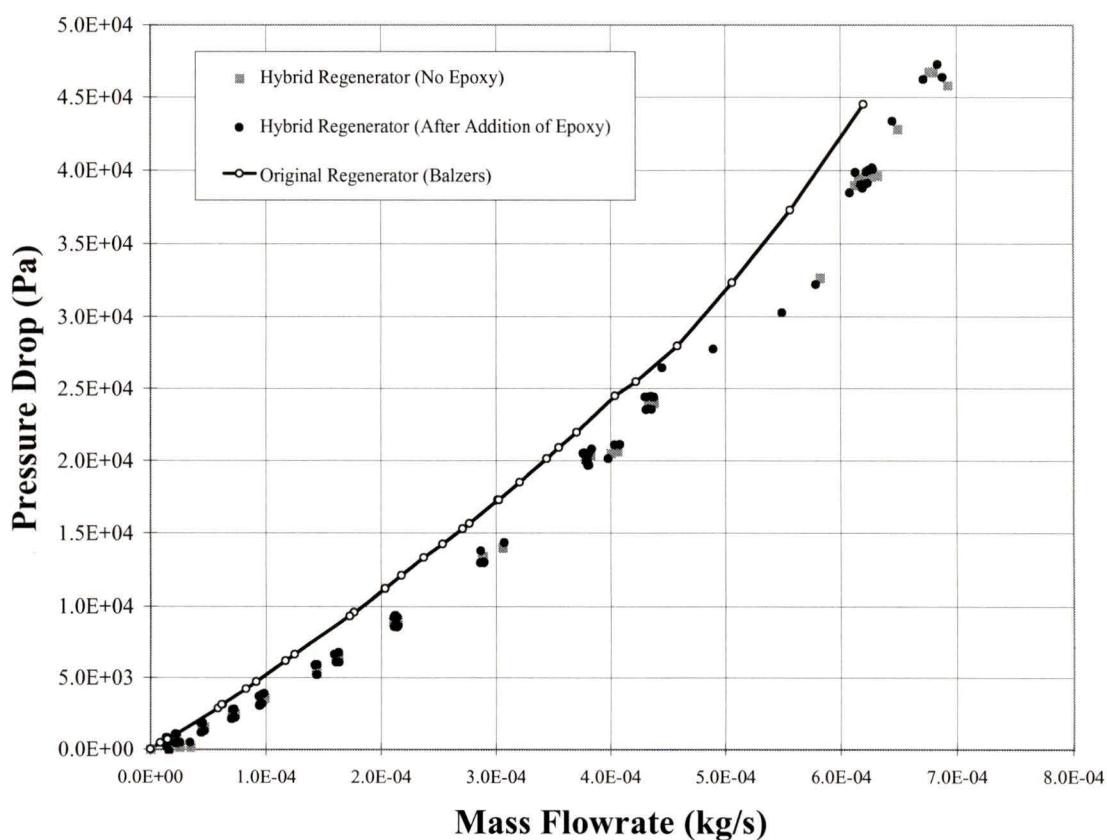


**Figure 4-16: Pressure drop across the hybrid  $\text{Er}_3\text{Ni} + \text{ErNi}_{0.9}\text{Co}_{0.1}$  regenerator bed. The fluid used was helium gas at room temperature and at a mean pressure of 100 psig (error bars are not shown, see Appendix I).**

The new regenerator was placed at the second stage of the GM cryocooler. The cooling times were similar to those obtained with the original lead-based, but the minimum temperature achieved was only  $7.2 \pm 0.1$  K. This temperature was higher than that obtained with the lead-based regenerator even if the volumetric thermal mass of the hybrid bed was much higher (see Appendix H). These surprising results indicated that the new hybrid regenerator had some serious performance limitations that needed to be corrected. Some of the possible causes for performance degradation included:

- **Defective sealing:** as stated in Page 89, the tolerances associated with the second-stage seal assembly are very important. A close examination of the regenerator container, revealed that the seal assembly did not fit tightly on its groove. A loose fit implied that the split-ring seal could rotate from its original position to a new position  $180^\circ$  apart. This resulted in some warm gas leaking into the cold expansion volume thereby reducing the cooling power.
- **Increased longitudinal conduction:** the presence of an epoxy matrix implied a semi-continuous conductive path for thermal leaks between the warm and cold ends of the regenerator. This could have reducing the cooling capacity and increased the minimum (no load) temperature. This possibility was not confirmed experimentally.
- **Channeling:** preferential flow along the walls of the container may have occurred due to defective sealing between the surface of the monolithic bed and the container.
- **Other effects:** any modification in the geometry and composition of a regenerator bed has repercussions in the thermal ( $k_T$ ,  $C_p$ ), hydrodynamic ( $\Delta P$ ), and heat transfer properties of the regenerator as a whole. The pressure drop effects were found to be minimal, but the presence of epoxy could have had an effect on the

other properties. A second regenerator was built to test the performance of a hybrid, multilayer bed without the presence of epoxy.

#### **4.7.2 Regenerator 2: A Three-layer, Hybrid Regenerator Bed without Epoxy.**

The second regenerator bed (REG2) was essentially a modified version REG1 with an extra layer of lead at the warm end. This extra layer of lead was used to ensure that the volumetric thermal mass in REG2 was larger than the corresponding value in REG1. The additional modifications implemented were as follows:

- A new seal groove was machined in an existing regenerator container to ensure a tight fit for the second-stage seal assembly.
- The total length of the regenerator space was increased in order to accommodate an extra layer of lead at the warm end.

REG2 was placed in the GM cryocooler without applying any epoxy (i.e., REG2 was not a monolithic regenerator). This was done to isolate the effect(s) that the epoxy matrix could have had. A short test run was carried out to test the performance of the bed with a larger thermal mass and without the possible effects associated with the presence of epoxy.

The cooling curves obtained with REG2 at the second stage of the cryocooler were very similar to those obtained with the original lead-based regenerator: the temperature at the second stage is very close to its minimum value after approximately 1 hour. The lowest, no-load temperature was obtained after the entire radiation shield was cooled and this required an additional 1 ½ hours. The minimum temperature obtained with REG2 was  $3.78 \pm 0.02$  K at an operating frequency of 1.2 Hz. This result represented the first successful reduction of the second-stage temperature to sub-liquid helium levels. The performance of REG2, however, degraded rapidly with time.

### 4.7.2.1 Degradation of Performance Due to Particle Fragmentation

Figure 4-17 shows the minimum, no-load temperatures obtained at different operating frequencies. These temperatures became increasingly higher and, after approximately 12 hours of continuous operation, the lowest temperature had increased by almost a full degree. In order to prevent possible contamination of the entire refrigerator and helium gas circuit, the operation of the GM cryocooler was halted and REG2 was detached from the displacer assembly.

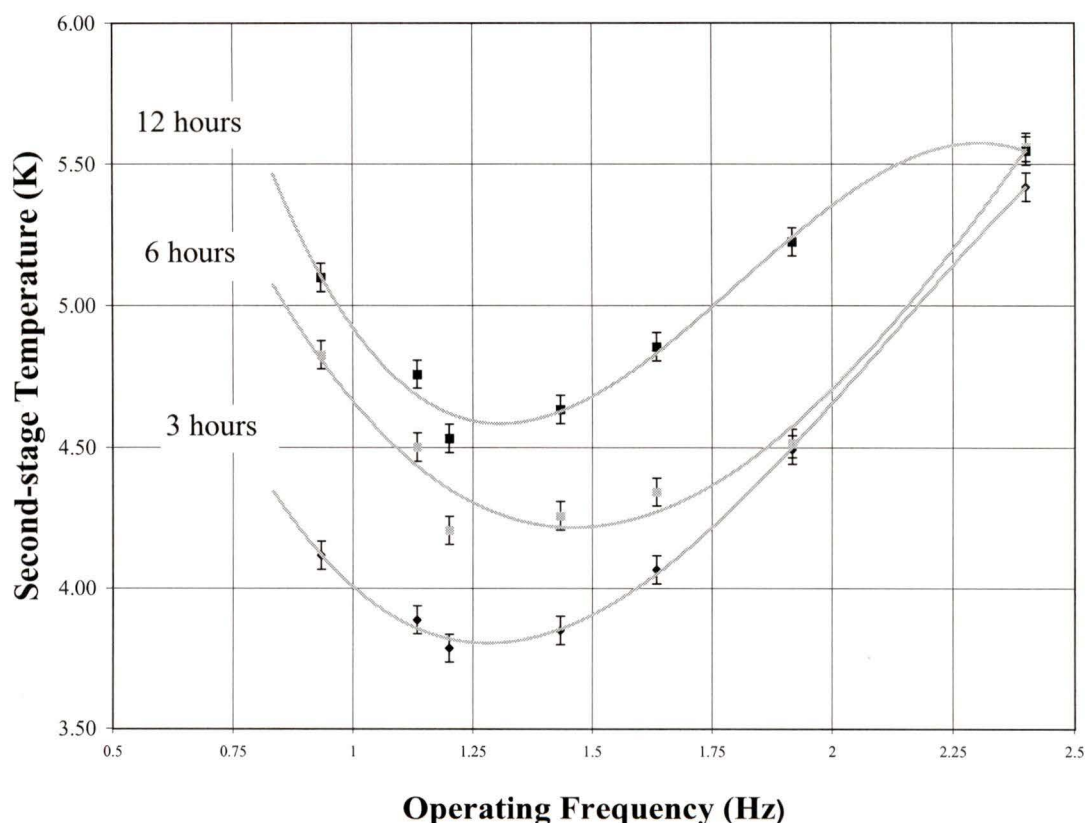


**Figure 4-17: The performance of REG2 degraded rapidly with time. The operation of the GM Cryocooler was halted after approximately 12 hours of continuous operation.**

Upon examination, the second-stage expansion space was found to be free of particle contamination. No metal particles were found anywhere else inside the cold-head

enclosure. Although contamination had not occurred, the disintegration of the original RE/TM particles was still the most likely cause for the degradation of REG2. To establish if this was indeed the case, the end plug was carefully bored from the regenerator container. The perforated plate/screen assembly was also carefully removed to gain access to the bed of packed particles.

The particles in each of the layers were weighed and separated into different size ranges. Table 4-4 shows the results of these measurements. As can be seen, a significant fraction (~ 20%) of the original RE/TM materials had been pulverized into particles of smaller size. These powders filled the interstitial spaces between the original particles thereby obstructing the passage of gas into the second-stage expansion space. This reduction in the total gas flow resulted in a reduction in the cooling power and an increase in the minimum temperature at the second stage.

**Table 4-4: Particle-size distribution in REG2 after 12 hours of continuous operation. The total amount of fragmented particles was approximately 20% of the original total mass for both materials. All masses were measured to a precision of  $\pm 0.002$  g.**

Size Range ( $\mu\text{m}$ )	$\text{Er}_3\text{Ni}$ (mass in g) [%]	$\text{ErNi}_{0.9}\text{Co}_{0.1}$ (mass in g) [%]
250 - 300 (original size)	(45.593) [79.6]	(46.118) [83.3]
212 - 250	(9.639) [16.8]	(6.600) [12.0]
180 - 212	(1.063) [1.9]	(1.011) [1.8]
106 -180	(0.589) [1.0]	(0.958) [1.7]
< 106	(0.384) [0.7]	(0.662) [1.2]

These results confirmed that particle disintegration was a serious limiting factor for beds of irregularly-shaped particles made of RE/TM alloys. On the other hand, the minimum temperatures obtained also demonstrated that the volumetric thermal mass of REG2 had been considerably increased thereby increasing the effectiveness of the regenerator bed at low temperatures.

### 4.7.3 Regenerator 3: A Three-layer, Monolithic Regenerator Bed

A third regenerator (REG3) was built using the same regenerator container used for REG2. This regenerator was essentially a replica of REG2 with similar total masses for

each of the materials (see Table 4-5). This bed of packed particles, however, was converted into a monolithic regenerator following a procedure that was slightly different from that used to fabricate REG1.

Instead of using the technique described in Section 4.6, the epoxy mixture was applied directly to a finished regenerator container (see Figure 4-18). This change simplified the manufacturing technique and eliminated the possibility of channeling. In addition, material losses due to extraction, cutting and handling of the monolithic bed were eliminated.

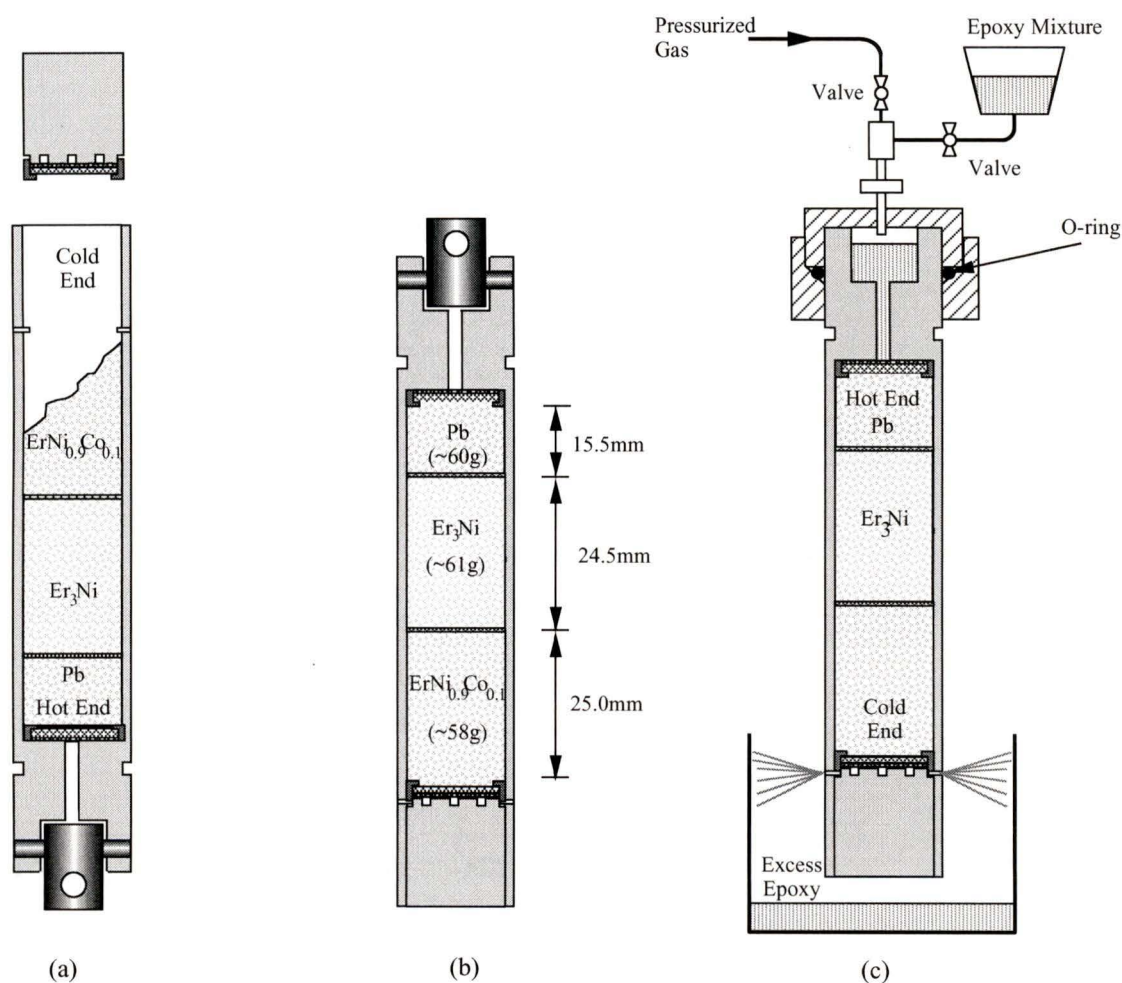


**Figure 4-18: Modified manufacturing technique for monolithic regenerator beds. The epoxy mixture was applied directly to the entire regenerator assembly. A regenerator container was filled with particles (a), sealed (b). A diluted solution of epoxy was applied directly to the particle bed (c). The intermediate step involving a Teflon tube was eliminated.**

After the epoxy had cured, REG3 was placed at the second stage in the GM cryocooler. The cooling times were similar to those observed with REG2 (i.e., about 2½ hours for complete cooldown). The minimum, no-load temperature was  $3.42 \pm 0.05$  K at an operating frequency of 1.2 Hz. Figure 4-19 shows the minimum temperature obtained at different operating frequencies.

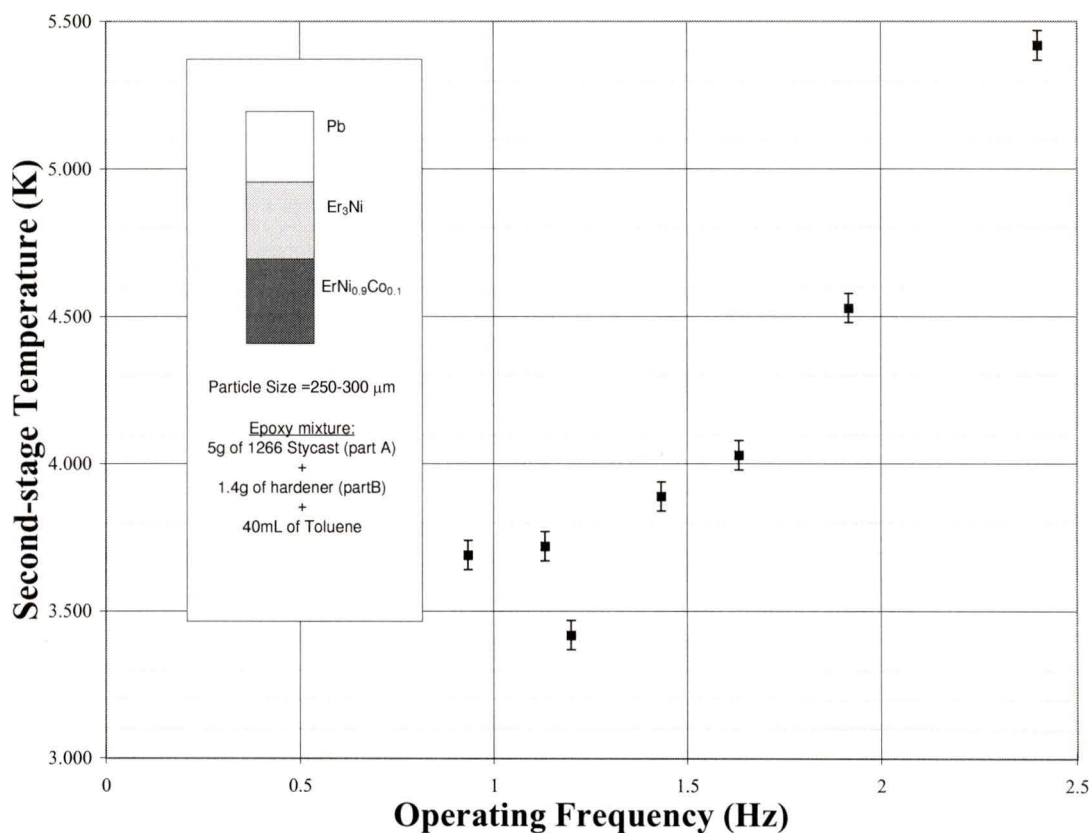


**Figure 4-19: Measured minimum, no-load temperatures obtained with REG3.**

Unlike the results given in Section 4.7.2.1, the performance of REG3 did not degrade with time and it was still repeatable after 10 days of continuous operation (this corresponds to approximately  $10^6$  cycles). Table 4-5 shows a summary of the results obtained with different regenerators at the second stage of the modified GM cryocooler. The measured cooling powers at different temperatures are presented in the following sections.

**Table 4-5: Summary of the results obtained with different regenerators at the second stage of the modified GM cryocooler.**

	Regenerator Materials (mass in g) [layer length in mm]			Stycast® 1266 Epoxy solution (A and B in g, Toluene in mL)			Minimum Temperature <sup>b</sup> (K)
	Pb	Er <sub>3</sub> Ni	ErNi <sub>0.9</sub> Co <sub>0.1</sub>	A	B	Toluene	T <sub>2min</sub>
REG0 <sup>a</sup>	(191.23) [51]	–	–	–	–	–	6.1 ± 0.1
REG1	–	(66.410) [24]	(59.870) [22]	5.010	1.416	40.0	7.2 ± 0.1
REG2	(50.048) [12]	(65.643) [28]	(59.998) [26]	–	–	–	3.78 ± 0.05
REG3	(60.314) [16]	(60.838) [25]	(57.952) [25]	5.002	1.401	40.0	3.42 ± 0.05

a Original design using 300 μm lead particles only.

b At the second stage with zero thermal load.

## 4.8 Refrigeration Power

Different cooling loads were simulated as described in Section 3.5.2. Figure 4-20 shows the temperature at the second stage as a function of cooling power. The superconducting magnets in the AMRL have been designed to operate at 4.5 K. As can be seen, the available cooling power at this temperature was measured to be 0.504 W with a simultaneous first-stage load of 20 W at  $42.8 \pm 0.5$  K.

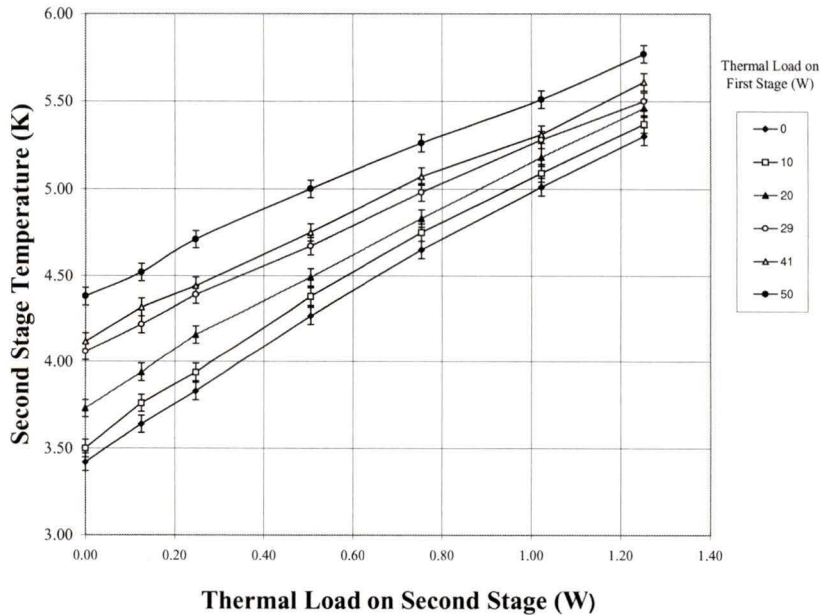


**Figure 4-20: Measured temperature at the second stage of the GM cryocooler as a function of cooling load.**

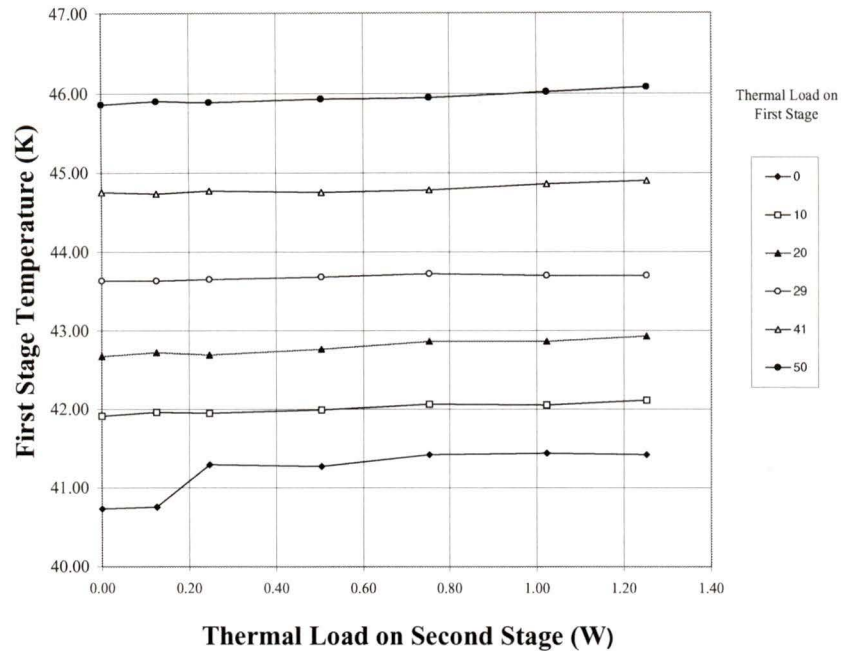


**Figure 4-21: Measured temperature at the first stage of the GM cryocooler as a function of second-stage cooling load (error bars are not shown).**

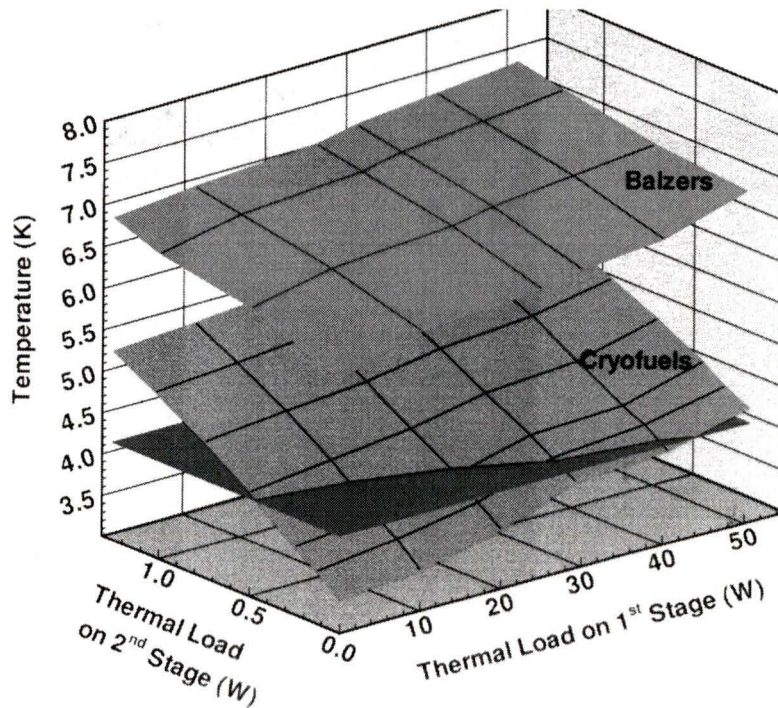


**Figure 4-22: The ultimate temperature obtained with the GM cryocooler immediately after was purchased (Balzers), and after it was modified (Cryofuels). The horizontal plane represents the normal boiling point of helium (4.2 K)**

# Chapter 5

## Conclusions and Future Work

### 5.1 Summary

All the thesis objectives outlined in Section 6.1 were successfully fulfilled. A commercial, two-stage GM cryocooler was modified to obtain non-zero cooling powers at 4.2 K. The reduction of the second-stage temperature to sub-liquid helium levels is a significant accomplishment only achieved by a few laboratories around the world. Unlike previously reported developments, the work presented in this thesis made use of very simple and inexpensive materials, and required no special hardware or dedicated facilities.

The modified refrigeration unit will be used to produce and maintain the low temperatures required by the SCMs in an AMRL. Using this unit instead of liquid cryogenics simplifies the overall system design and eliminates the need for the peripheral equipment and procedures (refilling, storage, etc.) associated with the safe handling of cryogenic liquids. A general-purpose, cryogen-free materials characterization system has also been designed as a potential application for the modified GM cryocooler (see Appendix K).

The modification of the original GM unit included its characterization immediately after it was purchased, the reverse-engineering of the second-stage regenerator to reproduce the original performance, and the fabrication of new, hybrid second-stage regenerators. These regenerators were built using irregularly shaped particles made of RE/TM alloys and a novel manufacturing technique. This technique ensured the structural integrity of the resulting monolithic regenerator while simultaneously reducing the associated manufacturing costs. The following sections describe each of these accomplishments in more detail.

### **5.1.1 Validation of Baseline Regenerator Manufacturing Techniques**

After an initial validation of the manufacturer's specifications, the second-stage regenerator in the GM cryocooler was successfully reverse-engineered to reproduce the performance of the original unit. The regenerator container was made of the same cotton fabric base, phenolic plastic used by the manufacturer and the total regenerator volume was  $28.57 \text{ cm}^3$ . The interior of this container was filled with hardened, spherical lead particles (5% Sb/95% Pb) with a mean diameter of  $300 \pm 25 \text{ }\mu\text{m}$ . The plugging technique at either end of the regenerator container made use of a perforated plate and stainless steel screen assembly that was glued in place using a cryogenic epoxy. The minimum, no-load temperatures achieved with this regenerator were  $37.1 \pm 0.5 \text{ K}$  and  $6.1 \pm 0.1 \text{ K}$  at the first and second stages, respectively.

The tolerances associated with this container were found to be crucial for the performance of the second stage regenerator. In particular, the second-stage seal groove had to be machined to tolerances of  $\pm 0.002 \text{ in}$  ( $\pm 51 \text{ }\mu\text{m}$ ) or better. This ensured good sealing at the second stage and prevented warm gas from bypassing the regenerator and leaking into the second-stage expansion volume. Another manufacturing detail consisted of making the second-stage end plug about 2 cm longer than required and machining the excess length after the plug was glued in place. This facilitated the insertion of the plug at the bottom of the regenerator container, and the alignment of the gas flow channels during assembly.

### **5.1.2 Manufacturing Techniques for Brittle Regenerator Materials**

The performance of conventional GM cryocoolers below 10 K is limited by the vanishing heat capacity of lead (the regenerator material commonly used at the second stage). This limitation was circumvented by replacing lead with materials that have larger heat capacities. After careful analysis, three RE/TM alloys ( $\text{Er}_3\text{Ni}$ ,  $\text{ErNi}_{0.9}\text{Co}_{0.1}$  and  $\text{Er}_{0.9}\text{Yb}_{0.1}\text{Ni}$ ) were selected as the best candidate materials to improve the performance of the second-stage regenerator in a conventional GM cryocooler. Two of these alloys

(Er<sub>3</sub>Ni and ErNi<sub>0.9</sub>Co<sub>0.1</sub>) were manufactured using standard arc-melting techniques. The compositions of these alloys were subsequently analyzed using energy dispersive X-ray spectroscopy, and inductively-coupled plasma analysis. The results of these measurements confirmed that both alloys had the prescribed compositions. These materials were used to manufacture irregularly-shaped particles by simple mechanical crushing using an automated mortar and pestle. The resulting particles were then separated into different size ranges. The sizes of interest in this work ranged from 250 to 300  $\mu\text{m}$ . The yields for particles in this size range were modest ( $\sim 13\%$ ) but the results were reliable and repeatable. In addition, the mechanical mortar and pestle technique made it possible to control some of the parameters determining particle size and yield. The amounts of materials processed were limited to a few grams at the time to allow a higher yield of the desired particle sizes. The resulting powders were sieved continuously as the crushing process took place. Particles whose dimensions were larger than desired were recycled through the mortar and pestle apparatus. Smaller particles were collected and stored.

Previous improvements in GM cryocooler technology have reported on the use of spherical particles made of RE/TM alloys to improve the performance of the second-stage regenerator. The production of spherical particles requires expensive manufacturing techniques and dedicated hardware. Irregularly-shaped particles are a comparatively inexpensive option. However, the structural integrity of the regenerator can be compromised if brittle, irregularly-shaped particles are used instead of their spherical counterparts. This limitation was clearly demonstrated by the results obtained with a three-layer, hybrid regenerator (REG2). This regenerator consisted of a layer of lead (at the warm end), and two layers of irregularly-shaped particles (Er<sub>3</sub>Ni and ErNi<sub>0.9</sub>Co<sub>0.1</sub> for the middle and bottom layers, respectively). Although the volumetric thermal mass was increased and the lowest, no-load temperature was reduced from  $6.1 \pm 0.1$  K to  $3.78 \pm 0.05$  K, the performance of this regenerator degraded rapidly with time.

After 12 hours of continuous operation, approximately 20% of the original 250-300  $\mu\text{m}$ , RE/TM particles had been fragmented into smaller powders. The resulting smaller

particles filled the interstitial sites between the original particles. This increased the pressure drop across the bed, reduced the gas flow into the second-stage expansion volume, and resulted in an overall increase of the lowest, no-load temperature (from  $3.78 \pm 0.05$  K to  $4.5 \pm 0.1$  K after approximately 52,000 cycles).

A new and proprietary manufacturing technique has been developed to ensure the structural integrity of regenerator beds made of irregularly-shaped, brittle particles. This technique uses a cryogenic epoxy to bind the particles and prevent their desintegration during normal operation. The manufacturing process consists of filling a regenerator container with layers of the required magnetic particles, plugging the bottom end, and applying a diluted solution of Stycast® 1266 epoxy in Toluene. The epoxy mixture consists of 28 parts of part B and 100 parts of part A (by weight). The concentration of epoxy in Toluene used in this work was approximately  $160 \text{ g L}^{-1}$  (e.g., 5.0 g of part A + 1.4 g of part B in 40 mL of Toluene). After the entire bed had been permeated by the epoxy solution, the excess was removed by applying pressurized gas from the top end of the regenerator container.

A hybrid regenerator was built using this technique (see Section 5.1.3). This regenerator made it possible to reduce the lowest, no-load temperature in the GM cryocooler, while simultaneously reducing the associated manufacturing costs. Because of its simplicity, this manufacturing method could be easily implemented to mass-produce cryogenic regenerators. The need for expensive centrifugal or gas atomization hardware has been eliminated because spherical particles are not required. To the author's knowledge, this is the first time that such a technique has been successfully used to enable a conventional, two-stage GM cryocooler to reach temperatures below 4.2 K.

### **5.1.3 Refrigeration Power Available at 4.2 K**

A three-layer ( $\text{Pb} + \text{Er}_3\text{Ni} + \text{ErNi}_{0.9}\text{Co}_{0.1}$ ), monolithic regenerator was built using the newly developed technique based on an epoxy matrix. Using this regenerator, the lowest, no-load temperature at the second stage was successfully reduced from  $6.1 \pm 0.1$  K to

$3.42 \pm 0.05$  K, at an operating frequency of 1.2 Hz. The performance of this regenerator did not show any signs of degradation after 10 days of continuous operation (this corresponds to approximately  $10^6$  cycles).

The total cooling power at  $4.2 \pm 0.1$  K was measured to be 0.430 W with zero load at the first stage. The SCM system in the AMRL has been designed to operate at  $4.5 \pm 0.1$  K. The available cooling power at this temperature was measured to be 0.504 W with a simultaneous load of 20 W at  $42.8 \pm 0.5$  K. These values do not include parasitic thermal loads.

#### **5.1.4 Cryogen Free Materials Characterization System (CFMCS)**

The preliminary conceptual design of the CFMCS and a heat capacity insert has been completed (see Appendix K). The CFMCS uses readily available components and is based on the modified GM cryocooler described in previous sections. The modularity implemented in the design makes it possible to exchange material samples or entire experimental inserts without interrupting the operation of the SCM system. A preliminary bill of materials and vendor list has been produced for the main components. Detailed engineering drawings for the CFMCS and a heat capacity insert were produced using I-DEAS™. Electronic versions of all the drawings and solid model files for this device were archived in the Cfs library\*. Future work can make use of these files for the design of additional components of the refinement of the current system. If required, these files can also be used to perform additional thermal and finite-element analysis on the different components.

Although the design of the CFMCS was focused on the characterization of metal samples, there are other important types of materials that could be investigated. Elastomers, for example, are an important class of materials for which little or no characterization has

---

\* NOTE: These files are not compatible with I-DEAS Master Series™ 2.0 and must be converted into a special format before they can be accessed.

been undertaken at cryogenic temperatures. Other materials include plastics, composites and ceramics.

## **5.2 Recommendations and Future Work**

Although the GM cryocooler has been successfully modified to improve its performance below 10 K, there remain several potential improvements that merit further research. Some of these topics as well as other practical recommendations are discussed in the following sections.

### **5.2.1 Cleanliness**

The importance of proper cleaning procedures for the cold head space cannot be overemphasized. A small amount of contamination can seriously degrade the performance of the entire refrigeration unit. In extreme cases (frozen substances, solid contaminants, etc.) contamination will permanently damage the cryocooler. In this work, the stainless steel enclosure and regenerator containers were carefully cleaned with 2-propanol and a lint-free tissue after the cold head was exposed to air. A heat gun was also used to gently warm the surfaces and evaporate any residual water or solvent. Latex gloves were used to prevent contamination with skin oils that could freeze during operation. Vacuum grease was used sparingly and only on the room-temperature O-ring seal.

### **5.2.2 Sealing**

The sealing at the second stage was found to be crucial for the performance of the cryocooler. To ensure adequate results with the current system, the backing split ring and the split second-stage seal must be assembled 180 degrees from each other. This is because, during operation, the two splits tend to align and this configuration can significantly degrade the overall performance of the cryocooler. The original seals are made by Kaydon Corporation and there seems to be a quality control problem (i.e., not all seals perform equally well). Alternative suppliers could be considered as possible

candidates to offer better performance. Additional changes could include the addition of positioning pins on the split-ring seal and backing spring to prevent their alignment during operation. Other suggestions include the addition of a thin ribbon of self-adhesive Goretex® material behind the backing spring. These options have also been explored by other researchers working with similar refrigeration units [169].

Another possible solution consists of changing the seal design completely. Instead of the split-ring seals found in current GM units, a spring-energized, continuous, Teflon®-based seal could be used (see Figure 5-1).

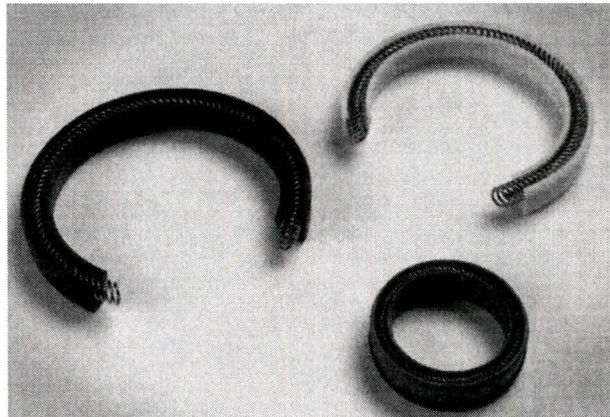


**Figure 5-1: Cross sectional view of spring-energized seals.**

Because these seals are continuous (i.e., there are no splits), the potential for gas leakage can be drastically reduced. In addition, the spring-force in these seals compensates for changes to the initial deflection caused by wear, temperature changes or tolerance variation (see Figure 5-2).

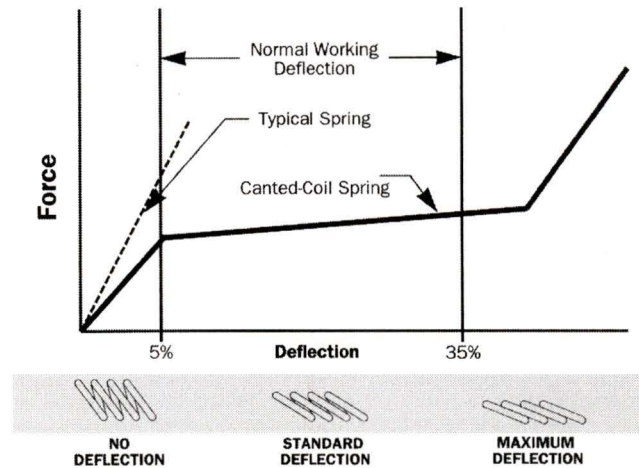


**Figure 5-2: In spring-energized seals, the spring force remains constant over a wide range of deflections.**

The seal could be mounted on the regenerator container or on the stainless steel housing (see Figure 5-3). The latter option implies that the seal will be static and the regenerator container will slide inside the inner surface of the ring. Although this configuration could offer some advantages (e.g., a fixed seal with only one sliding contact), there are some potential limitations that must be considered: the first is related to the assembly of the regenerator container and its insertion into the stainless steel enclosure. If the seal is mounted on the metal housing, it will be necessary to design an assembly procedure by which the second-stage regenerator container can be easily inserted into the seal. In addition, the seal will have to be permanently installed at the top of the second-stage or at the bottom of the first-stage housing.

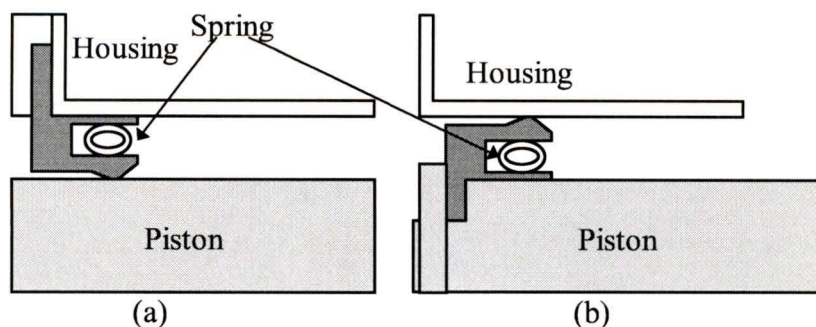


**Figure 5-3: Two alternative mounting techniques for the second-stage seal: housing mounting (a), and piston mounting (b).**

The stainless steel housing can be redesigned to accommodate the seal (e.g., by the addition of a groove and a bolted cover for the seal), but replacing the seal in case of failure will be cumbersome (the first stage enclosure has a diameter of 3 in and it is difficult to reach the bottom). Another possibility consists of making the second stage detachable so that its enclosure can be opened for assembly and/or seal replacement. This design, however, is not recommendable because it will require the sealing of the first to second-stage interface (i.e., cryogenic sealing at approximately 40 K). Although these considerations may be less relevant for commercial units that do not require servicing for long periods of time, mounting the seal on the regenerator container may be a more practical solution.

Mounting the seal on the phenolic plastic cylinder requires only small changes to the original design. For example, an independent, threaded plug could be added to the top of the cylinder. In this manner, the seal could slide into a tight-fitting shaft machined on the regenerator container and then pressed by screwing the plug from the top. Replacing the seal could then be accomplished by simply removing the second-stage container. Lowering the regenerator container assembly into the stainless steel enclosure could be done with the same retainer ring used in the current unit.

The choice of a mounting technique is one of the items that requires immediate attention and further investigation. In either case, a continuous seal is recommended as an improved alternative to the current seal design. Seals made of Fluorinated Ethylene Propylene and glass-filled PTFE could be good candidates to provide the sealing required at the second-stage of the cryocooler. These seals use 316 stainless steel springs and are available from Bal Seal Engineering Company, Incorporated (for example, the models FEP and GL-20 operate in the temperature range from 5 to 477 K) [170].

### 5.2.3 Material Layers in Hybrid Regenerators

The distribution and relative sizes of the different material layers in a hybrid regenerator should be optimized in future applications. Because the raw materials required to make the RE/TM alloys are relatively expensive, it would be convenient to minimize the amounts of these materials in a given regenerator. At temperatures above 20 K, the volumetric heat capacity of lead is comparable or larger than the corresponding values found in RE/TM alloys. This implies that, if a linear temperature profile is assumed, more than 50% of the regenerator volume could be filled with lead particles with minimal reduction of the total thermal mass. In addition, using only two more layers of different materials may not be sufficient to maximize the total volumetric thermal mass of the regenerator. For example, in REG3, the total regenerator length was 6.5 cm but the layer of lead particles was only 1.5 cm long. The layer lengths for  $\text{Er}_3\text{Ni}$  and  $\text{ErNi}_{0.9}\text{Co}_{0.1}$  were approximately 24 mm and 25 mm, respectively. In other words, the coordinates in Figure 5-4 were  $x_0 = 0$  cm,  $x_1 = x_2 = 2.55$  cm, and  $x_3 = 50$  cm (for REG3).

For a linear temperature profile ( $T = 5.615x + 3.5$ ;  $x$  in cm) these coordinates correspond to the following temperatures  $T_0 = 3.5$  K,  $T_1 = T_2 = 17.82$  K,  $T_3 = 31.56$  K (see Appendix H). As can be seen in Figure 5-4, these temperatures do not match the temperatures required to maximize the total volumetric thermal mass of the regenerator bed. In fact, the volumetric heat capacity values for  $\text{ErNi}_{0.9}\text{Co}_{0.1}$  in the temperature range from  $\sim 8$  K to  $\sim 18$  K are actually lower than the corresponding values found in  $\text{Er}_3\text{Ni}$  (i.e., a potential increase in the total thermal mass is lost by using too much  $\text{ErNi}_{0.9}\text{Co}_{0.1}$  at the cold end of the regenerator).

An optimized regenerator could consist of 4 layers of different materials ( $\text{ErNi}_{0.9}\text{Co}_{0.1}$ ,  $\text{Er}_{0.9}\text{Yb}_{0.1}\text{Ni}$ ,  $\text{Er}_3\text{Ni}$ , and Pb). The optimal coordinates in this case would be  $x_0 = 0$  cm,  $x_1 = 0.71$  cm,  $x_2 = 1.34$  cm, and  $x_3 = 2.94$  cm for a regenerator with a total length of 6.5 cm. This analysis is limited to the particular case of a linear temperature distribution. The

actual temperature profile in the regenerator bed was not determined in this work, and could be the subject of future investigations.

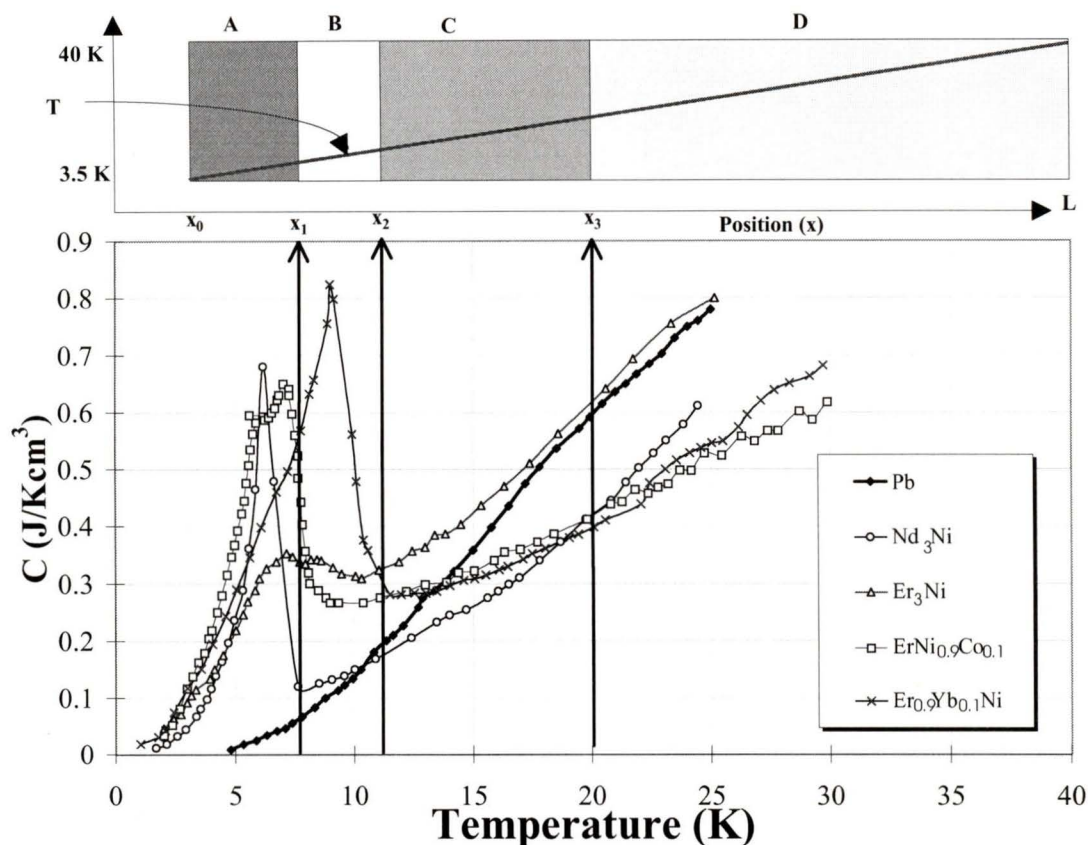


**Figure 5-4: An optimized hybrid regenerator using four layers of different materials (A =  $\text{ErNi}_{0.9}\text{Co}_{0.1}$ , B =  $\text{Er}_{0.9}\text{Yb}_{0.1}\text{Ni}$ , C =  $\text{Er}_3\text{Ni}$ , D = Pb). The temperature profile is assumed to be linear.**

Although different materials could be used at the second stage (i.e., materials other than the RE/TM alloys discussed thus far), it is recommended that future efforts be concentrated on the other possible improvements to the current GM cryocooler.

### 5.2.4 Regenerator Size

In addition to changing the regenerator materials, the volumetric thermal mass in the second-stage regenerator could be increased by simply altering its physical dimensions (i.e., making it bigger). There are two possible ways to accomplish this: using a regenerator with a larger diameter and the same length, or using a longer regenerator with the same diameter as the current stainless steel housing. In either case, the second stage

container and housing will have to be modified. These modifications, however, could be more than justified by the ability to obtain larger cooling powers. The selection of a given aspect ratio for the new regenerator will depend on several factors (pressure drop, longitudinal thermal conductivity of the new stainless steel housing and regenerator bed, etc.). The required analysis for an optimal design could be undertaken in future work. The work included in this thesis seems to indicate that these modifications are necessary to obtain refrigeration powers  $\geq 500$  mW at 4.2 K.

### **5.2.5 Increased Expansion Volume(s)**

Another possible modification to the present configuration could be the enlargement of the expansion volume at the second stage. This could be accomplished by increasing the diameter at the second stage. Another possibility consists of increasing the reciprocating travel of the regenerator/displacer assembly. In this case, both expansion volumes at the first and second stages will be altered.

### **5.2.6 Cycle Frequency**

The cycle frequencies investigated in this work ranged from 0.9 to 2.4 Hz. Lower frequencies could be explored by controlling the stepping motor in the cold head with an external motor controller. A compatible, computerized motor controller has already been purchased but was not used in this work. Although this device operates on PC-based software, its functions can be easily controlled from the current DAQ system in the Cfs laboratory. LabView® 3.1.1 offers extensive serial (RS232) emulation protocols that can be used to issue the required commands to the motor controller.

The decision to use this additional control device will depend on the results obtained by implementing the other modifications. The results in this work showed that the minimum, no-load temperature in the GM cryocooler reaches a minimum value at an operating frequency of 1.2 Hz and then starts to increase at lower frequencies. Whether or not this trend continues below 0.9 Hz is still undetermined. However, it may be advisable to improve the performance of the current GM unit without adding any additional

components (i.e., it will be better to concentrate on the dimensions and geometry of the second stage instead of modifying motor-dependent parameters). In this manner the total cost of a modified GM cryocooler could be minimized (the motor controlled represents 5 to 7% of the total cost for the current unit).

### **5.2.7 Valve Timing**

The possible effects of different valve timing schemes were not investigated in this work. Because valve timing is closely coupled to the reciprocating motion of the displacer, changing this parameter will involve modifications to the drive motor assembly. This could consist of adding spacers to the sliding ceramic valve, or changing the geometry of the existing gas distribution orifices. Once again, it is recommended that this parameter be explored after the other possible modifications have been investigated.

## **5.3 Implementation of a GM Cryocooler in the Overall AMRL Project**

The AMRL currently under development at the University of Victoria is a very complex device that requires the concurrent operation of various interrelated subsystems. The work presented in this thesis was focused on the cryogenic refrigeration unit used to cool the superconducting magnets and associated thermal shields. This subsystem is indispensable for the proper operation of the overall liquefier. The modifications described in Chapter 4 make it possible to place the GM cryocooler directly into the experimental chamber for the AMRL. The dimensions of the current GM cryocooler have been taken into consideration in the design of this chamber. Some of the additional modifications described in previous sections (e.g., Sections 6.2.4 and 6.2.5) would require changing the dimensions of the second-stage regenerator housing. These changes would affect the associated dimensions in the AMRL experimental chamber.

## References

---

- 1 Bos, E., M. T. Vu, A. Leven, and R.A. Bulatao, World Population Projections 1992-1993, John Hopkins University Press, Baltimore, USA, 1992.
- 2 World Energy Council (WEC), Energy for Tomorrow's World —The Realities, the Real Options and the Agenda for Achievements, Kogan Page, London, UK (1993).
- 3 United Nations (UN), Long-Range World Population Projections: Two Centuries of Population Growth 1950-2050, Department of International Economic and Social Affairs, United Nations, New York, USA (1992).
- 4 Lutz, W. (Ed), The Future Population of the World: What Can We Assume Today?, Earthscan, London, UK (1994).
- 5 International Institute for Applied Systems Analysis (IIASA), Global Energy Perspectives to 2050 and Beyond, World Energy Council, London, UK (1995).
- 6 David S. Scott, "Turning Out the Lights," *International Journal of Hydrogen Energy*, 19, p. 3 (1994).
- 7 Hans-Holger Rogner, Fuel Cells, Energy System Evolution and Electric Utilities, Institute for Integrated Energy Systems, University of Victoria, Canada (1993).
- 8 David S. Scott, Interpreting the Architecture of the Energy System, Institute for Integrated Energy Systems, University of Victoria, Canada (1995).
- 9 N. Georgescu-Roegen, The Entropy Law and the Economic Process, Harvard, University Press, USA (1971).
- 10 Department of Energy (DOE)/Energy Information Administration, Alternatives to Traditional Transportation Fuels, US Department of Energy, USA (1995).
- 11 Institute for Integrated Energy Systems, Mission Statement Brochure, University of Victoria, Canada (1995).
- 12 Smil, Energy in World History, Westview Press., Boulder, USA (1994).
- 13 Grübler, A. and N. Nkicenkovic, "The Dynamic Evolution of Methane Technologies". In The Methane Age, ed. T. H. Lee, H. R. Linden, D. A. Dreyfus, T. Vasko, pp. 34-44. Dordrecht, Boston, London: Kuwer Academic Publishers (1988).

- 
- 14 David S. Scott, "Interpreting the Architecture of the Energy System", Proceedings of the 16<sup>th</sup> World Energy Council 16<sup>th</sup> Congress, Tokyo, Japan (1995).
  - 15 Scott, D. S. And Hafele, W. "The Coming Hydrogen Age: Preventing World Climatic Disruption", *International Journal of Hydrogen Energy*, 15, (1990).
  - 16 Marchetti, C. And Nakicenovic, N. The Dynamics of Energy Systems and the Logistic Substitution Model, RR-79-13, International Institute for Applied Systems Analysis (1979).
  - 17 David S. Scott, Hydrogen In the Evolving Energy System, Institute for Integrated Energy Systems, University of Victoria, Canada (1992).
  - 18 Michael E. Himmel, John O. Baker, and Ralph P. Overend (Editors), "Enzymatic Conversion of Biomass for Fuels Production", ACS Symposium Series 566, Denver, Colorado, U.S.A (1993).
  - 19 Barclay, J. A., "Cryofuels, now and in the future", Plenary Session, Cryogenic Engineering Conference, Columbus, OH, (July 17-21 1995).
  - 20 Automotive Fleet Research Department, Automotive Fleet 1993 Fact Book, Bobit Publishing Company, Redondo Beach, CA, USA (1993).
  - 21 Energy Information Administration, Alternatives to Traditional Transportation Fuels: An Overview, DOE/EIA-0585/O, U.S. Department of Energy (1994).
  - 22 Energy Information Administration (EIA), Alternatives to Traditional Transportation Fuels 1993, DOE/EIA-0585 (93), U.S. Department of Energy (1995).
  - 23 Strnisa, F. , W. BeVier, R. Coleman and S. Gauthier, "Adsorbent Storage of Natural Gas", Proceeding os the Windsor LNG Workshop, Windsor, ON, Canada (1989).
  - 24 Richard O. Geiss, William M. Burkmyre, and james W. Lanigan, "Technical Highlights of the Dodge Compressed Natural Gas Ram Van/Wagon," Society of Automotive Engineers (SAE), Paper No. 921551, pp. 14-15, Warrendale, PA, USA (1992).
  - 25 F. Burke, "Battery Availability for Near-Term (1998) Electric Vehicles", Society for Automotive Engineers (SAE), Paper No. 911914, Warrendale, PA, USA (1991).

- 
- 26 Ballard Group, "Zero Emission Fuel Cell Engine", Ballard Power Systems, Information Brochure, Vancouver, B.C., Canada (1995).
  - 27 International Energy Agency, Energy Balances of OECD Countries 1992-1993, OECD/IEA, Paris (1995).
  - 28 J.E. Sinor Consultants Inc., The Clean Fuels Report, 7 No. 3, Niwot, Colorado, USA (June 1995).
  - 29 Energy Management Branch, Cleaner Fuels for Cleaner Air, Technical Report, Ministry of Energy, Mines and Petroleum Resources, Victoria, B.C., Canada (1994).
  - 30 Ministry of Energy, Mines and Petroleum Resources, The Role of Alternative Transportation Fuels in B.C. Cleaner Fuels for Cleaner Air, Technical Report, Victoria, B.C., Canada (1994).
  - 31 The Senate of Canada, Bill S-7, First Session, Thirty-fifth Parliament 42-43-44, Elizabeth II, Ottawa, Canada (1994-1995).
  - 32 Julio Lasky, "Logistics Technology in México", Canadian Customs Guide, Livingston International Inc. (1995).
  - 33 LNG Express, "Mexico City, Coming Up for Air", 2, pp.1-3, Zeus Development Corporation, 3827 Villanova, Houston, TX 77005-3639 USA (1992).
  - 34 Mr. Ricardo Solorio, Instituto Mexicano del Transporte, Personal communication (data correspond to 1992 totals)
  - 35 Kenneth Hoffman and José Cano, México Energy Update, presented to the Texas Mid-Continent Oil & Gas Association Legal Committee, Hoffman Stephens, P. C., (1995).
  - 36 Barclay, J.A., Corless A.J., "Cost Analysis of a Magnetic Liquefier in a Fleet-Size Cryofuel Refuelling System", Solar Energy Technology, SED, 13, pp. 43-50, American Society of Mechanical Engineers (1992).
  - 37 Barclay, J. A., Goudie, D. W., Reid, C. E. J., "Comparison of Natural Gas Liquefiers for Fleet-size LNG/CNG Refuelling Systems", Windsor Workshop on Alternate Fuels, Toronto, ON, June 12-14 (1995).

- 
- 38 Powars, C., Luscher, D., Moyer, C., Browning, L., A White Paper: Preliminary Assesment of LNG Vehicle Technology, Economics, and Safety Issues (Revision 1), GRI-91/0347, Gas research Institute (1991).
- 39 Lee T. H., Linden, H.R., Dreyfus D.A., Vasko, T., The Methane Age, Kugler Academic Publishers and International Institute for Applied Systems Analysis (1988).
- 40 Rogner, H-H., "Natural Gas as the Fuel for the Future", Annual review of Energy, 14, pp. 47-73 (1989).
- 41 Heer, C.V., C. B. Barnes, J. G. Daunt, "The Design and Operation of a Magnetic Refrigerator for Maintaining Temperatures below 1K", Review of Scientific Instruments, 25, pp. 1088-1098 (1954).
- 42 Barclay, J. A., O. Moze, I. Paterson, "A Reciprocating Magnetic Refrigerator for 2-4K Operation: Initial Results", Journal of Applied Physics, 50, pp. 5870-5877 (1979).
- 43 Spearing, I.G., "A Numerical Model for a Rotary Active Magnetic Regenerative Refrigerator", Master of Applied Science Thesis, University of Victoria, Canada (1995).
- 44 J. L. Hall, C. E. Reid, I. G. Spearing and J. A. Barclay, "Thermodynamic Considerations for the Design of Active Magnetic Regenerative Refrigerators", Cryogenic Engineering Conference, Columbus, Ohio, USA (July 17-21, 1995).
- 45 Weiss, P., A. Piccard, "On a New Magnetocaloric Effect", C.R. Academy of Sciences, 166, p. 352, Paris, France (1918).
- 46 P. Debye, Ann.Physick, 81, p. 1154 (1926).
- 47 P. J. Giauque, Americam Chemical Society, 49, p. 1870 (1927).
- 48 Giauque, W.F., D.P. MacDougall, "Attainment of Temperature Below 1 Degree Absolute by Demagnetization of  $Gd_2(SO_4)_3 \cdot 8H_2O$ ", Physics Review, Vol. 43, p. 768 (1933).
- 49 Geunes, J. R., "A Study of a New Magnetic Refrigeration Cycle", Thesis, University of Leiden, The Netherlands (1966).
- 50 Brown, G. V., "Magnetic Heat Pumping Near Room Temperature", Journal of Applied Physics, 47, pp. 3673-3680, (1976).

- 
- 51 Steyert, W. A., "Magnetic Refrigeration Development, September 1 - November 30, 1977", Los Alamos National Laboratory Progress report, No. LA-7165-PR, (1978).
- 52 Barclay, J.A., J.C. Bronson, W.A. Steyert, "Magnetic Refrigeration Development, June 1 - August 31, 1979", Los Alamos National Laboratory Progress report, No. LA-8066-PR (1979).
- 53 Barclay J. A., "Magnetic refrigeration: A Review of a Developing Technology", *Advances in Cryogenic Engineering*, Plenum Press, New York, Vol. 33, pp. 719-731, (1988).
- 54 Barclay, J. A., "A Review of Magnetic Heat Pump Technology", *International Cryogenic Conference*, Reno, NV, August 12-17 (1990).
- 55 Lacaze, A. F., "Magnetic Refrigeration - An Overview", *proceedings of the International Institute of Refrigeration Conference*, pp. 99-110, Prague, Czechoslovakia, (1986).
- 56 Zhang, L., Sherif, S. A., Veziroglu, T.N., Sheffield, J. W., "Performance Analysis of Reciprocating magnetic Liquefiers", *International Journal of Hydrogen Energy*, 19, pp. 945-956, Elsevier Science Ltd. (1994).
- 57 Serlemistos, A. T., B. A. Warner, S. Castles, S. R. Breon, M. San Sebastian, T. Hait., "Adiabatic demagnetization refrigerator for space use", *Proceedings of the 8<sup>th</sup> International Cryogenic Engineering Conference* (1989).
- 58 Leyarovsky, E., L. Leyarovska, Chr. Popov, "Techniques of the adiabatic experiments in high magnetic fields below 1K", *Proceedings of the 8<sup>th</sup> International Cryogenic Engineering Conference*, pp. 466-470, Geneva (1980).
- 59 Kittel, P., "Refrigeration below 1K in space", *Physics*, 108(B), pp. 1115-1118 (1981).
- 60 Yazawa, T., A. Sato, H. Ogiwara, J. Yamamoto, "Adiabatic demagnetization system for infrared detector", *Proceedings of the 12<sup>th</sup> International Cryogenic Engineering Conference*, pp. 621-625, Southampton, UK (1988).
- 61 A. J. DeGregoria, J. A. Barclay, P. J. Claybaker, S. R. Jaeger, S. F. Kral, R. A. Pax, J. R. Rowe, and C. B. Zimm, "Preliminary Design of a 100W 1.8K to 4.7K Regenerative Magnetic Refrigerator", *Proceeding of the Cryogenic engineering Conference*, Los Angeles, California, USA (1989).

- 
- 62 Barclay, J. A., "A 4K to 20K Rotational-Cooling Magnetic Refrigerator Capable of 1-mW to >1-W Operation", *Cryogenics*, Vol. 20, pp. 468-471 (1980).
- 63 Johnson, D. L., "Reciprocating magnetic refrigerator", *Proceedings of the 3<sup>rd</sup> NBS Cryocooler Conference*, pp. 33-41, Boulder Colorado, USA (1984).
- 64 Nakagome, H., N. Tanji, O. Horigami, H. Ogiwar, T. Numazawa, Y. Wantanabe, T. hasimoto, "The helium magnetic refrigerator I: development and experimental results", *Advances in Cryogenic Engineering*, Vol. 29, pp. 581-587, Plenum Press, New York (1984).
- 65 Steyfert, P., P. Bredy, G. Claudet, "Construction and testing of a magnetic refrigeration device for the temperature range of 5 to 15 K", *Proceedings of the 12<sup>th</sup> International Cryogenic Engineering Conference*, pp. 607-611, Southamton, UK (1988).
- 66 Barclay, J. A., "An analysis of magnetic refrigeration for air conditioning applications", Los Alamos National Laboratory, report LA-7950-MS (1979).
- 67 G. Patton, G. Green, J. Stevens, and J. Humphrey, "Magnetocaloric Refrigeration", David W. Taylor Naval Ship research and Development Center report DTNSRDC 87/032 (1987).
- 68 L. D. Kirol and M. W. Dacus, "Rotary Recuperative Magnetic Heat Pump", in *Advances in Cryogenic Engineering*, R. W. Fast Ed., Vol. 33, pp. 757-766, Plenum Press, New York, USA (1988).
- 69 David R. Lide, Editor in Chief, CRC Handbook of Chemistry and Physics, 74<sup>th</sup> Edition, pp. 4-114 - 4120, CRC Pres Inc., London, UK (1993-1994).
- 70 Barron, R. F., Cryogenic Systems, Monographs on Cryogenics 3, Second Edition, Oxford University Press, New York, USA (1985).
- 71 Kittel, C. Introduction to Solid State Physics, 6<sup>th</sup> edition, Wiley, New York, USA (1986).
- 72 Morrish, A. H., The Physical Principles of Magnetism, Wiley, New York, USA (1965).
- 73 Jiles, David, Introduction to Magnetism and Magnetic Materials, 1<sup>st</sup> edition, Chapman & Hall, New York, USA (1991).
- 74 Bouvier, M., Lethuillier, P. and Schmitt D., "Specific Heat in Some Gadolinium Compounds. I Experimental", *Physics Review B*, 43, pp. 13137-13144 (1990).

- 
- 75 J. L. Hall, C. E. Reid, I. G. Spearing and J. A. Barclay, "Thermodynamic Considerations for the Design of Active Magnetic Regenerative Refrigerators", Proceedings of the Cryogenic Engineering Conference, Columbus, OH, USA (July 17-21, 1995).
- 76 Kammerlingh Onnes, H. Akad. Van Wertenschappen, 14, p. 113, Amsterdam, The Netherlands (1911).
- 77 Wilson, M. N., Superconducting Magnets, Monographs on Cryogenics, Oxford University Press, New York (1983).
- 78 K. P. Jüngst, G. Ries, S. Förster, F. Graf, G. Obermaier, and W. Lehmann, "Magnet system for a superconducting magnetic separator", *Cryogenics*, 24, pp. 648-652 (November 1984).
- 79 Laskaris, E.T., Ackermann, R., Dorri, B., Gross, D., Herd, K., Minas, C., "A Cryogen-Free Open Superconducting magnet for Interventional MRI Applications", *IEEE Transactions on Applied Superconductivity*, 5, No. 2 (June 1995).
- 80 Dr. Jeffery Hall, Cryofuel Systems Group, University of Victoria, Personal communication (August 8, 1996).
- 81 Bednorz, J. G. and Muller A., *Z. Phys.*, B64, p. 189, (1986).
- 82 M. K. Wu et al., *Physics Review Letters*, 58, p. 908 (1987).
- 83 Hoenig, M. O., "Design Concepts for a Mechanically Refrigerated 13K Superconducting Magnet System", *IEEE Transactions on Magnetics*, MAG-19, No. 3, pp. 880-883 (May, 1983).
- 84 Furuyama, M., Yamamoto, H., Tanak, M., Kaneko, M., Matsubara, Y., Ogasawara, T., "Performance of a Nb<sub>3</sub>Sn Tape Magnet Cooled by Indirect Conduction Method", *Advances in Cryogenic Engineering*, 35, pp. 625-631, Plenum Press, New York, USA (1990).
- 85 Rowe, J. R., Hertel, J. A., Barclay, J. A., Cross, C. R., Trueblood, J. R., Hill, D. D., "Conductively Cooled Nb<sub>3</sub>Sn magnet System for a Magnetic Refrigerator", *IEEE Transactions on Magnetics*, 27, pp. 2377-2380 (1991).
- 86 van der Laan, M.T.G., Tax, R.B., ten Kate, H.HJ., van de Klundert, L.J.M., "The Cryogenic System of a Conduction Cooled 12 K Superconducting Magnet", *Cryogenics*, 30c, pp. 163-167 (1990).

- 
- 87 van der Laan, M.T.G., Tax, R.B., ten Kate, H.H.J., van de Klundert, L.J.M., "A 1T 0.33m Bore Superconducting magnet Operating with Cryocoolers at 12 K", IEEE Transactions on Magnetics, 28, pp. 633-636, (1992).
- 88 Hata, F., Sakubara, J., Chong, C.K., Yamada, Y., Hasebe, T., Ishibara, M., Watanabe, K., "A Conduction Cooled Superconducting Magnet Using High-Tc Oxide Current Leads", IEEE Transactions on Magnetics, MT-13, Proceedings of the 13<sup>th</sup> International Magnet Technology Conference, Victoria, Canada (September 20-24, 1993).
- 89 Cowey, L., Cetnik, P., Timms, K., Daniels, P., Mellors, J., McDougall, I., "Cryogen Free Nb<sub>3</sub>Sn Magnet, Operated at 9.5 K with High-T<sub>c</sub> BiSrCaCuO (2122) Current Leads", IEEE Transactions on Applied Superconductivity, 5, (June 1995).
- 90 Herd, K.G., Laskaris, E.T., Thompson, P. S., "A Dual Refrigerator Assembly for Cryogen Free Superconducting Magnet Applications", IEEE Transactions on Applied Superconductivity, 5, No. 2 (June 1995).
- 91 Kirk, A., "On the Mechanical Production of Cold", Proceedings of the Institute for Civil Engineering, 37, pp. 244-3315, London, UK (1874).
- 92 K. Timmerhaus and T. Flynn, Cryogenic Process Engineering, Plenum press, New York, USA (1989).
- 93 F. W. Schmidt and A. J., Wilmott, Thermal Energy Storage and Regeneration, Hemisphere, Washington, USA (1981).
- 94 Walker, G., Cryocoolers Part 1: Fundamentals, Plenum Press, New York, USA (1983).
- 95 Barclay, J. A., "Active and passive magnetic regenerators in gas/magnetic refrigerators", Journal of Alloys and Compounds, 207, pp. 355-361 (1994).
- 96 McMahan, H. O., and Gifford, W. E., "A New Low Temperature Gas Expansion Cycle - Part I.", Advances in Cryogenic Engineering, 5, pp. 354-366 (1960).
- 97 McMahan, H. O., and Gifford, W. E., "A New Low Temperature Gas Expansion Cycle — Part II.", Advances in Cryogenic Engineering, 5, pp. 368-372, Plenum Press, New York, USA (1960).

- 
- 98 Riedy, R. C., "Low Temperature, High Performance G-M Refrigerator", *Cryogenics*, 33, pp. 653-658 (1993).
- 99 Buschow, K. H. J., Olijhoek, J. F and Miedema, A. R., "Extremely large Heat capacities between 4 and 10 K", *Cryogenics*, 5, pp. 261-264 (1975).
- 100 T. Hashimoto, R. Li and K. Matsumoto, "Recent Progress in the Magnetic Materials for Regenerator in the Range from 4.2 K to 20 K", *Proceedings of the International Cryogenic Materials Conference, China* (1988).
- 101 Hideto Yoshimura, Masashi Nagao, Takashi Inaguchi, Tadatoshi Yamada and Masatami Iwamoto, "Helium liquefaction by a Gifford-McMahon cycle cryogenic refrigerator", *Review of Scientific Instruments*, 60, No. 11 (November, 1989).
- 102 Sahashi, M., Tokai, Y., Kuriyama, T., Nakagome, H., Li, R., Ogawa, M. and Hashimoto, T., "New Magnetic Material R3T System with Extremely Large Heat capacities Used as Heat Regenerators", *Advances in Cryogenic Engineering*, 35, pp. 1175-1182, Plenum Press, New York, USA (1990).
- 103 Kuriyama, T., Hakamada, R., Nakagome, H., Tokai, Y., Sahashi, M., Li, R., Yoshida, O., Matsumoto, K. and Hashimoto, T., "High Efficient Two-stage GM Refrigerator with Magnetic Material in the Liquid Helium Temperature Region", *Advances in Cryogenic Engineering*, 35, pp. 1261-1269 Plenum Press, New York, USA (1990).
- 104 R. Li, A. Onishi, T. Satoh, Y. Kanazawa, "Influence of Valve Open Timing and Interval on Performance of 4 K Gifford-McMahon Cycle Cryocooler", *Proceedings of the 1995 Cryogenic Engineering Conference, Columbus, OH* (July 17-21, 1995).
- 105 T. Kuriyama, Y. Ohtani, M. Takahashi, H. Nakagome, H. Nitta, T. Tsukagoshi, A. Yoshida, and T. hashimoto, "Optimization of Operating Parameters for a 4 K-GM Refrigerator", *Proceedings of the 1995 Cryogenic Engineering Conference, Columbus, OH* (July 17-21, 1995)
- 106 S. Masuyama, H. Yamamotoa and Y. Matsubara, "A NbTi Split Magnet Directly Cooled by a Cryocooler", *IEEE Transactions on Applied Superconductivity*, 3, No. 1 (March, 1993).
- 107 Onishi, A., Li, R., Satoh, T., Kanawaza, H., Aikawa, S., Hashimoto, T., "A 4 K GM Cryocooler with Hybrid Regenerator of Magnetic Materials", *Proceedings of the 7<sup>th</sup> International Cryocooler Conference, Santa Fe, NM* (November 17-19, 1992).

- 
- 108 Yabuki, M., Nitta, H., Hashimoto, T., Kuriyama, T., Takahashi, M., Nakagome, H., "Magnetic Regenerator material in the Liquid Helium Temperature Range — Recent Advances and its possibility", Proceedings of the 4<sup>th</sup> Joint Sino-Japanese Seminar on Cryocoolers and Concerned Topics", Beijing, P.R. China (October 19-23, 1993).
- 109 Kuriyama, T., Takahashi, M., Nakagome, H., Hashimoto, H., Nitta, H., Yabuki, M., "Development of 1Watt Class 4 K GM Refrigerator with Magnetic Materials", Advances in Cryogenic Engineering, 39b, pp. 1335-1342, Plenum Press, New York, USA (1994).
- 110 Tsukagoshi, T., Nitta, H., Yoshida, A., Matsumoto, K., Hashimoto, T., Kuriyama, T., Takahashi, M., Ohtani, Y., Nakagome, H., "Refrigeration Capacity of a GM Refrigerator with Magnetic Regenerator Materials", Cryogenic Engineering Conference, Columbus, OH, USA (July 17-21, 1995).
- 111 Satoh, T., Onishi, A., Li, R., Asami, H., Kanazawa, Y., "Development of 1.5W 4K GM Cryocooler with Magnetic Regenerator Material", Cryogenic Engineering Conference, Columbus, OH, USA (July 17-21, 1995).
- 112 I. Takashi, N. Masashi, N. Kouki and Y. Hideto, "Development of 2W Class 4 K Gifford-McMahon Cycle Cryocooler" (to be published).
- 113 K. A. Gschneidner, Jr., V. K. Pecharsky and M. Gailloux, "New Ternary lanthanide Regenerator Materials for the Low Temperature Stage of a Gifford-McMahon (G-M) Cryocooler", Paper presented at the 8<sup>th</sup> International Cryocooler Conference,vail, Colorado, USA (June 28-30, 1994).
- 114 Chafe, J., Green, G., Reidy, R. C., "Neodymium Regenerator Test Results in a Standard Gifford-McMahon Refrigerator", Proceedings of the 7<sup>th</sup> International Cryocooler conference, Santa Fe, NM, USA (November 17-19, 1992).
- 115 J. N. Chafe, G. F., Gree, and J. B., Hnedricks, "A Neodymium Plate Regenerator for Low Temperature Gifford-McMahon Cycle refrigerators", to be published.
- 116 Baldini, A., "Regenerator effectiveness of a two-stage Gifford-McMahon cryogenerator: experimental results", Cryogenics, 31, pp. 791-795 (1991)
- 117 Prices quoted by Mr. David Zhang, CRE Products Inc., 110-41, 63<sup>rd</sup> Avenue, Forest Hills, NY 11375, USA (1996).
- 118 Price for Nd obtained from Rhône-Poulenc, Inc., Rare Earths, One Corporate Drive. Box 881, Shelton, CT 05484, USA (1995).

- 
- 119 R. A. Ackermann, "The Characterization of Several High Specific Heat Regenerator Materials in a Gifford McMahon Refrigerator", *Advances in Cryogenic Engineering*, 37B, p. 981, Plenum Press, New York, USA (1992).
- 120 J. N. Chafe, G. Green, and P. Gifford, "The Low Temperature Performance of a Three Stage Gifford-Mcmahon Cryocooler", *Advances in Cryogenic Engineering*, 37B, p. 1011, Plenum Press, New York, USA (1992).
- 121 L. F. Aprigliano, G. Green, J. Chafe, L. O'Connor, F. Biancanello and S. Ridder, "Development of Neodymium and Er<sub>3</sub>Ni Regenerator Materials", *Advances in Cryogenic Engineering*, 37B, p. 1003, Plenum Press, New York, USA (1992).
- 122 E. M. Ludeman and C. B. Zimm, "Production of Spherical Powders of Rare earth Intermetallic Compunds for Use in Cryocooler Regenerators", *Proceedings of the Cryogenic Engineering Conference*, Huntsville, AL, USA (1991).
- 123 Lee, Peter W. (ed.), *Powder Metallurgy*, American Society for Metals, Metals Handbook Desk Edition, pp. 25.1-25.24 (1985).
- 124 Reid, C. E. J., Personal communication, Department of Mechanical Engineering, University of Victoria, Victoria, BC, Canada (September 1995).
- 125 M. G. Osborne, I. E. Anderson, K. A. Gschneidner, Jr., M. J. Gailloux, and T. W. Ellis, "Centrifugal Atomization of Neodymium and Er<sub>3</sub>Ni Regenerator Paarticulate", *Advances in Cryogenic Engineering*, 39, Plenum Press, New York, USA (1994).
- 126 Barron, R. F., *Cryogenic Systems*, Monographs on Cryogenics, 2<sup>nd</sup> Edition, Oxford University Press, New York, USA (1985).
- 127 Radebaugh, R. "Thermal Conductance of Indium Solder Joints at Low Temperature", *Review of Scientific Instruments*, 48, No. 1 (1977).
- 128 Deutsch, M., "Thermal Conductance in Screw-Fastened Joints at Helium Temperatures", *Cryogenics*, 19, pp. 273-274 (1979).
- 129 Salerno, L. J., Kittel, P., Spivak, A. L., "Thermal Conductance of Pressed Metallic Contacts Augmented with Indium Foil or Apiezon Grease at Liquid helium Temperatures", *Cryogenics*, 34, pp. 649-654 (1994).
- 130 Available from King Seely Company, Winchester, Massachusetts, USA.

- 
- 131 Garthright, T. R., Reeve, P. A., "Effect of Multilayer Insulation on Radiation Heat Transfer at Cryogenic Temperatures", *IEEE Transactions on Magnetics*, 24, pp. 1105-1108 (1988).
- 132 Vliet, G. C. and Coston, R. M., "Thermal Energy Transport Parallel to the laminations in Multilayer Insulations", *Advances in Cryogenic Engineering*, 13, pp. 671-679, (1968).
- 133 Scurlock, R. G. and Saull, B., "Development of Multilayer Insulations With Thermal Conductivities Below  $0.1\mu\text{W}/\text{cm}\cdot\text{K}$ ", *Cryogenics*, 16, p. 303 (1976).
- 134 Apple Computer Inc., 1 Infinite Loop, Cupertino, CA, 95014-2084, USA.
- 135 National Instruments Inc., 6504 Bridge Point Parkway, Austin, TX, 78730-5039, USA.
- 136 Klaus D. Timmerhaus and Thomas M. Flynn, Cryogenic Process Engineering, The International Cryogenics Monograph Series, K. D. Timmerhaus, Alan F. Clark, and Carlo Rizzuto, General Editors, Plenum Press, New York, USA (1989).
- 137 Available from LABTRONICS Inc., 95 Crimea St., Unit 2C, Gueph, ON, N1H 2Y6, Canada.
- 138 Scientific Instruments, Inc., "Calibration Table for Ruthenium Oxide Resistance Thermometer Model R0104GG1, Serial # 542", Job # 408500, Reference # 930326RI.P8 (1993).
- 139 Lake Shore Cryotronics, Inc., "Measurement and Control Technologies", Product Catalog, p. 35, USA (1994).
- 140 Scientific Instruments, Inc., 4400 West Tiffany Drive, Mangonia park, West Palm Beach, Florida, 33407, USA.
- 141 LakeShore Cryotronics Inc., 64 East Walnut St., Westerville, Ohio 43081-2399, USA.
- 142 Kurt J. Lesker Company, 1515 Worthington Avenue, Clairton, Pennsylvania, 15025, USA.
- 143 Rosemount Inc., Measurement Division, 8200 Market Boulevard, Chanhassen, MN 55317, USA.
- 144 Balzers, 8 Sagamore Park Road, Hudson, NH 03051, USA.

- 
- 145 CVI Inc., P. O. Box 2138, Columbus, OH 43216, USA.
- 146 Available from Laird Plastics, West Palm Beach, FL 33401, USA.
- 147 Available from TRI Research, 2303 Wycliff St., #2W, St. Paul, MN 55114 USA.
- 148 Myron Calkins, PhD., Balzers, 8 Sagamore Park Road, Hudson, NH 03051, USA, Personal communication (November 28, 1994).
- 149 Available from Structural Dynamics Research Corporation (SDRC), 2000 Eastman Drive, Milford, Ohio 45150, USA.
- 150 Cryofuel Systems Group, Technical Software Library, University of Victoria, Victoria, BC, Canada (1996).
- 151 Available from Emerson & Cumming Inc., 77 Dragon Court, Woburn, MA 01888, USA.
- 152 Available from CLAD Metal Industries, 40 Edison Av., Oakland, NJ 07436, USA.
- 153 Kaydon Ring and Seal, Inc., PO Box 626, Baltimore, MD, 21203, USA.
- 154 Kaye, Bruce, Personal Communication, Esquimalt Defence Research Detachment (EDRD), CFB Squimalt, Bldg. 199, FMO Victoria, B. C., Canada, (February 27, 1996).
- 155 Emerson & Cumming™, Stycast® 1266, Technical Bulletin # 7-2-26C, Emerson & Cumming™, USA (1995).
- 156 S. R. Elliot, Physics of Amorphous Materials, Longman, pp. 350-351 (1981).
- 157 R. Zallen, The Physics of Amorphous Solids, John Wiley & Sons, Inc., pp. 274-280 (1983).
- 158 R. Hasegawa, Glassy Metals: Magnetic, Chemical and Structural Properties, CRC Press, pp. 235-259 (1983).
- 159 Quantum Design, 11578 Sorrento Valley Road, San Diego, CA, 92121-1311, USA.
- 160 Oxford Instruments, 130A Baker Avenue, Concord MA, 01742 USA.

- 
- 161 Mr. Ian McIntyre, Personal Communication, Technical Support Engineer, Research Instruments Group, Magnet Sales Division, Oxford Instruments KK, 1-11-11, Kudankita, Chiyoda-Ku, Tokyo 102, Japan (August 1996).
- 162 P. McKenzie, I. McIntyre and D. Sheperd, "Design of a Heat Capacity Insert", Fourth-year Design Project Report, Presented to the Cryofuel Systems Group, University of Victoria, Canada (August 1995) .
- 163 E. Gmelin, "Modern Low-Temperature Calorimetry", *Thermochimica Acta*, 29, pp. 1-39 (1979).
- 164 R. A. Robie and B. S. Hemmingway, "Calorimeters for Heat of Solution and Low-Temperature Heat Capacity Measurements", Geological Survey, Professional Paper 755, United States Government Printing Office, Washington, USA (1972).
- 165 J. P. McCullough and D. W. Scott, eds., Experimental Thermodynamics Volume I, pp.146-157, 272-274, Butterworth & Co., London, UK (1968).
- 166 G. Bednardz, B. Millier and M. A. White, "High-Resolution, High-Sensitivity AC Calorimeter", *Review of Scientific Instruments*, 63, pp. 3944-3952 (1992).
- 167 Scientific Instruments Inc., "Model Ro-600 Ruthenium Oxide Sensors", Application Note 08/94 RO600, USA (1994).
- 168 LakeShore® Cryotronics Inc., "A Comparison of Physical Property and Performance Characteristics of Lake Shore Cernox Resistance Temperature Sensors with Commercially Available Thick Film Resistors", Application Note # 8/93 MILSC, USA (1993).
- 169 Dr. Joseph D. Walters, Naval Surface Warfare Centre, Annapolis Detachment, Code 812, Electrical Machinery Technology Branch, Annapolis, MD 21402-5067, USA, Personal communication, May 14 1996.
- 170 Bal Seal Engineering Company, Inc., 620 West Warner Avenue, Santa Ana, CA, 92707-3398, Tel: (714) 557-5192, Fax: (714) 241 0185 (USA).

## Appendix A

### The Magnetocaloric Effect (MCE)

The fundamental principle behind the MCE is associated with a change in the magnetic entropy of ordinary matter in the presence of an external field. In the case of solids, it is possible to simplify the analysis by neglecting pressure and volume effects and defining a thermodynamic system whose boundaries coincide with the volume occupied by the solid. The application of a magnetic field will result in a net torque on the individual atomic magnetic moments. This external force will have an effect on the thermo-mechanical properties of the solid. To account for this extra effect, it is necessary to include a magnetic work term in the equation for the internal energy equation of the system. In differential form, this equation can be written as:

$$dU = TdS - PdV + \sum \mu_i dN_i + \mu_o V_o HdM$$

**Equation A-1**

If the physical volume and molar quantities are kept constant, Equation A-1 becomes:

$$dU = TdS + \mu_o V_o HdM$$

**Equation A-2**

which can be considered as the first step in any thermodynamic description of magnetic solids.

The total entropy of a magnetic solid can be expressed as

$$S = \int \frac{C(T, H)}{T} dT$$

**Equation A-3**

The heat capacity at constant pressure,  $C$ , is a function of both temperature and field strength, and it consists of electronic  $C_E$ , lattice or phonon  $C_L$ , nuclear  $C_N$ , and magnetic  $C_H$  contributions:

$$C = C_E + C_L + C_N + C_H + \delta C$$

**Equation A-4**

The last factor,  $\delta C$ , is a correction for thermal expansion and is only important for measurements over a large temperature range. The nuclear contribution, on the other hand, is only important at very low temperatures where the effects of the other components are negligible. Ignoring these two components, the total entropy can be expressed as the sum of three separate values:

$$S = S_{lattice} + S_{electronic} + S_{magnetic}$$

**Equation A-5**

Under adiabatic conditions, the individual values on the right hand side of Equation A-5 may vary, but the total entropy must remain constant.

When an external field is applied, the individual magnetic moments in the solid tend to align in a direction parallel to the direction of the field. This configuration represents a state whose magnetic entropy is lower than that associated with a random distribution of magnetic moments. Because the total entropy must remain constant, this decrease in  $S_{magnetic}$  must be compensated by an increase in  $S_{lattice} + S_{electronic}$ . To quantify this redistribution, the total entropy can be expressed as a function of two independent variables,  $H$  and  $T$  :

$$S = S(H, T)$$

**Equation A-6**

Consequently, the change in entropy can be expressed as:

$$dS = \left( \frac{\partial S}{\partial T} \right)_H dT + \left( \frac{\partial S}{\partial H} \right)_T dH$$

**Equation A-7**

Equation A-7 is especially convenient because magnetic cycles usually include isothermal, isentropic and/or isofield processes. In addition, the magnetization of solids is usually measured as a function of H and T. After some manipulation, Equation A-7 can be rewritten as:

$$dS = \left( \frac{C_H}{T} \right) dT + \mu_0 V_M \left( \frac{\partial M}{\partial T} \right)_H dH$$

**Equation A-8**

Under adiabatic conditions ( $dS=0$ ), this equation can be further rearranged to yield:

$$dT_{ad} = - \left( \frac{T}{C_H} \right) \mu_0 V_m \left( \frac{\partial M}{\partial T} \right)_H dH$$

**Equation A-9**

The calculation of the corresponding integrals is difficult and must include the temperature dependence of  $C_H$  and  $\partial M/\partial T$ . For the particular case when neither of these properties is a function of T:

$$\frac{dT_{ad}}{T} = - \left( \frac{1}{C_H} \right) \mu_0 V_m \left( \frac{\partial M}{\partial T} \right)_H dH$$

**Equation A-10**

Therefore:

$$\ln \left( \frac{T_f}{T_i} \right) = - \int_{H_i}^{H_f} \left( \frac{1}{C_H} \right) \mu_0 V_m \left( \frac{\partial M}{\partial T} \right)_H dH$$

**Equation A-11**

This implies that the adiabatic change in temperature,  $\Delta T_{ad}$ , is given by:

$$\Delta T_{ad} = T_f - T_i$$

**Equation A-12**

This change in temperature results from a change in the external magnetic field intensity under adiabatic conditions. (from  $H_i$  to  $H_f$ ). This change in temperature is the observable phenomenon associated with the magnetocaloric effect.

## Appendix B

### Magnetic Refrigeration Cycles

A full thermodynamic analysis of each of the possible magnetic refrigeration cycles is beyond the scope of this thesis, but some of the main concepts will be briefly described.

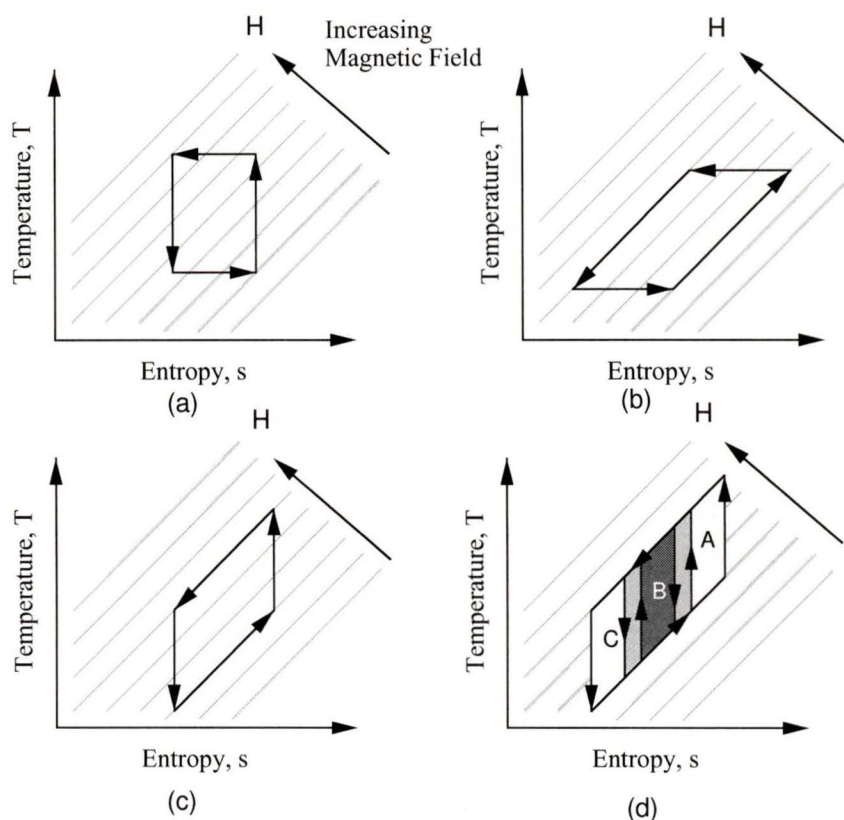


**Figure B-1: Schematic representation of idealized T-S diagrams for some common magnetic refrigeration cycles. Magnetic Carnot cycle (a), magnetic Ericsson cycle (b), magnetic Brayton cycle (c), and AMR cycle.**

The type of cycle implemented has repercussions on the temperature range accessible to a given MR device. Magnetic Carnot refrigerators [41] have been restricted to operate below 20K because the  $\Delta T_{ad}$  of most refrigerant materials is relatively small for practical values of magnetic field intensity (see Figure B-2). Devices based on Ericsson cycles are also used in low temperature applications [42].

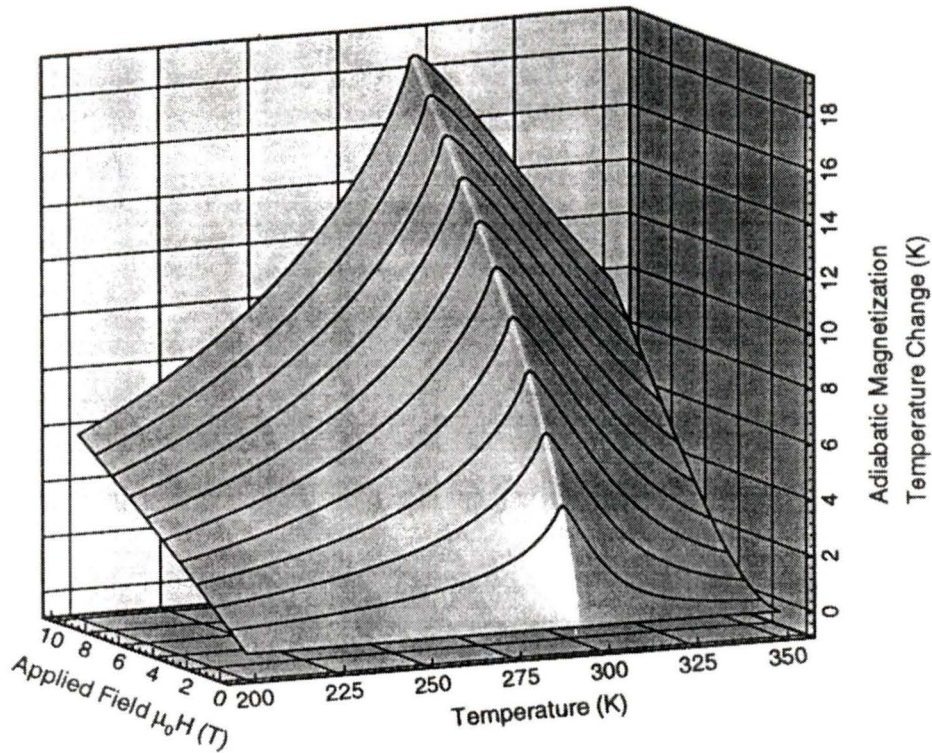


**Figure B-2: Adiabatic temperature change in gadolinium as a function of both temperature, and magnetic field strength [43].**

Regenerative and recuperative cycles are more appropriate for devices spanning temperature ranges that are larger than the  $\Delta T_{ad}$  of the refrigerant material. Brayton and AMR cycles require isentropic magnetization and demagnetization followed by isofield heat transfer processes. Although the magnetization requirements of these two cycles are similar, Hall et al. [44] have reported some fundamental differences in the associated thermodynamics. In their paper, the authors state that adjacent volume elements on the regenerator perform overlapping Brayton cycles as shown by the areas A, B, and C in Figure B-1(b).

Regardless of the thermodynamic cycle used, practical MR systems require very large magnetic fields. Currently, these fields can only be produced via low temperature superconducting magnets.

## Appendix C

### Magnetic Refrigeration Systems

The first experimental demonstration of the MCE was published by P. Weiss and A. Piccard in 1918 [44]. They used Ni near its Curie temperature to show that the adiabatic application and removal of a magnetic field resulted in a reversible temperature change.

The first application of this phenomenon for refrigeration purposes was proposed independently by P. Debye [45] and W. Giauque [46] in 1926 and 1927, respectively. They suggested that a single magnetic cycle could be used to cool paramagnetic samples from 2 K-3 K to much less than 1 K. In 1933 Giauque and D. MacDougal experimentally verified this method using  $\text{Gd}_2(\text{SO}_4)_3 \cdot 8\text{H}_2\text{O}$  to reach temperatures below 1 K [47].

Magnetic refrigeration remained restricted to applications below 1 K until 1966 when Van Geunes published his PhD. thesis on magnetic cycles between 20 K and 4 K [48]. Later developments included Brown's work in 1976 which made use of gadolinium near its Curie temperature in a room-temperature, regenerative refrigerator [49]. At about the same time, Steyert and Barclay, at Los Alamos National Laboratory, started working on magnetic refrigeration systems for room temperature applications [50][51].

Barclay [52][53] provides a very comprehensive review of MR technology up to 1990. Other excellent summaries include the work published by Lacaze [54] and Zhang et al. [55]. In most cases, the different MR systems have been classified according to the temperature range of interest. The temperature ranges reported in these publications are: 0.1-1.8 K, 1.8-4.2 K, 4.2-20 K, 20-77 K, 110-240 K and 270-300 K.

Applications in the lowest temperature range include the detection of very long wavelength infrared radiation, and the study of critical phenomena in quantum fluids [56][57][58][59]. The sensors used for this purposes need to be cooled to near 0.1K in order to obtain acceptable signal to noise ratios. Magnetic refrigeration can produce and maintain the desired low temperatures using liquid cryogenes or other gas-cycle schemes to provide the hot heat-sink temperature ( $\sim 1.8$  K).

The next temperature range (1.8-4.5K) is focused on the production of superfluid liquid helium. This cryogen is used to increase the heat transfer and current densities in large superconducting magnet systems<sup>1</sup>. Hybrid systems using magnetic and liquid cryogen refrigeration have been reported in the literature (the magnetic stage operated between 4.2 and 1.8 K). Some of these systems can be scaled from  $\sim 1$  W to 10 W or even larger cooling powers at 1.8 K [60].

The liquefaction temperatures of helium and hydrogen (at atmospheric pressure) are 4.2 K and 20.3 K, respectively. These values define the next temperature range of gas/magnetic or cryogen/magnetic hybrids. This range is primarily related to superconducting magnet systems operating at liquid helium temperatures. Current refrigeration systems in this range include liquid helium baths, two and three-stage Gifford-McMahon (GM) cryocoolers, and GM units coupled with a Joule-Thomson (JT) stage. Magnetic refrigeration systems operating in this range include rotating [61], reciprocating [62][63], and active regenerative devices [64].

The upper limit for the next temperature range (20-77K) is defined by the normal boiling point of nitrogen. The most important application in this temperature range consists of providing an upper stage for a 4 to 20 K or 1.5 to 20 K magnetic refrigerator. Other possible applications include the liquefaction of hydrogen, the production of slush

---

<sup>1</sup> As an example, NbTi wire shows a 40% increase in current density when cooled to 1.8 K (compared to the current density at 4.2K) [53]. This reduces the amount of wire required to produce a given field in a given geometry thereby lowering capital costs.

hydrogen (at 13.8 K), and the cooling of high temperature superconductors. Magnetic/LN<sub>2</sub> hybrids have also been proposed for large scale liquefaction of hydrogen.

The next temperature range (110-250 K) has received only limited attention. One important application in this case is related to the production of liquid natural gas via magnetic refrigeration. The device being developed by the Cfs group is based on an active magnetic regenerative refrigerator (AMRR) and it will be the first prototype of its kind in the world.

Applications for MR systems near room temperature include air conditioning [65], food preservation, and general cooling. Most of the reported devices use Gd as the working material [66][49][50] and rely on convective heat transfer between this material and a heat transfer fluid. The reported designs include systems with rotary [67] or reciprocating working materials, and systems with static working materials using magnets that can be periodically charged and discharged.

## Appendix D

### Heat Capacity of Solids at Low Temperatures

The lattice contribution to the heat capacity varies with temperature and can be satisfactorily approximated by the Debye model<sup>1</sup>:

$$C_L = \frac{9nRT}{\theta_D^3} \int_0^{\theta_D/T} \frac{x^4 e^x dx}{(e^x - 1)^2} = 3R \left( \frac{T}{\theta_D} \right)^3 D \left( \frac{T}{\theta_D} \right)$$

**Equation D-1**

The quantity  $\theta_D$  is called the Debye temperature and it is related to the total number of independent vibrational modes in the crystal lattice (i.e., it is a property of the material). In practice,  $\theta_D$  is not a constant and needs to be determined experimentally. Table D-1 shows the reported values for some metals and other elements [68][69].

**Table D-1: Debye characteristic temperatures of some selected elements (in Kelvins, at  $T = \theta_D/2$ ). The values for heavy rare-earths are lower than those found in transition metals.**

Ag	220	C <sup>a</sup>	2700	Mg	330	Pt	225	V	280
Al	385	Cu	310	Nd	150	Si	630	W	315
B	1220	K	100	Pb	85	Ti	355	Zn	250
Cr	430	Mn	420	Fe	460	Co	440	Ni	440
Gd	160	Tb	175	Dy	155	Ho	190 <sup>b</sup>	Er	165

<sup>a</sup> Graphite

<sup>b</sup> Obtained from elastic constant measurements [68].

At high temperatures ( $T > 3\theta_D$ ), the specific heat  $C_L$  approaches a constant value of  $3R$  (within 0.5%). At low temperatures ( $T < \theta_D/12$ ), the Debye function  $D(T/\theta_D)$  approaches

<sup>1</sup> Strictly speaking, this value corresponds to the heat capacity at constant volume,  $C_v$ . For solids and liquids at ordinary pressures, the difference between  $C_v$  and  $C_p$  is small.

a constant value, and the heat capacity varies as  $T^3$ . The resulting expression when  $n=1$ , is the following:

$$C_L = 3R \left( \frac{T}{\theta_D} \right)^3 D(0) = 3R \left( \frac{T}{\theta_D} \right)^3 \frac{4\pi^4}{5} = \frac{12\pi^4 T^3}{5\theta_D^3}$$

### Equation D-2

In metallic conductors, the electronic contribution to the heat capacity can be obtained using the quantum theory for a free-electron gas. The resulting expression for  $C_E$  is the following:

$$C_E = \frac{4\pi^4 a m_e M_m R^2 T}{h^2 N_o (3\pi^2 n_e)^{2/3}} = \gamma_e T$$

### Equation D-3

In other words, the electronic contribution to the heat capacity varies linearly with temperature. The actual values for  $\gamma_e$  tend to be very small (see Table D-2).

**Table D-2: Electronic heat capacity coefficients for selected elements**

Element	$\gamma_e$ (mJ mol <sup>-1</sup> K <sup>-2</sup> )
Ag	5.65
Al	50.4
Be	24.6
Cr	29.8
Cu	11.0
Dy	<sup>a</sup>
Er	10
Fe	89.9
Gd	4.48
Ho	6
Ni	124.0
Tb	3.71
Ti	74.1
Yb	3.30

<sup>a</sup> Heat capacity measurements have been reported, but the  $\gamma_e$  values are unreliable because the presence of impurities and/or because the electronic contribution could not be isolated from the magnetic contribution to the heat capacity [68].

## Appendix C

### Magnetic Refrigeration Systems

The first experimental demonstration of the MCE was published by P. Weiss and A. Piccard in 1918 [44]. They used Ni near its Curie temperature to show that the adiabatic application and removal of a magnetic field resulted in a reversible temperature change.

The first application of this phenomenon for refrigeration purposes was proposed independently by P. Debye [45] and W. Giauque [46] in 1926 and 1927, respectively. They suggested that a single magnetic cycle could be used to cool paramagnetic samples from 2 K-3 K to much less than 1 K. In 1933 Giauque and D. MacDougal experimentally verified this method using  $\text{Gd}_2(\text{SO}_4)_3 \cdot 8\text{H}_2\text{O}$  to reach temperatures below 1 K [47].

Magnetic refrigeration remained restricted to applications below 1 K until 1966 when Van Geunes published his PhD. thesis on magnetic cycles between 20 K and 4 K [48]. Later developments included Brown's work in 1976 which made use of gadolinium near its Curie temperature in a room-temperature, regenerative refrigerator [49]. At about the same time, Steyert and Barclay, at Los Alamos National Laboratory, started working on magnetic refrigeration systems for room temperature applications [50][51].

Barclay [52][53] provides a very comprehensive review of MR technology up to 1990. Other excellent summaries include the work published by Lacaze [54] and Zhang et al. [55]. In most cases, the different MR systems have been classified according to the temperature range of interest. The temperature ranges reported in these publications are: 0.1-1.8 K, 1.8-4.2 K, 4.2-20 K, 20-77 K, 110-240 K and 270-300 K.

Applications in the lowest temperature range include the detection of very long wavelength infrared radiation, and the study of critical phenomena in quantum fluids [56][57][58][59]. The sensors used for this purposes need to be cooled to near 0.1K in order to obtain acceptable signal to noise ratios. Magnetic refrigeration can produce and maintain the desired low temperatures using liquid cryogenes or other gas-cycle schemes to provide the hot heat-sink temperature ( $\sim 1.8$  K).

The next temperature range (1.8-4.5K) is focused on the production of superfluid liquid helium. This cryogen is used to increase the heat transfer and current densities in large superconducting magnet systems<sup>1</sup>. Hybrid systems using magnetic and liquid cryogen refrigeration have been reported in the literature (the magnetic stage operated between 4.2 and 1.8 K). Some of these systems can be scaled from  $\sim 1$  W to 10 W or even larger cooling powers at 1.8 K [60].

The liquefaction temperatures of helium and hydrogen (at atmospheric pressure) are 4.2 K and 20.3 K, respectively. These values define the next temperature range of gas/magnetic or cryogen/magnetic hybrids. This range is primarily related to superconducting magnet systems operating at liquid helium temperatures. Current refrigeration systems in this range include liquid helium baths, two and three-stage Gifford-McMahon (GM) cryocoolers, and GM units coupled with a Joule-Thomson (JT) stage. Magnetic refrigeration systems operating in this range include rotating [61], reciprocating [62][63], and active regenerative devices [64].

The upper limit for the next temperature range (20-77K) is defined by the normal boiling point of nitrogen. The most important application in this temperature range consists of providing an upper stage for a 4 to 20 K or 1.5 to 20 K magnetic refrigerator. Other possible applications include the liquefaction of hydrogen, the production of slush

---

<sup>1</sup> As an example, NbTi wire shows a 40% increase in current density when cooled to 1.8 K (compared to the current density at 4.2K) [53]. This reduces the amount of wire required to produce a given field in a given geometry thereby lowering capital costs.

hydrogen (at 13.8 K), and the cooling of high temperature superconductors. Magnetic/LN<sub>2</sub> hybrids have also been proposed for large scale liquefaction of hydrogen.

The next temperature range (110-250 K) has received only limited attention. One important application in this case is related to the production of liquid natural gas via magnetic refrigeration. The device being developed by the Cfs group is based on an active magnetic regenerative refrigerator (AMRR) and it will be the first prototype of its kind in the world.

Applications for MR systems near room temperature include air conditioning [65], food preservation, and general cooling. Most of the reported devices use Gd as the working material [66][49][50] and rely on convective heat transfer between this material and a heat transfer fluid. The reported designs include systems with rotary [67] or reciprocating working materials, and systems with static working materials using magnets that can be periodically charged and discharged.

## Appendix E

### Selection Criteria for Cryogenic Regenerator Materials with High Thermal Mass.

As stated in Chapter 2, the selection criteria for regenerator materials with large thermal mass at low temperatures include:

1. Low Debye temperature,  $\theta_D$ .
2. Magnetic ordering temperature in the appropriate range.
3. Large magnetic entropy.
4. Large number of magnetic atoms per unit volume.
5. Presence of lanthanide elements from the beginning or the end of the series.
6. Broad (or narrow) heat capacity peaks.

Low Debye temperatures imply that the lattice contribution to the heat capacity will be significant at low temperatures. The heavy lanthanides have  $\theta_D$  values that are consistently lower than the values found in transition metals.

Requiring low magnetic ordering temperatures also implies that the preferred candidates are magnetic lanthanides rather than magnetic elements in the 3d transition series. This choice is reinforced by the third requirement because the magnetic entropy  $S_{magnetic}$  is proportional to the total angular momentum quantum number, J:

$$S_{magnetic} = R \ln(2J + 1)$$

#### Equation E-1

The elements with the largest J values (i.e., with the largest magnetic moments) are found in the second half of the lanthanide series. Although some 3d transition metal ions have theoretical magnetic moments comparable to the corresponding values for the lanthanides, the measured moments are consistently lower than predicted. This deviation from theoretical values has been discussed by Kittel [70] and others [71]. They explain it

in terms of a quenching of the orbital angular momentum by the crystal field interaction [72]. In special cases, this results in the time-averaged angular momentum being equal to zero (i.e.,  $\mathbf{J} = \mathbf{S}$ ).

**Table E-1: The theoretical magnetic moments of TM and RE compared to the observed values [68][69].**

Ion	Electronic Configuration	S	L	J	Magnetic moment in multiples of $\mu_B$			Term Symbol	$T_C$ (K)
					$g_S(S(S+1))^{1/2}$	$g_J(J(J+1))^{1/2}$	Observed		
Ti <sup>3+</sup>	[Ar]3d <sup>1</sup>	1/2	2	3/2	1.735	1.549	1.8	<sup>2</sup> D <sub>3/2</sub>	
V <sup>3+</sup>	[Ar]3d <sup>2</sup>	1	3	3	2.833	1.633	2.8	<sup>3</sup> F <sub>2</sub>	
Cr <sup>3+</sup>	[Ar]3d <sup>3</sup>	3/2	3	3/2	3.879	0.775	3.8	<sup>4</sup> F <sub>3/2</sub>	
Mn <sup>3+</sup>	[Ar]3d <sup>4</sup>	2	2	0	4.906	0.000	4.9	<sup>3</sup> D <sub>0</sub>	
Fe <sup>3+</sup>	[Ar]3d <sup>5</sup>	5/2	0	5/2	5.925	5.916	5.9	<sup>6</sup> S <sub>5/2</sub>	
Fe <sup>2+</sup>	[Ar]3d <sup>6</sup>	2	2	4	4.906	6.708	5.4	<sup>5</sup> D <sub>4</sub>	
Co <sup>2+</sup>	[Ar]3d <sup>7</sup>	3/2	3	5/2	3.879	6.633	4.8	<sup>4</sup> F <sub>5/2</sub>	
Ni <sup>2+</sup>	[Ar]3d <sup>8</sup>	1	3	4	2.833	5.590	3.2	<sup>3</sup> F <sub>4</sub>	
Cu <sup>2+</sup>	[Ar]3d <sup>9</sup>	1/2	2	5/2	1.735	3.550	1.9	<sup>2</sup> D <sub>5/2</sub>	
La <sup>3+</sup>	[Xe]5s <sup>2</sup> 5p <sup>6</sup>	0	0	0	0.000	0.000		<sup>1</sup> S <sub>0</sub>	
Ce <sup>3+</sup>	[Xe]4f <sup>1</sup> 5s <sup>2</sup> 5p <sup>6</sup>	1/2	3	5/2	1.735	2.535	2.4	<sup>2</sup> F <sub>5/2</sub>	
Pr <sup>3+</sup>	[Xe]4f <sup>2</sup> 5s <sup>2</sup> 5p <sup>6</sup>	1	5	4	2.833	3.578	3.5	<sup>3</sup> H <sub>4</sub>	
Nd <sup>3+</sup>	[Xe]4f <sup>3</sup> 5s <sup>2</sup> 5p <sup>6</sup>	3/2	6	9/2	3.879	3.618	3.5	<sup>4</sup> I <sub>9/2</sub>	
Pm <sup>3+</sup>	[Xe]4f <sup>4</sup> 5s <sup>2</sup> 5p <sup>6</sup>	2	6	4	4.906	2.683	-	<sup>5</sup> I <sub>4</sub>	
Sm <sup>3+</sup>	[Xe]4f <sup>5</sup> 5s <sup>2</sup> 5p <sup>6</sup>	5/2	5	5/2	5.925	0.845	1.5	<sup>6</sup> H <sub>5/2</sub>	
Eu <sup>3+</sup>	[Xe]4f <sup>6</sup> 5s <sup>2</sup> 5p <sup>6</sup>	3	3	0	6.939	0.000	3.4	<sup>7</sup> F <sub>0</sub>	
Gd <sup>3+</sup>	[Xe]4f <sup>7</sup> 5s <sup>2</sup> 5p <sup>6</sup>	7/2	0	7/2	7.949	7.937	8.0	<sup>8</sup> S <sub>7/2</sub>	293
Tb <sup>3+</sup>	[Xe]4f <sup>8</sup> 5s <sup>2</sup> 5p <sup>6</sup>	3	3	6	6.939	9.721	9.5	<sup>7</sup> F <sub>6</sub>	219
Dy <sup>3+</sup>	[Xe]4f <sup>9</sup> 5s <sup>2</sup> 5p <sup>6</sup>	5/2	5	15/2	5.925	10.646	10.6	<sup>6</sup> H <sub>15/2</sub>	89
Ho <sup>3+</sup>	[Xe]4f <sup>10</sup> 5s <sup>2</sup> 5p <sup>6</sup>	2	6	8	4.906	10.607	10.4	<sup>5</sup> I <sub>8</sub>	20.0
Er <sup>3+</sup>	[Xe]4f <sup>11</sup> 5s <sup>2</sup> 5p <sup>6</sup>	3/2	6	15/2	3.879	9.581	9.5	<sup>4</sup> I <sub>15/2</sub>	20.0
Tm <sup>3+</sup>	[Xe]4f <sup>12</sup> 5s <sup>2</sup> 5p <sup>6</sup>	1	5	6	2.833	7.561	7.3	<sup>3</sup> H <sub>6</sub>	32.0
Yb <sup>3+</sup>	[Xe]4f <sup>13</sup> 5s <sup>2</sup> 5p <sup>6</sup>	1/2	3	3/2	1.735	4.536	4.5	<sup>2</sup> F <sub>7/2</sub>	
Lu <sup>3+</sup>	[Xe]4f <sup>14</sup> 5s <sup>2</sup> 5p <sup>6</sup>	0	0	0	0.000	0.000		<sup>1</sup> S <sub>0</sub>	

The fourth requirement implies that the fraction of lanthanide elements in the alloy should be large (50% or more). Larger fractions of non magnetic elements (or elements with smaller magnetic moments) will result in magnetically diluted alloys. The fifth requirement arises because the magnetic ordering temperature tends to follow the De Gennes factor, G:

$$G = J(J+1)(g-1)^2$$

**Equation E-2**

The factor g is called the gyromagnetic ratio and it is given by:

$$g = 1 + \frac{J(J+1) + S(S+1) - L(L+1)}{2J(J+1)}$$

**Equation E-3**

As can be seen in Figure E-1, low magnetic ordering temperatures will correspond to elements at either end of the lanthanide series (i.e., elements with low G values).

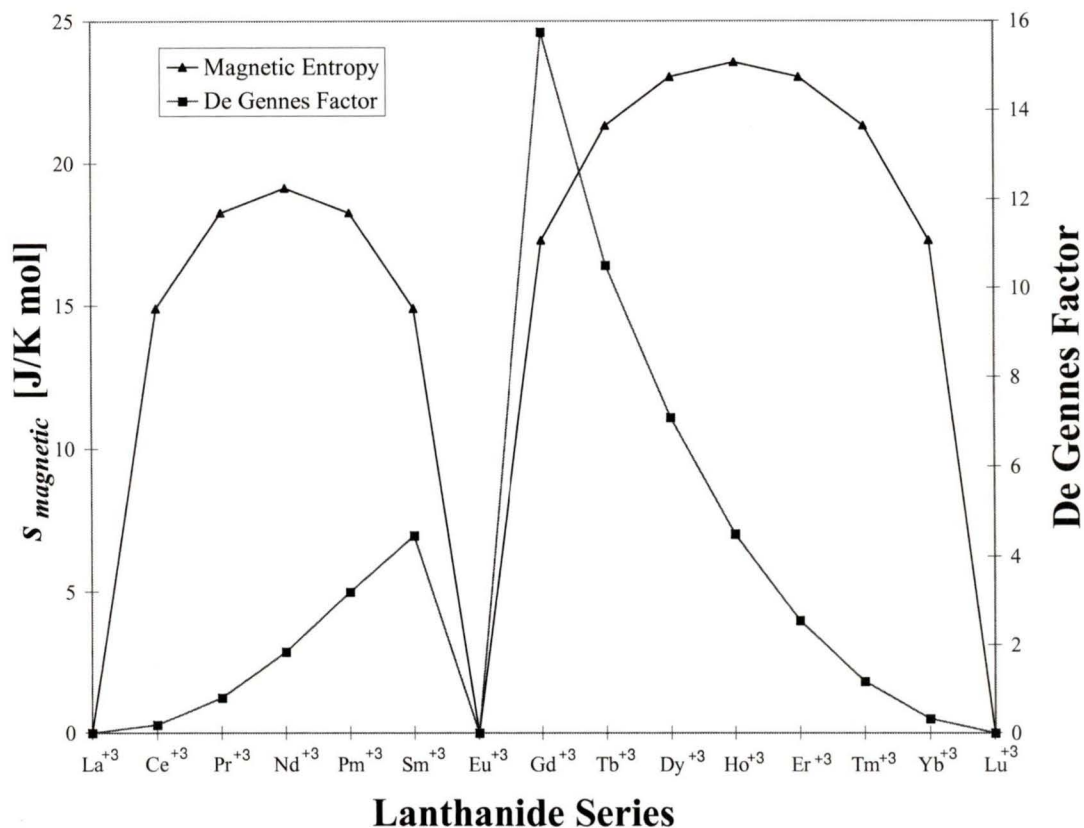


**Figure E-1: Magnetic entropy and de Gennes factors for the trivalent lanthanide ions.**

The last requirement depends entirely on the specific application. Layered hybrid regenerators can use materials with relatively narrow heat capacity peaks. This is done by using more than one material and matching the different peaks with the temperature profile in the regenerator bed. Other applications, however, dictate the use of a single material over an extended temperature range. In this case, a broad ordering peak would be preferred. The width and distribution of heat capacity peaks appear to be intrinsic properties of a given alloy [73] with impurities having only a small effect on their shape.

# Appendix F

## Heat Leaks

The heat leaks into the cold surfaces of a cryogenic experiment can be minimized but not completely eliminated. The following sections include a detailed calculation of the heat leaks associated with some of the most important heat transfer mechanisms. The calculations were performed using a mathematical model developed in MathcadPLUS™ 6.0. The corresponding file has been archived in the Cfs software library.

### F.1 Conductive Heat Leaks

The first and second stage temperatures have been assumed to be 40 K and 4 K, respectively. The principal conductive paths were the walls of the stainless steel housing. The heat leak through these walls were calculated using the following variables (variable names are given in Nomenclature):

$$\begin{aligned}
 \text{Dout1} &:= 0.0796544\text{m} \\
 \text{Lss1} &:= 0.2381\text{m} \\
 \text{Din1} &:= 0.0762\text{m} \\
 \text{Dout2} &:= 0.0319659\text{m} \\
 \text{Lss2} &:= 0.127\text{m} \\
 \text{Din2} &:= 0.03004\text{m} \\
 A2 &:= \frac{\pi}{4} \cdot (\text{Dout2}^2 - \text{Din2}^2) \\
 A1 &:= \frac{\pi}{4} \cdot (\text{Dout1}^2 - \text{Din1}^2)
 \end{aligned}$$

Because the heat transfer is occurring over a wide temperature range, the values for the thermal conductivity of stainless steel must be integrated to account for their temperature dependence:

$$\theta_1 = \int_0^{T_1} k(T) dT$$

**Equation F-1**

The heat flow will then be given by:

$$\dot{Q} = -G(\theta_2 - \theta_1)$$

**Equation F-2**

where the geometry factor,  $G$ , is given by:

$$\frac{1}{G} = \int_{x_1}^{x_2} \frac{dx}{A(x)}$$

**Equation F-3**

where  $A(x)$  is the cross sectional area at position  $x$  along the path of heat flow ( $G = A/L$  for a body of length  $L$  and uniform cross sectional area  $A$ ). The values for stainless steel are:

$$\theta_{300} := 14.90 \frac{\text{watt}}{\text{m}}$$

$$\theta_{40} := 4.70 \frac{\text{watt}}{\text{m}}$$

$$\theta_4 := 0.3 \frac{\text{watt}}{\text{m}}$$

Using these values, the conductive heat leaks to the first and second stages are given by:

$$Q_{c1} := (\theta_{300} - \theta_{40}) \cdot \left( \frac{A1}{L_{ss1}} \right)$$

**Equation F-4**

$$Q_{c2} := (\theta_{40} - \theta_4) \cdot \left( \frac{A2}{L_{ss2}} \right)$$

**Equation F-5**

which yield:

$$Q_{c1} = 0.018 \text{ kg} \cdot \text{m}^2 \cdot \text{sec}^{-3}$$

$$Q_{c2} = 3.249 \cdot 10^{-3} \cdot \text{kg} \cdot \text{m}^2 \cdot \text{sec}^{-3}$$

The conduction through the pressurized helium inside the stainless steel housing can be approximated by considering the limiting case when the entire space is filled with gas. Under these conditions, the heat leak to the first and second stages can be expressed as:

$$Q_{\text{cond\_He300psi\_stage1}} := \int_{40\text{ K}}^{300\text{ K}} kt_{300\text{psi}}(T) \cdot \frac{A_{1\_He}}{L_{ss1}} dT$$

**Equation F-6**

and

$$Q_{\text{cond\_He300psi\_stage2}} := \int_{4\text{ K}}^{40\text{ K}} kt_{300\text{psi}}(T) \cdot \frac{A_{2\_He}}{L_{ss2}} dT$$

**Equation F-7**

The thermal conductivity of helium has been approximated by a linear function of temperature:

$$\begin{aligned} kt_{300\text{psi}}(T) &:= a_{300\text{psi}} + b_{300\text{psi}} \cdot T \\ kt_{50\text{psi}}(T) &:= a_{50\text{psi}} + b_{50\text{psi}} \cdot T \end{aligned}$$

where

$$a_{50\text{psi}} := 0.02535 \frac{\text{watt}}{\text{m} \cdot \text{K}}$$

$$a_{300\text{psi}} := 0.0302115 \frac{\text{watt}}{\text{m} \cdot \text{K}}$$

$$b_{50\text{psi}} := 0.000456034 \frac{\text{watt}}{\text{m} \cdot \text{K}^2}$$

$$b_{300\text{psi}} := 0.00043936 \frac{\text{watt}}{\text{m} \cdot \text{K}^2}$$

The calculated values for  $Q_{\text{con\_He300psi\_stage1}}$  and  $Q_{\text{con\_He300psi\_stage2}}$  were calculated to be:

$$\begin{aligned} Q_{\text{cond\_He300psi\_stage1}} &= 0.522 \text{ kg} \cdot \text{m}^2 \cdot \text{sec}^{-3} \\ Q_{\text{cond\_He300psi\_stage2}} &= 8.012 \cdot 10^{-3} \cdot \text{kg} \cdot \text{m}^2 \cdot \text{sec}^{-3} \end{aligned}$$

Similarly, for helium at 50psig, the values were:

$$\begin{aligned} Q_{\text{cond\_He50psi\_stage1}} &= 0.512 \text{ kg} \cdot \text{m}^2 \cdot \text{sec}^{-3} \\ Q_{\text{cond\_He300psi\_stage2}} &= 8.012 \cdot 10^{-3} \cdot \text{kg} \cdot \text{m}^2 \cdot \text{sec}^{-3} \end{aligned}$$

The conductive leaks due to the copper wire used to power the heaters were calculated using the following variables:

$$\begin{aligned} D_{\text{copper}} &:= 0.0005 \text{ m} \\ L_{\text{copper\_stage1}} &:= 1.5 \cdot \text{m} \\ L_{\text{copper\_stage2}} &:= 0.30 \cdot \text{m} \\ N_{\text{leads\_copper1}} &:= 4 \\ N_{\text{leads\_copper2}} &:= 2 \\ \theta_{300} &:= 200000 \frac{\text{watt}}{\text{m}} \\ \theta_{40} &:= 30000 \frac{\text{watt}}{\text{m}} \\ \theta_4 &:= 200 \frac{\text{watt}}{\text{m}} \end{aligned}$$

The calculated values were found to be:

$$\begin{aligned} Q_{\text{copper\_stage1}} &:= N_{\text{leads\_copper1}} \cdot \pi \cdot \frac{D_{\text{copper}}^2}{4 \cdot L_{\text{copper\_stage1}}} \cdot (\theta_{300} - \theta_{40}) \\ Q_{\text{copper\_stage1}} &= 0.089 \text{ kg} \cdot \text{m}^2 \cdot \text{sec}^{-3} \\ Q_{\text{copper\_stage2}} &:= N_{\text{leads\_copper2}} \cdot \pi \cdot \frac{D_{\text{copper}}^2}{4 \cdot L_{\text{copper\_stage2}}} \cdot (\theta_{40} - \theta_4) \\ Q_{\text{copper\_stage2}} &= 0.039 \text{ kg} \cdot \text{m}^2 \cdot \text{sec}^{-3} \end{aligned}$$

Similarly, the heat leak through the phosphor bronze instrumentation wire were calculated using:

$$\begin{aligned} D_{\text{phosphor}} &:= 0.0002 \text{ m} \\ L_{\text{phosphor\_stage1}} &:= 1.5 \cdot \text{m} \\ L_{\text{phosphor\_stage2}} &:= 0.30 \cdot \text{m} \\ N_{\text{leads\_phosphor}} &:= 10 \\ \theta_{300} &:= 4000 \frac{\text{watt}}{\text{m}} \\ \theta_{40} &:= 300 \frac{\text{watt}}{\text{m}} \\ \theta_4 &:= 2 \cdot \frac{\text{watt}}{\text{m}} \end{aligned}$$

The resulting values for conductive heat leaks were found to be:

$$\begin{aligned} Q_{\text{phosphor\_stage1}} &:= N_{\text{leads\_phosphor}} \cdot \pi \cdot \frac{D_{\text{phosphor}}^2}{4 \cdot L_{\text{phosphor\_stage1}}} \cdot (\theta_{300} - \theta_{40}) \\ Q_{\text{phosphor\_stage1}} &= 7.749 \cdot 10^{-4} \cdot \text{kg} \cdot \text{m}^2 \cdot \text{sec}^{-3} \\ Q_{\text{phosphor\_stage2}} &:= N_{\text{leads\_phosphor}} \cdot \pi \cdot \frac{D_{\text{phosphor}}^2}{4 \cdot L_{\text{phosphor\_stage2}}} \cdot (\theta_{40} - \theta_4) \\ Q_{\text{phosphor\_stage2}} &= 3.121 \cdot 10^{-4} \cdot \text{kg} \cdot \text{m}^2 \cdot \text{sec}^{-3} \end{aligned}$$

## F.2 Radiative Heat Leaks

The radiative heat leak to a body fully enclosed by an outer vessel is given by:

$$\dot{Q}_{rad} = F_e \sigma A_1 (T_2^4 - T_1^4)$$

**Equation F-8**

where the emissivity factor,  $F_e$ , is defined as:

$$F_e = \left[ \frac{1}{e_1} + \frac{A_1}{A_2} \left( \frac{1}{e_2} - 1 \right) \right]^{-1}$$

**Equation F-9**

The variables used in these calculations are as follows (please refer to Nomenclature for a list of variable names):

$$\begin{aligned} T1 &:= 4 \cdot \text{K} \\ T2 &:= 40 \cdot \text{K} \\ T3 &:= 298 \cdot \text{K} \\ Dshield &:= 0.13 \cdot \text{m} \\ Lshield &:= 0.26 \cdot \text{m} \\ Dvessel &:= 0.61 \cdot \text{m} \\ Lvessel &:= 0.93 \cdot \text{m} \\ ebrass77K &:= 0.029 \\ ebrass4K &:= 0.018 \\ eAl273K &:= 0.043 \\ ess4K &:= 0.03 \\ Dstage2 &:= 0.038 \cdot \text{m} \\ Lstage2 &:= 0.127 \cdot \text{m} \\ ebrass77K &:= 0.029 \\ ebrass4K &:= 0.018 \\ eAl273K &:= 0.043 \\ ess4K &:= 0.03 \\ sigma &:= 5.671 \cdot 10^{-8} \cdot \frac{\text{watt}}{\text{m}^2 \cdot \text{K}^4} \end{aligned}$$

The calculated values are as follows:

$$\begin{aligned} A_{in} &:= \pi \cdot Dshield \cdot Lshield + 2 \cdot \left( \pi \cdot \frac{Dshield^2}{4} \right) \\ A_{in} &= 0.133 \text{m}^2 \end{aligned}$$

$$A_{out} := \pi \cdot D_{vessel} \cdot L_{vessel} + 2 \cdot \left( \pi \cdot \frac{D_{vessel}^2}{4} \right)$$

$$A_{out} = 2.367 \text{ m}^2$$

$$Fe := \frac{1}{\left[ \frac{1}{e_{brass77K}} + \frac{A_{in}}{A_{out}} \cdot \left( \frac{1}{e_{Al273K}} - 1 \right) \right]}$$

$$Fe = 0.028$$

$$Q_{rad\_1} := Fe \cdot \sigma \cdot A_{in} \cdot (T_3^4 - T_2^4)$$

$$Q_{rad\_1} = 0.195 \text{ kg} \cdot \text{m}^2 \cdot \text{sec}^{-3}$$

$$Q_{rad\_2} := Fe \cdot \sigma \cdot A_{in} \cdot (T_2^4 - T_1^4)$$

$$Q_{rad\_2} = 6.317 \cdot 10^{-5} \cdot \text{kg} \cdot \text{m}^2 \cdot \text{sec}^{-3}$$

These calculations do not take into account the multi-layer insulation. The effective thermal conductivity of N layers of insulation compacted to have a thickness  $\Delta x$  can be approximated as follows:

$$k(T)_{MLI} = \frac{\Delta x}{N_{MLI}} \left[ \left( \frac{\sigma e_{MLI} T_2^2}{2 - e_{MLI}} \right) \left\{ 1 + \left( \frac{T_1}{T_2} \right)^2 \right\} \left( 1 + \frac{T_1}{T_2} \right) \right]$$

### Equation F-10

Using this formula, the following values were obtained:

$$N_{MLI} := 25$$

$$\text{thickness} := 0.01 \cdot \text{m}$$

$$e_{MLI} := 0.04$$

$$kT_{MLIstage2} := \frac{1}{\left( \frac{N_{MLI}}{\text{thickness}} \right)} \cdot \left[ \left( \frac{\sigma \cdot e_{MLI} \cdot T_2^2}{2 - e_{MLI}} \right) \cdot \left[ 1 + \left( \frac{T_1}{T_2} \right)^2 \right] \cdot \left( 1 + \frac{T_1}{T_2} \right) \right]$$

$$kT_{MLIstage2} = 8.229 \cdot 10^{-10} \cdot \text{kg} \cdot \text{m} \cdot \text{sec}^{-3} \cdot \text{K}^{-2}$$

$$kT_{MLIstage1} := \frac{1}{\left( \frac{N_{MLI}}{\text{thickness}} \right)} \cdot \left[ \left( \frac{\sigma \cdot e_{MLI} \cdot T_3^2}{2 - e_{MLI}} \right) \cdot \left[ 1 + \left( \frac{T_2}{T_3} \right)^2 \right] \cdot \left( 1 + \frac{T_2}{T_3} \right) \right]$$

$$kT_{MLIstage1} = 4.747 \cdot 10^{-8} \cdot \text{kg} \cdot \text{m} \cdot \text{sec}^{-3} \cdot \text{K}^{-2}$$

$$Q_{MLIstage1} := kT_{MLIstage1} \cdot A_{in} \cdot \left( \frac{T_3 - T_2}{\text{thickness}} \right)$$

$$Q_{MLIstage1} = 1.996 \cdot 10^{-5} \cdot \text{kg} \cdot \text{m}^2 \cdot \text{sec}^{-3} \cdot \text{K}^{-1}$$

$$Q_{MLIstage2} := kT_{MLIstage2} \cdot A_{in} \cdot \left( \frac{T_2 - T_1}{\text{thickness}} \right)$$

$$Q_{MLIstage2} = 4.828 \cdot 10^{-8} \cdot \text{kg} \cdot \text{m}^2 \cdot \text{sec}^{-3} \cdot \text{K}^{-1}$$

### F.3 Joule Heating

The heat leak due to the passage of a current  $I$  across a resistor of resistance  $R$  is given by:

$$\dot{Q}_{Joule} = I^2 R$$

**Equation F-11**

Joule heating of the instrumentation wires was calculated using the following variables:

$$R_{\text{phosphor}} := 2.9 \frac{\Omega}{\text{m}}$$

$$R_{\text{total\_phosphor}} := R_{\text{phosphor}} \cdot (L_{\text{phosphor\_stage1}} + L_{\text{phosphor\_stage2}})$$

$$R_{\text{total\_phosphor}} = 5.22 \text{ kg} \cdot \text{m}^2 \cdot \text{sec}^{-1} \cdot \text{coul}^{-2}$$

$$I_{\text{phosphor2}} := 10^{-3} \cdot \text{amp}$$

$$I_{\text{phosphor1}} := 10^{-5} \cdot \text{amp}$$

The calculated values were found to be:

$$Q_{\text{joule\_phosphor1}} := 2 \cdot (I_{\text{phosphor1}}^2 \cdot R_{\text{total\_phosphor}})$$

$$Q_{\text{joule\_phosphor2}} := 2 \cdot (I_{\text{phosphor2}}^2 \cdot R_{\text{total\_phosphor}})$$

$$Q_{\text{joule\_phosphor1}} = 4.64 \cdot 10^{-10} \cdot \text{kg} \cdot \text{m}^2 \cdot \text{sec}^{-3}$$

$$Q_{\text{joule\_phosphor2}} = 4.64 \cdot 10^{-6} \cdot \text{kg} \cdot \text{m}^2 \cdot \text{sec}^{-3}$$

Similarly for the copper wires used to power the heaters:

$$R_{\text{copper}} := 7 \cdot 10^{-7} \cdot \frac{\Omega}{\text{m}}$$

$$R_{\text{total\_copper}} := R_{\text{copper}} \cdot (L_{\text{copper\_stage1}} + L_{\text{copper\_stage2}})$$

$$I_{\text{copper}} := 1 \cdot \text{amp}$$

$$Q_{\text{joule\_copper}} := I_{\text{copper}}^2 \cdot R_{\text{total\_copper}}$$

$$Q_{\text{joule\_copper}} = 1.26 \cdot 10^{-6} \cdot \text{kg} \cdot \text{m}^2 \cdot \text{sec}^{-3}$$

The total heat leak into the first and second stages of the cryocooler have been summarized in Chapter 3.

## Appendix G

# Calculation of the Required Masses for Arc-melted RE/TM Samples

Most rare-earth materials are sold as ingots that need to be cut into smaller pieces before they can be alloyed with other materials. Calculating a given mass and then cutting the pieces to the required sizes can be a time-consuming process. The pure RE metals have relatively high toughness so that so that small chips cannot be easily obtained to add small amounts of material at the time. Because most of the RE/TM alloys consist of a large percentage of RE, it is easier to take the mass of a RE sample as the starting point, and then calculate the other masses.

This process has been automated using a Microsoft Excel™ program. The main input window allows the user to specify the amount of starting material, and then calculates the other masses (see Figure G-1).

2nd-Stage Regenerator Materials						
Starting with (g)	Of	To Prepare	Requires (g)	Of		
40	Er	Er3Ni	40.000	Er		
	Ni	ErNi0.9Co0.1	14.0356331	Ni		
	Co	Er0.9Yb0.1Ni	X	Co		
	Yb	Er3Co	4.59803101	Yb		
	Nd	Nd3Ni	X	Nd		
porosity	40.00%					
yield	5.00%					
Masses for Sample Preparation (g)					Total volume (cm3)	
Total mass (g)	Er	Ni	Co	Yb	Nd	Occupied by particles
15.00	13.429	1.571				0.116 Er3Ni
	11.103	3.506	0.391	0.000	0.000	0.117 ErNi0.9Co0.1
	9.968	3.886		1.14582		0.118 Er0.9Yb0.1Ni
	7.292		7.708			0.118 Er3Co
		1.791			13.209	0.140 Nd3Ni

**Figure G-1: The main input windows for a spreadsheet program designed to calculate material masses.**

It is also possible to specify a desired total mass for a given sample. The program calculates the required masses for each alloy and also gives an estimate of the total

volume that could be occupied if this sample were used to produce particles. This calculation is based on porosity and yield values that can be varied This program has been archived in the CFS Technical Software Library.

## Appendix H

# Thermal Masses in the Second-stage Regenerator of a GM Cryocooler

A mathematical model was developed using MathcadPLUS 6.0™. This model calculates the total thermal mass in a hybrid regenerator (Pb + Er<sub>3</sub>Ni + ErNi<sub>0.9</sub>Co<sub>0.1</sub>) and compares it to the total mass in regenerator using lead particles only.

The model variables are as follows (see Nomenclature):

Reg\_length := 6.5 cm  
Reg\_radius := 1.27 cm  
 $\rho_{\text{Pb}} := 11.3 \text{ g cm}^{-3}$   
 $\rho_{\text{Er3Ni}} := 9.02 \text{ g cm}^{-3}$   
 $\rho_{\text{ErNiCo}} := 8.98 \text{ g cm}^{-3}$

Assumptions:

- $\alpha := 0.40$
- T at the hot end of the regenerator = 40 K
- T at the cold end of the regenerator = 3.5 K
- Linear temperature profile (x in cm, T(x) in K):

$$T(x) := 5.615 \cdot x + 3.5$$

**Equation H-1**

The temperature-dependent, volumetric heat capacities (for materials and helium gas at different pressures) are approximated by continuous functions. Because these curves have been implemented as implicit functions of position (x), it is relatively easy to change the linear temperature profile to a more realistic representation. This changes could be the subject of future research. The approximated functions for the heat capacity values as a function of temperature are as follows:

$$Cp\_Pb(x) := \frac{a + c \cdot T(x) + e \cdot T(x)^2 + g \cdot T(x)^3 + i \cdot T(x)^4}{1 + b \cdot T(x) + d \cdot T(x)^2 + f \cdot T(x)^3 + h \cdot T(x)^4}$$

**Equation H-2**

$$Cp\_Er3Ni(x) = \frac{a2 + c2 \cdot T(x) + e2 \cdot T(x)^2 + g2 \cdot T(x)^3 + i2 \cdot T(x)^4 + k2 \cdot T(x)^5}{1 + b2 \cdot T(x) + d2 \cdot T(x)^2 + f2 \cdot T(x)^3 + h2 \cdot T(x)^4 + j2 \cdot T(x)^5}$$

**Equation H-3**

$$Cp\_ErNiCo(x) := \frac{a1 + c1 \cdot T(x) + e1 \cdot T(x)^2 + g1 \cdot T(x)^3 + i1 \cdot T(x)^4 + k1 \cdot T(x)^5}{1 + b1 \cdot T(x) + d1 \cdot T(x)^2 + f1 \cdot T(x)^3 + h1 \cdot T(x)^4 + j1 \cdot T(x)^5}$$

**Equation H-4**

$$Cp\_70psi\_He(x) := \frac{a3 + c3 \cdot T(x)^{0.5} + e3 \cdot T(x) + g3 \cdot T(x)^{1.5} + i3 \cdot T(x)^2}{1 + b3 \cdot T(x)^{0.5} + d3 \cdot T(x) + f3 \cdot T(x)^{1.5} + h3 \cdot T(x)^2}$$

**Equation H-5**

$$Cp\_310psi\_He(x) := \frac{a4 + c4 \cdot T(x) + e4 \cdot T(x)^2 + g4 \cdot T(x)^3 + i4 \cdot T(x)^4 + k4 \cdot T(x)^5}{1 + b4 \cdot T(x) + d4 \cdot T(x)^2 + f4 \cdot T(x)^3 + h4 \cdot T(x)^4 + j4 \cdot T(x)^5}$$

**Equation H-6**

These approximations were obtained by curve-fitting the appropriate data (using TableCurve™ 2D). The coefficients for these approximations are shown in table B1:

**Table H-1: Polynomial coefficient for the approximated heat capacity curves (Cp in  $\text{J K}^{-1} \text{cm}^{-3}$ , T in K, x in cm).**

Cp_Pb(T):	Cp_ErNiCo(T):	Cp_Er3Ni(T)	Cp_70psi_He(T)	Cp_310psi_He(T)
a := -0.00880331	a1 := -0.09593263	a2 := -0.0244059	a3 := 0.027055404	a4 := -1.15402422
b := -0.18967281	b1 := -0.48366971	b2 := -0.33986266	b3 := -1.67476808	b4 := -0.48673551
c := -0.00302905	c1 := 0.099062015	c2 := 0.039743087	c3 := -0.02167115	c4 := 0.014362199
d := 0.014180905	d1 := 0.089726553	d2 := 0.041279737	d3 := 1.069962524	d4 := 0.627941416
e := 0.002039488	e1 := -0.03062991	e2 := -0.01040669	e3 := 0.007183998	e4 := 0.346869785
f := -0.00055617	f1 := -0.00741803	f2 := -0.00192311	f3 := -0.30803025	f4 := -0.05628288
g := -0.00022539	g1 := 0.004329919	g2 := 0.001094338	g3 := -0.00218021	g4 := -0.04783439
h := $1.0587610^{-5}$	h1 := 0.000207818	h2 := $3.4589910^{-5}$	h3 := 0.03361341	h4 := -0.00150894
i := $7.0652610^{-6}$	i1 := -0.00030114	i2 := $-4.469510^{-5}$	i3 := 0.000428622	i4 := 0.003209487
	j1 := $2.3309410^{-6}$	j2 := $-1.347610^{-7}$		j4 := 0.00035281
	k1 := $8.5833610^{-6}$	k2 := $6.4189510^{-7}$		k4 := $-1.881610^{-5}$

The resulting functions are plotted in Figure E-1.

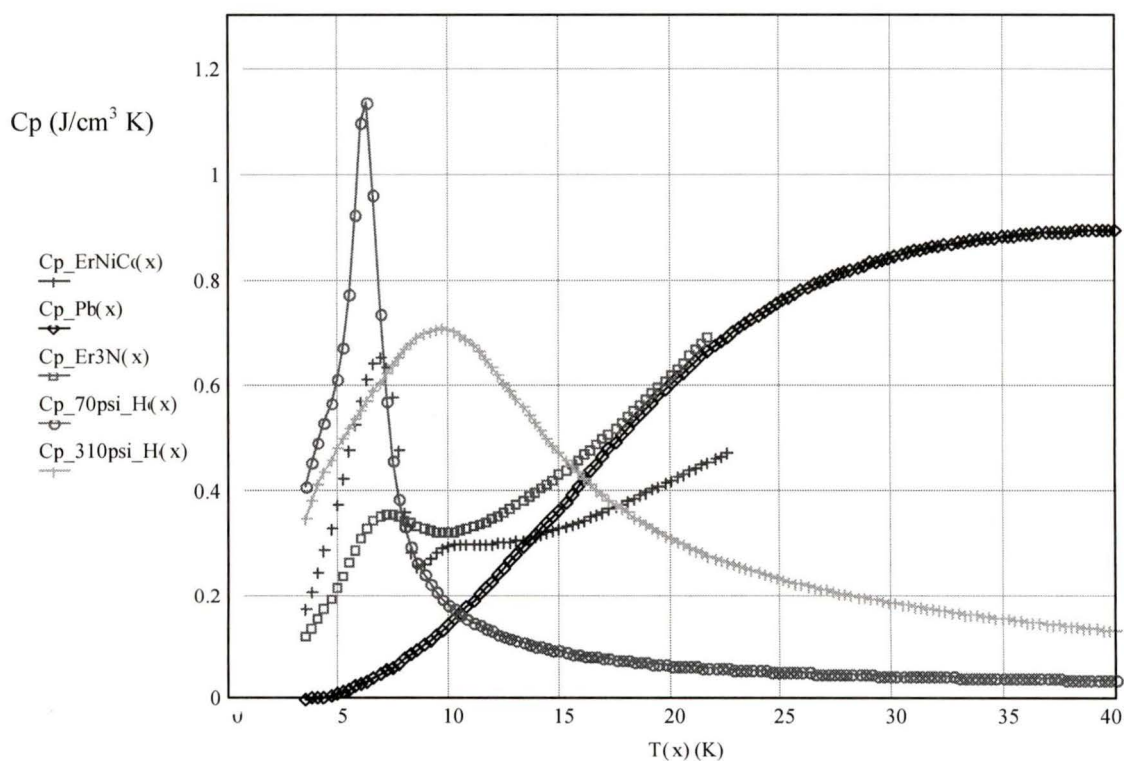


**Figure H-1: Approximated heat capacity curves for different materials and helium gas at different pressures. The approximations for RE/TM alloys are not valid at temperatures higher than 25 K.**

The linear temperature profile across the regenerator bed is schematically shown in Figure E-2.

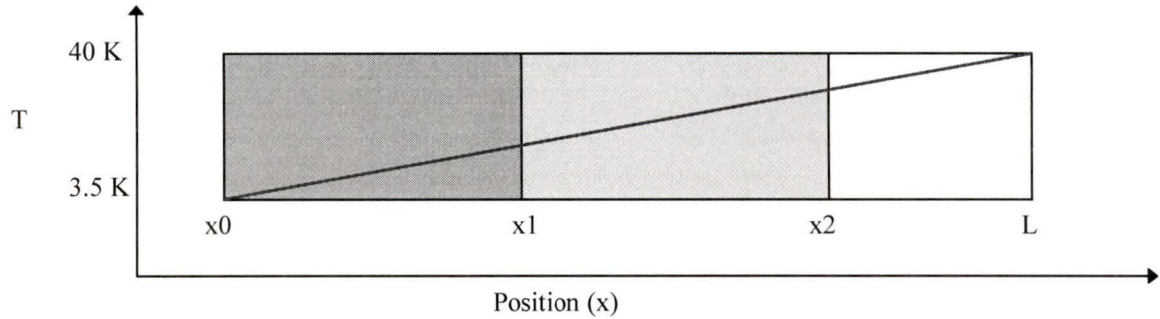


**Figure H-2: A linear temperature profile across a regenerator bed.**

The coordinates and associated temperatures for REG3 are as follows:

$x_0 := 0 \text{ cm}$	$T(x_0) := 3.5 \text{ K}$
$x_1 := 2.5 \text{ cm}$	$T(x_1) := 17.54 \text{ K}$
$x_2 := 4.9 \text{ cm}$	$T(x_2) := 31.01 \text{ K}$
$L := 6.5 \text{ cm}$	$T(L) := 39.99 \text{ K}$

This implies that the total thermal mass for each of the material layers in REG3 is given by:

$$MCp1 := \int_0^{x_1} (1 - \alpha) \cdot \pi \cdot \text{Reg\_radius}^2 \cdot Cp\_ErNiC(x) dx$$

**Equation H-7**

$$MCp2 := \int_{x_1}^{x_2} (1 - \alpha) \cdot \pi \cdot \text{Reg\_radius}^2 \cdot Cp\_Er3N(x) dx$$

**Equation H-8**

$$MCp3 := \int_{x_2}^L (1 - \alpha) \cdot \pi \cdot \text{Reg\_radius}^2 \cdot Cp\_Pb(x) dx$$

**Equation H-9**

The total thermal mass for REG3 is simply given by:

$$MCp\_hybrid := MCp1 + MCp2 + MCp3$$

**Equation H-10**

The corresponding total thermal mass for a regenerator using only lead is given by:

$$MCp\_Pb := \int_0^L (1 - \alpha) \cdot \pi \cdot Reg\_radius^2 \cdot Cp\_Pb(x) dx$$

**Equation H-11**

The calculated values are  $MCp\_hybrid = 12.66 \text{ J K}^{-1}$  and  $MCp\_Pb = 10.93 \text{ J K}^{-1}$ , respectively. This implies that the total thermal mass has been increased by almost 16 %. More importantly, the thermal mass below 10 K has been drastically increased by using  $ErNi_{0.9}Co_{0.1}$  instead of lead ( $T(X\_lim) = 10 \text{ K}$ ):

$$MCp\_hybrid\_10K := \int_0^{X\_lim} (1 - \alpha) \cdot \pi \cdot Reg\_radius^2 \cdot Cp\_ErNiCo(x) dx$$

**Equation H-12**

$$MCp\_hybrid\_10K = 1.405$$

**Equation H-13**

$$MCp\_Pb\_10K := \int_0^{X\_lim} (1 - \alpha) \cdot \pi \cdot Reg\_radius^2 \cdot Cp\_Pb(x) dx$$

**Equation H-14**

$$MCp\_Pb\_10K = 0.178$$

**Equation H-15**

$$\frac{MCp\_hybrid\_10K}{MCp\_Pb\_10K} = 7.895$$

**Equation H-16**

In other words, the thermal mass below 10 K has been increased by almost 790 %. Table compares the low temperature thermal mass of a layered, hybrid regenerator to that of its lead-based counterpart:

**Table H-2: Comparison between the total thermal masses below certain temperatures.**

T(X_lim) (K)	MCp_hybrid_T(X_lim) (J K <sup>-1</sup> )	MCp_Pb_T(X_lim) (J K <sup>-1</sup> )	$\frac{MCp\_hybrid\_T(X\_lim)}{MCp\_Pb\_T(X\_lim)}$
15	2.22	0.857	2.60
10	1.41	0.178	7.90
9	1.25	0.111	11.3
8	1.10	0.062	17.7
7	0.816	0.03	27.5
6	0.479	0.01	47.5
5	0.221	$6 \times 10^{-4}$	329

It is also possible to compare the total thermal mass below 10 K by calculating the corresponding values for pressurized helium (T(X\_lim) = 10 K):

$$M_{70psi\_He} := \int_0^{X\_lim} \alpha \cdot \pi \cdot Reg\_radius^2 \cdot Cp_{70psi\_He}(x) dx$$

**Equation H-17**

$$M_{310psi\_He} := \int_0^{X\_lim} \alpha \cdot \pi \cdot Reg\_radius^2 \cdot Cp_{310psi\_He}(x) dx$$

**Equation H-18**

$$\frac{M_{310psi\_He}}{MCp\_Pb_{10K}} = 7.606$$

**Equation H-19**

$$\frac{M_{70psi\_He}}{MCp\_Pb_{10K}} = 7.052$$

**Equation H-20**

$$\frac{M_{310psi\_He}}{MCp\_hybrid_{10K}} = 0.963$$

**Equation H-21**

$$\frac{M_{70psi\_He}}{MCp\_hybrid_{10K}} = 0.893$$

**Equation H-22**

As can be seen, the total thermal mass of helium gas at either pressure is about seven times larger than the thermal mass of a lead regenerator for temperatures below 10 K. Using a layer of  $\text{ErNi}_{0.9}\text{Co}_{0.1}$  makes it possible to increase the thermal mass above the corresponding values for pressurized helium.

# Appendix I

## Error Analysis

Every experimental measurement has sources of error that can be minimized but not completely eliminated. Some of the most common sources of error found in cryogenic temperature measurement are:

- DAQ system resolution
- Applied excitation error
- Thermoelectric voltages and zero offsets
- Ground-loops and electromagnetic noise
- Sensor self-heating
- Sensor calibration uncertainty, and
- Interpolation uncertainty

The total error due to these different sources is usually calculated in two ways. The worst case error,  $\varepsilon^+$ , can be estimated by the direct summation of all errors:

$$\varepsilon^+ = \sum_1^n \varepsilon_i$$

**Equation I-1**

where  $\varepsilon_i$  is the  $i^{\text{th}}$  member of series composed of  $n$  total errors. The second method considers the most probable error,  $\varepsilon^x$ , which can be estimated by assuming a statistical distribution of errors. In this case,  $\varepsilon^x$  is given by:

$$\varepsilon^x = \sqrt{\sum_1^n \varepsilon_i^2}$$

**Equation I-2**

### I.1 DAQ System Resolution

The temperature resolution of a thermometer,  $\varepsilon_T$ , is limited by the resolution of the measurement system,  $\varepsilon_{\text{DAQ}}$ . In most cases, the DAQ system measures voltages that

correspond a temperature-dependent change in a physical property of the sensor. In the case of resistive transducers, the relationship between  $\varepsilon_T$  and  $\varepsilon_{DAQ}$  is given by:

$$\varepsilon_T = \frac{\varepsilon_{DAQ}}{dV/dT}$$

**Equation I-3**

when the sensitivity  $dV/dT$  of the sensor does not change significantly over the temperature range of interest. The sensitivity can also be written as  $I(dR/dT)$  for ohmic resistance thermometers operating under a constant current excitation  $I$ . The resolution of the DAQ system used in this work was  $\pm 152.59 \mu\text{V}$ , and  $\pm 3.05 \mu\text{V}$  for the  $\text{RuO}_2$  and PRT sensors, respectively (see Section 3.3.2). This implies that the DAQ dependent error associated with temperature readings below 4.2 K will be given by (see Table 3-2):

$$\varepsilon_T = \frac{\varepsilon_{DAQ}}{I(dR/dT)} = \frac{\pm 152.59 \times 10^{-6} \text{ V}}{(10^{-5} \text{ A})(13,700 \Omega / \text{K})} = \pm 1.11 \times 10^{-3} \text{ K}$$

**Equation I-4**

Similarly, the error value for the PRTs at approximately 40 K was found to be  $\pm 1.22 \times 10^{-2} \text{ K}$ . The error values for other temperature ranges can be calculated in a similar manner.

## I.2 Applied Excitation Error

All the temperature sensors used in this work operated under a constant-current excitation. The excitation currents were  $1.000 \pm 0.005 \text{ mA}$ , for the PRTs, and  $10.000 \pm 0.005 \mu\text{A}$  for the calibrated ruthenium oxide sensor (see Chapter 3). The error associated with an excitation current uncertainty can be calculated using Equation I-3 and replacing  $\varepsilon_{DAQ}$  by the voltage change associated with the current difference. For the ruthenium oxide sensor at  $T < 4.2 \text{ K}$ , this error is given by:

$$\varepsilon_{PS} = \frac{\varepsilon_I}{I(dR/dT)} = \frac{\pm (0.005 \times 10^{-6} \text{ A})(2.14 \times 10^6 \Omega)}{(10^{-5} \text{ A})(13,700 \Omega / \text{K})} = \pm 7.81 \times 10^{-3} \text{ K}$$

**Equation I-5**

The corresponding error for the PRTs at approximately 40 K was found to be  $\pm 0.102 \text{ K}$ .

### I.3 Thermoelectric Voltages and Zero Offsets

Electrical conductors develop a potential difference as a response to temperature gradients when no current is allowed to flow (open-circuit EMFs). This is exactly the same type of phenomenon (Seebeck effect) that makes the operation of thermocouples possible. These thermoelectrical voltages appear when dissimilar metals are joined and joints are held at different temperatures. Typical values for this type of error are small (a few  $\mu\text{V}$ ) and can be further reduced by keeping all the connections between dissimilar metals at the same temperature. In this work, all the electrical connections were thermally anchored to the first and second stages of the cryocooler by applying a thin layer of GE 7031 varnish (see Chapter 3). All the electrical connectors used to join the second-stage sensors to the DAQ system wiring were bolted to the radiation shield. This shield was in turn bolted and thermally anchored to the first stage copper flange.

Zero offsets are essentially spurious voltage signals that occur with zero input at the measuring device. This offset values can drift with time and/or temperature and are usually included in equipment specifications. The maximum offset error associated with the DAQ board was  $\pm 76 \mu\text{V}$  after factory calibration [National Instruments Corporation, PCI-MIO E Series User Manual, Part Number 320945A-01, December 1995 ed., p. A-2, USA (1995)]. Typical values, however, were found to be only a few  $\mu\text{V}$  with properly grounded, differential input signals. This voltage was measured using a high precision multimeter (Hewlet Packard Model 34401A) Additional tests included reversing the polarity of the excitation current to obtain  $V_+$  and  $V_-$ , the voltages corresponding to each polarity. Assuming a forward current direction for  $V_+$ , this volatge was given by:

$$V_+ = (V_S + V_C)$$

**Equation I-6**

where  $V_S$  corresponds to the true reading from the sensor and  $V_C$  is the voltage associated with thermal EMFs. When the current is reversed, the reading from the sensor

changes sign, but the thermal voltages do not. This implies that the voltage in the reverse current case will be given by:

$$V_- = (-V_S + V_C)$$

**Equation I-7**

These two voltages can be used to eliminate thermoelectric voltages, by expressing the sensor's voltage as  $V_S$  :

$$V_S = \frac{(V_+ + V_-)}{2}$$

**Equation I-8**

Both the thermoelectric and the zero offset voltages were found to be very small (a few  $\mu\text{V}$ ). It was therefore decided to estimate the associated errors as values close to the resolution of the DAQ system (i.e.,  $\pm 1.11 \times 10^{-3}$  K and  $\pm 1.22 \times 10^{-2}$  K for the ruthenium oxide at  $T < 4.2$  K and PRTs at  $T \approx 40$  K, respectively).

## **I.4 Ground Loops and Electromagnetic Noise**

Ground loops arise when the devices in a DAQ circuit (power supplies, signal conditioning modules etc.) do not share a common electrical ground. Electromagnetic noise is commonly associated with alternating current devices operating in the vicinity of the DAQ system. The associated electrical signals generate an induced AC voltage on the signal wires connecting sensors to the DAQ system. A common solution to this problem consists of using shielded cable to make all the connections. One potential problem with this technique arises when the cables are improperly grounded (e.g., grounding at both ends). Both of these sources of error were considered and essentially eliminated.

The first preventive measure consisted of ensuring that all the active elements in the DAQ circuit (including the experimental chamber) shared a common ground. This was accomplished by physically linking all the power supplies, and DAQ equipment to a common ground from the main electrical outlet. The second measure consisted of using

shielded, twisted pair cable for all connections between the experimental chamber and the DAQ system. A single ground wire was used at the DAQ end of the circuit.

The SCXI modules used for signal conditioning also have a built-in low-pass filter at each of the input channels. In addition, a large number of voltage measurements (2,000 - 8,000) were taken to calculate a single temperature value. Digital filtering was implemented by calculating the mean voltage value after each scan. More sophisticated digital filters can be easily used in the DAQ software by simply replacing the appropriate functions (see Appendix H).

Ground loop and electromagnetic noise errors were neglected in the calculation of the total error associated with temperature measurement.

## **I.5 Lead Wire Resistance**

The wires used to power the sensors had a finite length and therefore a corresponding finite resistance. This implies that the voltage drop across the entire circuit was slightly larger than the voltage across the sensor. The total resistance of the phosphor bronze wires used to operate the ruthenium oxide resistor was calculated (see Appendix F) and found to be approximately 5.22  $\Omega$ . Because the sensor operated under a constant current excitation of  $10^{-5}$  A, the corresponding uncertainty in the temperature measurement was:

$$\varepsilon_{\Omega} = \frac{(10^{-5} A)(5.22\Omega)}{I(dR / dT)} = \frac{\pm (5.22 A\Omega)}{13,700\Omega / K} = \pm 3.81 \times 10^{-4} K$$

**Equation I-9**

## **I.6 Sensor Self-heating**

Resistive temperature sensors are essentially low-power electrical heaters. The power dissipated, P, is given by:

$$P = I^2 R$$

**Equation I-10**

where  $I$  is the excitation current, and  $R$  is the sensor's resistance. For temperatures below 4.2 K, the power dissipated by the  $\text{RuO}_2$  resistor was approximately  $1.4 \mu\text{W}$ . The powers at higher temperatures were smaller. The power dissipated by the PRTs was approximately  $5 \mu\text{W}$  at 40 K. Estimating self-heating errors under different operating conditions is difficult. One common practice consists of measuring the temperature in a liquid bath and in a vacuum and comparing the resistive sensor's reading with that from a sensor that does not require a current excitation (e.g., a thermocouple).

A practical way to minimize self-heating errors consists of ensuring good thermal contact between the sensor and the body whose temperature is being measured. In this work, the temperature sensors were mounted on a special copper attachments that could be tightly bolted to the cold surfaces at the first and second stages of the cryocooler. These attachments were simply copper bobbins with an orifice into which the sensors could be inserted. The four wires on each sensor were then wound around the bobbin and held in place by a thin layer of GE7031 varnish. Self-heating errors were not included in the calculation of the total error for temperature measurements.

## **I.7 Sensor Calibration**

Commercially calibrated temperature sensors are usually referenced to an international standard. The only calibrated temperature sensor used in this work was the ruthenium oxide resistor described in Chapter 3. This sensor was calibrated using the international temperature scale of 1990 (ITS-90). The associated calibration errors are given in Table 3-2.

## **I.8 Interpolation Uncertainty**

A calibration curve usually consists of a series of discrete temperature vs. voltage (or resistance) pairs. To calculate temperatures that lie between these calibration points, the discrete data must be converted into an interpolation curve. In some cases the response of the sensors' active property (e.g., resistance) is highly non-linear. Hence, care must be exercised in selecting an appropriate interpolation curve. Continuous polynomials

reflecting the physical principles behind the sensor's response are the ideal choice. In most cases, however, the best approximations require the use of more than one function to cover different temperature ranges. In some cases precision must be sacrificed to reduce function complexity. This is particularly important for computerized data acquisition systems that must devote memory resources to the calculation of the temperature values. Multiple simple functions with only a few terms are better than a single, more complex function. Another precaution consists of using the adequate software to perform the voltage or resistance to temperature conversions. Some of the commercial software packages used to manipulate experimental data (Microsoft® Excel, Lotus® 123, QuattroPro®, etc.) do not provide the mathematical engines required to effectively calculate temperature values from complex polynomial functions. Truncation errors are common because the memory allocated to most data entities is simply insufficient to calculate small differences between very large (or very small) numbers. In all cases, the error introduced by the interpolation function should not be larger than the errors associated with the calibration and/or measurement system.

Using an interpolation curve implies the introduction of additional errors in the measurement. These errors can be estimated by considering the fidelity with which the interpolation function reproduces the original data. The transfer functions for the temperature sensors used in this work were calculated using TableCurve™ 2D, a commercial software package that automates the curve fitting process. This program evaluates hundreds of different candidate functions and then ranks according to the fidelity with which they reproduce the original data. The data set used for the calibrated ruthenium oxide sensor was obtained directly from the manufacturer. The values for the uncalibrated PRTs correspond to a standard curve for 100  $\Omega$  commercial units.

The calibration curves and original data used to calculate the transfer functions for each sensor are given in the following sections.

#### Transfer Functions

The calculated transfer function for PRTs operating with a constant current excitation of  $10^{-3}$  A is given by:

$$T(V) = a + bV + \frac{c}{V} + dV^2 + \frac{e}{V^2} + fV^3$$

**Equation I-11**

where  $T(V)$  is measured in kelvins and  $V$  in volts. This approximation was obtained using TableCurve™ 2D and is valid for temperatures between 30 and 300 K. The required coefficients for the polynomial approximation are given Table I-1:

**Table I-1: Polynomial coefficients for the transfer function used for PRTs operating under a constant current of 1.000 mA.**

a	35.1435318
b	2112.843839
c	-0.0467801
d	3799.737706
e	8.44E-06
f	-10782.371

The interpolation errors at different temperature ranges are given in table I-2. These values were calculated as the average deviation associated with the temperature values predicted by Equation I-11.

**Table I-2: Interpolation errors at different temperature ranges for values calculated using Equation I-11.**

Temperature Range (K)	Interpolation error (K)
30-77	$\pm 0.119$
77-150	$\pm 0.045$
150-300	$\pm 0.031$

Three different polynomial approximations were required to calculate the temperatures measured with the ruthenium oxide sensor operating under a constant current excitation of  $10^{-5}$  A. These approximations cover three different temperature ranges and are given as follows:

$$T(V) = a + bV + cV^2 + dV^3 + eV^4 + fV^5 + gV^6 + hV^7$$

For 2 K ≤ T ≤ 20 K

**Equation I-12**

$$T(V) = \frac{1}{u + wV^{2.5}}$$

For 20 K ≤ T ≤ 40 K

**Equation I-13**

$$T(V) = \frac{1}{x + yV^3 + \frac{zV}{\ln(V)}}$$

For 40 K ≤ T ≤ 273 K

**Equation I-14**

The coefficients used in this approximations are given in table I-3.

**Table I-3: Polynomial coefficients for the transfer function used for the ruthenium oxide sensor operating under a constant current of 10.000 μA.**

2 K ≤ T ≤ 20 K	
a	15145.3234
b	-58143.3112
c	95985.7113
d	-88046.6464
e	48378.0242
f	-15903.1827
g	2893.38998
h	-224.599915
20 K ≤ T ≤ 40 K	
u	-0.05199557
w	0.05583922
40 K ≤ T ≤ 273 K	
z	-0.0405164
y	0.04458389
z	-1.8745E-06

The interpolation errors at different temperature ranges are given in Table I-4.

**Table I-4: Interpolation errors at different temperature ranges for the ruthenium oxide sensor.**

Temperature Range	Interpolation error (K)
2 K ≤ T ≤ 20 K	± 0.00327
20 K ≤ T ≤ 40 K	± 0.0171
40 K ≤ T ≤ 273 K	± 0.161

## I.9 Total Error

The total error can be calculated using Equations I-1 and I-2. Using the results given in previous sections, the worst case error for the ruthenium oxide sensor at temperatures below 4.2 K will be given by:

$$\varepsilon^+ = \sum_1^n \varepsilon_i = \varepsilon_{DAQ} + \varepsilon_{PS} + \varepsilon_{\mp} + \varepsilon_{GL} + \varepsilon_{\Omega} + \varepsilon_{Cal} + \varepsilon_{V \rightarrow T}$$

**Equation I-15**

$$\begin{aligned} \varepsilon_{RuO_2}^+ &= (1.11 \times 10^{-3} \text{ K}) + (7.81 \times 10^{-3} \text{ K}) + (1.11 \times 10^{-3} \text{ K}) + (0 \text{ K}) + (3.81 \times 10^{-4} \text{ K}) \\ &\quad + (5.0 \times 10^{-2} \text{ K}) + (3.27 \times 10^{-3} \text{ K}) = 0.063 \text{ K} \end{aligned}$$

**Equation I-16**

Similarly, the most probable error will be given by:

$$\varepsilon_{RuO_2}^{\times} = \sqrt{(1.11 \times 10^{-3} \text{ K})^2 + (7.81 \times 10^{-3} \text{ K})^2 + (1.11 \times 10^{-3} \text{ K})^2 + (0 \text{ K})^2 + (3.81 \times 10^{-4} \text{ K})^2 + (5.0 \times 10^{-2} \text{ K})^2 + (3.27 \times 10^{-3} \text{ K})^2} = 0.051 \text{ K}$$

**Equation I-17**

The total errors for PRTs at approximately 40 were calculated in a similar fashion. The values for the worst case and most probable errors ere found to be:

$$\begin{aligned} \varepsilon_{PRT}^+ &= (1.22 \times 10^{-2} \text{ K}) + (1.02 \times 10^{-1} \text{ K}) + (1.22 \times 10^{-2} \text{ K}) + \\ &\quad + (5.0 \times 10^{-1} \text{ K}) + (1.19 \times 10^{-1} \text{ K}) = 0.75 \text{ K} \end{aligned}$$

**Equation I-18**

and,

$$\varepsilon_{PRT}^{\times} = 0.52 \text{ K}$$

**Equation I-19**

The original voltage data for the calibrated ruthenium oxide resistor and the uncalibrated PRTs are given in Tables I-5 and I-6, respectively [138][139].

## I.10 Other Sensors

The differential pressure transmitter and the gas flowmeters were calibrated by the manufacturers. The transfer function for the Rosemount® pressure transmitter was:

$$\Delta P = mV + c$$

**Equation I-20**

where  $m = 62.15$  and  $c = 62.15$  (V in volts and  $\Delta P$  in Pa). The transfer function and calibration curve(s) for the flowmeters depends on the gas used and the mean pressure. For helium, at STP conditions, the calibration curve from the manufacturer is given in Table I-5.

**Table I-5: Calibration data for the MKS® flowmeter used to measure helium flow.**

Voltage (V)	Gas Flow (SLM)
0.1825	25.2981
0.3450	49.7102
0.5020	74.9352
0.6465	99.5753
0.7880	125.0050
0.9175	149.6230
1.0435	174.8323
1.1650	199.7970
1.2780	224.8080
1.3880	249.2583

The resulting transfer function was calculated using TableCurve™ 2D. This function is given by:

$$\dot{V} = \frac{1}{a + \frac{b}{V}}$$

**Equation I-21**

for volumetric gas flow in SLM and output voltages in volts. This function is valid for values of gas flow between 0 and approximately 250 SLM. The conversion to  $\text{kg s}^{-1}$  was performed using the average property values for helium at any given mean pressure. The conversion tables were created using MS Excel 5.0 and archived in the CFs software library.

The error associated with the pressure drop and flow measurements was calculated using the same analysis described in previous sections. All these measurements were performed at room temperature and the special cryogenic considerations were therefore not required. In most cases, the error associated with the DAQ system, power supplies, etc. was smaller than the error given in the calibration curves from the manufacturers. The error for the pressure drop measurements was  $\pm 625$  Pa for the pressure range between 0 and 248.6 kPa. The error for the flow measurements was approximately 3.23 % of full scale.

**Table I-6: Calibration data for the ruthenium oxide resistive sensor. The predicted temperature values were obtained using Equations I-12, I-13, and I-14.**

Voltage (V)	Temperature (K)	Predicted T	Difference (K)	Difference (%)
2.1808	2.00	2.000	0.00006	0.00305
2.01094	3.00	3.001	-0.00106	-0.03537
1.89321	4.00	3.995	0.00492	0.12292
1.78899	5.00	5.010	-0.01017	-0.20335
1.70553	6.00	5.994	0.00571	0.09521
1.63671	7.00	6.992	0.00751	0.10732
1.57912	8.00	8.005	-0.00480	-0.06003
1.53112	9.00	9.006	-0.00600	-0.06663
1.49034	10.00	9.998	0.00152	0.01515
1.45466	11.00	11.002	-0.00191	-0.01735
1.42383	12.00	11.997	0.00314	0.02619
1.39665	13.00	12.997	0.00316	0.02428
1.37264	14.00	13.998	0.00207	0.01480
1.35126	15.00	15.002	-0.00169	-0.01129
1.33222	16.00	16.001	-0.00135	-0.00845
1.31506	17.00	17.002	-0.00193	-0.01137
1.29955	18.00	18.000	0.00029	0.00162
1.29955	18.00	18.016	-0.01550	-0.08613
1.28534	19.00	19.002	-0.00215	-0.01130
1.28534	19.00	19.014	-0.01392	-0.07326
1.2724	20.00	19.997	0.00268	0.01340
1.2724	20.00	20.008	-0.00778	-0.03889
1.26051	21.00	21.002	-0.00182	-0.00865
1.24952	22.00	21.998	0.00163	0.00743
1.23929	23.00	23.001	-0.00147	-0.00637
1.22981	24.00	24.004	-0.00374	-0.01558
1.22096	25.00	25.010	-0.00979	-0.03917
1.2127	26.00	26.017	-0.01689	-0.06495
1.20516	27.00	27.000	0.00031	0.00114
1.19797	28.00	27.999	0.00092	0.00330
1.19122	29.00	28.998	0.00202	0.00695
1.18489	30.00	29.993	0.00677	0.02257
1.17893	31.00	30.987	0.01319	0.04256
1.17329	32.00	31.982	0.01799	0.05620
1.16796	33.00	32.976	0.02410	0.07303
1.1629	34.00	33.971	0.02853	0.08392
1.15816	35.00	34.954	0.04622	0.13205
1.15354	36.00	35.961	0.03882	0.10783
1.14886	37.00	37.036	-0.03594	-0.09712
1.14458	38.00	38.070	-0.07041	-0.18529
1.14081	39.00	39.026	-0.02552	-0.06543
1.13717	40.00	39.989	0.01053	0.02632
1.13717	40.00	39.953	0.04683	0.11707
1.10713	50.00	50.086	-0.08572	-0.17145
1.08641	60.00	60.140	-0.14010	-0.23350
1.07119	70.00	70.156	-0.15571	-0.22244
1.06273	77.00	77.147	-0.14675	-0.19059
1.05959	80.00	80.078	-0.07807	-0.09759
1.05048	90.00	89.881	0.11922	0.13246
1.04298	100.00	99.798	0.20248	0.20248
1.02917	125.00	124.737	0.26256	0.21005
1.01978	150.00	149.966	0.03389	0.02260
1.01316	175.00	175.265	-0.26452	-0.15115
1.00857	200.00	199.918	0.08166	0.04083
1.00542	225.00	224.836	0.16430	0.07302
1.00349	250.00	250.251	-0.25077	-0.10031
1.00262	270.00	270.229	-0.22896	-0.08480
1.00254	273.00	272.682	0.31806	0.11651

**Table I-7: Typical voltage data for uncalibrated PRTs. The temperature values are compared to those predicted by Equation I-11.**

V (V)	T (K)	Predicted T (K)	Difference (K)	Difference (%)	V (V)	T (K)	Predicted T (K)	Difference (K)	Difference (%)	V (V)	T (K)	Predicted T (K)	Difference (K)	Difference (%)
0.004	30.00	29.95	0.048	0.159	0.047	140.00	140.00	-0.002	-0.001	0.081	224.00	224.00	-0.004	-0.002
0.006	40.00	40.18	-0.183	-0.456	0.047	141.00	141.01	-0.013	-0.009	0.081	225.00	225.01	-0.008	-0.004
0.009	50.00	49.99	0.014	0.029	0.048	142.00	142.01	-0.010	-0.007	0.081	226.00	226.02	-0.018	-0.008
0.013	60.00	60.15	-0.150	-0.250	0.048	143.00	143.00	-0.003	-0.002	0.082	227.00	227.01	-0.008	-0.003
0.014	61.00	61.14	-0.135	-0.222	0.048	144.00	144.00	0.003	0.002	0.082	228.00	228.01	-0.013	-0.006
0.014	62.00	62.12	-0.116	-0.187	0.049	145.00	144.99	0.008	0.006	0.083	229.00	229.02	-0.023	-0.010
0.014	63.00	63.09	-0.092	-0.146	0.049	146.00	145.99	0.013	0.009	0.083	230.00	230.01	-0.014	-0.006
0.015	64.00	64.04	-0.045	-0.070	0.050	147.00	146.98	0.018	0.012	0.083	231.00	231.02	-0.020	-0.009
0.015	65.00	65.01	-0.009	-0.014	0.050	148.00	148.00	0.002	0.002	0.084	232.00	232.03	-0.032	-0.014
0.016	66.00	65.98	0.025	0.037	0.050	149.00	149.00	0.001	0.000	0.084	233.00	233.02	-0.023	-0.010
0.016	67.00	66.94	0.061	0.091	0.051	150.00	150.00	0.003	0.002	0.085	234.00	234.03	-0.030	-0.013
0.016	68.00	67.90	0.100	0.148	0.051	151.00	150.99	0.005	0.003	0.085	235.00	235.02	-0.023	-0.010
0.017	69.00	68.86	0.142	0.206	0.052	152.00	151.99	0.006	0.004	0.085	236.00	236.03	-0.030	-0.013
0.017	70.00	69.81	0.185	0.265	0.052	153.00	152.99	0.007	0.005	0.086	237.00	237.02	-0.023	-0.010
0.018	71.00	70.79	0.209	0.295	0.052	154.00	153.99	0.007	0.005	0.086	238.00	238.03	-0.031	-0.013
0.018	72.00	71.79	0.213	0.296	0.053	155.00	154.97	0.029	0.019	0.087	239.00	239.02	-0.025	-0.010
0.018	73.00	72.79	0.214	0.293	0.053	156.00	155.38	0.621	0.398	0.087	240.00	240.03	-0.034	-0.014
0.019	74.00	73.82	0.176	0.238	0.054	157.00	156.97	0.029	0.018	0.087	241.00	241.03	-0.028	-0.011
0.019	75.00	74.85	0.151	0.202	0.054	158.00	157.97	0.027	0.017	0.088	242.00	242.04	-0.037	-0.015
0.020	76.00	75.87	0.133	0.174	0.054	159.00	158.98	0.024	0.015	0.088	243.00	243.03	-0.032	-0.013
0.020	77.00	76.89	0.115	0.149	0.055	160.00	159.98	0.020	0.013	0.089	244.00	244.04	-0.042	-0.017
0.021	78.00	77.90	0.098	0.125	0.055	161.00	160.98	0.016	0.010	0.089	245.00	245.04	-0.037	-0.015
0.021	79.00	78.92	0.082	0.103	0.056	162.00	161.97	0.034	0.021	0.089	246.00	246.03	-0.027	-0.011
0.021	80.00	79.93	0.066	0.083	0.056	163.00	162.97	0.031	0.019	0.090	247.00	247.04	-0.038	-0.015
0.022	81.00	80.95	0.051	0.063	0.057	164.00	163.97	0.025	0.016	0.090	248.00	248.03	-0.034	-0.014
0.022	82.00	81.96	0.037	0.045	0.057	165.00	164.96	0.041	0.025	0.091	249.00	249.04	-0.045	-0.018
0.023	83.00	82.98	0.023	0.027	0.057	166.00	165.96	0.037	0.022	0.091	250.00	250.04	-0.041	-0.017
0.023	84.00	83.99	0.009	0.010	0.058	167.00	166.97	0.029	0.018	0.091	251.00	251.03	-0.033	-0.013
0.024	85.00	85.00	-0.005	-0.006	0.058	168.00	167.96	0.044	0.026	0.092	252.00	252.04	-0.045	-0.018
0.024	86.00	86.02	-0.018	-0.021	0.059	169.00	168.96	0.038	0.022	0.092	253.00	253.04	-0.042	-0.017
0.024	87.00	87.03	-0.031	-0.036	0.059	170.00	169.96	0.041	0.024	0.092	254.00	254.03	-0.034	-0.013
0.025	88.00	88.02	-0.023	-0.027	0.059	171.00	170.96	0.041	0.024	0.093	255.00	255.05	-0.047	-0.018
0.025	89.00	89.03	-0.034	-0.039	0.060	172.00	171.97	0.033	0.019	0.093	256.00	256.04	-0.045	-0.018
0.026	90.00	90.05	-0.048	-0.053	0.060	173.00	172.96	0.045	0.026	0.094	257.00	257.04	-0.038	-0.015
0.026	91.00	91.06	-0.061	-0.067	0.061	174.00	173.96	0.036	0.021	0.094	258.00	258.03	-0.031	-0.012
0.027	92.00	92.05	-0.053	-0.058	0.061	175.00	174.95	0.046	0.026	0.094	259.00	259.04	-0.045	-0.017
0.027	93.00	93.06	-0.065	-0.070	0.061	176.00	175.96	0.036	0.021	0.095	260.00	260.04	-0.043	-0.017
0.027	94.00	94.06	-0.058	-0.061	0.062	177.00	176.95	0.046	0.026	0.095	261.00	261.04	-0.037	-0.014
0.028	95.00	95.07	-0.069	-0.073	0.062	178.00	177.97	0.035	0.019	0.096	262.00	262.03	-0.031	-0.012
0.028	96.00	96.06	-0.063	-0.065	0.063	179.00	178.96	0.043	0.024	0.096	263.00	263.05	-0.045	-0.017
0.029	97.00	97.08	-0.075	-0.077	0.063	180.00	179.97	0.031	0.017	0.096	264.00	264.04	-0.045	-0.017
0.029	98.00	98.07	-0.069	-0.070	0.063	181.00	180.96	0.038	0.021	0.097	265.00	265.04	-0.039	-0.015
0.030	99.00	99.08	-0.082	-0.083	0.064	182.00	181.97	0.025	0.014	0.097	266.00	266.03	-0.034	-0.013
0.030	100.00	100.08	-0.077	-0.077	0.064	183.00	182.97	0.031	0.017	0.098	267.00	267.03	-0.029	-0.011
0.030	101.00	101.07	-0.069	-0.069	0.065	184.00	183.96	0.040	0.021	0.098	268.00	268.02	-0.024	-0.009
0.031	102.00	102.08	-0.084	-0.082	0.065	185.00	184.98	0.025	0.013	0.098	269.00	269.04	-0.040	-0.015
0.031	103.00	103.08	-0.080	-0.077	0.065	186.00	185.97	0.030	0.016	0.099	270.00	270.04	-0.040	-0.015
0.032	104.00	104.07	-0.074	-0.071	0.066	187.00	186.96	0.036	0.019	0.099	271.00	271.04	-0.036	-0.013
0.032	105.00	105.07	-0.068	-0.065	0.066	188.00	187.96	0.043	0.023	0.100	272.00	272.03	-0.032	-0.012
0.033	106.00	106.08	-0.085	-0.080	0.067	189.00	188.97	0.026	0.014	0.100	273.00	273.03	-0.028	-0.010
0.033	106.00	106.08	-0.085	-0.080	0.067	190.00	189.97	0.029	0.015	0.100	274.00	274.02	-0.024	-0.009
0.033	107.00	107.08	-0.082	-0.077	0.067	191.00	190.97	0.034	0.018	0.101	275.00	275.02	-0.020	-0.007
0.033	108.00	108.08	-0.078	-0.072	0.068	192.00	191.96	0.038	0.020	0.101	276.00	276.02	-0.017	-0.006
0.034	109.00	109.07	-0.075	-0.069	0.068	193.00	192.98	0.020	0.010	0.102	277.00	277.01	-0.013	-0.005
0.034	110.00	110.07	-0.072	-0.065	0.069	194.00	193.98	0.021	0.011	0.102	278.00	278.01	-0.010	-0.004
0.035	111.00	111.07	-0.069	-0.062	0.069	195.00	194.98	0.023	0.012	0.102	279.00	279.01	-0.007	-0.002
0.035	112.00	112.07	-0.067	-0.060	0.069	196.00	195.97	0.026	0.013	0.103	280.00	280.00	-0.004	-0.001
0.035	113.00	113.07	-0.066	-0.059	0.070	197.00	196.97	0.028	0.014	0.103	281.00	281.00	-0.001	0.000
0.036	114.00	114.07	-0.065	-0.057	0.070	198.00	197.97	0.030	0.015	0.103	282.00	282.00	0.002	0.001
0.036	115.00	115.07	-0.065	-0.057	0.071	199.00	198.97	0.031	0.015	0.104	283.00	283.00	0.005	0.002
0.037	116.00	116.07	-0.066	-0.057	0.071	200.00	199.97	0.032	0.016	0.104	284.00	283.99	0.007	0.002
0.037	117.00	117.07	-0.067	-0.057	0.071	201.00	200.97	0.032	0.016	0.105	285.00	284.99	0.009	0.003
0.038	118.00	118.07	-0.068	-0.058	0.072	202.00	201.97	0.032	0.016	0.105	286.00	285.99	0.012	0.004
0.038	119.00	119.05	-0.051	-0.043	0.072	203.00	202.97	0.031	0.015	0.105	287.00	286.99	0.014	0.005
0.038	120.00	120.05	-0.049	-0.041	0.073	204.00	203.97	0.030	0.015	0.106	288.00	287.98	0.016	0.006
0.039	121.00	121.05	-0.053	-0.044	0.073	205.00	204.97	0.029	0.014	0.106	289.00	288.98	0.018	0.006
0.039	122.00	122.06	-0.057	-0.047	0.073	206.00	205.97	0.027	0.013	0.107	290.00	289.98	0.020	0.007
0.040	123.00	123.04	-0.042	-0.035	0.074	207.00	206.98	0.024	0.012	0.107	291.00	290.98	0.022	0.007
0.040	124.00	124.04	-0.043	-0.035	0.074	208.00	207.98	0.022	0.010	0.107	292.00	291.95	0.046	0.016
0.040	125.00	125.05	-0.049	-0.039	0.075	209.00	208.98	0.019	0.009	0.108	293.00	292.95	0.050	0.017
0.041	126.00	126.04	-0.036	-0.029	0.075	210.00	209.98	0.015	0.007	0.108	294.00	293.95	0.052	0.018
0.041	127.00	127.04	-0.039	-0.030	0.075	211.00	210.99	0.011	0.005	0.109	295.00	294.95	0.053	0.018
0.042	128.00	128.03	-0.027	-0.021	0.076	212.00	211.99	0.007	0.003	0.109	296.00	295.95	0.055	0.018
0.042	129.00	129.03	-0.031	-0.024	0.076	213.00	213.00	0.002	0.001	0.109	297.00	296.94	0.056	0.019
0.043	130.00	130.04	-0.040	-0.031	0.077	214.00	214.00	-0.003	-0.001	0.110	298.00	297.92	0.080	0.027
0.043	131.00	131.03	-0.030	-0.023	0.077	215.00	215.01	-0.009	-0.004					

## Appendix J

### DAQ Software Documentation

GM DAQ 1.0 is the data acquisition program used in the experiments presented in this thesis. This program was developed using LabView™ 3.1.1 to monitor the operation of a two-stage GM cryocooler.

During operation, four SCXI channels are continuously scanned, the PAUSE control specifies the time (in minutes) between scans. Data files are written as tab separated ASCII text. The data consist of elapsed time, the raw data (in volts) and the processed temperatures. Additional comments and experimental details can also be added by the user. The following sections include some details about the SubVIs included in the program. Although the original version was written and compiled using LabView 3.1.1, the program should also run under higher versions (4.0, etc.). Some minor modifications to the open/close file dialog boxes may be required. Although most of the controls and indicators in GM DAQ 1.0 are self-explanatory, the following sections include a detailed description of the most important items accessible to the user via the graphical interface.

#### J.1 List of SubVIs

Sub VIs are independent code modules that can be used to build more complex applications. The following sections describe some of the most important VIs used in GM DAQ 1.0.

##### J.1.1 AI Config.vi

This VI configures the hardware and allocates a buffer for a buffered analog input operation for a specified group of channels. Before performing any configuration, AI Config checks to see if the input cluster error in indicates that an error has already

occurred. If so, then this VI does no configuration, but passes the error information unmodified through error out. In an error condition, taskID is 0.

Otherwise, this VI calls several low-level analog input VIs to set up a task for a buffered analog input acquisition. AI Config calls Analog Input Group Config for the specified device, group, and channels to create a taskID. AI Config then calls Analog Input Hardware Config to record information about the hardware configuration. The input limits input passes to Analog Input Hardware Config, which sets up the lower and upper voltage limits for each channel; if unspecified, the input limits do not change. This VI configures the number of AMUX boards, the coupling used for each channel (that is, AC, DC, ground, or internal reference), and the input configuration (differential, referenced single-ended, or non-referenced single ended). You can use the low-level Analog Input Hardware Config VI instead if you prefer to specify the input signal range in terms of signal range, polarity, and gain.

### **J.1.2 AI Start.vi**

This VI starts a buffered analog input operation. This VI sets the scan rate and trigger conditions and then starts an acquisition. AI Start first checks to see if the input cluster error in indicates that an error has already occurred. If so, this VI does not start an acquisition, but passes the error information unmodified through error out.

Otherwise, this VI calls several lower-level analog input VIs to start the buffered analog input acquisition. AI Start calls Analog Input Clock Config for the specified taskID to configure the acquisition to use the specified scan clock source (internal by default) and the specified scan rate.

AI Start then calls Analog Input Trigger Config to set a trigger according to trigger type. If trigger type is 0, then it clears the trigger; otherwise it sets the specified type of trigger.

Finally, AI Start calls Analog Input Control to start the acquisition, using total scans, pretrigger scans, and number of buffers to acquire to determine how much data to acquire.

### **J.1.3 AI Read.vi**

This VI reads data from a buffered data acquisition. Before reading any data, AI Read checks to see if the input cluster error in indicates that an error has already occurred. If so, this VI does not read any data, but passes the error information unmodified through error out. Otherwise, this VI calls the Analog Input Buffer Read VI to read the specified amount of data from a buffered analog input acquisition.

### **J.1.4 General Error Handler.vi**

This error handler is used primarily to inform the user if an input error exists, to describe the error, and to identify where it occurred. The information for this is derived from the inputs error in, error code, and error source, and from an internal error description table. The table describes all errors that can be created by LabVIEW or its associated I/O operations. The handler has provisions to take alternative actions, such as to cancel or set an error status, and to test for and describe user-defined errors.

### **J.1.5 V2T CFS.vi 1.1**

V2T CFS.vi is a general purpose voltage to temperature conversion program specifically developed to convert voltage reading into temperature values. The expected inputs are voltage arrays. The outputs are temperature values in kelvins. The transfer functions for different cryogenic temperature sensors can be easily replaced the main conversion module. The different temperature ranges for the sensors can be discriminated by the parameters controlling the True/False statements before each conversion. Lastly, possible offsets (ground loops, power supplies, etc.) can be compensated in software just before the mean voltages are converted into temperatures.

The possible noise in the voltage arrays is filtered out by taking their mean value. This is particularly important for the T-waves during the normal operation of the GM cryocooler.

These waves are essentially sinusoidal and their frequency follows the frequency of operation of the GM device. In this way, the final temperature is the time-average of the temperature during one or more full cycle(s).

The normal levels of AC superimposed noise have been partially removed by the DAQ hardware.

## **J.2 Front Panel Controls**

The following list contains the descriptions for some of the most important controls in GM DAQ 1.0.

### **Control #1:device (1)**

Data Type: word

The device number is the ID number of the plug-in data acquisition card to be used for the acquisition. You can check the device numbers using the configuration utility. The configuration utility displays a board number or slot number next to each National Instruments board; you use that number as the device number for the board.

### **Control #2:channels (0)**

Data Type: 1-D array of string

The channels string array contains the list of input channels to scan. To read an onboard data acquisition channel, type in that channel number. To read a range of input channels, the user can type the first and last channels to read, separated by a colon; for example 0:3 samples channels 0,1,2, and 3. If an SCXI module is used, type the following string to read channel 0 on module 1 in SCXI chassis 1:

```
ob0 ! sc1 ! md1 ! 0
```

To read channels 0 through 3 use the following string:

```
ob0 ! sc1 ! md1 ! 0:3
```

Refer to the Getting Started with SCXI section in chapter 1 for more information on SCXI channel strings. If you are using AMUX-64T boards, use the following string to read channel 0 on AMUX board 1:

```
am1!0
```

To scan multiple AMUX-64T channels, use the onboard channel numbers that map to the desired AMUX channels. Each onboard channel maps to 4 channels on each AMUX board. Onboard channel 0 maps to channels 0 through 3 on each AMUX board, onboard channel 1 maps to channels 4 through 7 on each AMUX board, and so on.

**Control #3:scan rate**

(4000 scans/sec)

Data Type: single

Description: the scan rate determines how many scans per second to acquire. Because all channels in the channel list are sampled during each scan, each channel is sampled at the chosen scan rate.

**Control #4:number of scans to acquire**

Data Type: long

Description: a scan is defined as a reading taken from each channel in the channel list, taken in the order specified. The number of scans to acquire is the number of times to scan through all channels in the list; which also is the number of samples to acquire from each channel in the list.

**Control #5:FROM**

Data Type: double

Description: controls the first channel to read from the SCXI module

**Control #6:TO**

Data Type: double

Description: controls the last channel to read during one scan.

**Control #7:Stop Operation**

Data Type: boolean

Description: stops program operation, closes any open files.

**Control #8:PAUSE (min)**

Data Type: double

Description: controls the time between two successive scans (in minutes)

**Control #9: CONTINUOUS**

Data Type: boolean

Description: control for continuous or single scan operation.

**Control #10:T-WAVE AT**

Data Type: double

Description: controls the channel from which data from a single scan is acquired and stored (i.e., all data points in during that scan are written to a file).

**Control #11:OFFSET**

Data Type: double

Description: manual compensations for floating grounds and/or offset voltages (not used).

**Control #12:COMMENTS FOR T-WAVE**

Data Type: string

Description: comments to be added to the header of the data file containing the voltage data collected in a single scan (see T-WAVE AT)

**Control #13:PHigh**

Data Type: string

Description: comment specifying the high pressure measured in the supply line to the cryocooler.

**Control #14:PLow**

Data Type: string

Description: comment specifying the low pressure measured in the return line to the cryocooler.

**Control #15:Qc1**

Data Type: string

Description: comment specifying the electrical power delivered to the first stage of the cryocooler. This information is written to the data file containing the voltage and temperature data.

**Control #16:Qc2**

Data Type: string

Description: comment specifying the electrical power delivered to the second stage of the cryocooler. This information is written to the data file containing the voltage and temperature data

---

**Control #17:REG#**

Data Type: string

Description: comments required to identify the regenerator being used (REG1, REG2, etc.).

**Control #18:FREQ**

Data Type: string

Description: comments identifying the frequency of operation as set by the motor controller included with the helium compressor.

**Control #19:Comments**

Data Type: string

Description: any additional comments.

**J.3 Indicators****Indicator #1:transposed voltage graph**

Data Type: 2-D array of single

Description: A Waveform Graph of the voltages acquired from the channel(s) specified in the channel list.

The Transpose Array option is turned on to put the 2D array of analog input data in row-major order. When an analog input VI returns a 2D array of data, the first dimension indexes the scans, and the second dimension indexes the channels; this is column-major order because the data for a particular channel is in a column. The Waveform Graph and X-Y Graph expect data in row-major order, so you must use the Transpose Array option.

**Indicator #2:DATA FILE**

Data Type: file path

Description: location of the current data file.

**Indicator #6:ELAPSED TIME**

Data Type: string

Description: a clock showing the time elapsed since execution was initiated.

**Indicator #7:DATE & TIME**

Data Type: string

Description: date and time

**Indicator #10:TEMPERATURE (K)**

Data Type: 2-D array of double      Description: Converted temperature values

## Appendix K

# Variable Temperature and Field Cryostat

A detailed knowledge of material properties at low temperatures is indispensable for the design of cryogenic equipment. Heat capacity measurements, for example, were crucial for the development of RE/TM alloys that improved the performance of two-stage GM cryocoolers below 10 K (see Chapter 2). In the particular case of magnetic refrigeration systems, the properties of materials at low temperatures must be studied taking into consideration their responses to externally applied magnetic fields. The measurement of material properties under these conditions requires specialized hardware that allows precise control of both, temperature and magnetic field intensity. Traditional characterization systems complying with these requirements have relied on liquid cryogenics to operate the SCM systems, and to provide the cooling required by material samples.

This chapter describes the conceptual design of a cryogen-free materials characterization apparatus for low temperatures and high magnetic fields. Unlike currently available systems based on liquid cryogenics, this piece of hardware uses a modified GM cryocooler to cool a SCM system and the associated thermal shields. This device will be used to investigate a variety of new candidate materials for passive regenerators in GM cryocoolers, AMRLs, and other regenerative refrigeration systems. Amorphous magnetic refrigerants, for example, are an important class of materials currently being developed by the Cfs group at the University of Victoria. This is part of an ongoing collaborative research effort with the Université du Québec à trois Rivières. Amorphous materials have many unique properties that make them excellent candidates for MR applications. Some of these properties include:

- Tailorable Curie temperatures;
- Lower coercive force with correspondingly lower hysteresis loss [156];

- Higher electrical resistivity and thus smaller eddy currents when exposed to an externally Applied magnetic field [157];
- Better corrosion resistance [158]; and,
- High strength and good ductility.

These material characteristics are superior to those found in crystalline or intermetallic compounds but no work has been reported on the application of amorphous magnetic material to specific MR systems. In addition, many important properties of these materials remain unexplored ( $C(T,H)$ ,  $\chi(T,H)$ ,  $\Delta T_{ad}(T,H)$ , etc.). The characterization system described in the following sections will be used to investigate many of these important material properties.

## **K.1 Comparison with Current Technologies**

Commercial versions of dedicated materials characterization devices include the Physical Property Measurement System (PPMS<sup>®</sup>) available from Quantum Design<sup>™</sup> [159] and the Maglab<sup>2000®</sup> and PulseLab<sup>®</sup> systems from Oxford Instruments<sup>™</sup> [160]. These two platforms include some of the most advanced technology currently available. In general, there are five main components in each of these systems:

- a superconducting solenoid;
- a liquid helium cryostat;
- an experimental insert;
- a magnet support assembly and radiation shields; and
- a computerized control unit.

In most cases, the measurement of different material properties is automated and uses specialized data acquisition and control software. Figure K-1 shows a commercially available magnetometer for high magnetic field intensities (0 to 16 T) and temperatures between 2 and 1000 K [160].

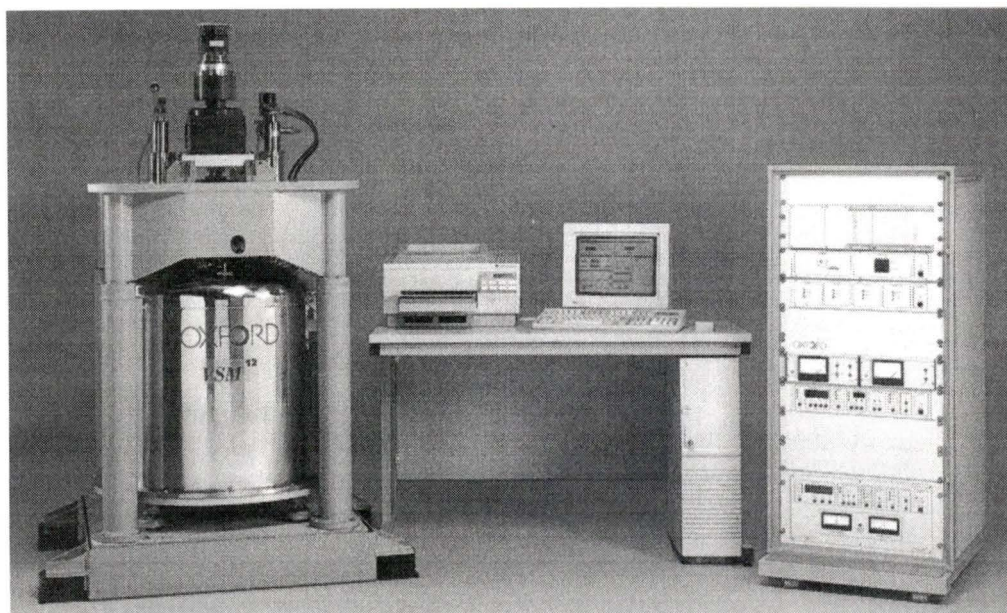


**Figure K-1: The Maglab<sup>VSM®</sup> magnetometer from Oxford Instruments<sup>TM</sup>.**

In typical applications, the measurement of different material properties can be carried out using a dedicated measurement insert, or by modifying built-in circuitry that interfaces directly with the control modules in each apparatus. The PPMS<sup>®</sup> uses a permanent wiring system with electrical connections at the bottom of the sample chamber. The built-in circuitry consists of twelve hard-wired leads that provide three current supply pairs with the corresponding voltage probes. This makes it possible to perform three separate four-wire measurements or to implement a custom-designed circuit layout. These connections can be used by multiple sample “pucks” dedicated to analyze different material properties (heat capacity, hall effect, resistivity, etc.). The material samples are mounted on these pucks and then wired to make contact with the built-in electronics (see Figure K-2).

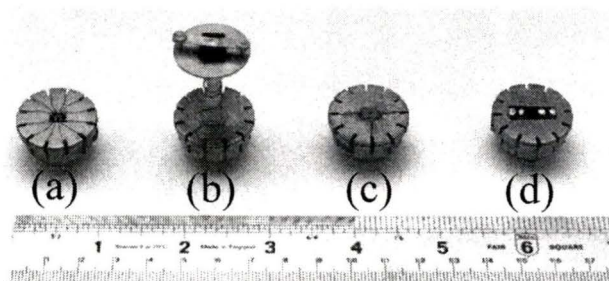


**Figure K-2: Sample pucks used in the PPMS<sup>®</sup>. The samples in the picture have been wired to perform four different types of measurement: electrical properties of a SQUID (a), heat capacity (b), Hall effect (c), and electrical resistivity (d).**

After the samples have been mounted, the puck is lowered into the experimental compartment and locked into place at the bottom of the chamber. The electrical connectors also function as conductive paths to provide sample cooling (see Figure K-3).

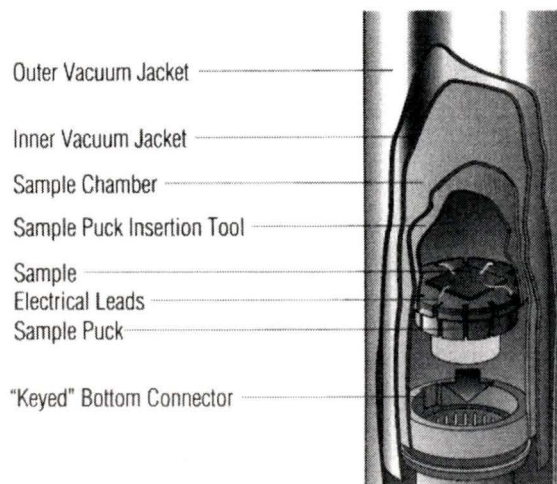


**Figure K-3: The sample space in the PPMS<sup>®</sup>.**

The PPMS can be controlled from extensive command menus available from a main control panel. Additional options include Windows<sup>™</sup>-based software and general purpose interface boards (GPIBs) that can be used with a computer running user-defined programs (i.e., non-proprietary software written in C, C<sup>++</sup>, VirtualBasic<sup>™</sup>, etc.).

The PulseLab<sup>®</sup> and Maglab<sup>2000®</sup> systems use individual inserts to measure different material properties (see Figure K-4) Each of these inserts can be easily exchanged to perform magnetic, thermal, and electrical property measurements. The experimental capabilities in a MagLab<sup>2000®</sup> device, for example, include AC susceptibility, critical current measurement, adiabatic and thermal relaxation calorimetry, AC/DC resistivity, and cantilever magnetometry. Each of these options is also available as a separate, single purpose apparatus. All these systems are controlled from a proprietary software package (Oxford ObjectBench 2000<sup>™</sup>) running under the Windows 95<sup>™</sup> operating system. This package includes a series of preconfigured experimental routines and device drivers for each of the experimental inserts. Additional routines can also be programmed via an imbedded programming language (Microsoft Virtual Basic<sup>™</sup>).

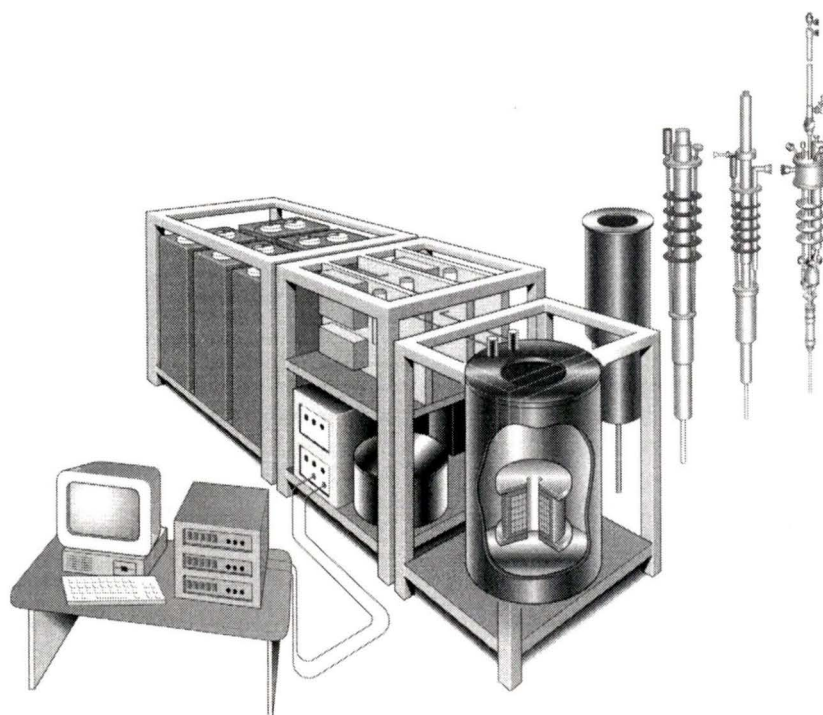


**Figure K-4: A schematic representation of the Pulselab<sup>®</sup> system from Oxford Instruments<sup>™</sup>.**

Providing liquid cryogens for superconducting magnets can be expensive and inconvenient. Although the systems described thus far are fully automated, the refilling and maintenance procedures still require regular operator intervention. In addition, special considerations are needed for the safe storage, delivery and handling of liquid cryogens. SCM systems using a mechanical cooler instead of liquid cryogen baths provide an attractive alternative to reduce operating costs and facilitate the design of truly automated systems. This idea has recently received some attention by commercial manufacturers.

The Cryofree<sup>®</sup> magnet system from Oxford Instruments<sup>™</sup>, for example, makes use of a modified GM cryocooler (Balzers KelCool<sup>™</sup> 4.2 GM) to cool a low-temperature SCM powered by high- $T_c$  current leads. This cryocooler uses Nd particles in the second-stage regenerator. More recent versions make use of spherical RE/TM particles as the regenerator material and provide larger cooling capacities at low temperatures [161]. Sample cooling is achieved by allowing an exchange gas (helium) into the sample space.

The standard systems offer large size (10 cm), room-temperature bores with optional inserts for variable temperature applications (see Figure K-5). The temperature range, however, is currently limited to temperatures above 40 K. Current research efforts at Oxford Instruments™ are aimed at extending this temperature range to include sub-liquid helium temperatures [161]. .

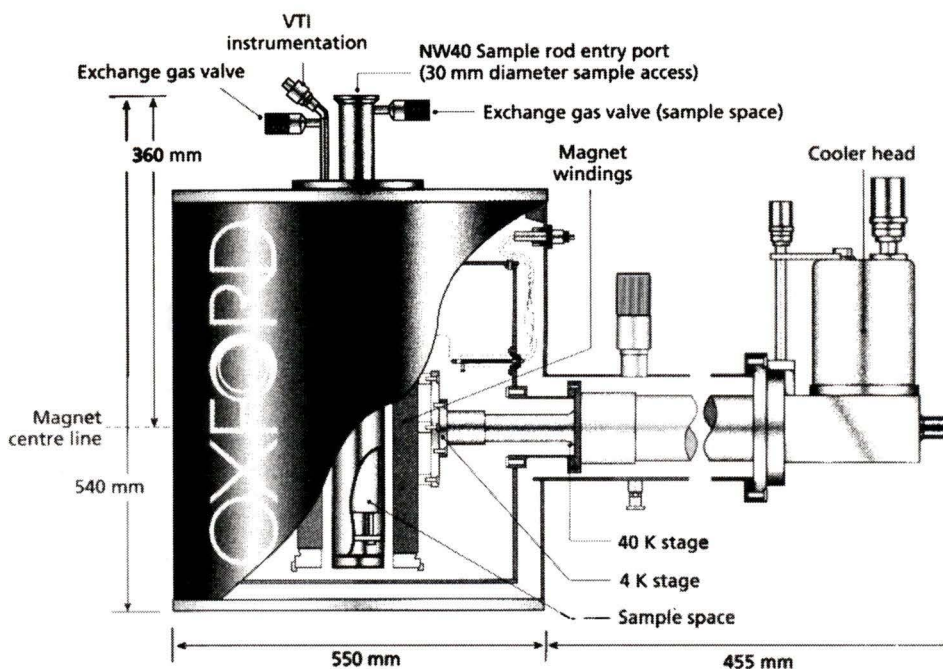


**Figure K-5: A cryogen-free SCM system with a variable temperature insert.**

The following sections describe the conceptual design of a materials characterization system that uses some of these ideas but is based on a novel approach for sample cooling. The design of an entire unit for heat capacity measurement is complete, but none of the components described in the following sections has been built yet. Although this device was originally designed for internal use at the University of Victoria, its potential commercial value could make it a good competitor for similar systems described in previous sections.

## **K.2 A Novel Cryogen Free Materials Characterization System (CFMCS).**

This thesis reports on the development of a novel, cryogen-free materials characterization system based on the modified two-stage cryocooler described in previous chapters. Because the manufacturing costs of the second-stage regenerator have been drastically reduced, the cooling system in the CFMCS can be potentially cheaper than other systems based on spherical particles of RE/TM alloys. Another feature that differentiates this device from existing technology is the way in which the sample is cooled: instead of a static heat-exchange fluid, a continuous flow of helium is used for temperature control (see Section 2). Lastly, the CFMCS has been designed to allow different material samples or even entire experimental inserts to be exchanged without interrupting the operation of the SCM or the flow of helium gas. This minimizes the down-time between different experiments and allows the measurement of the same property on many samples, or the characterization of many samples with different inserts.

The application of a mechanical cooling system for materials characterization also makes it possible to design completely automated systems that can run for long periods of time with little or no maintenance. Manual sample and insert exchange are still required for the CFMCS, but future versions could have a robotic carousel or a multiple sample/insert holder to automate this task. The CFMCS uses readily available materials and components. The only non-standard part is the second-stage regenerator in the GM cryocooler. This component, however, can be easily manufactured using the new techniques developed as part of this thesis (please refer to Chapter 4 for details).

Figure K-6 shows a schematic of the CFMCS currently under development at the Cfs laboratories. As stated before, a modified two-stage GM cryocooler provides the cooling for the superconducting magnet system, the current leads, and the associated thermal shields.

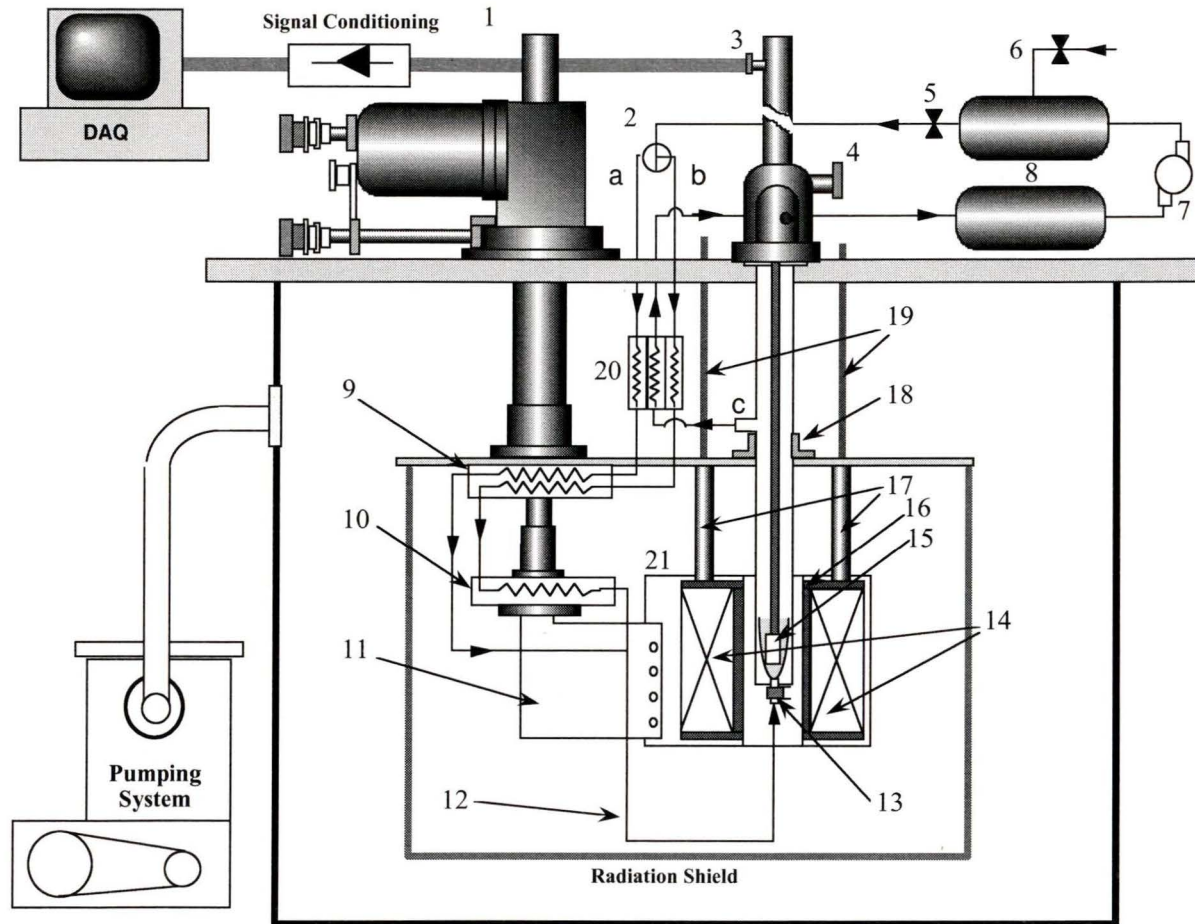


**Figure K-6: A conceptual representation of the CFMCS currently under development at Uvic. GM cryocooler (1), Flow control valve (2), Instrumentation port (3), Pumping port (4), Flowrate control valve (5), Purge/filling valve (6), Diaphragm compressor (7), Gas reservoirs (8), First stage heat exchangers (9), second-stage heat exchanger (10), OFHC conductive path (11), Helium line (12), Gas heater (13), magnet coils (14), Sample holder (15), Magnet bobbin (16), High  $T_c$  current leads (17), Heat switch (18), Current leads (19), Counterflow heat exchanger (20), Magnet outer jacket (21).**

The conductive pathway for the magnet consists of an oxygen-free copper jacket that surrounds the magnet coils and bobbin, and is attached to the second stage of the cryocooler. Similar conduction-cooling systems for SCMs have recently become available and have been proven to provide satisfactory results (see Chapter 2).

Heat exchangers located at the first and second stages cool a continuous stream of low-pressure helium gas. The gas is recirculated by an oil-free diaphragm compressor and it provides the cooling required by material samples. A two-way valve directs the gas flow to two alternative routes. If the temperature range of interest is above 40K, the second stage heat exchanger is bypassed (path **a** in Figure K-6). If lower temperatures are required, the gas stream passes through the second stage heat exchanger (path **b** in Figure K-6). Although this implementation requires a redundant heat exchanger at the first stage, the need for a cryogenic valve is eliminated thereby simplifying the overall design and reducing costs. An electric heater located at the bottom of the sample space will be used to warm the incoming gas thereby controlling sample temperature. The helium gas is collected at point **c** in Figure K-6 and passed to a counterflow heat exchanger that pre-cools the incoming helium stream. The gas then enters a low-pressure buffer volume before being delivered to the compressor for recirculation.

Different material properties can be measured by dedicated experimental insert with the appropriate instrumentation. Each of these inserts is completely independent of the CFMCS and can be easily exchanged without interrupting the operation of the SCM or the flow of helium gas. Sample exchange is accomplished by a gate valve that isolates sample-exchange chamber from the low temperature sample space. This is the only operation that has to be performed manually at this stage in the design. The following sections give a more detailed description of the main subsystems within the CFMCS.

## K.2.1 Superconducting Magnet Subsystem

One of the main design criteria for the CFMCS consisted of using readily available components and materials as much as possible. The SCM specified in the design should provide at least a 2½ in (63.4 mm) clear bore to accommodate the stainless steel tube into which each of the experimental inserts will be lowered. Additional components must include a persistent-mode switch, a quench control and protection system, high- $T_c$  current leads, and a DC power supply to charge the magnet. Table K-1 shows some of the detailed specifications for the SCM.

**Table K-1: Design specifications for the SCM subsystem in the CFMCS.**

<b>Maximum field intensity</b>	8-10 T
<b>Inner bore diameter</b>	2½ - 3.0 in
<b>Field Uniformity</b>	± 0.5% Longitudinal (4 cm) ± 1.0% Transverse (2.0 cm)
<b>Power supply</b>	0-10 V, 0-100 A (DC). IEEE-488 or GPIB compatible Programmable
<b>High-<math>T_c</math> current leads</b>	≥ 30 cm
<b>Persistent mode switch and quench protection system</b>	To be included by manufacturer

All of these specifications can be satisfied by currently available commercial SCM systems. The only non-standard characteristic of the SCM in the CFMCS is the way in which the magnet is cooled (i.e., using a cryocooler instead of liquid cryogen). This approach, however, has been successfully used to cool similar SCM systems (for more details, refer to Section ).

## K.2.2 Sample Cooling Loop

The temperature of material samples will be controlled by a continuous flow of helium gas. The mean pressure inside the loop will be adjusted by partially evacuating or charging the buffer volumes at either side of the compressor. Lower mean pressures (~50 kPa) will be used for measurements requiring temperatures below the normal boiling point of helium (4.2 K). The gas will be cooled by two heat exchangers located at the first and second stages of the GM cryocooler. These heat exchangers will be made of

thin-wall ( $3/32$ " OD,  $0.020$ " wall thickness), oxygen-free copper tubes wound around a bobbin of the same material. High conductivity solder will be used to ensure good thermal contact between the bobbins and the tubing. The bobbins will be attached to the first and second-stage flanges of the cryocooler following the procedures described in Chapter 3. The rest of the loop will be completed with thin wall stainless steel tubing. This tubing will connect the heat exchangers to the insert space and the other components in the cooling loop (compressor, valves, buffer volumes, etc.). The flow of helium will be controlled by partially opening or closing a valve in series with the helium loop circuit. Alternatively, the flow could be controlled by a DC-powered compressor.

Figure K-7 shows a partial view of the cooling loop and the way in which the heat exchangers are attached to the first and second-stages of the cryocooler. The connections between the two heat exchangers consist of helicoidal stainless steel tubes.

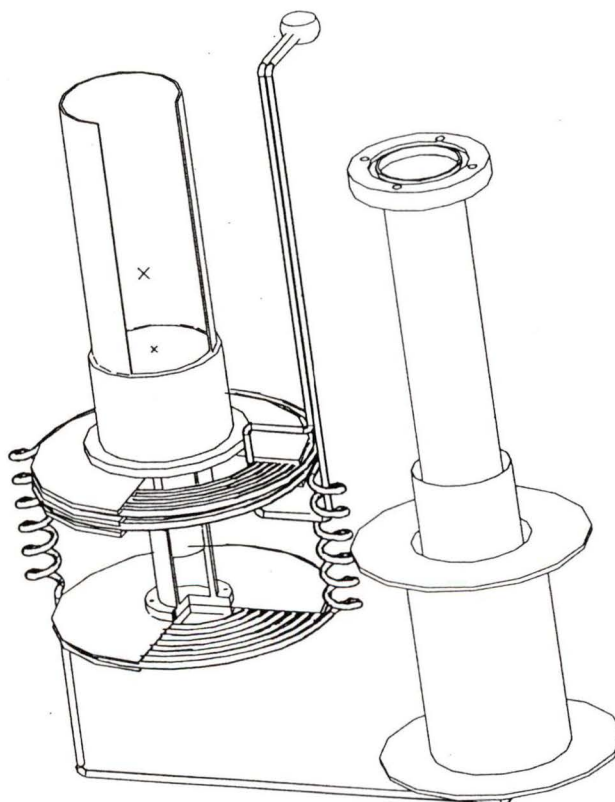


**Figure K-7: Heat exchangers will be attached to the first and second stages of the cryocooler.**

Although it is difficult to bend thin wall tubes without buckling, straight connections have been avoided for two main reasons:

- to increase the overall length between the first and second stage heat exchangers (thereby reducing conductive heat leaks), and
- to accommodate for the possibility of differential thermal contraction on different parts of the helium circuit.

Techniques to bend thin wall tubes include filling them with sand during the forming process or using thermal clamps to soften the metal. Another possibility consists of filling the tubes with water, freezing the water, and then using normal tube bending equipment.

Preliminary calculations for a heat capacity insert have shown that a helium flowrate of  $3 \times 10^{-5}$  kg/s at a mean pressure of 50 kPa will be sufficient to cool a small sample ( $\sim 15$  g) from room temperature to 4 K in about 4 hours [162]. Higher flowrates will be used at the beginning of each cooling run and then gradually reduced as the cooling power in the GM cryocooler decreases with temperature. The total pressure drop across the helium loop will depend on the specific insert being used but a pressure differential of about 45 psi () will be sufficient to maintain the required flow of helium in most applications.

### **K.2.3 Sample Exchange Chamber**

Different samples can be easily and quickly exchanged by accessing an independent chamber located at the top of the insert space. This chamber is isolated by a gate valve that separates it from the insert space and the helium circuit. An independent pumping port allows the evacuation of the chamber and can also be used to fill the chamber with helium gas during sample exchange.

### K.3 Experimental Insert

The first experimental insert for the CFMCS has been completely designed. This insert will be used to measure the heat capacity of solids as a function of both temperature and applied magnetic field. The temperature range of operation lies between 4 and 300 K with magnetic field intensities of up to 9 T. This insert uses adiabatic calorimetry techniques based on the heat pulse method [163][164][165][166]. This method involves bringing a sample of known mass to a given temperature. Once the desired temperature has been reached, the sample is thermally isolated and a short heat pulse from an external energy source is applied. This is typically accomplished by delivering a known amount of electrical power for a short period of time. The difference between the equilibrium temperatures before and after the heat pulse can be used to calculate the heat capacity of the material. The quantities of interest are related in the following manner:

$$C_p = \frac{Q_{in}}{m_s(T_f - T_i)}$$

#### Equation K-1

In most cases it is necessary to perform a calibration to account for the heat capacity of the sample holder and other peripheral components. This process involves determining the heat capacity of the calorimeter without a sample. The measured values are then included in the calculation of individual  $C_p$  values for different materials.

Figure K-8 shows a detailed assembly drawing for the heat capacity insert. There are three concentric cylindrical containers at the bottom of the insert. The innermost container is the sample holder. This container will be made of oxygen-free, high purity copper (OFHC) and will be supported by Nylon threads. During each of the measurements, these threads will be the only thermal connection between the sample holder and its surroundings. A heater made of AW32 Nichrome wire will be wound around this cylinder to apply the heat pulse described before. The next container is a radiation shield that surrounds the sample holder and is made of highly polished OFHC.

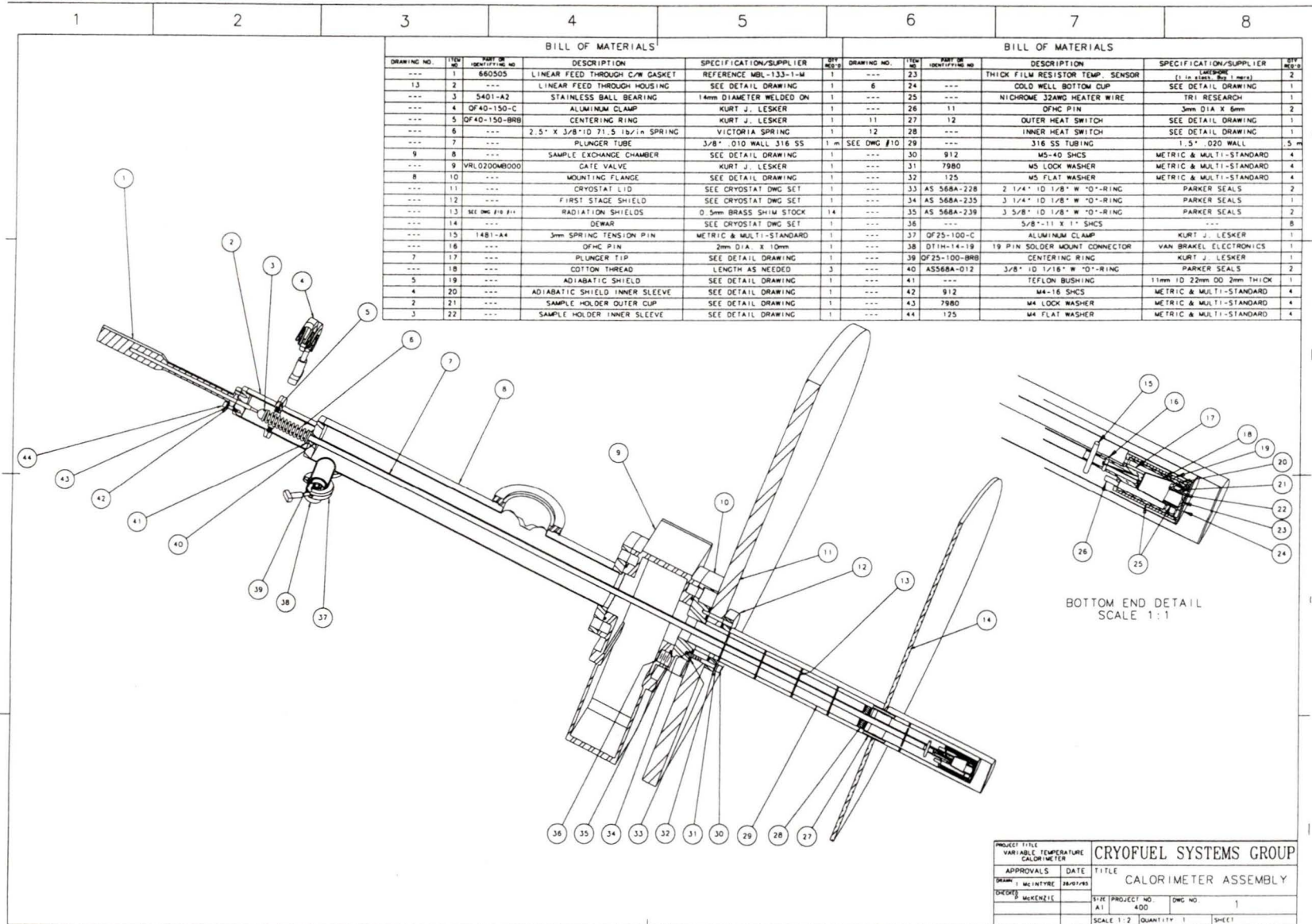
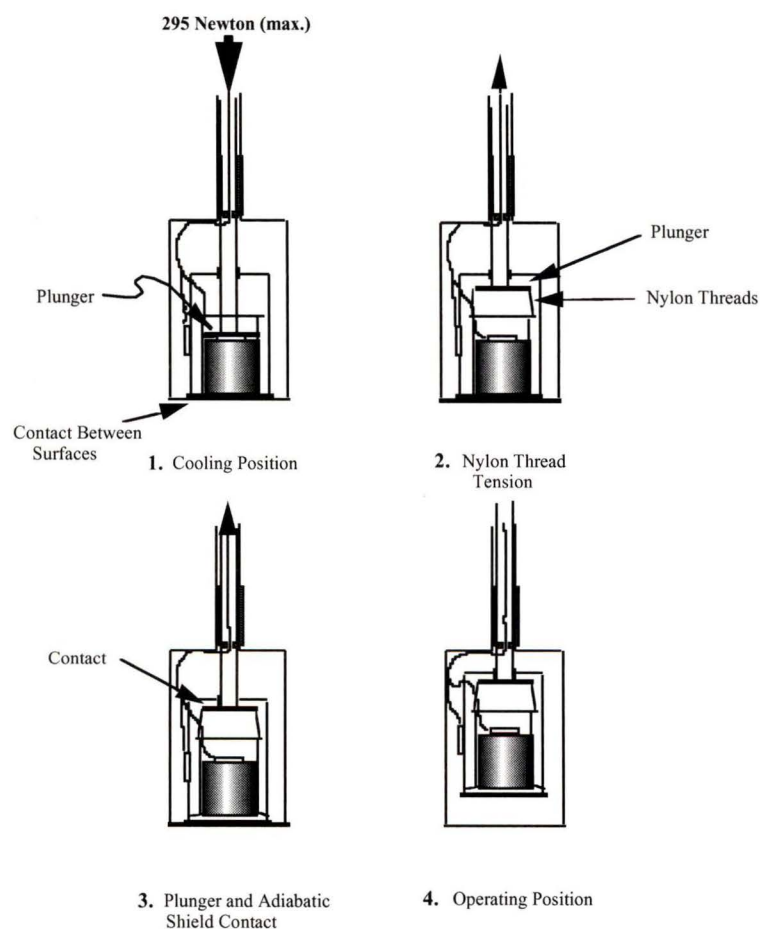


Figure K-8: Assembly drawing for the experimental insert designed to measure heat capacity.

A second heater around this container will be used to keep its temperature as close as possible to the temperature in the sample holder. This will prevent radiative heat leaks from the sample space. The third container is the overall insert enclosure. During operation, this enclosure will be evacuated via the pumping port above the sample exchange compartment (item 9 in Figure K-8). By doing this, the inner contents of the insert will be isolated from the helium flow.

There are two operating positions for the sample holder: the cooling position and the measuring position (see Figure K-9). In the cooling position, the sample is firmly pressed down to maintain good thermal contact with the bottom of the sample holder, the adiabatic radiation shield, and the bottom of the outer enclosure. Each of these surfaces (except from the sample itself) will be made of OFHC.



**Figure K-9: Cooling and measurement positions for heat capacity measurements.**

Sample cooling will be achieved by the impinging stream of helium gas entering at the bottom of the insert space. The contact pressure will be applied by a linear motion feedthrough and transmitted to the sample by a stainless steel tube with an extension of low conductivity material (the plunger). The maximum pressure that will be applied is approximately 300 N. The linear motion of the feedthrough will be controlled manually or via a motor actuator. The sample holder will be maintained in this position until the desired temperature is reached. Once the cooling process is completed, the pressure will be removed and the sample container will be lifted to the measuring position. In this position, the sample holder will be maintained in position by additional nylon threads attached to the bottom of the adiabatic radiation shield. At this point the sample holder is essentially isolated from its surroundings and testing can be initiated.

Additional material properties can be measured by designed the appropriate experimental inserts. Some of the most important properties to consider include magnetic susceptibility, adiabatic temperature change due to the MCE, thermal conductivity, electrical resistivity, etc. The design for the heat capacity insert can be easily modified to perform these measurements.

#### **K.4 Instrumentation**

Two types of transducers will be used in the CFMCS: permanent and measurement-specific. Permanent sensors will be used to monitor the operation of the magnet system, the flow and temperature of helium gas, and the temperatures at the first and second stage of the GM cryocooler. Measurement specific sensors should be included in the design of each individual insert.

PRTs are recommended for temperature measurement above 30 K (second stage heat exchanger, current leads, radiation shields, etc.). Ga-Al-As diodes or carbon-glass resistors can be used to measure lower temperatures in areas exposed to moderate magnetic fields ( i.e., < 2.5 T). The temperature in the high magnetic field regions (2.5-10 T) should be monitored using different sensors.

Some thick-film temperature sensors provide satisfactory performance in the presence of high magnetic fields. Ruthenium dioxide resistors and the Cernox® family of resistive temperature sensors from LakeShore® are among the best options for high-magnetic field applications. RuO<sub>2</sub> resistors can be used to monitor the temperature of the SMC and current leads. These sensors are rugged and reliable but their response times are longer than those found in Cernox® sensors (see Table 5-2). A Cernox® sensor (model CX1030 or CX1070) has been selected as the best option to measure sample temperature under high magnetic fields. This type of sensor provides the lowest magnetoresistivity at low temperatures (4-20 K) as well as the fastest response time [167] when used as a bare chip (i.e., without a container). These chips can be relatively small (1.2 × 1.2 × 0.5 mm) [168]. This implementation is particularly appropriate for temperature measurement in small metal samples. At least two of these sensors will be required for the heat capacity measurement insert (one for the sample holder and one for the adiabatic radiation shield).

**Table K-2: Typical magnetic field-induced errors and thermal response times for different sensors.**

	Magnetoresistive errors (in Kelvins at T = 4.2 K)					Response times (ms)		
	2 T	7 T	8 T	10 T	20 T	4.2 K	77 K	273 K
1 kΩ RuO <sub>2</sub>	+ 0.042	--	+ 0.330	--	--	500	1300	NA
100 kΩ RuO <sub>2</sub>	+ 0.042	--	+ 0.330	--	--	1200	Noisy	Noisy
Cernox® CX-1030 <sup>a</sup>	+ 0.004	+ 0.030	--	+ 0.017	- 0.011	1.5	50	135
Cernox® CX-1070	+ 0.004	- 0.013	--	- 0.042	- 0.100	--	--	--

<sup>a</sup> Bare chip mounted

Magnetic field intensity can be measured using a Hall-effect probe permanently mounted inside the insert chamber. Individual magnetic field intensity sensors may be required for measurements.

## **K.5 Control System**

The ultimate design goal for the CFMCS is to build a truly automated device that requires little operator intervention and/or training. In an ideal case, the entire system (including the SCMs and the GM cryocooler) would be under computer control. Under these conditions, extensive self testing routines will be necessary to avoid improper use or catastrophic failure of the main components (SCM, GM cryocooler, etc.). This built-in intelligence should be an integral part of the SCMCS control system and independent of application-specific software. Initially, the degree of automation will probably be restricted to the measurement process itself, and the control software could be similar to that available in commercial systems.

If the CFMCS is successfully converted into a commercial product, the application specific software could be sold separately with each individual insert. This software could be an extremely valuable product requiring relatively low investment (e.g., once a given program has been written and tested it can be easily reproduced). Each of these software packages could be an extension or “plug-in” that interfaces with a main program sold with the basic unit. In this manner, potential users can decide to use pre-designed measurement subroutines or to implement their own programs.

Fourth-generation programming environments such as LabView™ or LabWindows™ are excellent options to generate the required software. Although the error-free operation of these programs is indispensable, they should also be flexible enough to accommodate individual user needs (i.e., the source code should not be completely inaccessible to users). Insert-specific drivers and hardware interfacing programs could be written in a lower level language such as C or C++. This could reduce execution time and memory requirements for programs performing real-time data acquisition.

## Vita

Surname: Mérida Donis

Given Names: Walter Roberto

Place of Birth: Guatemala City, Guatemala

### Educational Institutions Attended:

University of Victoria	1993 to 1996
Trent University	1989 to 1993
United World College of the Adriatic	1987 to 1989

### Degrees Awarded:

Bachelor of Science	Trent University	1993
International Baccalaureate	United World College of the Adriatic	1989

### Honours and Awards:

Connaught Scholarship	University of Toronto	1993
Trent C.I.D.A. Scholarship	Trent University	1989-1993
UWC Scholarship	UWC of the Adriatic	1987-1989

### Publications:

Mérida, W.R., Barclay, J.A., "Development of Monolithic Regenerator Technology for Low Temperature (4 K) Gifford-McMahon Cryocoolers", to be presented at the Cryogenic Engineering Conference, Portland, Oregon, USA (July 28 - August 1<sup>st</sup>, 1997).

Slavin, A.J., Narine, S., Mérida W.R., "Measuring Metal Oxidation Rates and Stoichiometry Using a Quartz Microbalance", Proceedings of the Canadian Association Of Physicists Conference, Ottawa, ON, Canada (1996).

Earnshaw, J., Mérida, W.R., "Measurement of the Thermal Conductivity Coefficient of  $\text{LiZr}_2\text{O}_3$  Beads", Proceedings of the Canadian Fusion Fuel Technology Project (CFFTP) Seminar, Chalk River, ON, Canada (1993).

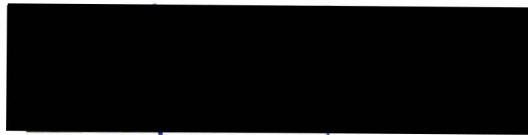
## Partial Copyright License

I hereby grant the right to lend my thesis to users of the University of Victoria Library, and to make single copies only for such users or in response to a request from the Library of any other university, or similar institution, on its behalf or for one of its users. I further agree that permission for extensive copying of this thesis for scholarly purposes may be granted by me or a member of the University designated by me. It is understood that copying or publication of this thesis for financial gain shall not be allowed without my written permission.

Title of Thesis:

Development of Monolithic Regenerator Technology for Low Temperature (4 K) Gifford-McMahon Cryocoolers.

Author:



Walter R. Mérida-Donis

November 4, 1997.